The Formation of Stellar Halos in Late-Type Galaxies

Agostino Renda

PhD Thesis

arXiv:1506.04238v1 [astro-ph.GA] 13 Jun 2015

The Formation of Stellar Halos in Late–Type Galaxies

by

Agostino Renda

A Dissertation
Presented in fulfilment of the requirements
for the degree of
Doctor of Philosophy
at Swinburne University Of Technology

May 2007

Abstract

Near–field observations may provide tight constraints - i.e. “boundary conditions” - on any model of structure formation in the Universe. Detailed observational data have long been available for the Milky Way (e.g., Freeman & Bland-Hawthorn 2002) and have provided tight constraints on several Galaxy formation models (e.g.: Abadi et al. 2003; Bekki & Chiba 2001). An implicit assumption still remains unanswered though: *is the Milky Way a “normal” spiral?* Searching for directions, it feels natural to look at our neighbour: Andromeda. An intriguing piece of the “puzzle” is provided by contrasting its stellar halo with that of our Galaxy, even more so since Mouhcine et al. (2005) have suggested that a correlation between stellar halo metallicity and galactic luminosity is in place and would leave the Milky Way halo as an outlier with respect to other spirals of comparable luminosities. Further questions hence arise: *is there any stellar halo–galaxy formation symbiosis?* Our first step has been to contrast the chemical evolution of the Milky Way with that of Andromeda by means of a semi–analytic model. We have then pursued a complementary approach through the analysis of several semi–cosmological late–type galaxy simulations which sample a wide variety of merging histories. We have focused on the stellar halo properties in the simulations at redshift zero and shown that - at any given galaxy luminosity - the metallicities of the stellar halos in the simulations span a range in excess of ~ 1 dex, a result which is strengthened by the robustness tests we have performed. We suggest that the underlying driver of the halo metallicity dispersion can be traced to the diversity of galactic mass assembly histories inherent within the hierarchical clustering paradigm.

Acknowledgements

Whether we are still on speaking terms or not, I thank all the people, dispersed all over this planet, without whom this thesis would not have been, neither completed, nor written.

Among them, I thank my supervisors, Brad Gibson and Daisuke Kawata, and Mustapha Mouhcine, for their unfaltering support and encouragement through difficult times.

Declaration

This thesis contains no material that has been accepted for the award of any other degree or diploma. To the best of my knowledge, this thesis contains no material previously published or written by another author, except where due reference is made in the text of the thesis. All work presented is primarily that of the author.

Science is a collaborative pursuit, and the studies presented in this thesis are very much part of a team effort. The collaborators listed below have great experience and knowledge, and were all integral in obtaining the presented results:

Brad K. Gibson; Daisuke Kawata; Mustapha Mouhcine; Chris B. Brook;
Yeshe Fenner; Rodrigo A. Ibata; Amanda I. Karakas; John C. Lattanzio;
Simon C. Campbell; Alessandro Chieffi; Katia Cunha; Chris Flynn; Verne V. Smith.

Chapter 2 was published in

Renda A., Kawata D., Fenner Y., Gibson B.K.,
Mon. Not. R. Astron. Soc., 356, 1071 (2005)

Chapter 3 was partially published in

Renda A., Gibson B.K., Mouhcine M., Ibata R.A.,
Kawata D., Flynn C., Brook C.B.,
Mon. Not. R. Astron. Soc. Lett., 363, L16 (2005)

Appendix A was published in

Renda A., Fenner Y., Gibson B.K., Karakas A.I.,
Lattanzio J.C., Campbell S., Chieffi A., Cunha K., Smith V.V.,
Mon. Not. R. Astron. Soc., 354, 575 (2004)

Minor alterations and redistribution has been made to these studies
in order to maintain consistency of style throughout the thesis.

Agostino Renda

May 7, 2007

Contents

1 Introduction **1**

2 Contrasting the Milky Way and Andromeda **3**
2.1 Introduction 3
2.2 The model 5
2.2.1 Infall 7
2.2.2 Disc and halo surface density profiles 9
2.2.3 Star Formation Rate 10
2.3 The Milky Way model 10
2.4 The M31 models 14
2.4.1 M31a model: MW analogue 14
2.4.2 M31b model: our best model 15
2.4.3 M31c model: another possible model 18
2.5 Discussion 20
2.5.1 Prospect 22

3 The Halo Metallicity–Luminosity Relationship **25**
3.1 Introduction 25
3.2 Simulations 27
3.3 Results 28
3.3.1 Robustness 38
3.4 Discussion 51

4 Galaxy Mass Assembly since z $\sim$ 1 **57**
4.1 Introduction 57
4.2 Results 58
4.3 Conclusions 69

5 The Mass–Metallicity Relation since z $\sim$ 1. **71**
5.1 Introduction 71
5.2 Results 72
5.2.1 Gas–phase Oxygen abundance vs. stellar mass 73
5.2.2 Gas–phase Oxygen abundance vs. galaxy luminosity 79
5.2.3 Stellar metallicity/age vs. stellar mass 80

5.2.4 The Colour–Magnitude Relation 80
5.3 Conclusions 81

6 Conclusions and Future Directions 83

A The origin of fluorine in the Milky Way 89
A.1 Introduction 89
A.2 Nucleosynthesis of ^{19}F 90
A.2.1 Type II Supernovae 90
A.2.2 Asymptotic Giant Branch stars 91
A.2.3 Wolf–Rayet stars 92
A.3 The model 92
A.3.1 Fluorine yields 93
A.4 Results 95
A.5 Discussion 98

B Stellar Halo Metallicity Distributions 103

C Stellar Halo [O/Fe] Distributions 123

D Stellar Halo Age Distributions 141

E Galaxy Rotation Curves 159

F (Once More) Stellar Halo MDF 175

G Stellar Halo (V - I) Colour Distributions 187

H Halo MDF via Metallicity–Colour 203

Publications 232

List of Figures

2.1 Comparison between the results of the MW model (solid lines) and the observations of: "a" the MDF in the MW in the solar neighbourhood (closed boxes with error–bars, Kotoneva et al. 2002); "b" the halo MDF at $R = R_{\odot}$ (Ryan & Norris 1991, closed boxes with statistical Poissonian error–bars); "c" [O/Fe] and [Fe/H] for stars observed in the solar neighbourhood (Carretta et al. 2000, who included reanalysis of Sneden et al. 1991, Tomkin et al. 1992, Kraft et al. 1992, Edvardsson et al. 1993; Gratton et al. 2003; Bensby, Feltzing & Lundström 2003; Cayrel et al. 2003); "d" the present–day SFR in the solar neighbourhood as summarised in Rana (1991, the shaded region). . . 12

2.2 Radial distributions of the present–day hydrogen surface density (upper) and of the present–day oxygen (middle) and sulfur (bottom) abundances for the MW model (left) and the M31 models (right). In the left panels, the solid lines are for the MW model results. In the right panels, solid, dotted and dashed lines display the M31a, M31b and M31c models, respectively. The observed distributions of the total surface density of hydrogen for the MW are from Dame (1993, open boxes), and those for M31 are from Dame et al. (1993, open boxes) and Loinard et al. (1999, closed boxes). Observations of abundances in HII regions in the MW, from Vilchez & Esteban (1996) and Afflerbach et al. (1997) (closed and open boxes, respectively), are shown in the left panels. Those in M31, from Dennefeld & Kunth (1981) and Blair et al. (1982) (closed and open boxes, respectively), are shown in the right panels. 13

2.3 Radial profile of the present–day mean stellar metallicity of both disc (upper panel) and halo (lower panel). Solid, dotted and dashed lines represent the results of the M31a, M31b and M31c models, respectively. The mean metallicities from Bellazzini et al. (2003) are also shown (closed boxes with 1 σ dispersion of their MDF). 16

2.4 The MDFs of the M31b and M31c models (dotted and dashed lines, respectively). The MDFs observed from Bellazzini et al. (2003) are also shown (closed boxes). 17

3.1 The stellar halo metallicity–total galactic V–band luminosity relation ($\langle[\mathrm{Fe/H}]\rangle_{\mathrm{halo}} - \mathrm{M_V}$). A filled box corresponds to the peak of the MDF for a simulation. The related MDFs are displayed in Appendix B. Open (unlabelled) boxes represent the data of Mouhcine et al. (2005); labelled boxes represent additional data taken from the literature (see the text for details). 68% of the stars in the simulated (observed) MDFs are typically enclosed within ±0.7 dex (±0.35 dex) of the peak of the related MDF. 29

3.2 Upper panels: Projected distribution of the gas particles at redshift z = 1.5 for simulations with $\mathrm{M_{tot}} = 10^{12}\ \mathrm{M_\odot}$. Lower panels: The associated stellar age distributions at z = 0 for the galaxies in the upper panels. The solid (dotted) histogram corresponds to the stellar age distribution for the entire galaxy (stellar halo). The corresponding z = 0 halo metallicities are denoted in each panel. 31

3.3 Distributions of the z = 0 MDF peaks for the semi–cosmological simulations in Renda et al. (2005b) with $\mathrm{M_{tot}} =: 5\times10^{11}\ \mathrm{M_\odot};\ 10^{12}\ \mathrm{M_\odot};\ 5\times10^{12}\ \mathrm{M_\odot}$. 32

3.4 The relation between the mean stellar halo age and the peak of the halo MDF in our simulations. The halo ADFs are displayed in Appendix D. 33

3.5 The relation between the mean halo age and the mean age for the entire galaxy in our simulations. Both the halo and the galaxy ADFs for each simulation are displayed in Appendix D. 34

3.6 The relation between the peak of the halo [O/Fe] distribution and the peak of the halo MDF in our simulations. The related MDFs are displayed in Appendix B. The halo [O/Fe] distributions are displayed in Appendix C. 35

3.7 Upper panels: Stellar halo metallicity–halo I–band surface brightness relation ($\langle[\mathrm{Fe/H}]\rangle_{\mathrm{halo}} - \mu_{\mathrm{I}}^{\mathrm{halo}}$). In the left panel, our fiducial simulations with $\mathrm{M_{tot}} = 10^{12}\ \mathrm{M_\odot}$ and 14147×2 particles are shown, while the middle panel shows the corresponding lower–resolution simulations with 5575×2 (crosses) and 9171×2 (open boxes) particles. The error bars show the 68% Confidence Level around each MDF peak. The average number of halo particles is shown in the bottom right corner of each panel. Simulations with fewer than 100 stellar halo particles (at $\mathrm{R} > 15$ kpc) are not included here. Simulations A – C of Fig. 3.2 are displayed in the left panel. The right panel shows the $\langle[\mathrm{Fe/H}]\rangle_{\mathrm{halo}} - \mu_{\mathrm{I}}^{\mathrm{halo}}$ relation for all the simulations. Lower panels: Halo metallicity–stellar mass relation ($\langle[\mathrm{Fe/H}]\rangle_{\mathrm{halo}} - \mathrm{M}_*^{\mathrm{halo}}$). In the left panel, our fiducial simulations with $\mathrm{M_{tot}} = 10^{12}\ \mathrm{M_\odot}$, while the middle panel shows the corresponding lower–resolution simulations. The right panel shows the $\langle[\mathrm{Fe/H}]\rangle_{\mathrm{halo}} - \mathrm{M}_*^{\mathrm{halo}}$ relation for all the simulations. 36

3.8 The stellar halo metallicity–total galactic V–band luminosity relation ($^{\mathrm{halo}}\langle[\mathrm{Fe/H}]\rangle^{\mathrm{kine}}$ – $\mathrm{M_V}$). A filled box corresponds to the peak of the MDF which refers, for a simulation, to the ensemble of counter–rotating ($\mathrm{v}_\theta < 0$) stellar particles within each topographical halo (at a projected radius $\mathrm{R} > 15$ kpc). The related MDFs are displayed in Appendix F. The observational data label–code is as in Fig. 3.1. . . . 39

3.9 The relationship between $^{\mathrm{halo}}\langle[\mathrm{Fe/H}]\rangle^{\mathrm{topos}}$ (the "topographical" halo metallicity) and $^{\mathrm{halo}}\langle[\mathrm{Fe/H}]\rangle^{\mathrm{kine}}$ (the metallicity of the ensemble of counter–rotating stellar particles within each topographical halo). . . 41

3.10 The discrepancy between $^{\mathrm{halo}}\langle[\mathrm{Fe/H}]\rangle^{\mathrm{topos}}$ (the "topographical" halo metallicity) and $^{\mathrm{halo}}\langle[\mathrm{Fe/H}]\rangle^{\mathrm{kine}}$ (the metallicity of the ensemble of counter–rotating stellar particles within each topographical halo) as a function of the "topographical" halo metallicity. 42

3.11 Left panels: For each subset, the distribution of the discrepancy between $^{\mathrm{halo}}\langle[\mathrm{Fe/H}]\rangle^{\mathrm{topos}}$ (the "topographical" halo metallicity) and $^{\mathrm{halo}}\langle[\mathrm{Fe/H}]\rangle^{\mathrm{kine}}$ (the metallicity of the ensemble of counter–rotating stellar particles within each topographical halo). Right panels: For each subset, the distribution of the "topographical" halo mass fraction the ensemble of its counter–rotating stellar particles amounts to. 43

3.12 The Padova theoretical isochrones (Girardi et al., 2002) up to the RGB tip in the metallicity range of $0.0001 < \mathrm{Z} < 0.030$ which have been used to generate the simulated CMD out of the ensemble of stellar particles in the "topographical" halo for each galaxy simulation. They are shown as black dots. Red dots display the fiducial RGB tracks (i.e. 0.8 $\mathrm{M}_\odot$ VandenBerg et al. 2000 RGB tracks and the empirical NGC 6791 RGB track) which are used, as in Mouhcine et al. (2005), to construct a metallicity–colour relationship to derive [Fe/H] out of the (V - I) colour of each (generated) star in the RGB of the (simulated) CMD at $-3.5 < \mathrm{I} < -3.0$ (i.e. the shaded region). The histogram in the top panel displays the (V - I) colour distribution for the Padova theoretical isochrones at $-3.5 < \mathrm{I} < -3.0$. 44

3.13 Topographical halo simulated CMD for the label "A" semi–cosmological simulation (Figures 3.2 and 3.7) at $\mathrm{M_{tot}}$ 10^{12} $\mathrm{M}_\odot$. The observational errors are taken into account (e.g., Secker & Harris 1993) and are randomly drawn for $\mathrm{I} < -1$ from a Normal distribution with $\sigma_\mathrm{I} = \sigma_\mathrm{V} = \exp(\mathrm{I} - 0.6)$ and $\sigma_{\mathrm{V-I}} = \sqrt{\sigma_\mathrm{I}^2 + \sigma_\mathrm{V}^2}$ which implies $\sigma_\mathrm{I} \approx 0.01$ at I = -4.0 and $\sigma_\mathrm{I} \approx 0.2$ at I = -1 whereas at $\mathrm{I} > -1$ $\sigma_\mathrm{I} = \sigma_\mathrm{V} = 0$. Red dots display the simulated CMD without taking observational errors into account. Black dots display the simulated CMD when taking observational errors into account. 46

3.14 Topographical halo simulated CMD for the label "B" semi–cosmological simulation (Figures 3.2 and 3.7) at M_{tot} 10^{12} $M_{\odot}$. The observational errors are taken into account (e.g., Secker & Harris 1993) and are randomly drawn for $I < -1$ from a Normal distribution with $\sigma_I = \sigma_V = \exp(I - 0.6)$ and $\sigma_{V-I} = \sqrt{\sigma_I^2 + \sigma_V^2}$ which implies $\sigma_I \approx 0.01$ at I = -4.0 and $\sigma_I \approx 0.2$ at I = -1 whereas at $I > -1$ $\sigma_I = \sigma_V = 0$. Red dots display the simulated CMD without taking observational errors into account. Black dots display the simulated CMD when taking observational errors into account. 47

3.15 Topographical halo simulated CMD for the label "C" semi–cosmological simulation (Figures 3.2 and 3.7) at M_{tot} 10^{12} $M_{\odot}$. The observational errors are taken into account (e.g., Secker & Harris 1993) and are randomly drawn for $I < -1$ from a Normal distribution with $\sigma_I = \sigma_V = \exp(I - 0.6)$ and $\sigma_{V-I} = \sqrt{\sigma_I^2 + \sigma_V^2}$ which implies $\sigma_I \approx 0.01$ at I = -4.0 and $\sigma_I \approx 0.2$ at I = -1 whereas at $I > -1$ $\sigma_I = \sigma_V = 0$. Red dots display the simulated CMD without taking observational errors into account. Black dots display the simulated CMD when taking observational errors into account. 48

3.16 The stellar halo metallicity–total galactic V–band luminosity relation (${}^{halo}\langle[Fe/H]\rangle^{CMD}$ – M_V). A filled box corresponds to the peak of the MDF which is derived out of the (V - I) colour distribution at $-3.5 < I < -3.0$ via metallicity–colour relationship through the same pipeline as in Mouhcine et al. (2005). The metallicity of each artificial star of the ensemble the MDF refers to is derived via metallicity–colour relationship out of the (V - I) colour of the generated star in the RGB of the simulated "topographical" halo CMD at $-3.5 < I < -3.0$. The related (V - I) colour distributions are displayed in Appendix G whereas the related MDFs derived via metallicity–colour relationship are shown in Appendix H. The observational data label–code is as in Fig. 3.1. 49

3.17 The relationship between ${}^{halo}\langle[Fe/H]\rangle^{topos}$ (the "topographical" halo metallicity) and ${}^{halo}\langle[Fe/H]\rangle^{CMD}$ (the "topographical" halo metallicity as derived from the halo simulated CMD via metallicity–colour relationship). 50

3.18 The discrepancy in metallicity between ${}^{halo}\langle[Fe/H]\rangle^{topos}$ (the "topographical" halo metallicity) and ${}^{halo}\langle[Fe/H]\rangle^{CMD}$ (the "topographical" halo metallicity as derived from the halo simulated CMD via metallicity–colour relationship) as a function of the "topographical" halo metallicity. 52

3.19 For each subset, the distribution of the discrepancy between ${}^{halo}\langle[Fe/H]\rangle^{topos}$ (the "topographical" halo metallicity) and ${}^{halo}\langle[Fe/H]\rangle^{CMD}$ (the "topographical" halo metallicity as derived from the halo simulated CMD via metallicity–colour relationship). 53

4.1 The redshift evolution of the total mass within the 100 kpc central region, normalised to the $z = 0$ value for each simulation. The semi–cosmological simulations with collapse redshift $z_c = 2$ are shown as black lines. Magenta for the collapse redshift $z_c = 1.5$ runs. The cosmological simulations are shown in red. 60

4.2 The redshift evolution of the stellar mass within the 15 kpc central region, normalised to the $z = 0$ value for each simulation. The semi–cosmological simulations with collapse redshift $z_c = 2$ are shown as black lines. Magenta for the collapse redshift $z_c = 1.5$ runs. The cosmological simulations are shown in red. 61

4.3 The redshift evolution of the gaseous mass within the 15 kpc central region, normalised to the $z = 0$ value for each simulation. The semi–cosmological simulations with collapse redshift $z_c = 2$ are shown as black lines. Magenta for the collapse redshift $z_c = 1.5$ runs. The cosmological simulations are shown in red. 62

4.4 The redshift evolution of the stellar (within the 15 kpc central region) to total (within the 100 kpc central region) mass ratio, normalised to the $z = 0$ value for each simulation. The semi–cosmological simulations with collapse redshift $z_c = 2$ are shown as black lines. Magenta for the collapse redshift $z_c = 1.5$ runs. The cosmological simulations are shown in red. 63

4.5 The redshift evolution of the gaseous–to–stellar mass ratio (within the 15 kpc central region), normalised to the $z = 0$ value for each simulation. The semi–cosmological simulations with collapse redshift $z_c = 2$ are shown as black lines. Magenta for the collapse redshift $z_c = 1.5$ runs. The cosmological simulations are shown in red. 64

4.6 The relationship between baryonic mass (i.e. gaseous and stellar mass within the 15 kpc central region) and total mass (within the 100 kpc central region), at different redshifts. The semi–cosmological simulations with collapse redshift $z_c = 2$ are shown as filled symbols (heptagons for $M^{tot} = 5 \times 10^{12}$ $M_\odot$, hexagons for $M^{tot} = 10^{12}$ $M_\odot$, pentagons for $M^{tot} = 5 \times 10^{11}$ $M_\odot$, boxes for $M^{tot} = 10^{11}$ $M_\odot$). Larger empty boxes for the collapse redshift $z_c = 1.5$ runs. The cosmological simulations are shown as large open triangles. 65

4.7 The relationship between gaseous mass and stellar mass (within the 15 kpc central region), at different redshifts. Symbols are the same as in Fig. 4.6. 66

4.8 The relationship between baryonic gas fraction and stellar mass, at different redshifts. Symbols are the same as in Fig. 4.6. 67

4.9 Stellar mass (within the 15 kpc central region) against total mass (within the 100 kpc central region), at different redshifts. Symbols are the same as in Fig. 4.6. The stellar–to–total mass ratio in the simulations is compared with the ratio drawn from the observations in Conselice et al. (2005) and Böhm & Ziegler (2006), displayed as six and four vertices stars, respectively. 68

5.1 Gas–phase Oxygen abundance against integrated stellar mass in the simulations, at different redshifts. The semi–cosmological simulations with collapse redshift $z_c = 2$ are shown as filled symbols (heptagons for $M^{tot} = 5\times10^{12}$ $M_\odot$, hexagons for $M^{tot} = 10^{12}$ $M_\odot$, pentagons for $M^{tot} = 5\times10^{11}$ $M_\odot$, boxes for $M^{tot} = 10^{11}$ $M_\odot$). Larger empty boxes for collapse redshift $z_c = 1.5$ runs. The cosmological simulations are shown as large empty triangles. The $z = 0$ gas–phase Oxygen abundance in the simulations is compared with $z \sim 0.1$ galaxies in the SDSS (Tremonti et al., 2004): solid line for the median; dotted line for 16 and 84 percentile; dashed line for 2.5 and 97.5 percentile. The results at low and intermediate redshifts are compared with the samples observed in Savaglio et al. (2005) and Liang et al. (2006), shown as five and six vertices stars, respectively. 74

5.2 Gas–phase Oxygen abundance against B–band luminosity. Symbols are the same as in Fig. 5.1. The redshift evolution in the simulations is compared with the relationship between the observed luminosity and the gas–phase metallicity at intermediate redshifts in Lilly et al. (2003), Liang et al. (2004), and Mouhcine et al. (2006), shown as four, five and six vertices stars, respectively. 75

5.3 The V–band luminosity–weighted metallicity of the integrated stellar populations against the integrated stellar mass, at different cosmic epochs. Symbols are the same as in Fig. 5.1. The results at $z = 0$ are compared with the $z \sim 0.1$ relation between stellar mass and metallicity in the SDSS (Gallazzi et al., 2005): solid line for the median; dotted line for 16 and 84 percentile. 76

5.4 The V–band luminosity–weighted age of the integrated stellar populations, against the stellar mass at redshift $z = 0$. Symbols are the same as in Fig. 5.1. The results are compared with the $z \sim 0.1$ relation between stellar mass and age in the SDSS (Gallazzi et al., 2005): solid line for the median; dotted line for 16 and 84 percentile. 77

5.5 The $z = 0$ Colour–Magnitude relation in the simulations. Symbols are the same as in Fig. 5.1. The CMR in the simulations is compared with the local CMR for a sample of disc–dominated SDSS galaxies selected by Pizagno et al. (2005), shown as empty boxes. 78

A.1 Fluorine yields from: "a", SNe II (Woosley & Weaver 1995); "b", WR (Meynet & Arnould 2000); "c", AGB stars. 94

A.2 [F/O] and $\langle$[F/O]$\rangle_{\rm IMF}$ for SNe II and AGB yields (upper and lower panels, respectively). Here, A(^{19}F)$_\odot$ = 4.55 (see discussion in Cunha et al. 2003) and A(O)$_\odot$ = 8.736 (e.g., Holweger 2001). The shaded regions in panels "a" and "b" show the observed [F/O] in ω Cen giants (Cunha et al. 2003). The $\langle$[F/O]$\rangle_{\rm IMF}$ are weighted by the IMF over the SNe II (11 – 40 M$_\odot$) and AGB (1 – 6.5 M$_\odot$) mass range, respectively. In panel "d", both $\langle$[F/O]$_{\rm AGB}\rangle_{\rm IMF}$ and $\langle$[F/O]$_{\rm SNe\ II}\rangle_{\rm IMF}$ are shown (closed boxes and open triangles, respectively). 96

A.3 Predicted evolution in the solar neighbourhood of: "a", the gas infall rate $\dot{\sigma}_{infall}$; "b", A(O); "c", [F/O]; "d", the star formation rate (SFR); "e", the SNe II rate; "f", the metallicity Z (MWa, solid line; MWb, dotted; MWc, short–dashed). The SFR history at the solar neighbourhood obtained by Bertelli & Nasi (2001) is also shown as a thick solid line in panel "d", while the shaded region shows the range of values suggested by Rana (1991). A range of values corresponding to the estimated SNe II rate is shown in panel "e" (Cappellaro et al. 1999). 97

A.4 In panel "a", [F/O] as a function of A(O) for the MW models (MWa, solid line; MWb, dotted; MWc, short–dashed). Also shown are the values observed in Milky Way, LMC, and ω Cen giants (crosses, boxes and hexagons, respectively). In panel "b": [F/O] as a function of [O/Fe], compared with the IMF–weighted $\langle$[F/O]$_{\rm SNe\ II}\rangle_{\rm IMF}$ and $\langle$[O/Fe]$_{\rm SNe\ II}\rangle_{\rm IMF}$ yields for SNe II (open triangles). Within the open triangles: "0" corresponds to Z=0; "1", to Z=1.9×10^{-6}; "2", to Z=1.9×10^{-4}; "3", to Z=1.9×10^{-3}; "4", to Z=1.9×10^{-2}. The upper panels represent enlargements of the framed regions delineated in the corresponding bottom panels. 99

B.1 MDFs for the halo fields observed in Mouhcine et al. (2005), reanalysed by the same pipeline as in Renda et al. (2005b). The 68% Confidence Level range and the number of stellar particles each MDF refers to are also shown. 104

B.2 (continued) MDFs for the halo fields observed in Mouhcine et al. (2005), reanalysed by the same pipeline as in Renda et al. (2005b). The 68% Confidence Level range and the number of stellar particles each MDF refers to are also shown. 105

B.3 Halo stellar particle MDFs for the M$_{\rm tot}$ = 10^{11} M$_\odot$ semi–cosmological simulations in Renda et al. (2005b). The 68% Confidence Level range and the number of stellar particles each MDF refers to are also shown. 106

B.4 Halo stellar particle MDFs for the $M_{tot} = 5\times10^{11}$ $M_{\odot}$ semi–cosmological simulations in Renda et al. (2005b). The 68% Confidence Level range and the number of stellar particles each MDF refers to are also shown. 107

B.5 (continued) Halo stellar particle MDFs for the $M_{tot} = 5\times10^{11}$ $M_{\odot}$ semi–cosmological simulations in Renda et al. (2005b). The 68% Confidence Level range and the number of stellar particles each MDF refers to are also shown. 108

B.6 (continued) Halo stellar particle MDFs for the $M_{tot} = 5\times10^{11}$ $M_{\odot}$ semi–cosmological simulations in Renda et al. (2005b). The 68% Confidence Level range and the number of stellar particles each MDF refers to are also shown. 109

B.7 (continued) Halo stellar particle MDFs for the $M_{tot} = 5\times10^{11}$ $M_{\odot}$ semi–cosmological simulations in Renda et al. (2005b). The 68% Confidence Level range and the number of stellar particles each MDF refers to are also shown. 110

B.8 Halo stellar particle MDFs for the $M_{tot} = 10^{12}$ $M_{\odot}$ semi–cosmological simulations in Renda et al. (2005b). The 68% Confidence Level range and the number of stellar particles each MDF refers to are also shown. 111

B.9 (continued) Halo stellar particle MDFs for the $M_{tot} = 10^{12}$ $M_{\odot}$ semi–cosmological simulations in Renda et al. (2005b). The 68% Confidence Level range and the number of stellar particles each MDF refers to are also shown. 112

B.10 (continued) Halo stellar particle MDFs for the $M_{tot} = 10^{12}$ $M_{\odot}$ semi–cosmological simulations in Renda et al. (2005b). The 68% Confidence Level range and the number of stellar particles each MDF refers to are also shown. 113

B.11 (continued) Halo stellar particle MDFs for the $M_{tot} = 10^{12}$ $M_{\odot}$ semi–cosmological simulations in Renda et al. (2005b). The 68% Confidence Level range and the number of stellar particles each MDF refers to are also shown. 114

B.12 (continued) Halo stellar particle MDFs for the $M_{tot} = 10^{12}$ $M_{\odot}$ semi–cosmological simulations in Renda et al. (2005b). The 68% Confidence Level range and the number of stellar particles each MDF refers to are also shown. 115

B.13 Halo stellar particle MDFs for the $M_{tot} = 5\times10^{12}$ $M_{\odot}$ semi–cosmological simulations in Renda et al. (2005b). The 68% Confidence Level range and the number of stellar particles each MDF refers to are also shown. 116

B.14 (continued) Halo stellar particle MDFs for the $M_{tot} = 5\times10^{12}$ $M_{\odot}$ semi–cosmological simulations in Renda et al. (2005b). The 68% Confidence Level range and the number of stellar particles each MDF refers to are also shown. 117

B.15 (continued) Halo stellar particle MDFs for the $\mathrm{M_{tot}} = 5\times10^{12}$ $\mathrm{M_\odot}$ semi–cosmological simulations in Renda et al. (2005b). The 68% Confidence Level range and the number of stellar particles each MDF refers to are also shown. 118

B.16 (continued) Halo stellar particle MDFs for the $\mathrm{M_{tot}} = 5\times10^{12}$ $\mathrm{M_\odot}$ semi–cosmological simulations in Renda et al. (2005b). The 68% Confidence Level range and the number of stellar particles each MDF refers to are also shown. 119

B.17 (continued) Halo stellar particle MDFs for the $\mathrm{M_{tot}} = 5\times10^{12}$ $\mathrm{M_\odot}$ semi–cosmological simulations in Renda et al. (2005b). The 68% Confidence Level range and the number of stellar particles each MDF refers to are also shown. 120

C.1 Halo stellar particle [O/Fe] distribution for the $\mathrm{M_{tot}} = 10^{11}$ $\mathrm{M_\odot}$ semi–cosmological simulations in Renda et al. (2005b). The 68% Confidence Level range and the number of stellar particles each distribution refers to are also shown. 124

C.2 Halo stellar particle [O/Fe] distribution for the $\mathrm{M_{tot}} = 5\times10^{11}$ $\mathrm{M_\odot}$ semi–cosmological simulations in Renda et al. (2005b). The 68% Confidence Level range and the number of stellar particles each distribution refers to are also shown. 125

C.3 (continued) Halo stellar particle [O/Fe] distribution for the $\mathrm{M_{tot}} = 5\times10^{11}$ $\mathrm{M_\odot}$ semi–cosmological simulations in Renda et al. (2005b). The 68% Confidence Level range and the number of stellar particles each distribution refers to are also shown. 126

C.4 (continued) Halo stellar particle [O/Fe] distribution for the $\mathrm{M_{tot}} = 5\times10^{11}$ $\mathrm{M_\odot}$ semi–cosmological simulations in Renda et al. (2005b). The 68% Confidence Level range and the number of stellar particles each distribution refers to are also shown. 127

C.5 (continued) Halo stellar particle [O/Fe] distribution for the $\mathrm{M_{tot}} = 5\times10^{11}$ $\mathrm{M_\odot}$ semi–cosmological simulations in Renda et al. (2005b). The 68% Confidence Level range and the number of stellar particles each distribution refers to are also shown. 128

C.6 Halo stellar particle [O/Fe] distribution for the $\mathrm{M_{tot}} = 1\times10^{12}$ $\mathrm{M_\odot}$ semi–cosmological simulations in Renda et al. (2005b). The 68% Confidence Level range and the number of stellar particles each distribution refers to are also shown. 129

C.7 (continued) Halo stellar particle [O/Fe] distribution for the $\mathrm{M_{tot}} = 10^{12}$ $\mathrm{M_\odot}$ semi–cosmological simulations in Renda et al. (2005b). The 68% Confidence Level range and the number of stellar particles each distribution refers to are also shown. 130

C.8 (continued) Halo stellar particle [O/Fe] distribution for the $M_{tot} = 10^{12}$ $M_{\odot}$ semi–cosmological simulations in Renda et al. (2005b). The 68% Confidence Level range and the number of stellar particles each distribution refers to are also shown. 131
C.9 (continued) Halo stellar particle [O/Fe] distribution for the $M_{tot} = 10^{12}$ $M_{\odot}$ semi–cosmological simulations in Renda et al. (2005b). The 68% Confidence Level range and the number of stellar particles each distribution refers to are also shown. 132
C.10 (continued) Halo stellar particle [O/Fe] distribution for the $M_{tot} = 10^{12}$ $M_{\odot}$ semi–cosmological simulations in Renda et al. (2005b). The 68% Confidence Level range and the number of stellar particles each distribution refers to are also shown. 133
C.11 Halo stellar particle [O/Fe] distribution for the $M_{tot} = 5{\times}10^{12}$ $M_{\odot}$ semi–cosmological simulations in Renda et al. (2005b). The 68% Confidence Level range and the number of stellar particles each distribution refers to are also shown. 134
C.12 (continued) Halo stellar particle [O/Fe] distribution for the $M_{tot} = 5{\times}10^{12}$ $M_{\odot}$ semi–cosmological simulations in Renda et al. (2005b). The 68% Confidence Level range and the number of stellar particles each distribution refers to are also shown. 135
C.13 (continued) Halo stellar particle [O/Fe] distribution for the $M_{tot} = 5{\times}10^{12}$ $M_{\odot}$ semi–cosmological simulations in Renda et al. (2005b). The 68% Confidence Level range and the number of stellar particles each distribution refers to are also shown. 136
C.14 (continued) Halo stellar particle [O/Fe] distribution for the $M_{tot} = 5{\times}10^{12}$ $M_{\odot}$ semi–cosmological simulations in Renda et al. (2005b). The 68% Confidence Level range and the number of stellar particles each distribution refers to are also shown. 137
C.15 (continued) Halo stellar particle [O/Fe] distribution for the $M_{tot} = 5{\times}10^{12}$ $M_{\odot}$ semi–cosmological simulations in Renda et al. (2005b). The 68% Confidence Level range and the number of stellar particles each distribution refers to are also shown. 138

D.1 Halo (red) and galaxy (black) age distributions for the $M_{tot} = 10^{11}$ $M_{\odot}$ semi–cosmological simulations in Renda et al. (2005b). 142
D.2 Halo (red) and galaxy (black) age distributions for the $M_{tot} = 5{\times}10^{11}$ $M_{\odot}$ semi–cosmological simulations in Renda et al. (2005b). 143
D.3 (continued) Halo (red) and galaxy (black) age distributions for the $M_{tot} = 5{\times}10^{11}$ $M_{\odot}$ semi–cosmological simulations in Renda et al. (2005b).144
D.4 (continued) Halo (red) and galaxy (black) age distributions for the $M_{tot} = 5{\times}10^{11}$ $M_{\odot}$ semi–cosmological simulations in Renda et al. (2005b).145
D.5 (continued) Halo (red) and galaxy (black) age distributions for the $M_{tot} = 5{\times}10^{11}$ $M_{\odot}$ semi–cosmological simulations in Renda et al. (2005b).146

D.6 Halo (red) and galaxy (black) age distributions for the $M_{tot} = 10^{12}$ $M_\odot$ semi–cosmological simulations in Renda et al. (2005b). 147
D.7 (continued) Halo (red) and galaxy (black) age distributions for the $M_{tot} = 10^{12}$ $M_\odot$ semi–cosmological simulations in Renda et al. (2005b). 148
D.8 (continued) Halo (red) and galaxy (black) age distributions for the $M_{tot} = 10^{12}$ $M_\odot$ semi–cosmological simulations in Renda et al. (2005b). 149
D.9 (continued) Halo (red) and galaxy (black) age distributions for the $M_{tot} = 10^{12}$ $M_\odot$ semi–cosmological simulations in Renda et al. (2005b). 150
D.10 (continued) Halo (red) and galaxy (black) age distributions for the $M_{tot} = 10^{12}$ $M_\odot$ semi–cosmological simulations in Renda et al. (2005b). 151
D.11 Halo (red) and galaxy (black) age distributions for the $M_{tot} = 5{\times}10^{12}$ $M_\odot$ semi–cosmological simulations in Renda et al. (2005b). 152
D.12 (continued) Halo (red) and galaxy (black) age distributions for the $M_{tot} = 5{\times}10^{12}$ $M_\odot$ semi–cosmological simulations in Renda et al. (2005b). 153
D.13 (continued) Halo (red) and galaxy (black) age distributions for the $M_{tot} = 5{\times}10^{12}$ $M_\odot$ semi–cosmological simulations in Renda et al. (2005b). 154
D.14 (continued) Halo (red) and galaxy (black) age distributions for the $M_{tot} = 5{\times}10^{12}$ $M_\odot$ semi–cosmological simulations in Renda et al. (2005b). 155
D.15 (continued) Halo (red) and galaxy (black) age distributions for the $M_{tot} = 5{\times}10^{12}$ $M_\odot$ semi–cosmological simulations in Renda et al. (2005b). 156

E.1 Galaxy rotation curves for the $M_{tot} = 5{\times}10^{11}$ $M_\odot$ semi–cosmological simulations in Renda et al. (2005b). Black dots for the gaseous particles. Red dots for the stellar particles; red boxes for the ensemble of stellar particles (enclosed within the magenta frame) which are counter–rotating with $v_\theta < 0$ within each topographical halo at a projected radius $R > 15$ kpc. The size of such ensemble is also shown in each panel. 160
E.2 (continued) Galaxy rotation curves for the $M_{tot} = 5{\times}10^{11}$ $M_\odot$ semi–cosmological simulations in Renda et al. (2005b). Black dots for the gaseous particles. Red dots for the stellar particles; red boxes for the ensemble of stellar particles (enclosed within the magenta frame) which are counter–rotating with $v_\theta < 0$ within each topographical halo at a projected radius $R > 15$ kpc. The size of such ensemble is also shown in each panel. 161
E.3 (continued) Galaxy rotation curves for the $M_{tot} = 5{\times}10^{11}$ $M_\odot$ semi–cosmological simulations in Renda et al. (2005b). Black dots for the gaseous particles. Red dots for the stellar particles; red boxes for the ensemble of stellar particles (enclosed within the magenta frame) which are counter–rotating with $v_\theta < 0$ within each topographical halo at a projected radius $R > 15$ kpc. The size of such ensemble is also shown in each panel. 162

E.4 (continued) Galaxy rotation curves for the $M_{tot} = 5\times10^{11}$ $M_\odot$ semi–cosmological simulations in Renda et al. (2005b). Black dots for the gaseous particles. Red dots for the stellar particles; red boxes for the ensemble of stellar particles (enclosed within the magenta frame) which are counter–rotating with $v_\theta < 0$ within each topographical halo at a projected radius $R > 15$ kpc. The size of such ensemble is also shown in each panel. 163

E.5 Galaxy rotation curves for the $M_{tot} = 10^{12}$ $M_\odot$ semi–cosmological simulations in Renda et al. (2005b). Black dots for the gaseous particles. Red dots for the stellar particles; red boxes for the ensemble of stellar particles (enclosed within the magenta frame) which are counter–rotating with $v_\theta < 0$ within each topographical halo at a projected radius $R > 15$ kpc. The size of such ensemble is also shown in each panel. 164

E.6 (continued) Galaxy rotation curves for the $M_{tot} = 10^{12}$ $M_\odot$ semi–cosmological simulations in Renda et al. (2005b). Black dots for the gaseous particles. Red dots for the stellar particles; red boxes for the ensemble of stellar particles (enclosed within the magenta frame) which are counter–rotating with $v_\theta < 0$ within each topographical halo at a projected radius $R > 15$ kpc. The size of such ensemble is also shown in each panel. 165

E.7 (continued) Galaxy rotation curves for the $M_{tot} = 10^{12}$ $M_\odot$ semi–cosmological simulations in Renda et al. (2005b). Black dots for the gaseous particles. Red dots for the stellar particles; red boxes for the ensemble of stellar particles (enclosed within the magenta frame) which are counter–rotating with $v_\theta < 0$ within each topographical halo at a projected radius $R > 15$ kpc. The size of such ensemble is also shown in each panel. 166

E.8 (continued) Galaxy rotation curves for the $M_{tot} = 10^{12}$ $M_\odot$ semi–cosmological simulations in Renda et al. (2005b). Black dots for the gaseous particles. Red dots for the stellar particles; red boxes for the ensemble of stellar particles (enclosed within the magenta frame) which are counter–rotating with $v_\theta < 0$ within each topographical halo at a projected radius $R > 15$ kpc. The size of such ensemble is also shown in each panel. 167

E.9 (continued) Galaxy rotation curves for the $M_{tot} = 10^{12}$ $M_\odot$ semi–cosmological simulations in Renda et al. (2005b). Black dots for the gaseous particles. Red dots for the stellar particles; red boxes for the ensemble of stellar particles (enclosed within the magenta frame) which are counter–rotating with $v_\theta < 0$ within each topographical halo at a projected radius $R > 15$ kpc. The size of such ensemble is also shown in each panel. 168

E.10 Galaxy rotation curves for the $\mathrm{M}_{\mathrm{tot}} = 5\times10^{12}\ \mathrm{M}_{\odot}$ semi–cosmological simulations in Renda et al. (2005b). Black dots for the gaseous particles. Red dots for the stellar particles; red boxes for the ensemble of stellar particles (enclosed within the magenta frame) which are counter–rotating with $\mathrm{v}_{\theta} < 0$ within each topographical halo at a projected radius $\mathrm{R} > 15$ kpc. The size of such ensemble is also shown in each panel. 169

E.11 (continued) Galaxy rotation curves for the $\mathrm{M}_{\mathrm{tot}} = 5\times10^{12}\ \mathrm{M}_{\odot}$ semi–cosmological simulations in Renda et al. (2005b). Black dots for the gaseous particles. Red dots for the stellar particles; red boxes for the ensemble of stellar particles (enclosed within the magenta frame) which are counter–rotating with $\mathrm{v}_{\theta} < 0$ within each topographical halo at a projected radius $\mathrm{R} > 15$ kpc. The size of such ensemble is also shown in each panel. 170

E.12 (continued) Galaxy rotation curves for the $\mathrm{M}_{\mathrm{tot}} = 5\times10^{12}\ \mathrm{M}_{\odot}$ semi–cosmological simulations in Renda et al. (2005b). Black dots for the gaseous particles. Red dots for the stellar particles; red boxes for the ensemble of stellar particles (enclosed within the magenta frame) which are counter–rotating with $\mathrm{v}_{\theta} < 0$ within each topographical halo at a projected radius $\mathrm{R} > 15$ kpc. The size of such ensemble is also shown in each panel. 171

E.13 (continued) Galaxy rotation curves for the $\mathrm{M}_{\mathrm{tot}} = 5\times10^{12}\ \mathrm{M}_{\odot}$ semi–cosmological simulations in Renda et al. (2005b). Black dots for the gaseous particles. Red dots for the stellar particles; red boxes for the ensemble of stellar particles (enclosed within the magenta frame) which are counter–rotating with $\mathrm{v}_{\theta} < 0$ within each topographical halo at a projected radius $\mathrm{R} > 15$ kpc. The size of such ensemble is also shown in each panel. 172

E.14 (continued) Galaxy rotation curves for the $\mathrm{M}_{\mathrm{tot}} = 5\times10^{12}\ \mathrm{M}_{\odot}$ semi–cosmological simulations in Renda et al. (2005b). Black dots for the gaseous particles. Red dots for the stellar particles; red boxes for the ensemble of stellar particles (enclosed within the magenta frame) which are counter–rotating with $\mathrm{v}_{\theta} < 0$ within each topographical halo at a projected radius $\mathrm{R} > 15$ kpc. The size of such ensemble is also shown in each panel. 173

F.1 Kinematically selected halo MDFs for the $\mathrm{M}_{\mathrm{tot}} = 5\times10^{11}\ \mathrm{M}_{\odot}$ semi–cosmological simulations in Renda et al. (2005b). The 68% Confidence Level range and the number of stellar particles each MDF relates to are also shown. Each MDF refers to the stellar particles in the simulation which are counter–rotating with $\mathrm{v}_{\theta} < 0$ at a projected radius $\mathrm{R} > 15$ kpc. 176

F.2 (continued) Kinematically selected halo MDFs for the $M_{\rm tot} = 5\times10^{11}$ $M_\odot$ semi–cosmological simulations in Renda et al. (2005b). The 68% Confidence Level range and the number of stellar particles each MDF relates to are also shown. Each MDF refers to the stellar particles in the simulation which are counter–rotating with $v_\theta < 0$ at a projected radius $R > 15$ kpc. 177

F.3 Kinematically selected halo MDFs for the $M_{\rm tot} = 10^{12}$ $M_\odot$ semi–cosmological simulations in Renda et al. (2005b). The 68% Confidence Level range and the number of stellar particles each MDF relates to are also shown. Each MDF refers to the stellar particles in the simulation which are counter–rotating with $v_\theta < 0$ at a projected radius $R > 15$ kpc. 178

F.4 (continued) Kinematically selected halo MDFs for the $M_{\rm tot} = 10^{12}$ $M_\odot$ semi–cosmological simulations in Renda et al. (2005b). The 68% Confidence Level range and the number of stellar particles each MDF relates to are also shown. Each MDF refers to the stellar particles in the simulation which are counter–rotating with $v_\theta < 0$ at a projected radius $R > 15$ kpc. 179

F.5 Kinematically selected halo MDFs for the $M_{\rm tot} = 5\times10^{12}$ $M_\odot$ semi–cosmological simulations in Renda et al. (2005b). The 68% Confidence Level range and the number of stellar particles each MDF relates to are also shown. Each MDF refers to the stellar particles in the simulation which are counter–rotating with $v_\theta < 0$ at a projected radius $R > 15$ kpc. 180

F.6 (continued) Kinematically selected halo MDFs for the $M_{\rm tot} = 5\times10^{12}$ $M_\odot$ semi–cosmological simulations in Renda et al. (2005b). The 68% Confidence Level range and the number of stellar particles each MDF relates to are also shown. Each MDF refers to the stellar particles in the simulation which are counter–rotating with $v_\theta < 0$ at a projected radius $R > 15$ kpc. 181

F.7 (continued) Kinematically selected halo MDFs for the $M_{\rm tot} = 5\times10^{12}$ $M_\odot$ semi–cosmological simulations in Renda et al. (2005b). The 68% Confidence Level range and the number of stellar particles each MDF relates to are also shown. Each MDF refers to the stellar particles in the simulation which are counter–rotating with $v_\theta < 0$ at a projected radius $R > 15$ kpc. 182

F.8 (continued) Kinematically selected halo MDFs for the $M_{\rm tot} = 5\times10^{12}$ $M_\odot$ semi–cosmological simulations in Renda et al. (2005b). The 68% Confidence Level range and the number of stellar particles each MDF relates to are also shown. Each MDF refers to the stellar particles in the simulation which are counter–rotating with $v_\theta < 0$ at a projected radius $R > 15$ kpc. 183

F.9 (continued) Kinematically selected halo MDFs for the $M_{tot} = 5{\times}10^{12}$ $M_{\odot}$ semi–cosmological simulations in Renda et al. (2005b). The 68% Confidence Level range and the number of stellar particles each MDF relates to are also shown. Each MDF refers to the stellar particles in the simulation which are counter–rotating with $v_{\theta} < 0$ at a projected radius $R > 15$ kpc. 184

G.1 Halo synthetic CMD (V - I) colour distribution at -3.5 < I < -3.0 for the $M_{tot} = 5{\times}10^{11}$ $M_{\odot}$ semi–cosmological simulations in Renda et al. (2005b). Each panel also shows the number of generated stars at -3.5 < I < -3.0 in each synthetic CMD. 188

G.2 (continued) Halo synthetic CMD (V - I) colour distribution at -3.5 < I < -3.0 for the $M_{tot} = 5{\times}10^{11}$ $M_{\odot}$ semi–cosmological simulations in Renda et al. (2005b). Each panel also shows the number of generated stars at -3.5 < I < -3.0 in each synthetic CMD. 189

G.3 (continued) Halo synthetic CMD (V - I) colour distribution at -3.5 < I < -3.0 for the $M_{tot} = 5{\times}10^{11}$ $M_{\odot}$ semi–cosmological simulations in Renda et al. (2005b). Each panel also shows the number of generated stars at -3.5 < I < -3.0 in each synthetic CMD. 190

G.4 (continued) Halo synthetic CMD (V - I) colour distribution at -3.5 < I < -3.0 for the $M_{tot} = 5{\times}10^{11}$ $M_{\odot}$ semi–cosmological simulations in Renda et al. (2005b). Each panel also shows the number of generated stars at -3.5 < I < -3.0 in each synthetic CMD. 191

G.5 Halo synthetic CMD (V - I) colour distribution at -3.5 < I < -3.0 for the $M_{tot} = 1{\times}10^{12}$ $M_{\odot}$ semi–cosmological simulations in Renda et al. (2005b). Each panel also shows the number of generated stars at -3.5 < I < -3.0 in each synthetic CMD. 192

G.6 (continued) Halo synthetic CMD (V - I) colour distribution at -3.5 < I < -3.0 for the $M_{tot} = 10^{12}$ $M_{\odot}$ semi–cosmological simulations in Renda et al. (2005b). Each panel also shows the number of generated stars at -3.5 < I < -3.0 in each synthetic CMD. 193

G.7 (continued) Halo synthetic CMD (V - I) colour distribution at -3.5 < I < -3.0 for the $M_{tot} = 10^{12}$ $M_{\odot}$ semi–cosmological simulations in Renda et al. (2005b). Each panel also shows the number of generated stars at -3.5 < I < -3.0 in each synthetic CMD. 194

G.8 (continued) Halo synthetic CMD (V - I) colour distribution at -3.5 < I < -3.0 for the $M_{tot} = 10^{12}$ $M_{\odot}$ semi–cosmological simulations in Renda et al. (2005b). Each panel also shows the number of generated stars at -3.5 < I < -3.0 in each synthetic CMD. 195

G.9 (continued) Halo synthetic CMD (V - I) colour distribution at -3.5 < I < -3.0 for the $M_{tot} = 10^{12}$ $M_{\odot}$ semi–cosmological simulations in Renda et al. (2005b). Each panel also shows the number of generated stars at -3.5 < I < -3.0 in each synthetic CMD. 196

G.10 Halo synthetic CMD (V - I) colour distribution at -3.5 $<$ I $<$ -3.0 for the $\mathrm{M_{tot}} = 5\times10^{12}$ $\mathrm{M}_\odot$ semi–cosmological simulations in Renda et al. (2005b). Each panel also shows the number of generated stars at -3.5 $<$ I $<$ -3.0 in each synthetic CMD. 197

G.11 (continued) Halo synthetic CMD (V - I) colour distribution at -3.5 $<$ I $<$ -3.0 for the $\mathrm{M_{tot}} = 5\times10^{12}$ $\mathrm{M}_\odot$ semi–cosmological simulations in Renda et al. (2005b). Each panel also shows the number of generated stars at -3.5 $<$ I $<$ -3.0 in each synthetic CMD. 198

G.12 (continued) Halo synthetic CMD (V - I) colour distribution at -3.5 $<$ I $<$ -3.0 for the $\mathrm{M_{tot}} = 5\times10^{12}$ $\mathrm{M}_\odot$ semi–cosmological simulations in Renda et al. (2005b). Each panel also shows the number of generated stars at -3.5 $<$ I $<$ -3.0 in each synthetic CMD. 199

G.13 (continued) Halo synthetic CMD (V - I) colour distribution at -3.5 $<$ I $<$ -3.0 for the $\mathrm{M_{tot}} = 5\times10^{12}$ $\mathrm{M}_\odot$ semi–cosmological simulations in Renda et al. (2005b). Each panel also shows the number of generated stars at -3.5 $<$ I $<$ -3.0 in each synthetic CMD. 200

G.14 (continued) Halo synthetic CMD (V - I) colour distribution at -3.5 $<$ I $<$ -3.0 for the $\mathrm{M_{tot}} = 5\times10^{12}$ $\mathrm{M}_\odot$ semi–cosmological simulations in Renda et al. (2005b). Each panel also shows the number of generated stars at -3.5 $<$ I $<$ -3.0 in each synthetic CMD. 201

H.1 Halo MDF via Metallicity–Colour relationship by the same pipeline as in Mouhcine et al. (2005) for the $\mathrm{M_{tot}} = 5\times10^{11}$ $\mathrm{M}_\odot$ semi–cosmological simulations in Renda et al. (2005b). The 68% Confidence Level range and the number of stellar particles each MDF refers to are also shown. 204

H.2 (continued) Halo MDF via Metallicity–Colour relationship by the same pipeline as in Mouhcine et al. (2005) for the $\mathrm{M_{tot}} = 5\times10^{11}$ $\mathrm{M}_\odot$ semi–cosmological simulations in Renda et al. (2005b). The 68% Confidence Level range and the number of stellar particles each MDF refers to are also shown. 205

H.3 (continued) Halo MDF via Metallicity–Colour relationship by the same pipeline as in Mouhcine et al. (2005) for the $\mathrm{M_{tot}} = 5\times10^{11}$ $\mathrm{M}_\odot$ semi–cosmological simulations in Renda et al. (2005b). The 68% Confidence Level range and the number of stellar particles each MDF refers to are also shown. 206

H.4 (continued) Halo MDF via Metallicity–Colour relationship by the same pipeline as in Mouhcine et al. (2005) for the $\mathrm{M_{tot}} = 5\times10^{11}$ $\mathrm{M}_\odot$ semi–cosmological simulations in Renda et al. (2005b). The 68% Confidence Level range and the number of stellar particles each MDF refers to are also shown. 207

H.5 Halo MDF via Metallicity–Colour relationship by the same pipeline as in Mouhcine et al. (2005) for the $M_{tot} = 10^{12}$ $M_\odot$ semi–cosmological simulations in Renda et al. (2005b). The 68% Confidence Level range and the number of stellar particles each MDF refers to are also shown. 208
H.6 (continued) Halo MDF via Metallicity–Colour relationship by the same pipeline as in Mouhcine et al. (2005) for the $M_{tot} = 10^{12}$ $M_\odot$ semi–cosmological simulations in Renda et al. (2005b). The 68% Confidence Level range and the number of stellar particles each MDF refers to are also shown. 209
H.7 (continued) Halo MDF via Metallicity–Colour relationship by the same pipeline as in Mouhcine et al. (2005) for the $M_{tot} = 10^{12}$ $M_\odot$ semi–cosmological simulations in Renda et al. (2005b). The 68% Confidence Level range and the number of stellar particles each MDF refers to are also shown. 210
H.8 (continued) Halo MDF via Metallicity–Colour relationship by the same pipeline as in Mouhcine et al. (2005) for the $M_{tot} = 10^{12}$ $M_\odot$ semi–cosmological simulations in Renda et al. (2005b). The 68% Confidence Level range and the number of stellar particles each MDF refers to are also shown. 211
H.9 (continued) Halo MDF via Metallicity–Colour relationship by the same pipeline as in Mouhcine et al. (2005) for the $M_{tot} = 10^{12}$ $M_\odot$ semi–cosmological simulations in Renda et al. (2005b). The 68% Confidence Level range and the number of stellar particles each MDF refers to are also shown. 212
H.10 Halo MDF via Metallicity–Colour relationship by the same pipeline as in Mouhcine et al. (2005) for the $M_{tot} = 5{\times}10^{12}$ $M_\odot$ semi–cosmological simulations in Renda et al. (2005b). The 68% Confidence Level range and the number of stellar particles each MDF refers to are also shown. 213
H.11 (continued) Halo MDF via Metallicity–Colour relationship by the same pipeline as in Mouhcine et al. (2005) for the $M_{tot} = 5{\times}10^{12}$ $M_\odot$ semi–cosmological simulations in Renda et al. (2005b). The 68% Confidence Level range and the number of stellar particles each MDF refers to are also shown. 214
H.12 (continued) Halo MDF via Metallicity–Colour relationship by the same pipeline as in Mouhcine et al. (2005) for the $M_{tot} = 5{\times}10^{12}$ $M_\odot$ semi–cosmological simulations in Renda et al. (2005b). The 68% Confidence Level range and the number of stellar particles each MDF refers to are also shown. 215
H.13 (continued) Halo MDF via Metallicity–Colour relationship by the same pipeline as in Mouhcine et al. (2005) for the $M_{tot} = 5{\times}10^{12}$ $M_\odot$ semi–cosmological simulations in Renda et al. (2005b). The 68% Confidence Level range and the number of stellar particles each MDF refers to are also shown. 216

H.14 (continued) Halo MDF via Metallicity–Colour relationship by the same pipeline as in Mouhcine et al. (2005) for the $M_{tot} = 5\times10^{12}$ $M_\odot$ semi–cosmological simulations in Renda et al. (2005b). The 68% Confidence Level range and the number of stellar particles each MDF refers to are also shown. 217

List of Tables

2.1 The parameters for the MW and the M31 models. 7

2.2 Radial gradients (dex/kpc) for the present–day mean stellar metallicity of the MDFs in the M31 models. The results for the MW model and for the M31 fields observed in Bellazzini et al. (2003) are also presented as reference. $(\Delta\langle[Fe/H]\rangle/\Delta R)$ refers to the range 4 – 16 kpc for the MW model and 4 – 20 kpc for the M31 models. $(\Delta\langle[Fe/H]\rangle/\Delta R)_{halo}$ refers to the range 4 – 30 kpc in the halo for both the MW and the M31 models. 19

Chapter 1

Introduction

> *"Ne osservava le rughe,*
> *e provava ad immaginarne la storia."*
> – *Anonimo*

Near–field observations - e.g. in the Local Group and in the nearby low redshift Universe - of properties such as metallicity, luminosity and kinematics may provide tight constraints - i.e. "boundary conditions" - on any model of structure formation in the Universe. This "near–field" approach to cosmology is the overarching theme of this PhD Thesis.

The focus narrows here on stellar halos in late–type galaxies. Understanding the formation history of stellar halos is one of the challenges of galactic astrophysics. The problem is generally framed within the context of two competing scenarios: one of "rapid collapse" (Eggen, Lynden–Bell & Sandage, 1962), in which the stellar halo is formed by the rapid collapse of a proto–galaxy within a dynamical timescale ($\sim 10^8$ yr), and one of "galactic assembly" (Searle & Zinn, 1978), whereby the stellar halo is assembled over a longer timescale ($\sim 10^9$ yr) by the accretion of "building–blocks", each with separate enrichment history. Both scenarios have their strengths and weaknesses, and it would appear that a hybrid model is the most plausible picture consistent with extant data (e.g.: Chiba & Beers 2000; Freeman & Bland-Hawthorn 2002).

Detailed observational data have long been available for the Milky Way (e.g., Freeman & Bland-Hawthorn 2002) and have provided tight constraints on several Galaxy formation models (e.g.: Abadi et al. 2003; Bekki & Chiba 2001). An implicit assumption still remains unanswered though: *is the Milky Way a "normal" spiral?* Searching for directions, it feels natural to look at our neighbour: Andromeda is the closest spiral to the Milky Way, ≈ 780 kpc (more than 2 million light–years) away from our Galaxy. There has recently been an astonishing progress in the observations of Andromeda (e.g., Ibata et al. 2007). An intriguing piece of the "puzzle" is provided by contrasting the stellar halo of our Galaxy with that of its neighbour, even more so since the Hubble Space Telescope imaging of nearby spiral galaxy stellar halos in Mouhcine et al. (2005) suggests that a correlation between stellar halo metallicity and galactic luminosity is in place and would leave the Milky Way halo as an outlier with respect to other spirals of comparable luminosities. Further questions hence arise: *is there any stellar halo–galaxy formation symbiosis? Is the Milky Way an outlier?... Which is "normal"?*

The layout of the PhD Thesis we present here reflects the path we have undertaken to face the challenge these questions pose. Our first step has been to contrast the chemical evolution of the Milky Way with that of Andromeda by means of a semi–analytical model (Chapter 2; Renda et al. 2005), which, in passing, has also led to a new understanding of the origin of Fluorine in the Milky Way (Appendix A; Renda et al. 2004). We have then pursued a complementary approach through the analysis of several semi–cosmological late–type galaxy simulations which sample a wide variety of merging histories. We have first focused on the stellar halo properties in the simulations at redshift zero (Chapter 3, which synthesises the background which is presented in Appendices B – H; Renda et al. 2005b), we have then traced galaxy mass assembly and metal enrichment in the simulations over the second half of the age of the Universe (Chapters 4 and 5, respectively). We finally summarise what (we think that) we see from our point of view in Chapter 6.

Chapter 2

Contrasting the Milky Way and Andromeda Stellar Halos

The chemical evolution history of a galaxy hides clues about how it formed and has been changing through time. We have studied the chemical evolution history of the Milky Way (MW) and Andromeda (M31) to find which are common features in the chemical evolution of disc galaxies as well as which are galaxy–dependent. We use a semi–analytic multi–zone chemical evolution model. Such models have succeeded in explaining the mean trends of the observed chemical properties in these two Local Group spiral galaxies with similar mass and morphology. Our results suggest that while the evolution of the MW and M31 shares general similarities, differences in the formation history are required to explain the observations in detail. In particular, we found that the observed higher metallicity in the M31 halo can be explained by either a) a higher halo star formation efficiency or b) a larger reservoir of infalling halo gas with a longer halo formation phase. These two different pictures would lead to a) a higher [O/Fe] at low metallicities or b) younger stellar populations in the M31 halo, respectively. Both pictures result in a more massive stellar halo in M31, which suggests a possible correlation between the halo metallicity and its stellar mass.

2.1 Introduction

The chemical properties of galaxies hide clues about their formation and evolution. Semi–analytic chemical evolution models (Talbot & Arnett 1971; Tinsley 1980) have succeeded in explaining the mean trends of galactic systems by numerically solving a set of equations governing the simplified evolution of the chemical elements as they cycle through gas and stars. One strength of these models is that they typically have the fewest number of free parameters, making convergence to a smaller set of solutions more likely.

Strong constraints can be placed on chemical evolution models only by contrasting them against a comprehensive set of observed properties. Since the most detailed observational data are generally available for the Milky Way (e.g., Freeman & Bland-Hawthorn 2002), successful agreement between model predictions and these observed properties has been obtained by several studies in the past, which help us to understand the formation history of the Milky Way (MW). Some models have focused on the evolution of the chemical abundances both in the solar neighbourhood and in the whole disc, adopting a framework in which the MW has been built–up inside–out by means of a single accretion event (e.g.: Matteucci & François 1989; Pagel & Tautvaišiene 1995). Others have used an early infall of gas to explain the thick disc formation, followed by a slower infall to form the thin disc (e.g., Chiappini, Matteucci & Gratton 1997). Several studies have paid particular attention to the chemical evolution of a larger range of elements (e.g.: Timmes, Woosley & Weaver 1995; Goswami & Prantzos 2000; Alibés, Labay & Canal 2001) or focused on the features of the Metallicity Distribution Function (MDF) in the solar neighbourhood (e.g., Fenner & Gibson 2003). However, an implicit assumption remains unanswered: *is the MW a typical spiral?*

Andromeda (M31) is the closest spiral to our MW (e.g., van den Bergh 2003). Previous theoretical studies of the chemical evolution of M31 have been done by Diaz & Tosi (1984) and Mollá, Ferrini & Diaz (1996), both emphasising the evolution of the M31 disc. They concluded that M31 has a formation history and chemical evolution similar to that of the MW. More recently, however, there has been considerable observational progress in the study of both galaxies. A striking difference between M31 and the MW is that the metallicity of the M31 halo ($\langle[\mathrm{Fe/H}]\rangle \approx -0.5$) [1] is significantly higher than its MW analogue ($\langle[\mathrm{Fe/H}]\rangle \approx -1.8$, e.g., Ryan & Norris 1991), as revealed by many recent studies (e.g.: Holland, Fahlman & Richer 1996; Durrell, Harris, & Pritchet 2001; Sarajedini & van Duyne 2001; Ferguson & Johnson 2001; Reitzel & Guhathakurta 2002; Ferguson et al. 2002; Worthey et al. 2005;

---

[1] Hereafter $[\mathrm{X/Fe}] = \log_{10}(\mathrm{X/Fe}) - \log_{10}(\mathrm{X/Fe})_{\odot}$.

Bellazzini et al. 2003; Brown et al. 2003; Reitzel et al. 2004; Rich et al. 2004).

It is therefore timely to attempt the construction of a chemical evolution model for both the MW and M31, using the same framework. Such an attempt may be helpful in highlighting the common features in the chemical evolution of spiral galaxies (at least in these two spirals) and those which remain galaxy–dependent.

In Section 2.2 we describe our multi–zone chemical evolution model, and in Section 2.3 we present the results of our MW model. In Section 2.4 we show the results for M31. Finally, our results are discussed in Section 2.5.

2.2 The model

In this study we use a semi–analytic multi–zone chemical evolution model for a spiral galaxy. This model is based on `GEtool` (Fenner & Gibson 2003; Gibson et al. 2003). We follow the chemical evolution of both halo and disc of M31 and the MW under the assumption that both galaxies have formed through two phases of gas infall. The first infall episode corresponds to the halo build–up, and the second to the inside–out formation of the disc. Similar formalisms have been successful in modeling the chemical evolution in the solar neighbourhood (e.g.: Chiappini, Matteucci & Gratton 1997; Chang et al. 1999; Alibés, Labay & Canal 2001). We assume that halo stars were born in a burst induced either by the collapse of a single proto–galactic cloud (Eggen, Lynden–Bell & Sandage 1962) or by the multiple merger of building–blocks (Searle & Zinn 1978; Bekki & Chiba 2001; Brook et al. 2003). The disc is assumed to be built–up inside–out by the smooth accretion of gas on a longer timescale. Observations of HI High Velocity Clouds (HVCs) which appear to be currently falling onto the MW (e.g., Putman et al. 2003 and references therein) may provide evidence for such gas infall. Recently, HVCs have also been detected in the M31 neighbourhood, though their interpretation as infalling clouds is debated (Thilker et al., 2004).

We monitor the face–on projected properties of the halo and disc components. While this geometrical simplification is suitable for approximating the flat disc, it is less appropriate for the halo, whose shape is roughly spherical rather than disc–like. However, we consider this choice acceptable in a simplified model of the chemical evolution of a spiral galaxy. We follow the chemical evolution of several independent rings, 2 kpc wide, out to a galactocentric radius $R = 10\ R_d$, where R_d is the disc scale–length. We also ignore the bulge component, because we are interested in the relatively outer region ($R > 4$ kpc). Each ring is a single zone onto which gas falls, without exchange of matter between the rings. We trace the chemical evolution of each zone. In our model, we assume that the age of the galaxy is $t_{now} = 13$ Gyr. The basic equations (e.g., Tinsley 1980), in a zone at a radius R, for the evolution of the gas surface density $\Sigma_{g,i}(R,t)$ of an element i are written as follows:

$$
\begin{array}{rl}
 & \dot{\Sigma}_{g,i}(R,t) \ = \\
- & \psi(R,t)X_i(R,t) \ + \displaystyle\int_{M_{min}}^{M_{Bmin}} \psi(R,t \ - \ \tau_m) \\
\times & Y_i(m, Z_{t \ - \ \tau_m}) \dfrac{\varphi(m)}{m} dm \ + \ k \displaystyle\int_{M_{B_{min}}}^{M_{B_{max}}} \dfrac{\varphi(M_B)}{M_B} \\
\times & \displaystyle\int_{\mu_{min}}^{0.5} f(\mu)\psi(R,t \ - \ \tau_{m_2}) Y_i(M_B, Z_{t \ - \ \tau_{m_2}}) d\mu \ dM_B \\
+ & (1 \ - \ k) \displaystyle\int_{M_{Bmin}}^{M_{Bmax}} \psi(R,t \ - \ \tau_m) Y_i(m, Z_{t \ - \ \tau_m}) \\
\times & \dfrac{\varphi(m)}{m} dm \ + \displaystyle\int_{M_{Bmax}}^{M_{max}} \psi(R,t \ - \ \tau_m) Y_i(m, Z_{t \ - \ \tau_m}) \\
\times & \dfrac{\varphi(m)}{m} dm \ + \ X_{i_{halo}}(t) h(R) e^{\frac{-t}{\tau_h}} \\
+ & X_{i_{disc}}(t) d(R) e^{\frac{-(t \ - \ t_{delay})}{\tau_d(R)}} .
\end{array}
\tag{2.1}
$$

Here, $X_i(R,t) = \frac{\Sigma_{g,i}(R,t)}{\Sigma_g(R,t)}$ is the mass fraction for the element i; $\psi(R,t)$ is the star formation rate (SFR); $\varphi(m)$ is the Initial Mass Function (IMF) with mass range M_{min} - M_{max}; τ_m is the lifetime of a star with mass m; $Y_i(m, Z_{t \ - \ \tau_m})$ is the stellar yield of the element from a star of mass m, age τ_m and metallicity $Z_{t \ - \ \tau_m}$. The first term describes the depletion of the element i which is locked–up in newly formed stars. The second and the fourth terms show the contribution of mass loss from low and intermediate mass stars. The third term describes the contribution from Type Ia SNe (SNe Ia). The contribution from SNe Ia is calculated as suggested in Greggio & Renzini (1983), where k, $M_{B_{min}}$, $M_{B_{max}}$, μ_{min}, μ, $f(\mu)$, τ_{m_2} are defined. The fifth term shows the contribution from Type II SNe (SNe II). The sixth and the seventh terms represent the infalling halo and disc gas, respectively.

The Kroupa, Tout & Gilmore (1993) IMF is used here. We have chosen a lower mass limit of $M_{min} = 0.08$ M$_\odot$ and imposed an upper mass limit of $M_{max} = 60$ M$_\odot$

Table 2.1: The parameters for the MW and the M31 models.

	α	$\frac{\Sigma_{t,h}(R_\odot,t_{now})}{\mathrm{M}_\odot\ \mathrm{pc}^{-2}}$	$\frac{R_d}{kpc}$	$\frac{\Sigma_{t,d}(R_\odot,t_{now})}{\mathrm{M}_\odot\ \mathrm{pc}^{-2}}$	$\frac{\tau_h}{\mathrm{Gyr}}$	$\frac{t_{delay}}{\mathrm{Gyr}}$	a_d	b_d	ν_h	ν_d
MW	2	6	3.0	48	0.1	1.0	2.0	1.25	0.125	0.03
M31a	2	6	5.5	46	0.1	1.0	2.0	1.25	0.125	0.03
M31b	2	6	5.5	46	0.1	1.0	0.7	0.50	12.5	0.08
M31c	2	57	5.5	46	0.5	6.0	0.1	0.10	0.125	0.08

in order to avoid the overproduction of oxygen and recover the observed trend of [O/Fe] at low metallicity in the solar neighbourhood in the MW. Such IMF upper mass limit is currently loosely constrained by stellar formation and evolution models. Yet, these stellar models, and the yields they provide, are one of the most important features in galactic chemical evolution, although questions remain concerning the precise composition of stellar ejecta, due to the uncertain role played by processes including mass loss, rotation, fall–back, and the location of the mass cut, which separates the remnant from the ejected material in SNe. The SNe II yields are from Woosley & Weaver (1995). We have halved the iron yields shown in Woosley & Weaver (1995), as suggested by Timmes et al. (1995). The SNe Ia yields are from Iwamoto et al. (1999). The metallicity–dependent yields of Renzini & Voli (1981) have been used for stars in the mass range 1 – 8 $\mathrm{M}_\odot$. The lifetimes of stars as a function of mass and metallicity have been taken from Schaller et al. (1992).

2.2.1 Infall

The infall rate during the halo and disc phases is simply assumed to decline exponentially, as seen by the adopted sixth and seventh terms in equation 2.1. The evolution of the total[2] surface mass density, $\Sigma_t(R,t)$, is described by:

$$\frac{d\Sigma_t(R,t)}{dt} \;=\; h(R)e^{\frac{-t}{\tau_h}} \;+\; d(R)e^{\frac{-(t\ -\ t_{delay})}{\tau_d(R)}}. \tag{2.2}$$

---

[2] Hereafter, by “total” density we mean the sum of the stellar density and of the gas density.

Here, the first term describes the infall rate in the halo phase. The infall time–scale in the halo phase, τ_h, is assumed to be independent of radius, for simplicity. The infall of disc gas starts with a delay of t_{delay}, as seen in the second term. The time–scale of the disc infall depends on radius as follows:

$$\tau_d(R) \;=\; a_d \;+\; b_d \frac{R}{\mathrm{kpc}} \ \mathrm{Gyr}. \tag{2.3}$$

The values for the constants a_d and b_d are free parameters. The infall coefficients $h(R)$ and $d(R)$ are chosen in order to reproduce the present–day total surface density in the disc, $\Sigma_{t,d}(R, t_{now})$, and in the halo, $\Sigma_{t,h}(R, t_{now})$, respectively, as follows (e.g., Timmes et al. 1995):

$$\begin{aligned} h(R) \;&=\; \Sigma_{t,h}(R, t_{now}) \\ &\quad \times \left\{ \tau_h \left[1 \;-\; \exp\left(\frac{-t_{now}}{\tau_h} \right) \right] \right\}^{-1}; \qquad (2.4) \\ d(R) \;&=\; \Sigma_{t,d}(R, t_{now}) \\ &\quad \times \left\{ \tau_d(R) \left[1 \;-\; \exp\left(-\frac{t_{now} \;-\; t_{delay}}{\tau_d(R)} \right) \right] \right\}^{-1}. \qquad (2.5) \end{aligned}$$

The infalling halo gas has been assumed to be of primordial composition. On the other hand, it is unlikely that the accreting gas has primordial abundance at a later epoch, since even low density inter–galactic medium, such as the Lyman α forest, has a significant amount of metals (e.g., Cowie & Songalia 1998), and it is known that the HVCs in the MW, which could be infalling gas clouds, have metallicities between 0.1 and 0.3 $Z_\odot$ (Sembach et al., 2002). Therefore, we assume that the gas accreting onto the disc is pre–enriched. The level of pre–enrichment can be loosely constrained from the observed metallicity of Galactic HVCs. We simply assume that the metallicity of the infalling disc material is $Z_{infall}(R,t) \;=\; Z(R,t)$ if $Z(R,t) \;<\; Z_{infall,max} \;=\; 0.3\ Z_\odot$, where $Z(R,t)$ is the metallicity of the gas at the radius R and the time t, otherwise $Z_{infall}(R,t) \;=\; Z_{infall,max} \;=\; 0.3\ Z_\odot$. The abundance pattern of the infalling disc gas is further unknown parameter. Following the above simple assumption, we set the infalling disc gas, at a given galactocentric radius R and time t, to have the same abundance pattern as the ISM at R and t. This guarantees the smooth evolution of the gas abundance and of the abundance patterns in each radial bin.

2.2.2 Disc and halo surface density profiles

We adopt the following exponential profile for the present–day total surface density of the disc component:

$$\Sigma_{t,d}(R, t_{now}) \;=\; \Sigma_{t,d}(R_\odot, t_{now}) e^{-(R \;-\; R_\odot)/R_d}. \tag{2.6}$$

Here $R_\odot \;=\; 8$ kpc, which is the galactocentric distance of the Sun within the MW. The same definition of $R_\odot \;=\; 8$ kpc is applied to the M31 models.

The surface density profiles of the MW and M31 disc are different. We have chosen a scale–length of $R_d \;=\; 3.0$ kpc for the MW (e.g.: Robin, Creze & Mohan 1992; Ruphy et al. 1996; Freudenreich 1998) and $R_d \;=\; 5.5$ kpc for M31 (Walterbos & Kennicutt, 1988). For the MW, we assume $\Sigma_{t,d}(R_\odot, t_{now}) \;=\; 48\ \mathrm{M}_\odot\ \mathrm{pc}^{-2}$ (Kuijken & Gilmore, 1991). We adopt $\Sigma_{t,d}(R_\odot, t_{now}) \;=\; 46\ \mathrm{M}_\odot\ \mathrm{pc}^{-2}$ in M31, such that the mass of the M31 disc is similar to that of the MW disc ($\approx 10^{11}\ \mathrm{M}_\odot$ as in Freeman 1999).

We adopt a modified Hubble law for the present–day total surface density profile of the halo (Binney & Tremaine, 1987):

$$\Sigma_{t,h}(R, t_{now}) \;=\; \frac{\Sigma_{t,h_0}}{1 \;+\; (R/R_\odot)^\alpha}. \tag{2.7}$$

Here we set $\alpha \;=\; 2$. This corresponds to a volume halo density profile:

$$\rho_{t,h}(r, t_{now}) \;=\; \frac{\rho_{t,h_0}}{\left[1 \;+\; (\frac{r}{R_\odot})^2\right]^{3/2}}, \tag{2.8}$$

with $\rho_{t,h_0} \;=\; 2^{3/2}\rho_{t,h}(R_\odot, t_{now})$ and $\Sigma_{t,h_0} \;=\; 2R_\odot\rho_{t,h_0}$. For the MW, we assume $\Sigma_{t,h}(R_\odot, t_{now}) \;=\; 6\ \mathrm{M}_\odot\ \mathrm{pc}^{-2}$ which yields a present–day stellar surface density at $R_\odot$ of $\Sigma_{\star,h}(R_\odot, t_{now}) \;=\; 1.3\ \mathrm{M}_\odot\ \mathrm{pc}^{-2}$ for our model (see Section 2.3), which is consistent with the observed halo stellar density at the solar radius $\rho_{\star,h}(R_\odot, t_{now}) \;=\; 5.7 \times 10^4\ \mathrm{M}_\odot\ \mathrm{kpc}^{-3}$ as estimated by Preston, Shectman & Beers (1991).

The assumption of $\alpha \;=\; 2$, which implies $\rho_{\star,h} \propto r^{-3}$, agrees with a recent analysis (Zibetti, White & Brinkmann 2003) of the halo emission for a sample of $\approx$ 1000 edge–on disc galaxies within the Sloan Digital Sky Survey (SDSS). This result is similar to the density profile $\propto r^{-3.5}$ which has been suggested for the MW stellar halo (Chiba & Beers 2000; Chiba & Beers 2001; Sakamoto, Chiba & Beers

2003).

2.2.3 Star Formation Rate

We assume that the halo star formation (SF) happens on a short time–scale because of a rapid infall event associated with the collapse of a single massive proto–galactic cloud (Eggen et al., 1962) or with multiple mergers of building–blocks (Searle & Zinn, 1978). The disc SF is assumed to be a more quiescent phenomenon, and likely to be driven by the spiral arms (e.g., Wyse & Silk 1989). Therefore, we adopt a different SF law for each component.

The adopted halo SFR is described as:

$$\psi_h(R,t) \;=\; \nu_h \Big(\frac{\Sigma_g(R,t)}{1\ M_\odot\ pc^{-2}}\Big)^{1.5}\ \mathrm{M_\odot\ Gyr^{-1}\ pc^{-2}}, \qquad (2.9)$$

where ν_h is the star formation efficiency (SFE) in the halo. Therefore, the halo SFR follows a Schmidt law with exponent 1.5 (e.g., Kennicutt 1998). The adopted halo SFE is $\nu_h \;=\; 0.125$, which is approximatively half of the value ($\nu_h \;=\; 0.25 \pm 0.07$) suggested by Kennicutt (1998) and is chosen to give the best fit to the observed halo MDF in the solar neighbourhood (see Section 2.3). Stars born before t_{delay}, when the disc phase starts (Section 2.2.1), are hereafter labelled as "halo stars".

The adopted disc SFR is written as:

$$\psi_d(R,t) \;=\; \nu_d \Sigma_g(R,t)^2\, \frac{R_\odot}{R}\ \mathrm{M_\odot\ Gyr^{-1}\ pc^{-2}}, \qquad (2.10)$$

where ν_d is the SFE in the disc. This formulation (Wyse & Silk, 1989) reflects the assumption that SF in the disc is triggered by the compression of the ISM by spiral arms. The efficiency factor ν_d is a free parameter. We have found that ν_d affects both the present–day gas fraction and the disc MDF. The value $\nu_d \;=\; 0.03$ is used in our MW model to reproduce the observed gas density profile of the MW disc and the observed MDF in the solar neighbourhood.

2.3 The Milky Way model

Using the multi–zone model described in the previous section, we construct a model which closely reproduces the known observational properties of the MW. The adopted parameters are summarised in Table 2.1 (MW model).

Fig. 2.1 "a" compares the model MDF in the solar neighbourhood with the observed MDF of K dwarfs (Kotoneva et al., 2002). Here we have assumed a K dwarf mass range of 0.8 – 1.4 $M_\odot$ and convolved the model MDF with a Gaussian error function with $\sigma = 0.15$ dex, consistent with the known empirical uncertainties of the observational data. There is good agreement between the model and the data. In Fig. 2.1 "b", the predicted halo MDF at the solar radius is shown. Our MDF includes all stars still on the main–sequence at the present–time. The MDF has been convolved with a Gaussian error function with $\sigma = 0.25$ dex (e.g., Asplund 2003). Our model is in agreement with the observed halo MDF in the solar neighbourhood (Ryan & Norris, 1991). The evolution of [O/Fe] as a function of [Fe/H] for the gas component in the solar neighbourhood is shown in Fig. 2.1 "c". The model result is consistent with the trend observed in local stars. Fig. 2.1 "d" displays the predicted SF history in the solar neighbourhood. The SF history has been estimated by several authors (e.g.: Bertelli & Nasi 2001; Hernandez et al. 2000). Unfortunately, such observational estimates are not defined well enough to provide useful constraints on a chemical evolution model. Nevertheless, Fig. 2.1 "d" demonstrates that our MW model is consistent with the broad range of the estimated SFR as summarised in Rana (1991).

The left panels of Fig. 2.2 show the predicted radial distribution of the present–day hydrogen column density (upper) and of the present–day oxygen (middle) and sulfur (bottom) abundances of the gas, and compare them to the observations. The observed hydrogen surface density is obtained by summing the surface densities of H_2 and HI (Dame, 1993)[3]. The result of our MW model is compatible with the observed hydrogen distribution at the inner radii within the uncertainties ($\approx 50\%$) of the observed values [4]. However, the hydrogen surface density at the outer radii is overestimated when compared with the observations.

The predicted present–day radial abundance profiles of oxygen and sulfur also reproduce the abundances observed in HII regions (Vilchez & Esteban 1996; Afflerbach et al. 1997), although at the outer radii the model overestimates the sulfur abundances.

Our semi–analytic model, whose parameter values are summarised in Table 2.1,

---

[3] The HI surface density profile has been recently confirmed by Nakanishi & Sofue (2003).

[4] The contribution of HII should also be considered. However, so far no reliable measurement has been achieved.

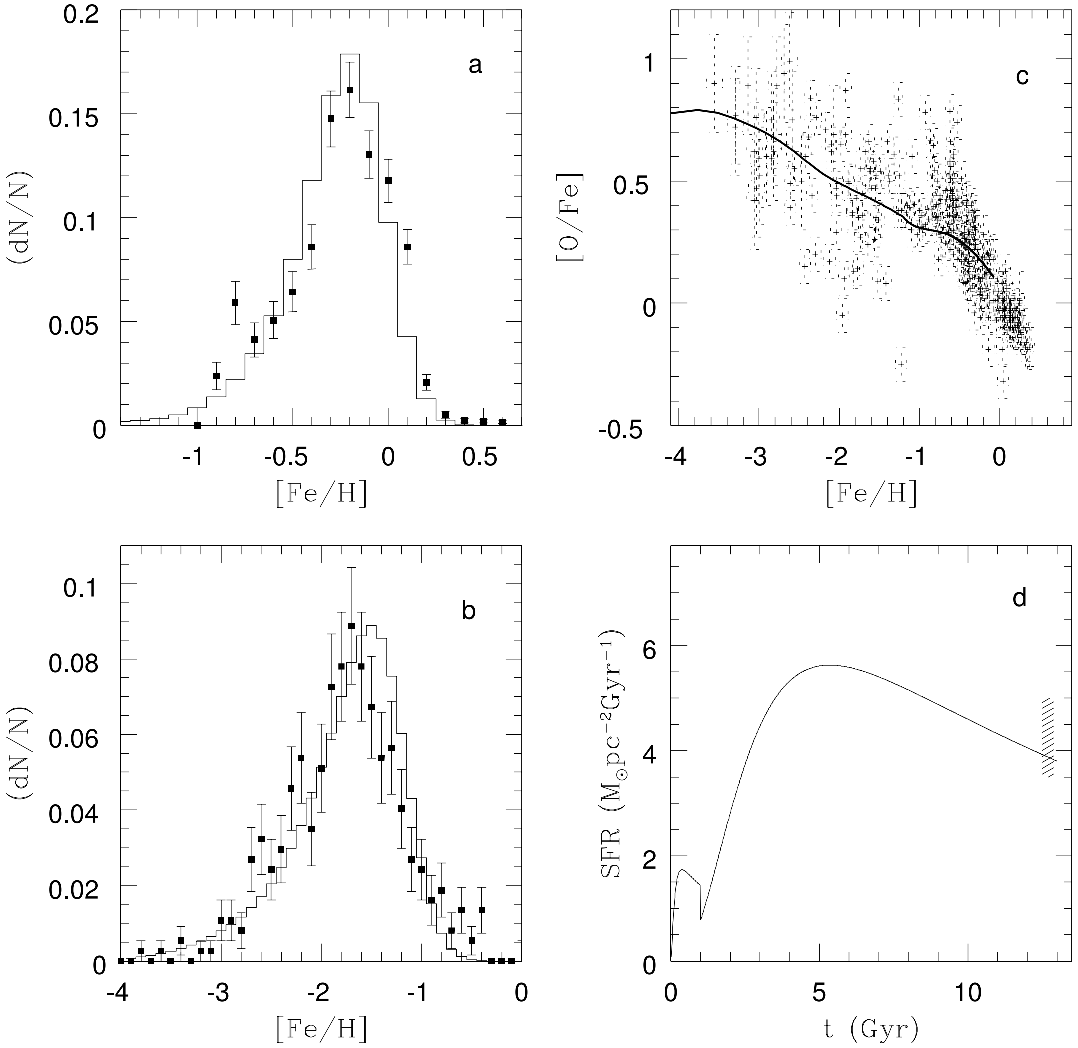

Figure 2.1: Comparison between the results of the MW model (solid lines) and the observations of: “a” the MDF in the MW in the solar neighbourhood (closed boxes with error–bars, Kotoneva et al. 2002); “b” the halo MDF at $R = R_\odot$ (Ryan & Norris 1991, closed boxes with statistical Poissonian error–bars); “c” [O/Fe] and [Fe/H] for stars observed in the solar neighbourhood (Carretta et al. 2000, who included reanalysis of Sneden et al. 1991, Tomkin et al. 1992, Kraft et al. 1992, Edvardsson et al. 1993; Gratton et al. 2003; Bensby, Feltzing & Lundström 2003; Cayrel et al. 2003); “d” the present–day SFR in the solar neighbourhood as summarised in Rana (1991, the shaded region).

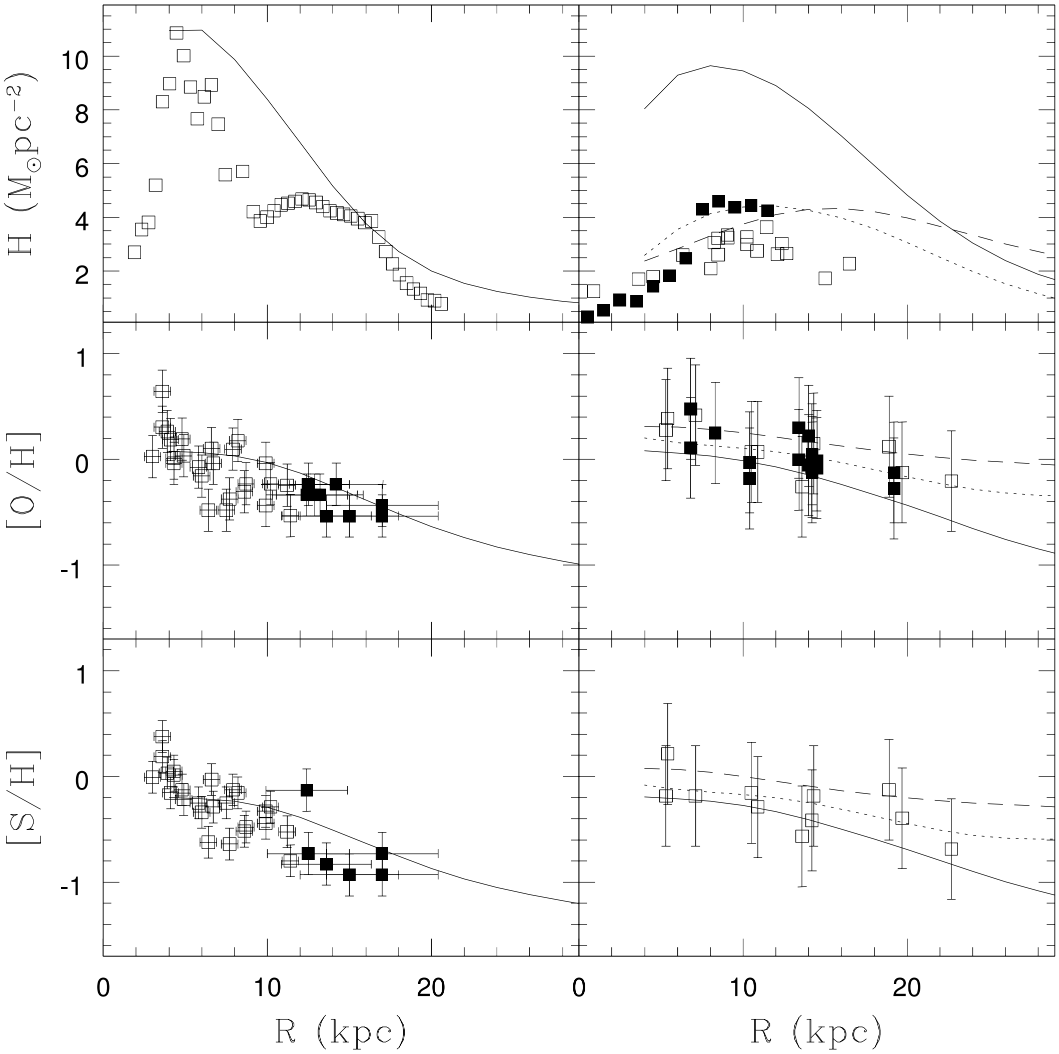

Figure 2.2: Radial distributions of the present–day hydrogen surface density (upper) and of the present–day oxygen (middle) and sulfur (bottom) abundances for the MW model (left) and the M31 models (right). In the left panels, the solid lines are for the MW model results. In the right panels, solid, dotted and dashed lines display the M31a, M31b and M31c models, respectively. The observed distributions of the total surface density of hydrogen for the MW are from Dame (1993, open boxes), and those for M31 are from Dame et al. (1993, open boxes) and Loinard et al. (1999, closed boxes). Observations of abundances in HII regions in the MW, from Vilchez & Esteban (1996) and Afflerbach et al. (1997) (closed and open boxes, respectively), are shown in the left panels. Those in M31, from Dennefeld & Kunth (1981) and Blair et al. (1982) (closed and open boxes, respectively), are shown in the right panels.

satisfies the general MW observational constraints. We now use the same framework to study the chemical evolution of M31.

2.4 The M31 models

The M31 models employ for the disc a different surface density profile from that of the MW model. Since the halo density profile of M31 is unknown, we adopt the same halo profile used in the MW model (see Section 2.3). The SF history of halo and disc is described by the parameters listed in Table 2.1. In Section 2.4.1, we first show a M31 model which adopts the same parameter set of our MW model. This model fails to reproduce some crucial features observed in M31. Therefore, in Sections 2.4.2 and 2.4.3, we present two models able to better explain the key observations.

2.4.1 M31a model: MW analogue

First, we construct a M31 model (M31a) with the same parameter values of our MW model. These parameters are summarised in Table 2.1. The right panels of Fig. 2.2 show the radial distributions of the present–day hydrogen surface density and the radial profiles of the present–day oxygen and sulfur abundances of the gas phase. The radial profiles of oxygen and sulfur abundances are reproduced within the observational errors. The M31a model results in too high hydrogen surface density when compared with the data. This is because the observed hydrogen surface density in M31 is smaller than in the MW.

Fig. 2.3 shows the radial profile for the mean [Fe/H] of main–sequence (MS) stars for the M31a model. Hereafter we simply call ⟨[Fe/H]⟩ the "mean metallicity". Model results are compared with observations by Bellazzini et al. (2003)[5]. We have chosen as reference fields those which are mostly disc– (or halo–) dominated, with estimated halo– (or disc–) contamination around or lower than 10% (see Table 1 in Bellazzini et al. 2003): the disc–dominated fields (G287, G119, G33, G76, G322 and G272) lie at deprojected[6] galactocentric distances $R \approx 8$ kpc, $R \approx 12$ kpc,

---

[5] The observed MDFs are derived from red giant branch (RGB) stars, whereas the model produces the MDFs of MS stars, since it is difficult to construct MDFs of RGB stars within our framework. We assume that this inconsistency does not significantly affect our comparison.

[6] The inclination angle of the M31 disc is $i_{M31} \approx 12.5°$.

$R \approx 13$ kpc, $R \approx 14$ kpc, $R \approx 15$ kpc and $R \approx 18$ kpc, respectively; the halo–dominated fields (G319, G11, G351, G219 and G1) lie at projected galactocentric distances $R \approx 16$ kpc, $R \approx 17$ kpc, $R \approx 19$ kpc, $R \approx 20$ kpc and $R \approx 34$ kpc, respectively. Fig. 2.3 shows that M31a is in broad agreement with the observed mean metallicity in the disc–dominated fields, though the metallicity gradient is slightly steeper than the observed one (Table 2.2). On the other hand, the mean metallicity of the halo in M31a is too low, compared to the data.

To overcome the failure of M31a, we explored the parameter space of the M31 models which could explain the observational properties of M31, and found two viable solutions. In the following, we present these two models.

2.4.2 M31b model: our best model

The model parameters of M31b are summarised in Table 2.1. Compared with the M31a model, i.e. the MW analogue, this model has a shorter time–scale for the infall of disc gas (i.e. smaller a_d and b_d) and higher disc and halo SFE. We found that a combination of higher disc SFE and shorter time–scale for the disc infall leads to better agreement with the observed radial profile of the present–day hydrogen surface density. In addition, a higher SFE in the halo phase leads to a more metal–rich halo, and we adopt a SFE 100 times higher in the halo phase than in the M31a model.

In M31b the radial profile of the present–day oxygen and sulfur abundances reproduces the observational data to roughly the same degree of the M31a model (Fig. 2.2). On the other hand, the higher disc SFE leads to stronger SF and therefore larger depletion of gas, and lower present–day hydrogen surface density than in M31a. Consequently, the result of the M31b model is in better agreement with the observed radial profile of the hydrogen surface density (Fig. 2.2). The hydrogen surface density profiles in both the M31b model and the observations peak at a radius of $\approx$ 8 kpc with a value of ≈ 4.5 $M_\odot$ pc^{-2} (Loinard et al., 1999). However, and similarly in the MW model, the hydrogen surface density at the outer radii is overestimated in M31b when compared with observations from Dame et al. (1993). We have tried to reproduce the observed hydrogen surface density at the outer radii by changing various parameters. However, we are unable to find a better parameter set. This might suggest that, to explain the low gas surface density at the outer radii in M31, another mechanism which is not included in our semi–analytic model

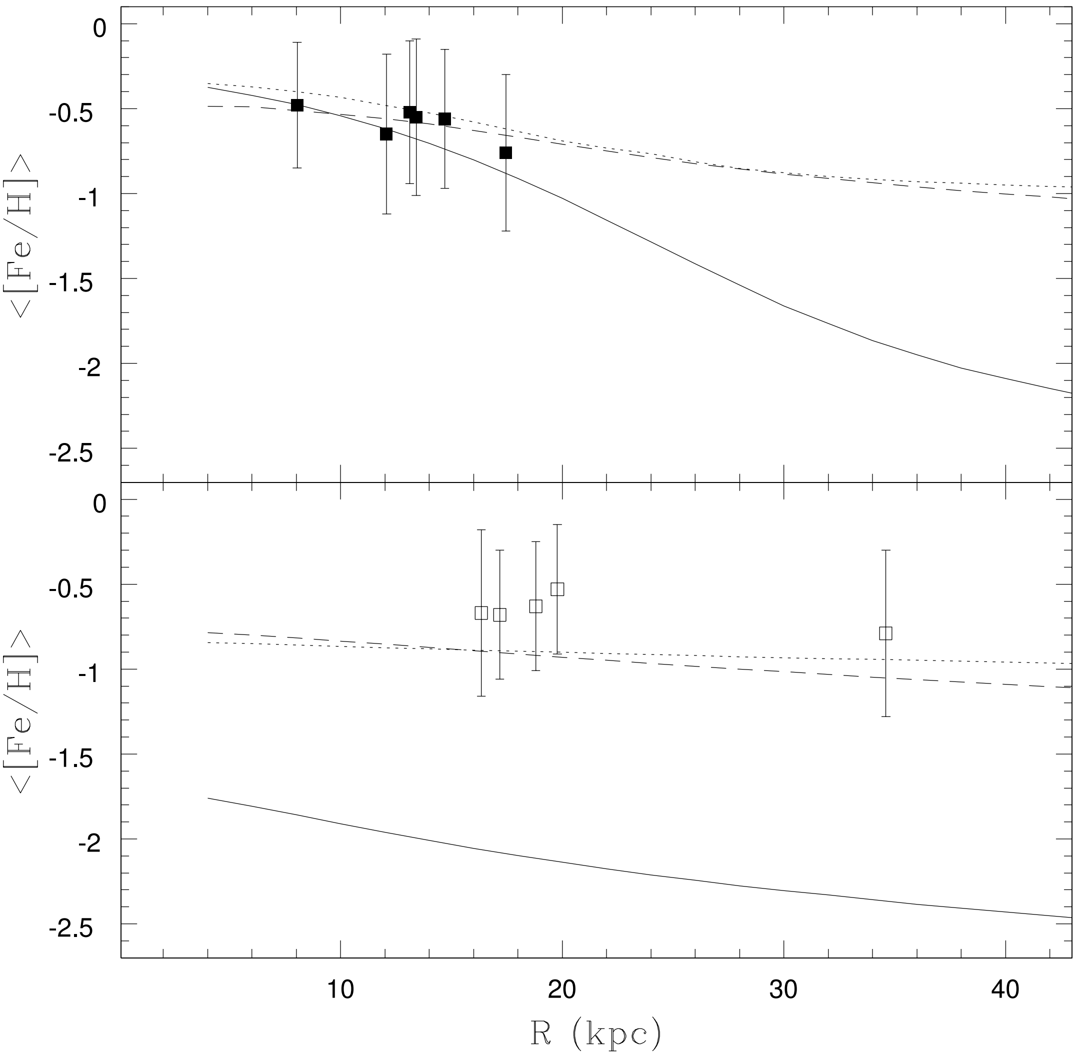

Figure 2.3: Radial profile of the present–day mean stellar metallicity of both disc (upper panel) and halo (lower panel). Solid, dotted and dashed lines represent the results of the M31a, M31b and M31c models, respectively. The mean metallicities from Bellazzini et al. (2003) are also shown (closed boxes with 1 σ dispersion of their MDF).

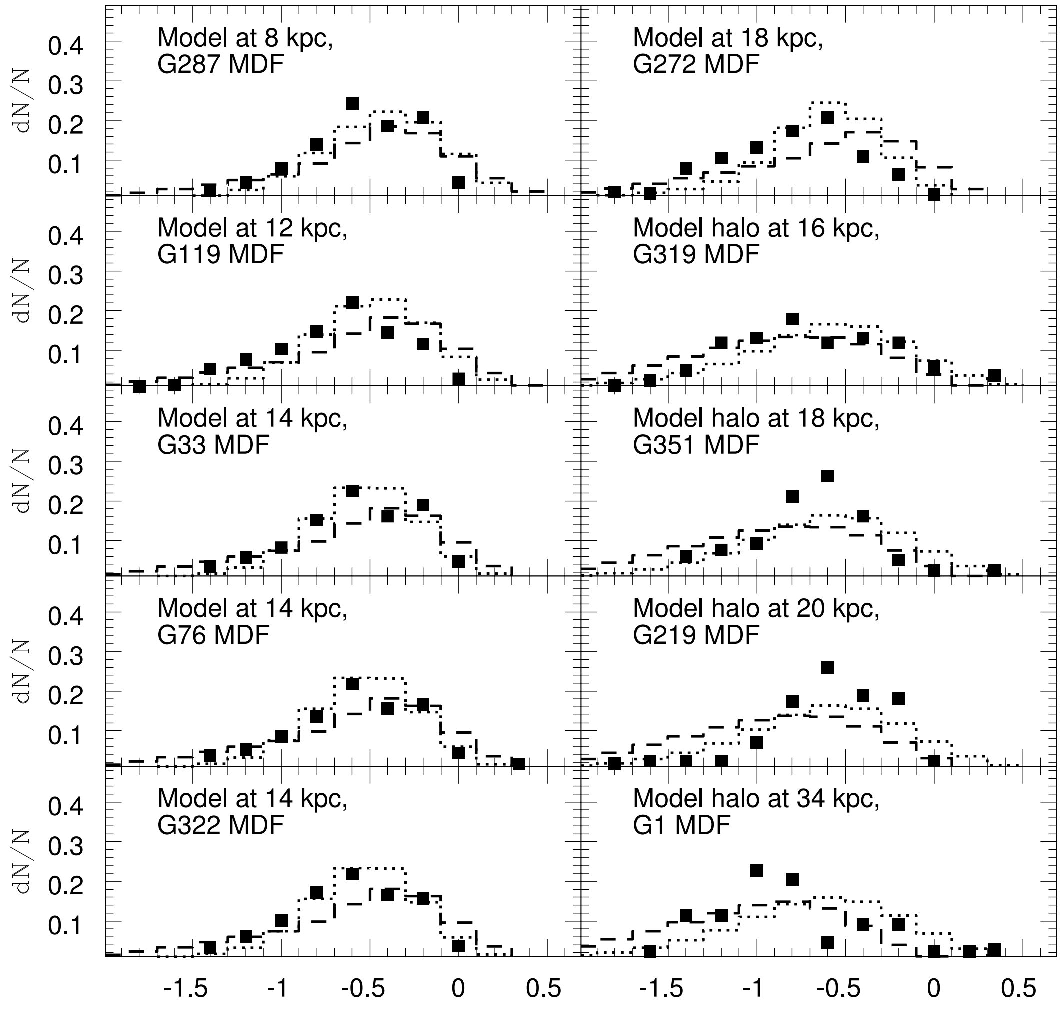

Figure 2.4: The MDFs of the M31b and M31c models (dotted and dashed lines, respectively). The MDFs observed from Bellazzini et al. (2003) are also shown (closed boxes).

is required.

The additional benefit of the shorter time–scale of the disc infall in M31b is its smaller SFR at the present–day. Since M31b has a SFR which peaks at an earlier epoch than in M31a, M31b predicts a lower present–day SFR (≈ 1.5 M$_\odot$ yr^{-1}) in the disc (4 – 20 kpc) than in M31a (≈ 2.4 M$_\odot$ yr^{-1}). The observational estimates of the present–day SFR in M31 still have a large uncertainty. For example, Williams (2002) estimated the SFR for the last $\approx$ 5 Gyr roughly between $\approx$ 2 and $\approx$ 20 M$_\odot$ yr^{-1}, while Williams (2003) inferred that the total SFR for the M31 disc has been $\approx$ 1 M$_\odot$ yr^{-1} over the past 60 Myr. This value is higher than the SFR of $\approx$ 0.2 M$_\odot$ yr^{-1} estimated from H α and Far Infra–Red luminosities (Devereux et al., 1994). In addition, all these values could be affected by systematic errors (e.g., Bell 2003). Nevertherless, these observations suggest that M31 has a lower SFR than in the MW, and M31b is consistent with this trend.

Fig. 2.3 shows improved agreement between the results of the M31b model and the observations of the present–day mean metallicity for both disc– and halo–dominated fields. In the disc, M31b has a shallower metallicity gradient than in M31a, and better reproduces the observed gradient (Table 2.2). This is mainly due to the small b_d we adopted (Table 2.1).

Fig. 2.4 directly compares the MDFs of M31b with the MDF obtained in Bellazzini et al. (2003) in different fields. The model MDFs are derived from main–sequence stars, and convolved with a Gaussian error function with $\sigma = 0.25$ dex. There is qualitative agreement between the MDFs of the M31b model and those observed, especially in the disc–dominated fields. The main exception is the G1 halo–dominated field, whose observed MDF is more metal–poor and bimodal. The MDFs of the G351 and G219 halo–dominated fields show narrower peaks than those of the model. Differences in the shape of the observed halo MDFs among the different fields suggest possible inhomogeneities in the M31 halo (see also Bellazzini et al. 2003).

In the framework of our semi–analytic models, M31b gives the best fit for the observational constraints available in M31. In Section 2.5, we discuss the formation process of M31 which is implied by these results.

2.4.3 M31c model: another possible model

The results of the M31b model suggest that a stronger halo SF can produce a metal–rich halo. However, applying the higher SFE is not the only way to induce stronger

Table 2.2: Radial gradients (dex/kpc) for the present–day mean stellar metallicity of the MDFs in the M31 models. The results for the MW model and for the M31 fields observed in Bellazzini et al. (2003) are also presented as reference. $(\Delta\langle[Fe/H]\rangle/\Delta R)$ refers to the range 4 – 16 kpc for the MW model and 4 – 20 kpc for the M31 models. $(\Delta\langle[Fe/H]\rangle/\Delta R)_{halo}$ refers to the range 4 – 30 kpc in the halo for both the MW and the M31 models.

	$(\Delta\langle[Fe/H]\rangle/\Delta R)$	$(\Delta\langle[Fe/H]\rangle/\Delta R)_{halo}$
MW	−0.058	−0.021
$\mathrm{M31_{obs}}$	−0.026	−0.008
M31a	−0.041	−0.021
M31b	−0.021	−0.003
M31c	−0.014	−0.009

SF. This can also be achieved by employing a larger reservoir of infalling halo gas, without increasing the SFE. Here we discuss the M31c model, which assumes a much larger present–day halo surface density and a longer (6 Gyr) halo phase (Table 2.1). Again, to explain the observed hydrogen surface density, M31c uses a shorter disc infall time–scale, and a weaker radial dependence, which also leads to a present–day SFR similar to that of the M31b model.

Fig. 2.2 shows the predicted present–day radial distributions of oxygen and sulfur abundances which are in agreement with the observational data to roughly the same degree of the other models. The present–day hydrogen surface density profile of the M31c model is consistent with Dame et al. (1993) in the inner region of the disc at $R < 12$ kpc. However, M31c has a broader peak at a larger radius than in M31b. Consequently, the model overestimates the surface density in the outer region at $R > 12$ kpc. Again, this result might suggest that additional physical mechanisms operate, to explain the observed low hydrogen surface density at the outer radii.

Fig. 2.3 shows that M31c also reproduces the observed present–day radial distributions of the metallicity, similarly to the M31b model. The metallicity gradient in M31c is flatter than in M31b at the inner radii as a consequence of the weaker radial dependence of the disc infall time–scale (i.e. a smaller b_d). In the halo fields, M31c also has systematically higher metallicity than in M31a and a steeper gradient than in M31b. Although the gradient is in better agreement with the observations than in M31b (Table 2.2), M31c has lower mean metallicities than observed, especially at the outer radii. In Fig. 2.4, the predicted MDFs at different radii are displayed. The MDFs of M31c are also in good agreement with those observed, especially in the disc. On the other hand, the halo MDFs show a more pronounced metal–poor tail than in M31b.

Thus, the M31c model also leads to acceptable results, although M31b is in better agreement with the observations. The next section discusses the formation history of M31 implied by the M31b and M31c models.

2.5 Discussion

The results in the previous section have shown that the main trends of the chemical evolution history of both the MW and M31 can be described using the same framework. We have also found that to explain the observations in more detail, different sets of parameter values for the formation history are required for the MW and M31, respectively. In this section, we discuss how these different parameters values relate to different galaxy formation histories.

The previous sections have shown that the main differences between the MW and M31 include the present–day hydrogen surface density in the disc and, more significantly, the present–day halo metallicity. The smaller hydrogen surface density in M31 can be explained by a combination of the shorter disc infall time–scale and the higher disc SFE.

The most striking difference is that the mean metallicity observed in the M31 halo is about ten times higher than that observed in the MW halo, though both galaxies have similar mass and morphology.

Which is a "typical" halo? Metal–rich halos seem more common than metal–poor ones, as pointed out by Zibetti et al. (2004) who analysed a sample of about 1000 edge–on disc galaxies within the SDSS. Harris & Harris (2001) have also shown that the NGC5128 halo MDF closely resembles that in the M31 halo. This similarity is perhaps suggestive of a common history in the halo formation of both galaxies, despite their different Hubble–type.

A straightforward way to obtain a more metal–rich halo would be by requiring homogeneous pre–enrichment of the infalling halo gas with a metallicity $Z \approx 0.1\ Z_{\odot}$. However, this metallicity seems too high, if such pre–enrichment occurred homogeneously in the whole universe. For example, although this value is close to the mean metallicity of Damped Lyman α systems (DLAs), many DLAs have much lower metallicity (Pettini 2003; Prochaska et al. 2003). If DLAs are more evolved systems than the infalling halo gas, their metallicity should be higher than that induced by pre–enrichment. Therefore, a pre–enrichment of $Z \approx 0.1\ Z_{\odot}$ may not be tenable.

We found that the observed metal–rich halo of M31 could be explained by two scenarios without any pre–enrichment: a) a higher halo SFE; b) a larger reservoir of infalling halo gas with a longer halo phase. Scenario a) might be explained in a hierarchical clustering regime, where the halo is formed by accretion of building–blocks. Theory predicts that gas removal by supernova–driven winds should be more effective in lower mass systems, leading to a consequent suppression of the SFR and a low SFE (e.g.: Dekel & Silk 1986; Efstathiou 2000). In addition, observations based on the SDSS also suggest that the SFE decreases with decreasing stellar mass in low mass galaxies with a stellar mass $\mathrm{M}_{\star} < 3 \times 10^{10}\ \mathrm{M}_{\odot}$ (Kauffmann et al., 2003). Therefore, higher SFE in the M31 halo phase would be explained if the building–blocks of the M31 halo are systematically higher mass systems than those of the MW halo (see also Harris & Harris 2001). This result again supports the notion of diversity in the formation of spiral galaxies which are apparently similar in mass and morphology and belong to the same Local Group. Admittedly, our model does not adhere to the hierarchical–clustering scenario in a self–consistent manner, however, our chemical evolution models can be interpreted as the "mean" SF and chemical evolution history of the stars which end up at each radius.

As an observational consequence of our models, we found that both scenarios a) and b) predict a more massive stellar halo in M31, respectively about 6 and 9 times more massive than in the MW, whose stellar halo mass is $\approx 10^{9}\ \mathrm{M}_{\odot}$. This result suggests that there might be a correlation between the halo metallicity and its stellar mass. Using dynamical simulations, Bekki, Harris & Harris (2003) show that the stellar halo comes from the outer part of the progenitor discs when the bulge is formed by a major merger of two spiral galaxies. Based on this, they also predict the correlation of the metallicity of the stellar halos and the mass of the bulges which were formed by major mergers, since larger bulges have the larger progenitors, and progenitor spiral galaxies should follow the observed mass–metallicity relation. Although they do not mention a correlation between the masses of the bulge and halo, it would naturally be expected. Thus, a major merger scenario could explain our conclusion. Future observational surveys will better quantify the correlation between the halo metallicity and its stellar mass (e.g., Mouhcine et al. 2005).

It is possible to distinguish scenarios a) and b) through observation. First, due to a longer halo phase, scenario b) predicts intermediate–age population in the M31 halo. This picture could explain the recent evidence of intermediate–age population by deep imaging of the M31 halo (Brown et al., 2003).

It is worth mentioning that the metallicity gradient in the stellar halo is sensitive to the assumed present–day stellar halo density profile, especially in scenario b); a steeper density profile leads to a steeper metallicity gradient. Pritchet & van den Bergh (1994) suggested that the outer halo of M31 can be modeled by a power law surface brightness profile of $I \propto R^{-4}$, which is much steeper than what we assumed ($\propto R^{-2}$). We found that such a steep profile rules out scenario b) to reproduce the flat metallicity gradient observed in the M31 halo. However, it is still difficult to accurately measure the halo surface brightness of M31 (e.g., Zibetti et al. 2004). Thus, more observational estimates of the M31 halo surface brightness profile would be an important test for this scenario.

We also found that the higher halo SFE in scenario a) leads to about 0.2 dex higher [O/Fe] when [Fe/H]< -1 dex, due to intense halo SF. Although measuring [O/Fe] is a hard challenge for the current available instruments, this task could be accomplished by the next–generation large–aperture optical telescope.

2.5.1 Prospect

The framework we have used can explain the main trends in the chemical properties of both the MW and M31. However, recent observations of stellar streams both in the MW (e.g.: Helmi et al. 1999; Chiba & Beers 2000; Ibata et al. 2002; Brook et al. 2003; Navarro, Helmi & Freeman 2004; Majewski et al. 2004) and M31 (Ibata et al. 2001; McConnachie et al. 2003; Merrett et al. 2003; Zucker et al. 2004; Lewis et al. 2004) clearly identify inhomogeneities in the chemical and dynamical history of both galaxies, which could suggest that a significant fraction of the halo stars results from late accretion of satellite galaxies. In light of these recent observations, it will be important to study both the MW and M31 in more detail by employing a self–consistent chemo–dynamical model (e.g., Brook et al. 2004) to trace their interrelated chemical and dynamical histories.

Chapter 3

Stellar Halo Metallicity–Luminosity Relationship for Late–Type Galaxies

The stellar halos of late–type galaxies bear important chemo–dynamical signatures of galaxy formation. We present here the analysis of 89 semi–cosmological late–type galaxy simulations, spanning ~ 4 magnitudes in total galactic luminosity. These simulations sample a wide variety of merging histories and show significant dispersion in halo metallicity at a given total luminosity - more than a factor of 10 in metallicity. Our analysis suggests that galaxies with a more extended merging history possess halos which have younger and more metal rich stellar populations than the stellar halos associated with galaxies with a more abbreviated assembly. A correlation between halo metallicity and its surface brightness has also been found, reflecting the correlation between halo metallicity and its stellar mass. Our simulations are compared with recent Hubble Space Telescope observations of resolved stellar halos in nearby spirals.

3.1 Introduction

Understanding the formation history of stellar halos is one of the classical pursuits of galactic astronomy. The problem is generally framed within the context of two competing scenarios: one of "rapid collapse" (Eggen, Lynden–Bell & Sandage, 1962), in which the stellar halo is formed by the rapid collapse of a proto–galaxy within a dynamical timescale ($\sim 10^8$ yr), and one of "galactic assembly" (Searle & Zinn, 1978), whereby the stellar halo is assembled on a longer timescale ($\sim 10^9$ yr) by the accretion of "building–blocks", each with separate enrichment history. Both scenarios have their strengths and weaknesses, and it would appear that a hybrid model is the most plausible option consistent with extant data (e.g.: Chiba & Beers 2000; Freeman & Bland-Hawthorn 2002).

An intriguing piece of the halo formation "puzzle" is provided by comparing the stellar halo of our own Milky Way with that of its neighbour, M31. First, despite their comparable total galactic luminosities, the stellar halo of M31 is *apparently* much more metal–rich than that of the Milky Way (e.g.: Ryan & Norris 1991; Mould & Kristian 1986; Durrell, Harris & Pritchet 2001; Ferguson et al. 2002; Brown et al. 2003; Bellazzini et al. 2003; Durrell et al. 2004; Ferguson et al. 2005; Irwin et al. 2005). In fact, the halo of M31 bears a closer resemblance to that of NGC 5128 (e.g., Harris & Harris 2001), despite their differing morphological classifications.

The stellar halo–galaxy formation symbiosis has been further brought to light by the recent work of Mouhcine et al. (see also Tikhonov, Galazutdinova & Drozdovsky 2005). The deep Hubble Space Telescope imaging of nearby spiral galaxy stellar halos in Mouhcine et al. (2005) suggests a correlation between stellar halo metallicity and total galactic luminosity. On the surface, this correlation appears to leave our own Milky Way halo as an outlier with respect to other spirals, with a stellar halo metallicity ~ 1 dex lower than spirals of comparable luminosities (such as M31, as alluded to earlier).

However, it must be noted that the metallicity of the Galactic halo in the Solar Neighbourhood (e.g., in Ryan & Norris 1991) comes from spectroscopic metallicities in a kinematically–selected sample, whereas that of the M31 halo, as well as those of the stellar halos of nearby spiral galaxies (Mouhcine et al., 2005), have primarily been derived from photometric metallicities in topographically–selected samples. Since it is now becoming possible to obtain spectroscopic metallicities for significant samples of kinematically–selected giants in the M31 halo (e.g.: Ibata et al. 2004; Kalirai et al. 2006; Chapman et al. 2006; Ibata et al. 2007), it will be crucial to assess the consistency of the M31 stellar halo metallicity as derived from kinematically– and from topographically–selected samples, respectively.

A grasp of the true scatter around the general trend in the halo metallicity–luminosity relation awaits a larger observational data set, however any theory which attempts to explain such a relation needs to simultaneously account for the *apparent* metallicity discrepancy between the Milky Way and the Andromeda stellar halos.

The question arises as to what is driving the scatter of halo metallicity for galaxies of comparable luminosities?

In what follows, we investigate whether differences in the stellar halo assembly history can explain the diversity seen in halo metallicities. Using chemo–dynamical simulations, we have constructed a sample of 89 late–type galaxies, spanning ~ 4 magnitudes in luminosity, and sampling a wide range of assembly histories at a given luminosity (or mass). We contrast the stellar halo metallicity–galactic luminosity relation in the simulations with the recent empirical determination of Mouhcine et al. (2005). The framework in which the simulations have been conducted is described in Section 3.2, while Sections 3.3 and 3.4 present the results and the related discussion, respectively.

3.2 Simulations

The simulations employed here are patterned after the semi–cosmological adiabatic feedback model of Brook et al. (2004), and were constructed using the chemo–dynamical code `GCD+` (Kawata & Gibson, 2003). `GCD+` self–consistently treats the effects of gravity, gas dynamics, radiative cooling, star formation, and chemical enrichment (including Type II and Ia Supernovae and relaxing the instantaneous recycling approximation). In this framework, gas within the SPH smoothing kernel of Type II Supernova explosions is prevented from cooling for the lifetime of the lowest mass star which ends as a Type II Supernova (Brook et al. 2004 and references therein). Details of both `GCD+` and the feedback model can be found in Kawata & Gibson (2003) and Brook et al. (2004), respectively.

This semi–cosmological version of `GCD+` is based on the seminal work of Katz & Gunn (1991). The initial condition for a given simulation is an isolated sphere of dark matter and gas. This "top–hat" overdensity has an amplitude $\delta_{\rm i}$ at initial redshift $z_{\rm i}$, which is approximately related to the collapse redshift $z_{\rm c}$ by $z_{\rm c} = 0.36\delta_{\rm i}(1 + z_{\rm i}) - 1$ (e.g., Padmanabhan 1993). We set $z_{\rm c} = 2.0$, which determines $\delta_{\rm i}$ at $z_{\rm i} = 40$. Small–scale density fluctuations based on a CDM power spectrum are superimposed on the sphere using `COSMICS` (Bertschinger, 1998), and the amplitude of the fluctuations is parameterised by σ_8. These fluctuations are the seeds for local collapse and subsequent star formation. Solid–body rotation corresponding to a spin parameter λ is imparted to the initial sphere to incorporate the effects of longer wavelength fluctuations. For the flat CDM model described here, the relevant parameters include $\Omega_0 = 1$, baryon fraction $\Omega_b = 0.1$, $H_0 = 50$ km s^{-1} Mpc^{-1}, spin parameter $\lambda = 0.06$, and $\sigma_8 = 0.5$. We employed 14147 dark matter and 14147 gas/star particles.

A series of 89 simulations - all with the *same* number of particles, collapse redshift z_c, and spin parameter λ - were completed spanning a factor of 50 in mass in four separate mass "bins", each with a related initial comoving radius R^i_{40} at $z_i = 40$: $M_{tot} = 10^{11}$ $M_\odot$ ($R^i_{40} = 0.7$ Mpc); 5×10^{11} $M_\odot$ (1.1 Mpc); 10^{12} $M_\odot$ (1.4 Mpc); 5×10^{12} $M_\odot$ (2.4 Mpc).

For each total mass, we run simulations with different patterns of small–scale density fluctuations which lead to different hierarchical assembly histories. This was controlled by setting different random seeds for the Gaussian perturbation generator in `COSMICS`.

3.3 Results

Our grid of 89 simulations was employed to populate the redshift $z = 0$ stellar halo metallicity–luminosity plane (i.e. $\langle[\mathrm{Fe/H}]\rangle_{\mathrm{halo}} - M_V$) shown in Fig. 3.1 (filled symbols). We have been conservative in our topographical definition of "stellar halo", adopting a projected cut–off radius of 15 kpc to delineate the halo from (possible) disc and bulge contaminants. Such a choice should also allow an easier comparison with the observations of halo fields in nearby spiral galaxies.

The stellar metallicity distribution (MDF) was then generated using all the stellar particles from the "halo region", convolved with a Gaussian with $\sigma_{[\mathrm{Fe/H}]} = 0.15$ dex, representing the typical observational uncertainties (e.g., Bellazzini et al. 2003). Only those simulations with > 100 halo stellar particles are included in the analysis here. The related MDFs are displayed in Appendix B.

For each MDF, the peak is displayed in Fig. 3.1; 68% of the stellar particles within a given (simulated) MDF[1] typically span 1.4 dex in metallicity. We confirmed that the halo MDFs are insensitive to projection effects, even in the most massive simulations, suggesting that our cut–off for the "halo region" is sufficient for minimising disc and bulge contamination. The optical properties of our simulated stellar populations were derived using the population synthesis models of Mouhcine

---

[1] Each MDF has been fitted by an univariate skew–normal distribution (e.g.: Azzalini 2005; `http://azzalini.stat.unipd.it/SN/Intro/intro.html`).

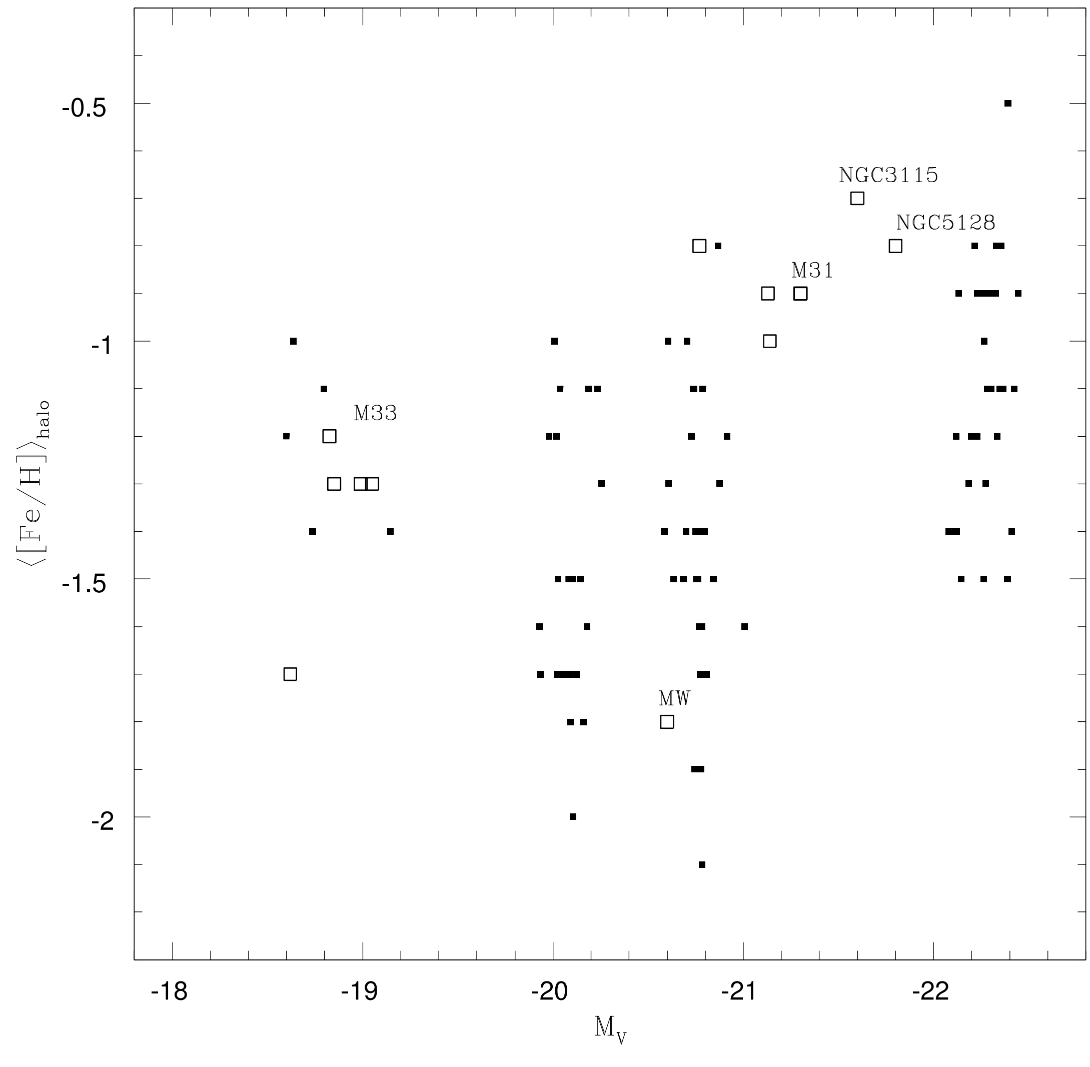

Figure 3.1: The stellar halo metallicity–total galactic V–band luminosity relation ($\langle[\mathrm{Fe/H}]\rangle_{\mathrm{halo}}$ – $\mathrm{M_V}$). A filled box corresponds to the peak of the MDF for a simulation. The related MDFs are displayed in Appendix B. Open (unlabelled) boxes represent the data of Mouhcine et al. (2005); labelled boxes represent additional data taken from the literature (see the text for details). 68% of the stars in the simulated (observed) MDFs are typically enclosed within ±0.7 dex (±0.35 dex) of the peak of the related MDF.

& Lançon (2003), taking into account the age and the metallicity of each stellar particle. We note that the V–band luminosity shown along the abscissa of Fig. 3.1 is the *total* galactic luminosity (i.e. halo + bulge + disc).

Fig. 3.1 also shows the observed halo metallicity–luminosity values for 13 nearby spirals, primarily taken from Mouhcine et al. (2005), supplemented with data from the literature (Binney & Merrifield 1998; Elson 1997; Harris, Harris & Poole 1999; Brooks, Wilson & Harris 2004)[2]. For the observational datasets we located the MDF peak exactly as we did for the simulated datasets. The related MDFs are displayed in Figures B.1 and B.2; 68% of the stars in the observed MDFs are typically enclosed within ± 0.35 dex of the MDF peak, a factor of ~ 2 narrower than the simulations[3].

What is readily apparent from Fig. 3.1 is that significant dispersion in halo metallicity ($\gtrsim 1$ dex) exists at any given total galactic luminosity in our simulations. For a set of simulations with the same initial total mass, the *only* difference among these runs can be traced to the random pattern of the initial small–scale density fluctuations; this translates directly into differing hierarchical assembly histories. Qualitiatively, it would appear that the assembly history alone may account for the diversity in halo metallicity at a given galactic luminosity, and thus account for the apparent outliers in the observed trend. The dispersion in halo metallicity at any given total galactic luminosity is summarised by the histograms in Fig. 3.3, where the distribution of the MDF peaks for the semi–cosmological simulations in Renda et al. (2005b) is shown, although such histograms should be taken as plain summaries, since for each simulation the pattern of the initial small–scale density fluctuations - and the related hierarchical assembly history - has been arbitrarily chosen rather than drawn from a hypothetical a priori distribution of patterns.

Fig. 3.2 shows snapshots of the gas particles at redshift $z = 1.5$ and the associated $z = 0$ stellar Age Distribution Function (ADF) for three of the simulations with $M_{tot} = 10^{12}\ M_{\odot}$. These representative runs show that simulations with more metal–rich halos are assembled over a longer timescale, and thus possess a broader ADF (in both the halo and the associated galaxy). Such a scenario is consistent with the evidence, presented by Brown et al. (2003), of a substantial intermediate–age

---

[2] Note that the identification of the stellar halo in M33 is still debated (e.g., Tiede, Sarajedini & Barker 2004; see also McConnachie et al. 2006).

[3] Our current model does not take into account any pre–enrichment scenario due to extremely metal–poor stars (Pop III hereafter) whose detailed physics is still much debated (e.g.: Woosley, Heger & Weaver 2002; Larson 2005). An early and homogeneous pre–enrichment of the proto–galactic masses due to Pop III could lead to narrower MDFs at lower redshift.

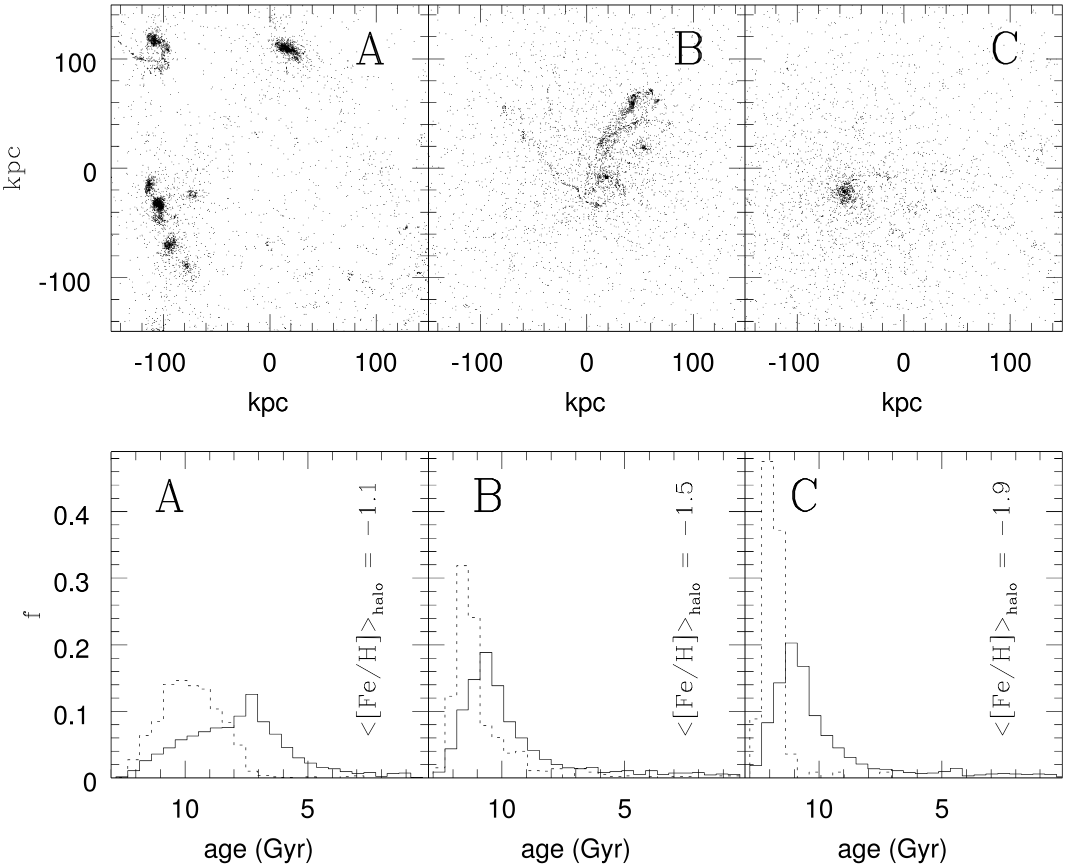

Figure 3.2: Upper panels: Projected distribution of the gas particles at redshift z = 1.5 for simulations with $M_{tot} = 10^{12}\ M_{\odot}$. Lower panels: The associated stellar age distributions at z = 0 for the galaxies in the upper panels. The solid (dotted) histogram corresponds to the stellar age distribution for the entire galaxy (stellar halo). The corresponding z = 0 halo metallicities are denoted in each panel.

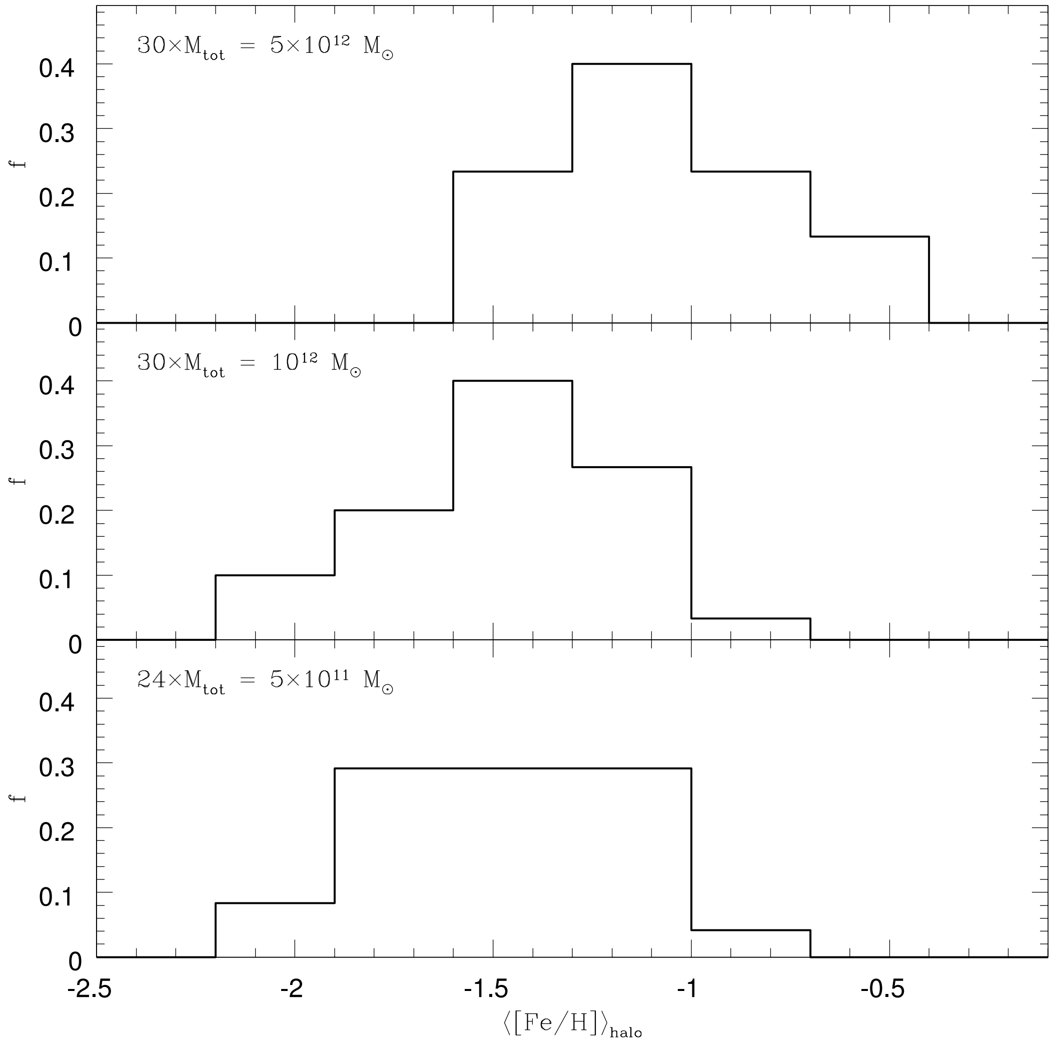

Figure 3.3: Distributions of the z = 0 MDF peaks for the semi–cosmological simulations in Renda et al. (2005b) with $M_{tot} = : 5\times10^{11}\ M_\odot;\ 10^{12}\ M_\odot;\ 5\times10^{12}\ M_\odot$.

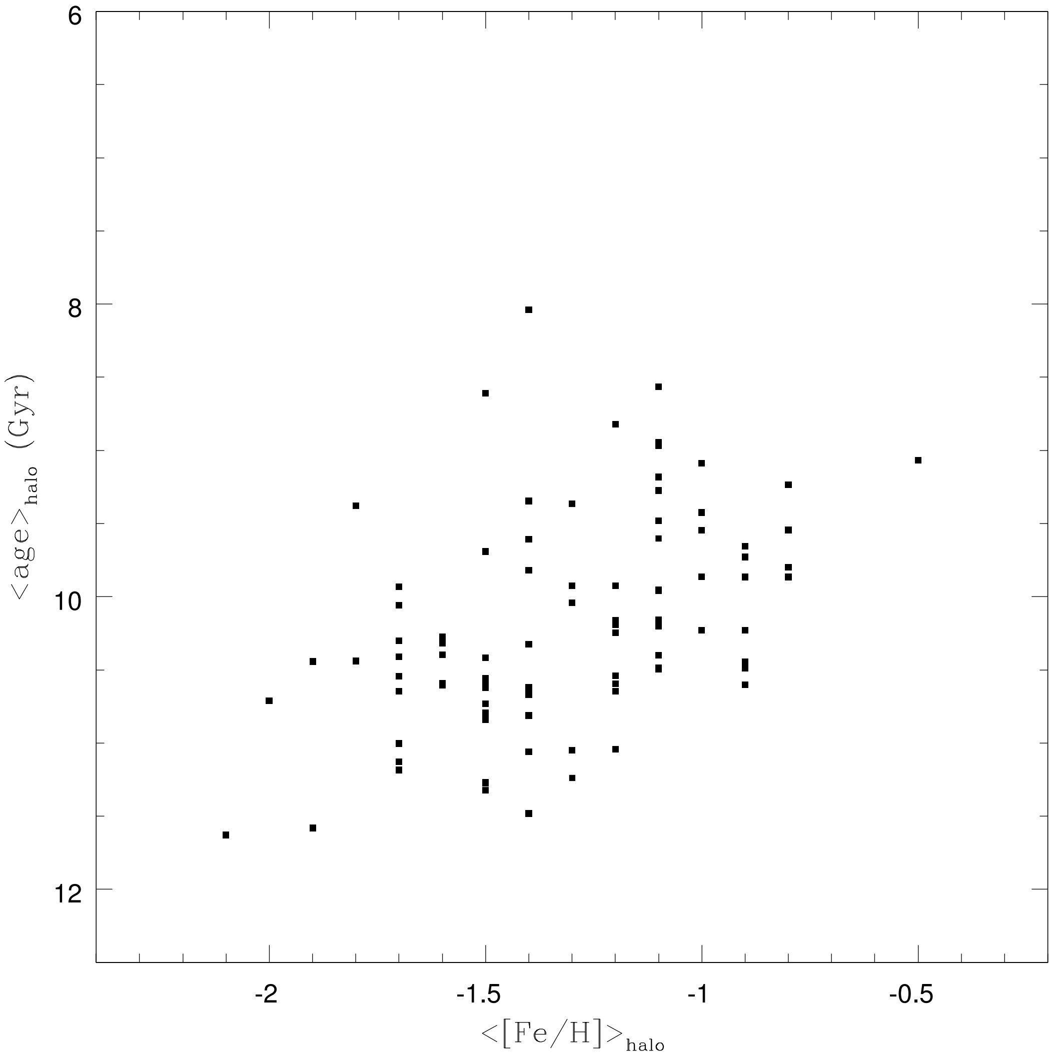

Figure 3.4: The relation between the mean stellar halo age and the peak of the halo MDF in our simulations. The halo ADFs are displayed in Appendix D.

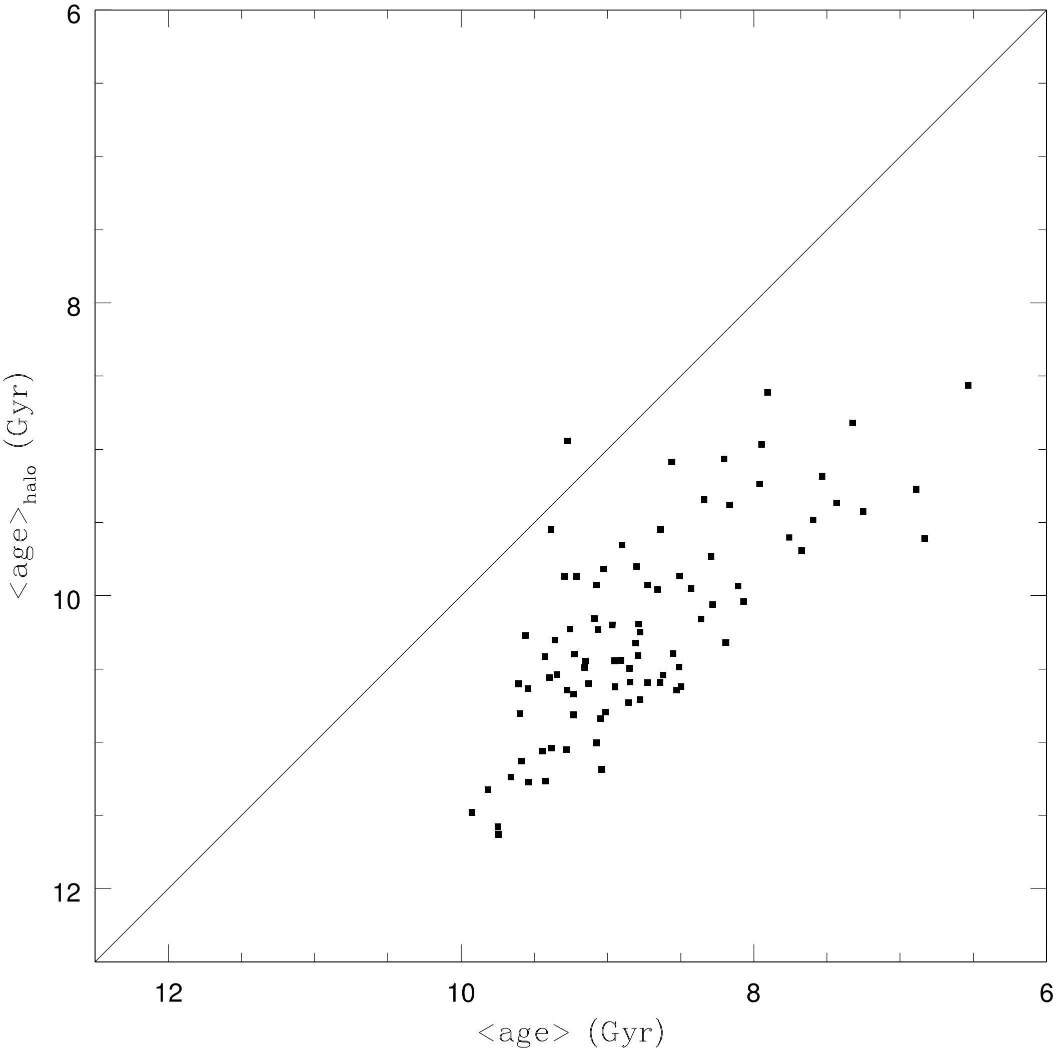

Figure 3.5: The relation between the mean halo age and the mean age for the entire galaxy in our simulations. Both the halo and the galaxy ADFs for each simulation are displayed in Appendix D.

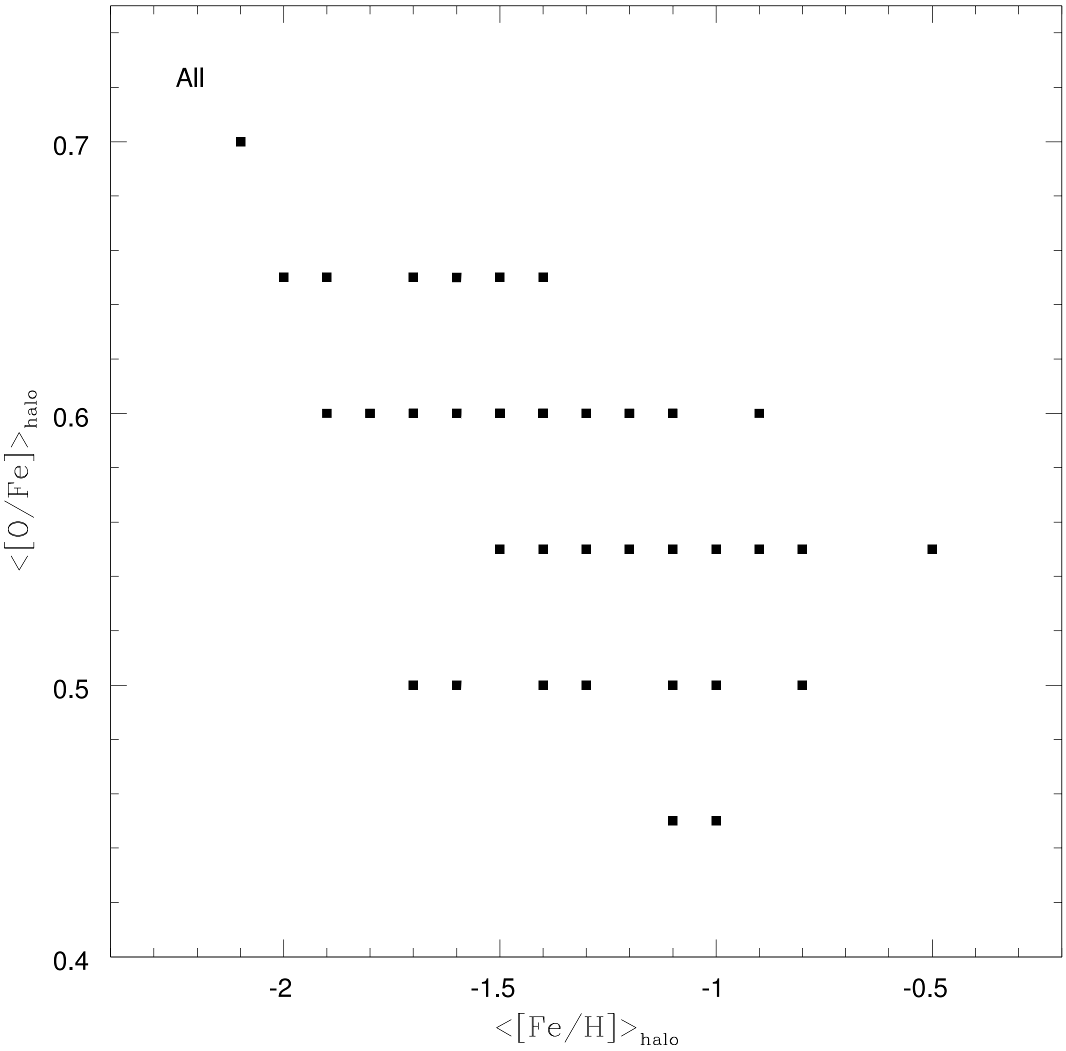

Figure 3.6: The relation between the peak of the halo [O/Fe] distribution and the peak of the halo MDF in our simulations. The related MDFs are displayed in Appendix B. The halo [O/Fe] distributions are displayed in Appendix C.

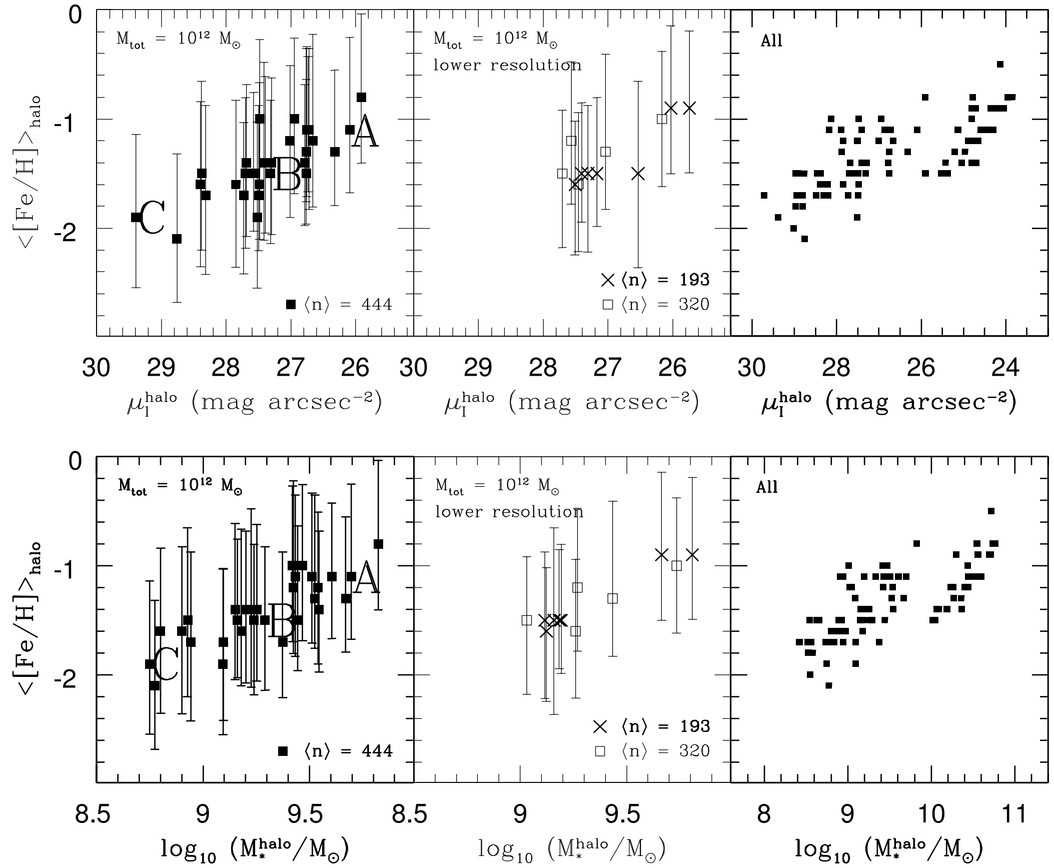

Figure 3.7: Upper panels: Stellar halo metallicity–halo I–band surface brightness relation ($\langle$[Fe/H]$\rangle_{\rm halo}$ – $\mu_{\rm I}^{\rm halo}$). In the left panel, our fiducial simulations with $\rm M_{tot} = 10^{12}\ M_\odot$ and 14147×2 particles are shown, while the middle panel shows the corresponding lower–resolution simulations with 5575×2 (crosses) and 9171×2 (open boxes) particles. The error bars show the 68% Confidence Level around each MDF peak. The average number of halo particles is shown in the bottom right corner of each panel. Simulations with fewer than 100 stellar halo particles (at $\rm R > 15$ kpc) are not included here. Simulations A – C of Fig. 3.2 are displayed in the left panel. The right panel shows the $\langle$[Fe/H]$\rangle_{\rm halo}$ – $\mu_{\rm I}^{\rm halo}$ relation for all the simulations. Lower panels: Halo metallicity–stellar mass relation ($\langle$[Fe/H]$\rangle_{\rm halo}$ – $\rm M_*^{halo}$). In the left panel, our fiducial simulations with $\rm M_{tot} = 10^{12}\ M_\odot$, while the middle panel shows the corresponding lower–resolution simulations. The right panel shows the $\langle$[Fe/H]$\rangle_{\rm halo}$ – $\rm M_*^{halo}$ relation for all the simulations.

metal–rich population in a topographically–selected halo field of M31. Conversely, simulations with more metal–poor halos are assembled earlier through more of a monolithic process, with a consequently narrower ADF. The relationship between the mean stellar halo age and the peak of the halo MDF is summarised in Fig. 3.4. We note that the mean halo age in the simulations broadly correlates with the mean galaxy age as shown in Fig. 3.5, thus suggesting that the assembly history of the halo "knows" of the formation history of the other galaxy structural components (e.g., bulge and disc). Both the halo and the galaxy ADFs for each simulation are displayed in Appendix D.

Further, the most metal–poor stellar halos (which, recall, formed preferentially via more of a monolithic collapse) possess α–elements to iron ratios a factor of ~ 2 higher than the most metal–rich halos (which formed preferentially over a more extended period of hierarchical clustering), as shown in Fig. 3.6. Such a trend is expected if the different amounts of α–elements and Iron released by Type II and Ia Supernovae over different timescales is taken into account (e.g.: Timmes, Woosley & Weaver 1995; Woosley et al. 2002). The halo [O/Fe] distributions are displayed in Appendix C.

Future analysis of higher resolution simulations will clarify whether or not the relationships Figures 3.4, 3.5 and 3.6 point to are broadened in our sample because of the current resolution - thus mimicking tighter correlations.

The upper panels of Fig. 3.7 show the stellar halo metallicity–I–band surface brightness relation ($\langle[\mathrm{Fe/H}]\rangle_{\mathrm{halo}} - \mu_{\mathrm{I}}^{\mathrm{halo}}$) for simulations with $\mathrm{M}_{\mathrm{tot}} = 10^{12}\ \mathrm{M}_{\odot}$; the surface brightness was measured at a projected distance of 20 kpc from the dynamical centre of each simulation. The halo metallicity–stellar mass relation ($\langle[\mathrm{Fe/H}]\rangle_{\mathrm{halo}} - \mathrm{M}_{*}^{\mathrm{halo}}$) is shown in the lower panels of Fig. 3.7. The three galaxies presented in Fig. 3.2 are also displayed in Fig. 3.7. An immediate correlation is apparent with more massive halos possessing higher surface brightness and also higher metallicity. This is consistent with a picture in which galaxies that experienced more extended assembly histories have more massive stellar halos, with both higher halo metallicity and halo surface brightness - i.e. higher stellar halo density.

3.3.1 Robustness

Resolution

The issue of model convergence (resolution) is always a concern when interpreting cosmological simulations (particularly when including baryons). To test this, we conducted a series of simulations for $M_{tot} = 10^{12}$ $M_\odot$, with 5575×2 and 9171×2 particles, to supplement the default grid (which used 14147×2 particles); the middle panels of Fig. 3.7 show where these lower–resolution simulations sit in the halo metallicity–surface brightness plane and in the halo metallicity–stellar mass plane, respectively.

The consistency between higher (left panels) and lower (middle panels) resolution simulations is reassuring[4].

Halo Semantics

Up to now we have dealt with a topographical definition of stellar halo: we have labelled as “halo” the ensemble of stellar particles in a simulation - at $z = 0$ - at a projected radius $R > 15$ kpc. What if the “halo” is defined in a different way? That’s to say: given a different “halo” labelling, how robust is the dispersion in halo metallicity at a given total luminosity? As a robustness test, we have tried to include kinematical information in our halo definition - in a simple way. We have relabelled as “halo” the ensemble of stellar particles in a simulation - at $z = 0$ - at a projected radius $R > 15$ kpc *and* counter–rotating i.e. with circular velocity $v_\theta < 0$. The galactic circular velocity profiles of the sample we have analysed are displayed in Appendix E. Here we focus on the stellar halo[5]. Only those simulations with > 100 stellar particles which are counter–rotating with $v_\theta < 0$ at a projected radius $R > 15$ kpc are included in the robustness test here. The related MDFs are displayed in Appendix F. The MDF peaks are shown in Fig. 3.8.

The dispersion in metallicity at a given total luminosity we found among the topographical halos is not wiped out when we include kinematical information in

---

[4] Since we limit our analysis to simulations with > 100 halo stellar particles, the $\mu_I^{halo} > 28$ mag arcsec^{-2} region of the halo metallicity–surface brightness plane and the $M_*^{halo} < 10^9$ $M_\odot$ region of the halo metallicity–stellar mass plane are underpopulated by the lower–resolution runs (middle panels of Fig. 3.7).

[5] Clearly, the galactic circular velocity profiles show a range of disc features among the late–type galaxy simulations we have analysed. Such features and their relations with both the framework we have chosen at the current resolution and the patterns of initial density fluctuations i.e. the formation histories we have arbitrarily sampled will be the topic of future studies.

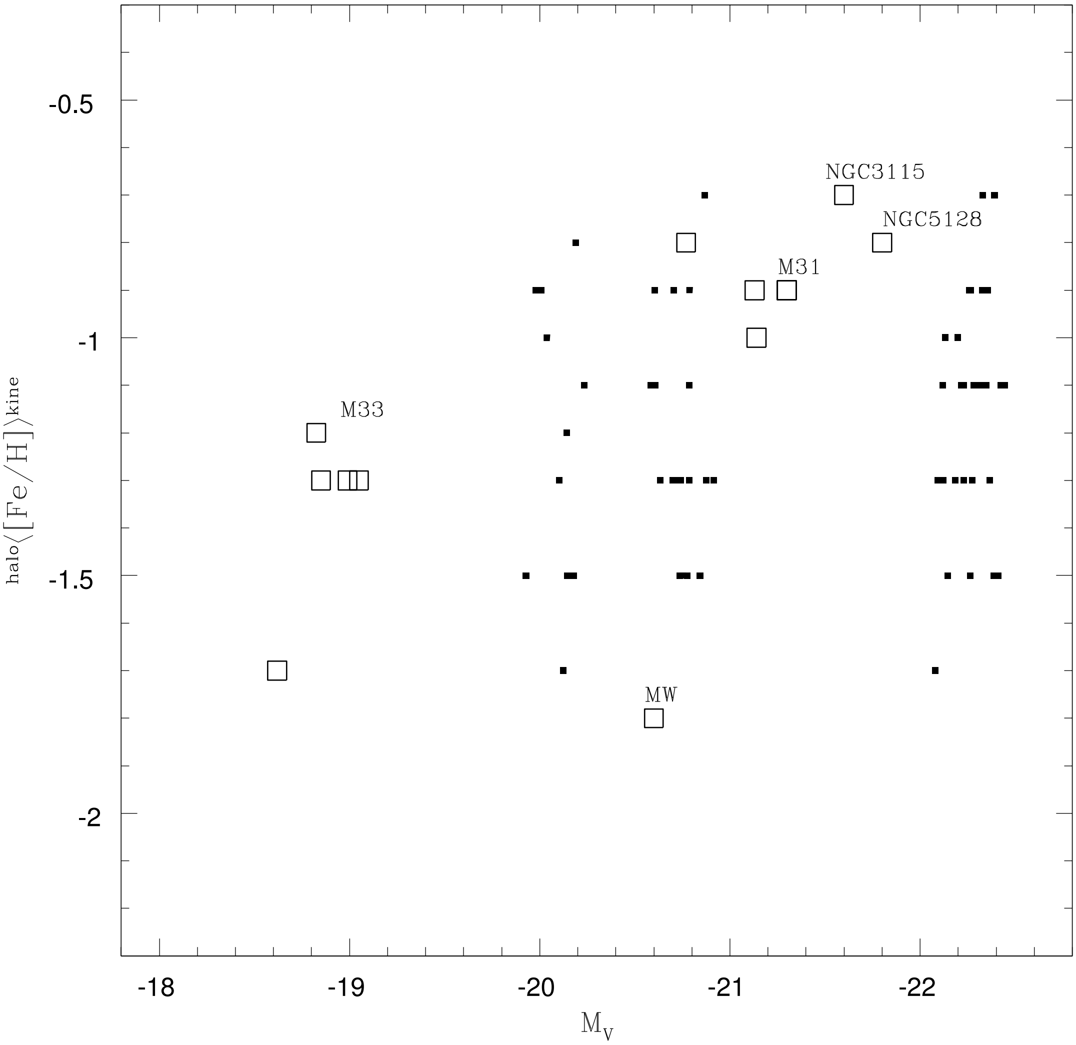

Figure 3.8: The stellar halo metallicity–total galactic V–band luminosity relation (${}^{halo}\langle[Fe/H]\rangle^{kine}$ – M_V). A filled box corresponds to the peak of the MDF which refers, for a simulation, to the ensemble of counter–rotating ($v_\theta < 0$) stellar particles within each topographical halo (at a projected radius $R > 15$ kpc). The related MDFs are displayed in Appendix F. The observational data label–code is as in Fig. 3.1.

our halo definition, as shown in Fig. 3.8 - to be compared with Fig. 3.1.

Given a simulation, the relationship between $^{\rm halo}\langle[{\rm Fe/H}]\rangle^{\rm topos}$ (the "topographical" halo metallicity) and $^{\rm halo}\langle[{\rm Fe/H}]\rangle^{\rm kine}$ (the metallicity of the ensemble of counter–rotating stellar particles within each topographical halo) is shown in Fig. 3.9 whereas the discrepancy in metallicity between the two "halo" labels is shown in Fig. 3.10 as a function of the "topographical" halo metallicity.

For each subset, the distribution of the "topographical" halo mass fraction the ensemble of its counter–rotating stellar particles amounts to is shown in the right panels of Fig. 3.11.

Both Figures 3.9 and 3.10 support what is summarised by the histograms in the left panels of Fig. 3.11 i.e. the discrepancy between $^{\rm halo}\langle[{\rm Fe/H}]\rangle^{\rm topos}$ and $^{\rm halo}\langle[{\rm Fe/H}]\rangle^{\rm kine}$ is distributed around ≈ 0 dex within a range of $\approx \pm 0.5$ dex - although the significance of such a distribution is undermined by both the small size and the current resolution of the sample of simulations which have been analysed. A larger sample size and higher resolution in the simulations will allow a stronger statistical analysis and more complex kinematical selections in the future.

Halo Metallicity

Up to now, each halo MDF we have analysed and the related metallicity peak have referred to the ensemble of stellar particles within what has been labelled as "halo" in a simulation, either the ensemble of stellar particles at a projected radius $R > 15$ kpc (the "topographical" halo) or the ensemble of counter–rotating ($v_\theta < 0$) stellar particles within the "topographical" halo.

As a robustness test, we generate the simulated Colour–Magnitude–Diagram (CMD hereafter) for each "topographical" halo. Next, we approach each simulated CMD the same way an observed CMD is approached in Mouhcine et al. (2005), i.e., through the same pipeline, a metallicity–colour relationship is constructed out of the fiducial Red Giant Branch (RGB hereafter) tracks to derive the metallicity of each (generated) star in the RGB of the (simulated) CMD.

The Padova[6] theoretical isochrones (Girardi et al., 2002) in the metallicity range of $0.0001 < Z < 0.030$ have been used to generate the simulated CMD out of the ensemble of stellar particles in the "topographical" halo for each simulation. The theoretical isochrones are taken into account up to the RGB tip and

---

[6] `http://pleiadi.pd.astro.it`

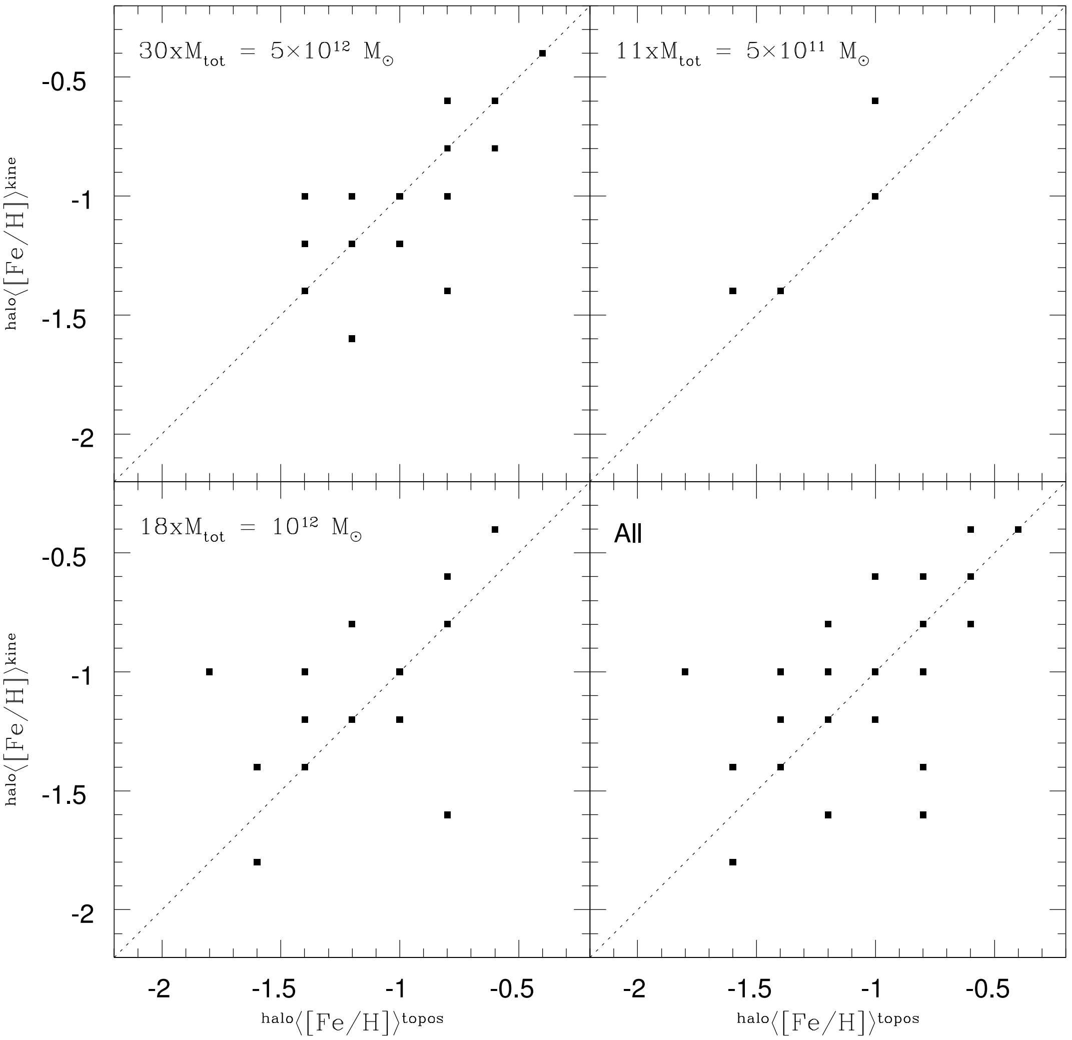

Figure 3.9: The relationship between ${}^{\rm halo}\langle[{\rm Fe/H}]\rangle^{\rm topos}$ (the "topographical" halo metallicity) and ${}^{\rm halo}\langle[{\rm Fe/H}]\rangle^{\rm kine}$ (the metallicity of the ensemble of counter–rotating stellar particles within each topographical halo).

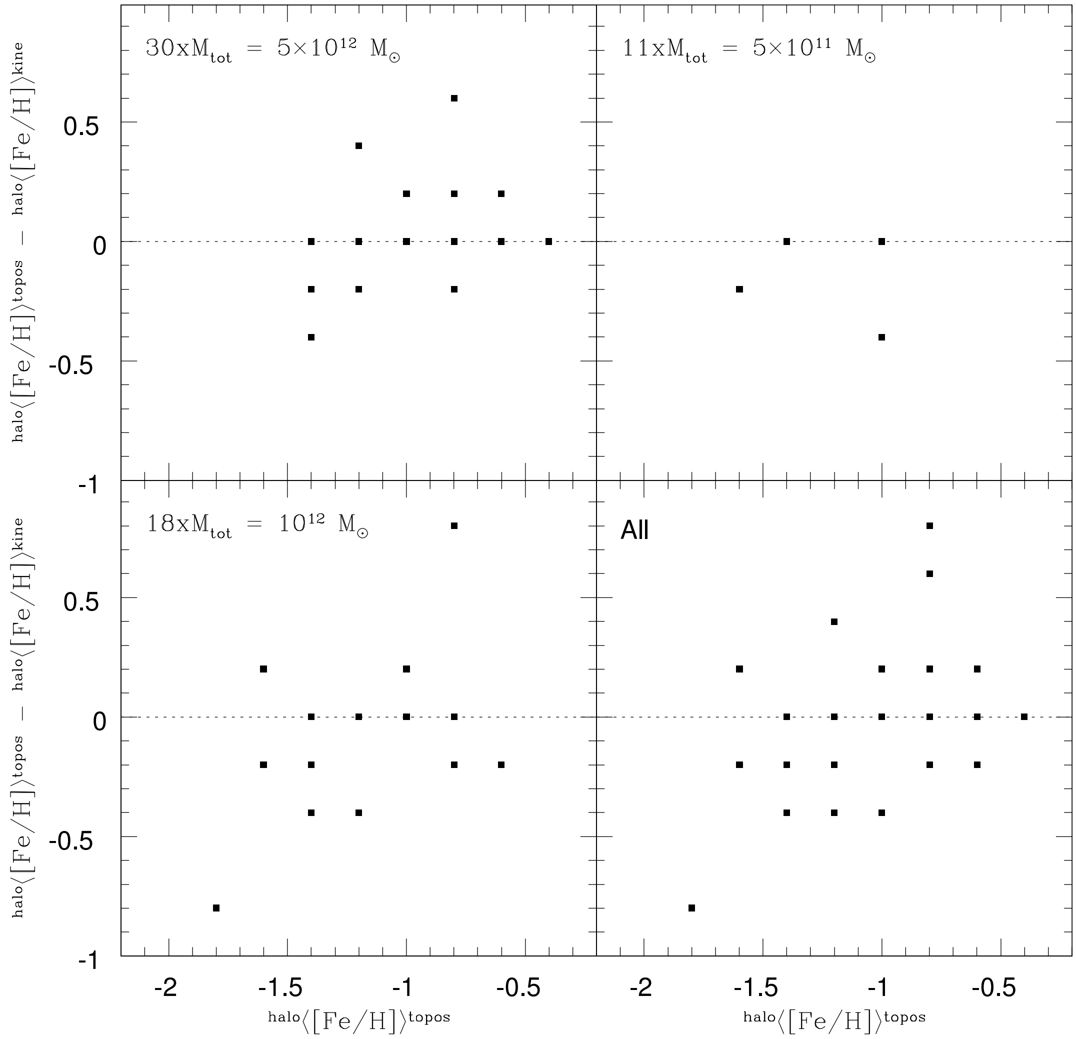

Figure 3.10: The discrepancy between $^{halo}\langle[Fe/H]\rangle^{topos}$ (the "topographical" halo metallicity) and $^{halo}\langle[Fe/H]\rangle^{kine}$ (the metallicity of the ensemble of counter–rotating stellar particles within each topographical halo) as a function of the "topographical" halo metallicity.

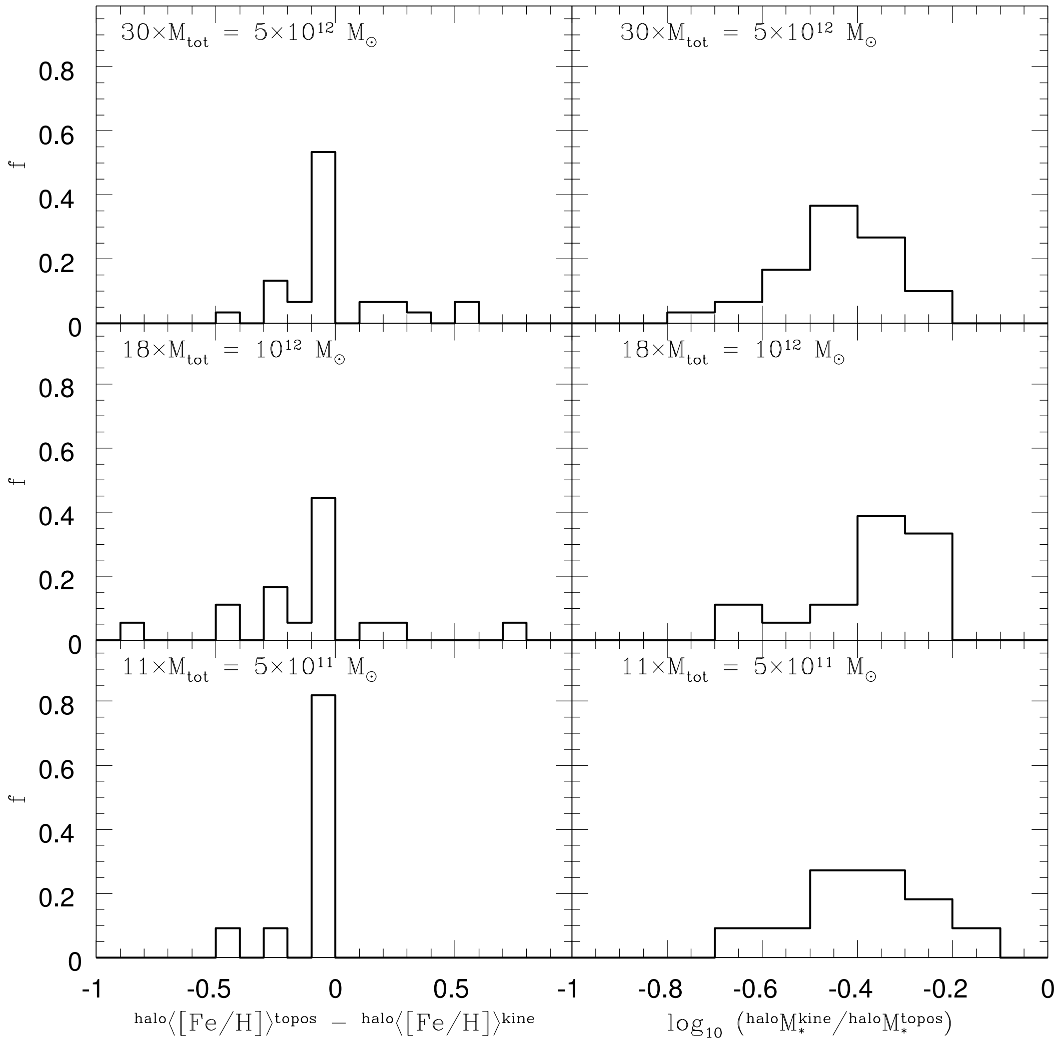

Figure 3.11: Left panels: For each subset, the distribution of the discrepancy between ${}^{\mathrm{halo}}\langle[\mathrm{Fe/H}]\rangle^{\mathrm{topos}}$ (the "topographical" halo metallicity) and ${}^{\mathrm{halo}}\langle[\mathrm{Fe/H}]\rangle^{\mathrm{kine}}$ (the metallicity of the ensemble of counter–rotating stellar particles within each topographical halo). Right panels: For each subset, the distribution of the "topographical" halo mass fraction the ensemble of its counter–rotating stellar particles amounts to.

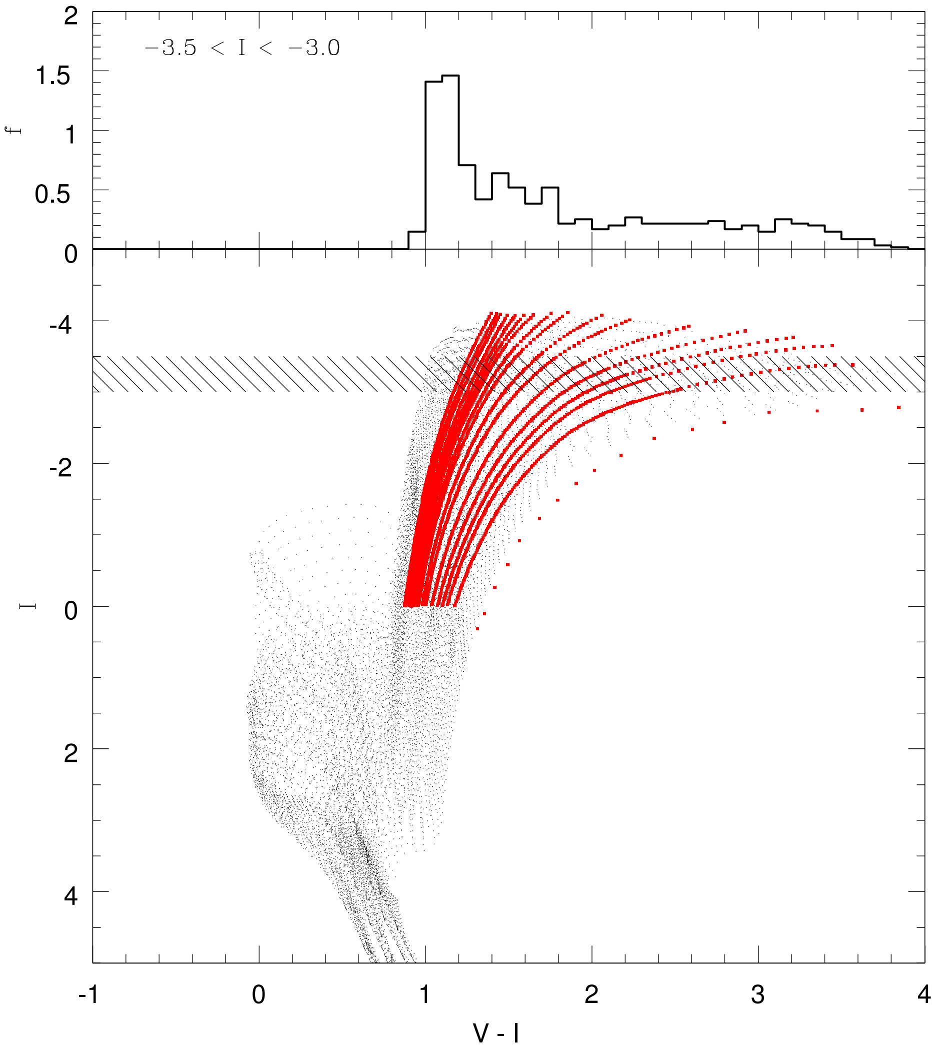

Figure 3.12: The Padova theoretical isochrones (Girardi et al., 2002) up to the RGB tip in the metallicity range of 0.0001 $<$ Z $<$ 0.030 which have been used to generate the simulated CMD out of the ensemble of stellar particles in the "topographical" halo for each galaxy simulation. They are shown as black dots. Red dots display the fiducial RGB tracks (i.e. 0.8 $M_\odot$ VandenBerg et al. 2000 RGB tracks and the empirical NGC 6791 RGB track) which are used, as in Mouhcine et al. (2005), to construct a metallicity–colour relationship to derive [Fe/H] out of the (V - I) colour of each (generated) star in the RGB of the (simulated) CMD at -3.5 $<$ I $<$ -3.0 (i.e. the shaded region). The histogram in the top panel displays the (V - I) colour distribution for the Padova theoretical isochrones at -3.5 $<$ I $<$ -3.0.

are shown in Fig. 3.12 as black dots. Data storage has constrained us to choose 5% halo mass resolution i.e. for each stellar particle a Simple Stellar Population, whose total mass amounts to 5% of the stellar particle mass, is generated, with a Salpeter (Salpeter, 1955) Initial Mass Function (IMF hereafter) over a mass range of $0.1 < \mathrm{m}_*/\mathrm{M}_\odot < \mathrm{m}_{\mathrm{top}}$ where $\mathrm{m}_{\mathrm{top}} = \mathrm{m}^{\mathrm{tip}}_{\mathrm{RGB}}$ is the largest stellar mass in the theoretical isochrones - at the given stellar particle age and metallicity - for a star behind the RGB tip. As a conservative choice, neither age nor metallicity extrapolation is performed. Given the IMF shape and both the age and the metallicity range of the ensemble of stellar particles the simulated CMD is generated out of, we consider the information–loss such IMF mass range implies not a significant one. The observational errors are taken into account (e.g., Secker & Harris 1993) and are randomly drawn for I < -1 from a Normal distribution with $\sigma_{\mathrm{I}} = \sigma_{\mathrm{V}} = \exp(\mathrm{I} - 0.6)$ and $\sigma_{\mathrm{V\,-\,I}} = \sqrt{\sigma_{\mathrm{I}}^2 + \sigma_{\mathrm{V}}^2}$ which implies $\sigma_{\mathrm{I}} \approx 0.01$ at I = -4.0 and $\sigma_{\mathrm{I}} \approx 0.2$ at I = -1 whereas (since our focus is on the upper RGB) at I > -1 we set $\sigma_{\mathrm{I}} = \sigma_{\mathrm{V}} = 0$. The simulated CMDs for the simulations labelled as A – C in Figures 3.2 and 3.7 are shown in Figures 3.13 – 3.15 at a resolution (0.5%) lower than that (5%) of the corresponding simulated CMDs because of image storage constraints.

Once the simulated CMD is generated, both the same fiducial RGB tracks (i.e. 0.8 $\mathrm{M}_\odot$ VandenBerg et al. 2000 RGB tracks and the empirical NGC 6791 RGB track) and the same pipeline as in Mouhcine et al. (2005) are used to construct a metallicity–colour relationship to derive [Fe/H] out of the (V - I) colour of each (generated) star in the RGB of the (simulated) CMD at $-3.5 < \mathrm{I} < -3.0$. The fiducial RGB tracks are shown in Fig. 3.12 as red dots. The related (V - I) colour distributions for each simulated CMD at $-3.5 < \mathrm{I} < -3.0$ are displayed in Appendix G whereas the related MDFs derived via metallicity–colour relationship (through the same pipeline as in Mouhcine et al. 2005) are shown in Appendix H. The MDF peaks are shown in Fig. 3.16.

The dispersion in metallicity at a given total luminosity we found among the topographical halos is not wiped out when the halo metallicity is derived from the halo simulated CMD via metallicity–colour relationship, as shown in Fig. 3.16 - to be compared with Fig. 3.1.

Given a simulation, the relationship between ${}^{\mathrm{halo}}\langle[\mathrm{Fe/H}]\rangle^{\mathrm{topos}}$ (the “topographical” halo metallicity) and ${}^{\mathrm{halo}}\langle[\mathrm{Fe/H}]\rangle^{\mathrm{CMD}}$ (the “topographical” halo metallicity as derived from the halo simulated CMD via metallicity–colour relationship) is shown in Fig. 3.17 whereas the discrepancy in metallicity between ${}^{\mathrm{halo}}\langle[\mathrm{Fe/H}]\rangle^{\mathrm{topos}}$ and

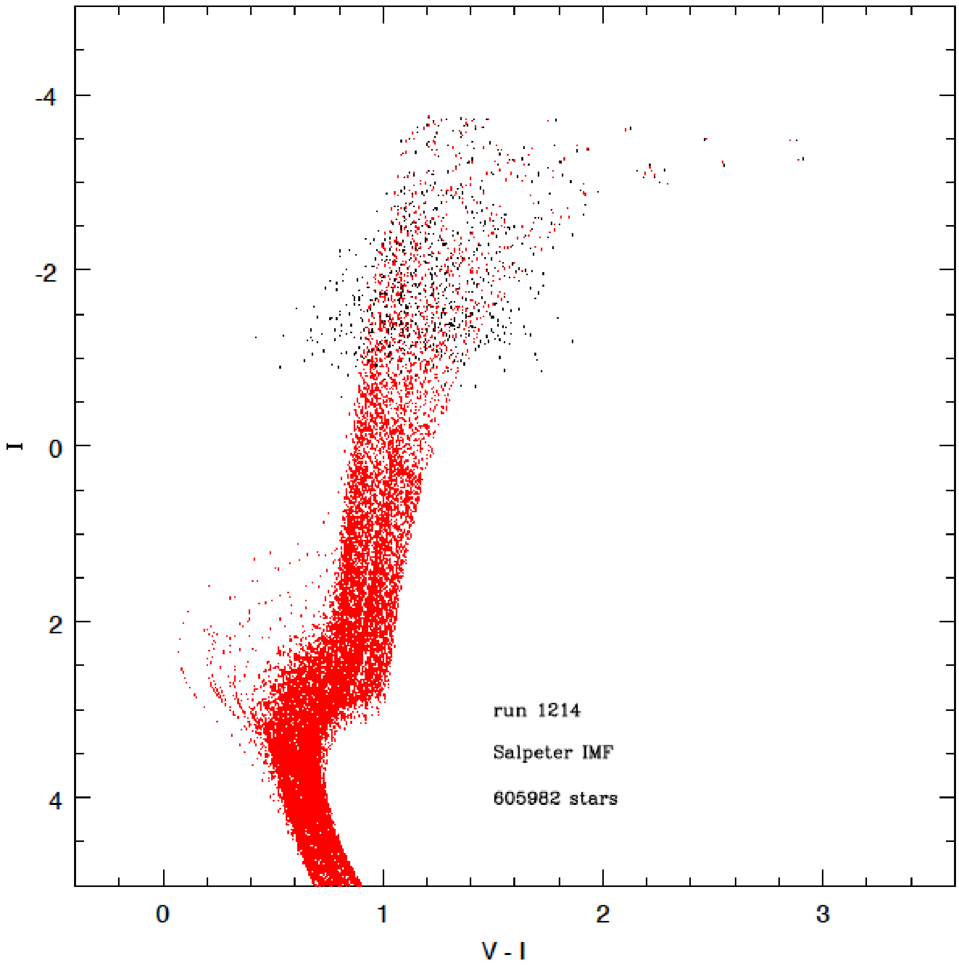

Figure 3.13: Topographical halo simulated CMD for the label "A" semi–cosmological simulation (Figures 3.2 and 3.7) at M_{tot} 10^{12} $M_{\odot}$. The observational errors are taken into account (e.g., Secker & Harris 1993) and are randomly drawn for $I <$ -1 from a Normal distribution with $\sigma_I = \sigma_V = \exp(I - 0.6)$ and $\sigma_{V-I} = \sqrt{\sigma_I^2 + \sigma_V^2}$ which implies $\sigma_I \approx 0.01$ at I = -4.0 and $\sigma_I \approx 0.2$ at I = -1 whereas at $I >$ -1 $\sigma_I = \sigma_V = 0$. Red dots display the simulated CMD without taking observational errors into account. Black dots display the simulated CMD when taking observational errors into account.

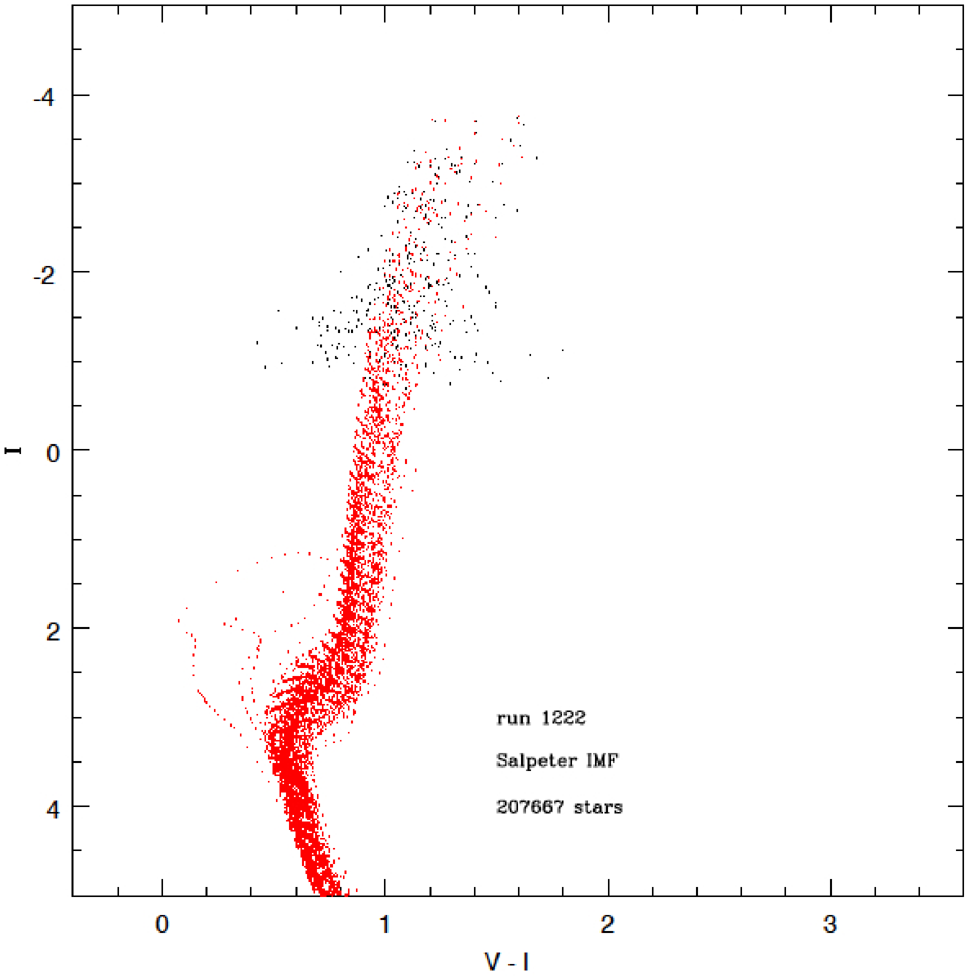

Figure 3.14: Topographical halo simulated CMD for the label "B" semi–cosmological simulation (Figures 3.2 and 3.7) at M_{tot} 10^{12} $M_{\odot}$. The observational errors are taken into account (e.g., Secker & Harris 1993) and are randomly drawn for I < -1 from a Normal distribution with $\sigma_I = \sigma_V = \exp(I - 0.6)$ and $\sigma_{V-I} = \sqrt{\sigma_I^2 + \sigma_V^2}$ which implies $\sigma_I \approx 0.01$ at I = -4.0 and $\sigma_I \approx 0.2$ at I = -1 whereas at I > -1 $\sigma_I = \sigma_V = 0$. Red dots display the simulated CMD without taking observational errors into account. Black dots display the simulated CMD when taking observational errors into account.

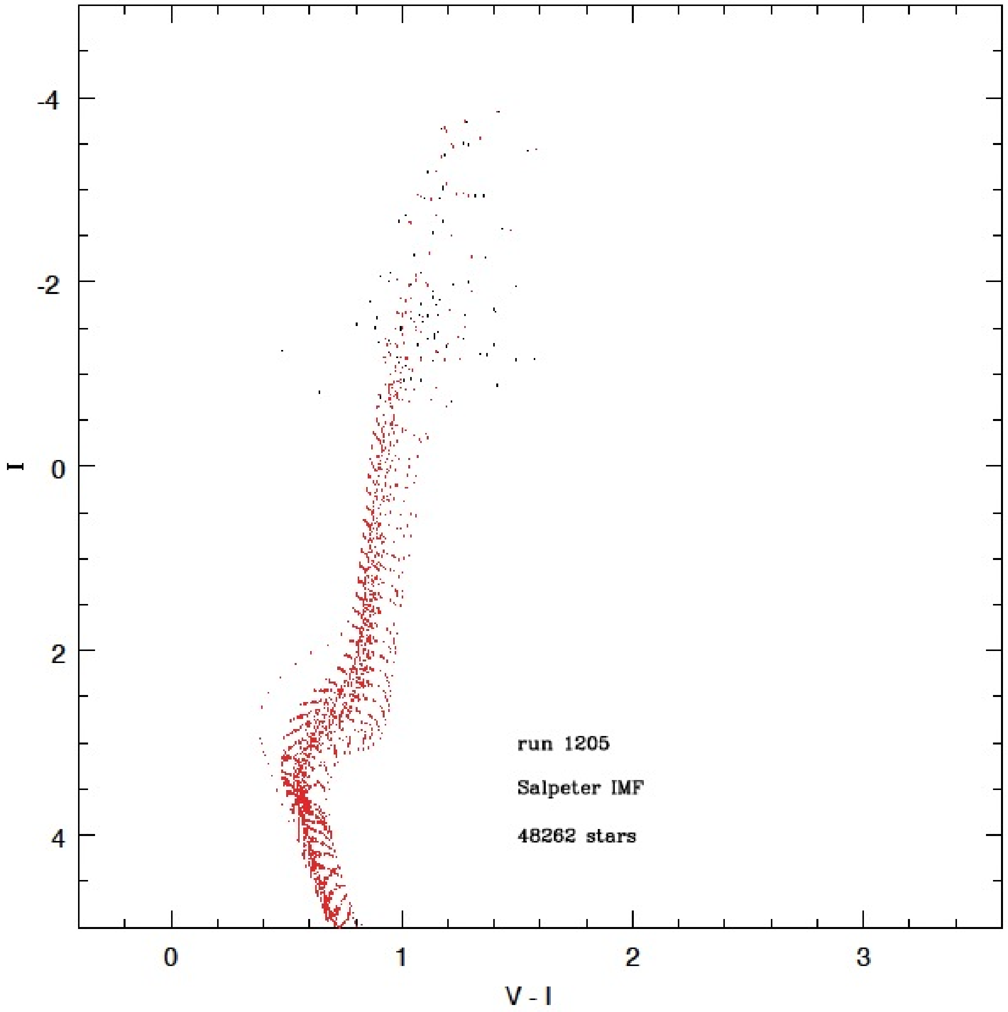

Figure 3.15: Topographical halo simulated CMD for the label “C” semi–cosmological simulation (Figures 3.2 and 3.7) at M_{tot} 10^{12} $M_{\odot}$. The observational errors are taken into account (e.g., Secker & Harris 1993) and are randomly drawn for $I < -1$ from a Normal distribution with $\sigma_I = \sigma_V = \exp(I - 0.6)$ and $\sigma_{V-I} = \sqrt{\sigma_I^2 + \sigma_V^2}$ which implies $\sigma_I \approx 0.01$ at $I = -4.0$ and $\sigma_I \approx 0.2$ at $I = -1$ whereas at $I > -1$ $\sigma_I = \sigma_V = 0$. Red dots display the simulated CMD without taking observational errors into account. Black dots display the simulated CMD when taking observational errors into account.

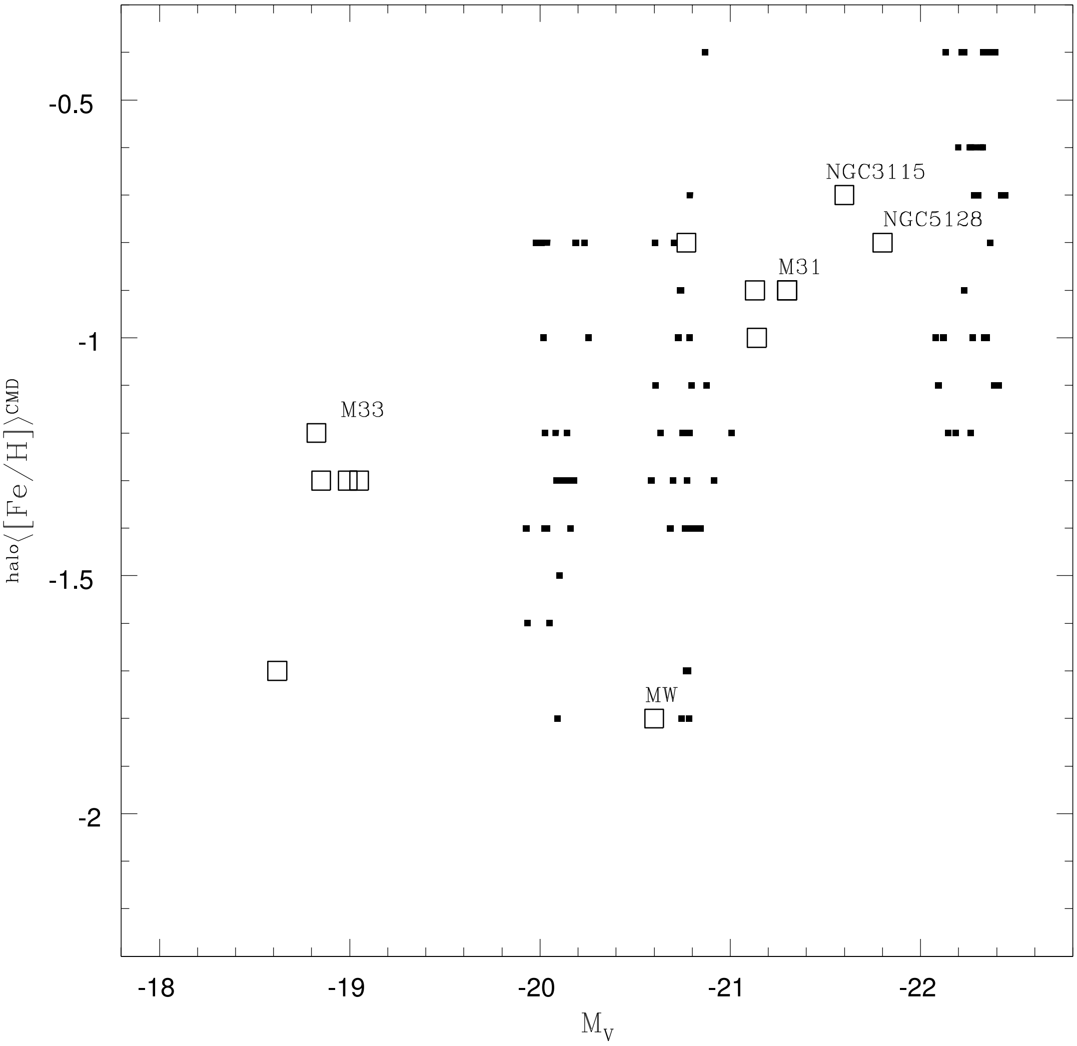

Figure 3.16: The stellar halo metallicity–total galactic V–band luminosity relation ($^{\mathrm{halo}}\langle[\mathrm{Fe/H}]\rangle^{\mathrm{CMD}}$ – M_V). A filled box corresponds to the peak of the MDF which is derived out of the (V - I) colour distribution at -3.5 $<$ I $<$ -3.0 via metallicity–colour relationship through the same pipeline as in Mouhcine et al. (2005). The metallicity of each artificial star of the ensemble the MDF refers to is derived via metallicity–colour relationship out of the (V - I) colour of the generated star in the RGB of the simulated "topographical" halo CMD at -3.5 $<$ I $<$ -3.0. The related (V - I) colour distributions are displayed in Appendix G whereas the related MDFs derived via metallicity–colour relationship are shown in Appendix H. The observational data label–code is as in Fig. 3.1.

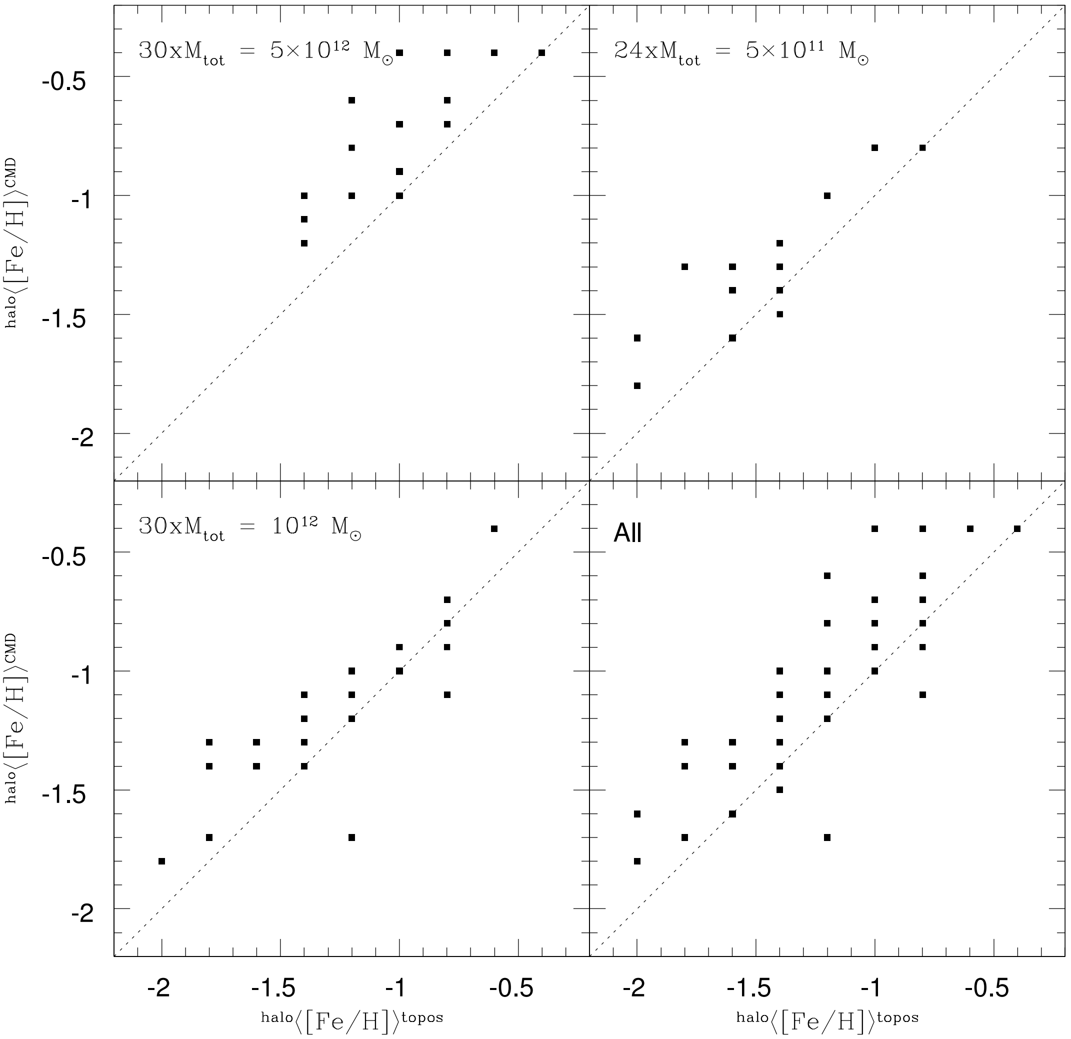

Figure 3.17: The relationship between $^{\mathrm{halo}}\langle[\mathrm{Fe/H}]\rangle^{\mathrm{topos}}$ (the "topographical" halo metallicity) and $^{\mathrm{halo}}\langle[\mathrm{Fe/H}]\rangle^{\mathrm{CMD}}$ (the "topographical" halo metallicity as derived from the halo simulated CMD via metallicity–colour relationship).

${}^{\rm halo}\langle[{\rm Fe/H}]\rangle^{\rm CMD}$ is shown in Fig. 3.18 as a function of ${}^{\rm halo}\langle[{\rm Fe/H}]\rangle^{\rm topos}$.

The histograms in Fig. 3.19 display the distribution of the discrepancy between ${}^{\rm halo}\langle[{\rm Fe/H}]\rangle^{\rm topos}$ and ${}^{\rm halo}\langle[{\rm Fe/H}]\rangle^{\rm CMD}$, for each subset, and show that ${}^{\rm halo}\langle[{\rm Fe/H}]\rangle^{\rm CMD}$ is generally biased towards higher metallicities ($\lesssim 0.3$ dex more metal–rich as shown in Fig. 3.19) because the fiducial RGB tracks do not extend towards colours as blue as those the Padova theoretical isochrones extend towards, as shown in Fig. 3.12, which (given that, as a conservative choice, no extrapolation has been performed beyond the range covered by the fiducial tracks) amounts to narrowing the metallicity range which is sampled at low metallicities, once the metallicity is derived out of the metallicity–colour relationship.

Interestingly, since the fiducial RGB tracks have globular cluster age, the robustness test above allows us to evaluate which bias could be brought in by such uniformly old halo age assumption when the halo metallicity is derived out of the metallicity–colour relationship by interpolating among fiducial RGB tracks (e.g., as in Mouhcine et al. 2005). Such bias can be quantified by the histograms in Fig. 3.19, even if, admittedly, the construction of each simulated CMD out of the corresponding "topographical" halo and its subsequent analysis via fiducial RGB tracks have been constrained by our conservative choice not to perform any extrapolation beyond the range covered by either the theoretical isochrones we used to generate the simulated CMDs or the fiducial RGB tracks we used to analyse them. The discrepancy between ${}^{\rm halo}\langle[{\rm Fe/H}]\rangle^{\rm topos}$ (i.e. the metallicity of the "topographical" halo as derived by the analysis of the MDF of the stellar particles in the simulation which constitute the "topographical" stellar halo ensemble - the stellar particles in the simulation at a projected radius $\rm R > 15$ kpc) and ${}^{\rm halo}\langle[{\rm Fe/H}]\rangle^{\rm CMD}$ (i.e. the metallicity of the "topographical" halo as derived from the halo simulated CMD via metallicity–colour relationship built out of the fiducial RGB tracks with globular cluster age) amounts to $\lesssim 0.3$ dex. Future analysis of higher resolution simulations would further improve such comparison.

3.4 Discussion

We have presented here an analysis of the characteristics of late–type galaxy stellar halos formed within a grid of 89 simulations, with particular emphasis placed upon the relationship between stellar halo metallicity and the associated galactic

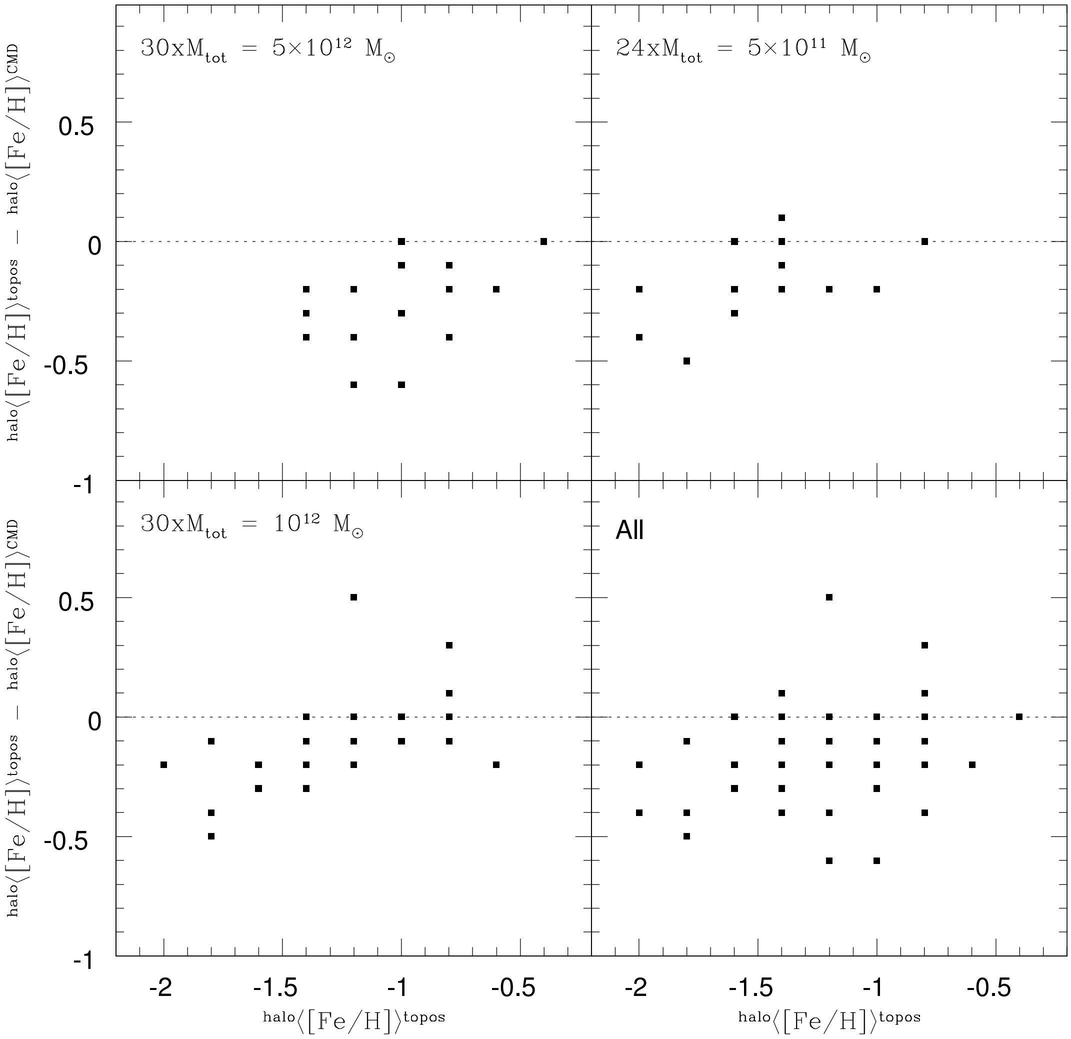

Figure 3.18: The discrepancy in metallicity between $^{halo}\langle[Fe/H]\rangle^{topos}$ (the "topographical" halo metallicity) and $^{halo}\langle[Fe/H]\rangle^{CMD}$ (the "topographical" halo metallicity as derived from the halo simulated CMD via metallicity–colour relationship) as a function of the "topographical" halo metallicity.

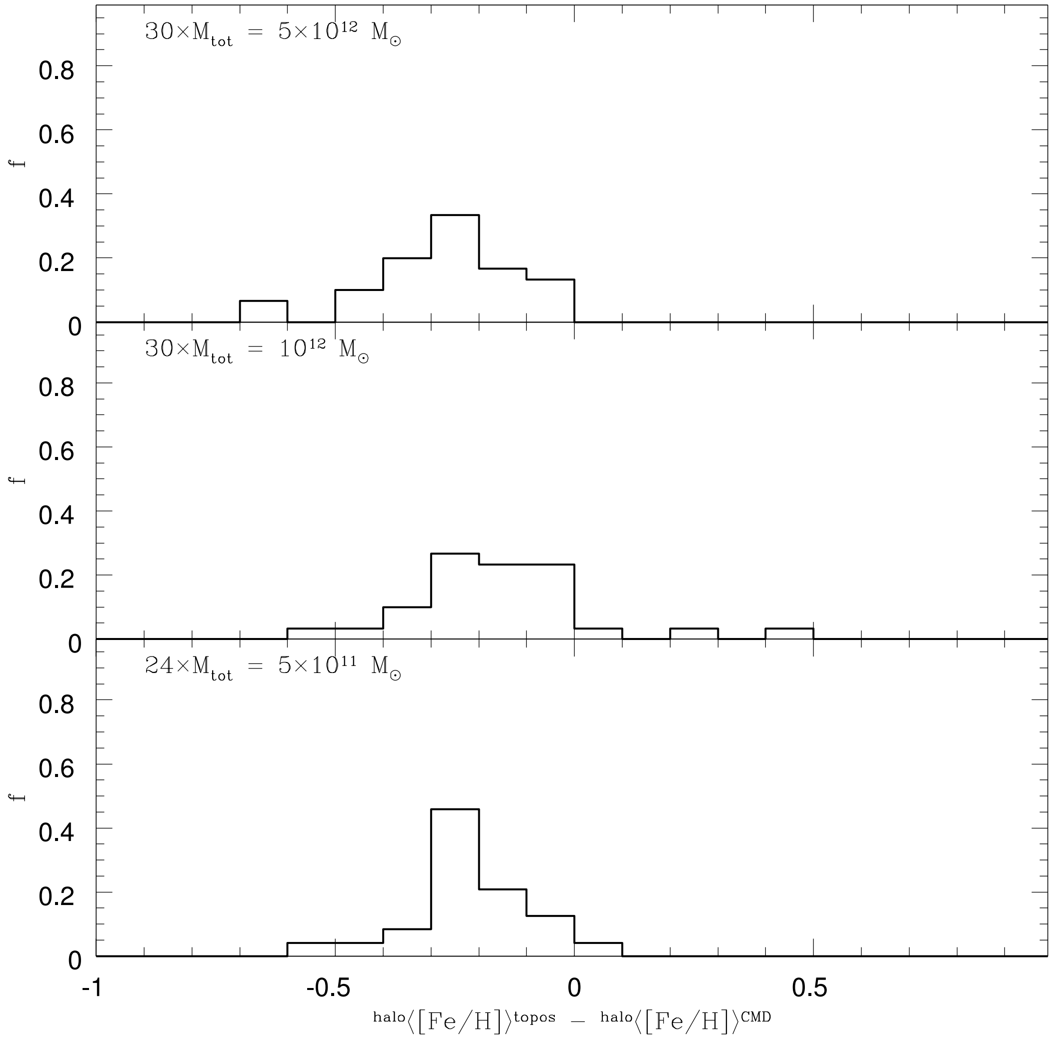

Figure 3.19: For each subset, the distribution of the discrepancy between ${}^{\mathrm{halo}}\langle[\mathrm{Fe/H}]\rangle^{\mathrm{topos}}$ (the "topographical" halo metallicity) and ${}^{\mathrm{halo}}\langle[\mathrm{Fe/H}]\rangle^{\mathrm{CMD}}$ (the "topographical" halo metallicity as derived from the halo simulated CMD via metallicity–colour relationship).

luminosity. It helps to stress here that “Halo Semantics” is currently a controversial topic (e.g., Ibata et al. 2007 and references therein): we have labelled as “topographical halo” the ensemble of stellar particles in a simulation at a projected radius R $>$ 15 kpc, at z = 0. Although future analysis of simulations at resolutions higher than the current would further improve the study we have undertaken, we have shown that - at any given total luminosity or conversely total dynamical mass - the stellar halo metallicities in the simulations span a range in excess of $\sim$ 1 dex, a result which is strengthened by the robustness tests we have performed.

We suggest that the underlying driver of this metallicity dispersion can be traced to the diversity of galactic mass assembly histories inherent within the hierarchical clustering paradigm. Galaxies with a more protracted assembly history possess more metal–rich and younger stellar halos, with an associated greater dispersion in age, than galaxies which experience more of a monolithic collapse.

For a given total luminosity (or dynamical mass), those galaxies with more extended assembly histories also possess more massive stellar halos, which in turn leads to a direct correlation between the stellar halo metallicity and its surface brightness (as anticipated by earlier semi–analytical models - e.g., Renda et al. 2005). By extension, such a correlation may prove to be a useful diagnostic tool for disentangling the formation history of late–type galaxies.

Recently, Mouhcine et al. (2005) have presented an observed correlation between stellar halo metallicity and total galactic luminosity, as shown in Fig. 3.1. The observed dispersion in the mean halo metallicity at a given galactic luminosity is *smaller* than what we find in our simulations. *However* the latter can account for the outliers in the observed trend. Since our motivation has been to study which is the effect of the pattern of the initial density fluctuations *alone* on the stellar halo features at redshift z = 0 in late–type galaxy simulations, it helps to note that galaxy formation, as it is observed, is an ongoing process which is the result of the interplay among different parameters, of which the pattern of initial density fluctuations (thus the merging history) is one. We have shown that the merging history *alone* may be held responsible of the dispersion in halo metallicity at comparable total galactic luminosities, as *apparently* observed for example in our Milky Way and in Andromeda (see Section 3.1).

This begs the question... *Which is normal*? Our study suggests that if the stellar halo was (primarily) assembled through more of a monolithic collapse, such a low metallicity is indeed what should be expected; conversely, the fact that the M31 stellar halo is significantly metal–rich is suggestive of a more protracted assembly history (see also Hammer et al. 2007). An observational consequence of these differing formation histories is the prediction that the M31 stellar halo should possess a high surface brightness; observations tentatively support this prediction (Reitzel, Guhathakurta & Gould 1998; Irwin et al. 2005).

Further observations are needed to tighten our grasp of the strength and scatter of the stellar halo metallicity–luminosity relation, which we have shown to be a useful diagnostic tool for disentangling the formation history of late–type galaxies.

Chapter 4

Galaxy Mass Assembly since z $\sim$ 1

We analyse 112 N–body/hydrodynamical late–type galaxy simulations to study the stellar mass assembly and the relationships between stellar, gaseous and total mass in galaxies since z $\sim$ 1 down to the present day, with an emphasis on the effects of the merging histories on the z = 0 galaxy properties.

The redshift evolution of the stellar mass in simulations with comparable luminosities at z = 0 shows a significant dispersion, which lies in their differing merging histories. This contrasts with the redshift evolution of the total mass within the central 100 kpc, which is already assembled by z $\sim$ 1.5. The stellar–to–total mass ratio in the simulations broadly agrees with the observed (e.g., Conselice et al. 2005). We find that massive simulations are generally more evolved than their lower mass counterparts.

4.1 Introduction

The hierarchical structure assembly has become a well established paradigm in the last decade. The properties of the cosmic microwave background and the large scale structure (e.g.: Spergel et al. 2003; Bahcall et al. 1999) support a picture where a large fraction of matter is non–baryonic, gravitationally interacting only, and assembled in a hierarchical fashion. Galaxy formation in such a scenario is a continuous process where galaxy properties are the results of its merging history, mass and environment.

Observationally, much progress has been made in studying the global star formation history and the build–up of the stellar mass over a significant fraction of the Hubble time (e.g.: Lilly et al. 1996; Madau et al. 1996). However, many details are still missing. The analysis of galaxy stellar and total masses at different cosmic epochs can thus assist in constraining the likely scenarios of galaxy evolution.

Conselice et al. (2005) have recently found a lack of evolution in the galaxy stellar–to–total mass ratio over the redshift range $0.2 \lesssim z \lesssim 1.2$ (see also Böhm & Ziegler 2006), thus implying that if galaxies continue to build up over the second half of the Hubble time stellar and dark components are then growing together.

Here, we focus on galaxy mass assembly over the last half of the age of the Universe. The results of the simulations, the comparison with the data, and the implications of our results are described in Sect. 4.2. We summarise our conclusions in Sect. 4.3.

4.2 Results

We have constructed an ensemble of 112 late–type galaxy simulations in a chemo–dynamical framework (Section 3.2), spanning a factor of $\sim$ 50 in total mass, and sampling a range of assembly histories at a given total mass.

This sample includes the same 89 semi–cosmological `GCD+` simulations analysed in Renda et al. (2005b) and 23 more simulations, completed within the same framework, with the same parameters described in Section 3.2, and distributed among the same mass “bins”. These latter simulations sample more patterns of small–scale density fluctuations, which lead to different hierarchical assembly histories. A subset of 9 simulations (with $M_{tot} = 10^{11} M_{\odot}$, collapse redshift $z_c = 1.5$ and spin parameter $\lambda = 0.054$) samples more density fluctuations patterns.

As a benchmark for the semi–cosmological framework, we have also analysed 2 among the disc galaxy simulations presented in Bailin et al. (2005), which are fully cosmological `GCD+` runs and adopt a Λ–dominated CDM cosmology (Bailin et al. 2005 and references therein). The photometric properties of a stellar particle in a simulation are modeled as those of a Simple Stellar Population (SSP hereafter) with the same age and metallicity. The evolution of the SSP properties as a function of age and metallicity is taken from Mouhcine & Lançon (2003).

In the following, the galaxy total mass, including both dark and baryonic (i.e. gaseous and stellar) matter, is measured for the region within 100 kpc from the centre of the stellar mass distribution, at each redshift, whereas the stellar and the gaseous mass are measured within 15 kpc from the centre of the stellar mass, at each redshift.

Figures 4.1, 4.2 and 4.3 display the redshift evolution of the total, stellar and gaseous mass normalised to the $z = 0$ value for each simulation. Fig. 4.4 displays the redshift evolution of the stellar–to–total mass ratio whereas Fig. 4.5 displays the redshift evolution of the gaseous–to–stellar mass ratio. Black (red) lines show the semi–cosmological (cosmological) runs. Magenta for the semi–cosmological simulations with collapse redshift $z_c = 1.5$.

The consistency between the assembly histories of total, stellar and gaseous mass in both semi–cosmological and cosmological simulations is reassuring as a robustness test for the semi–cosmological framework.

The assembly of the total mass within the inner 100 kpc in the simulations is $\sim$ completed by $z \gtrsim 1.5$, independently of their total mass. On the other hand, the stellar mass assembly histories within the central 15 kpc are more extended, i.e. at $z \sim 1$, $\sim$ half of the baryonic mass in the inner region is gaseous, with a large variety of assembly patterns. Massive simulations have assembled their stellar content early on (typically by $z \sim 1.5$) and have burnt a significant fraction of their gas supply by now, others continue to form stars to much later epochs, whereas the simulations with collapse redshift $z_c = 1.5$ have their baryonic content dominated by the gaseous component at all redshifts. Galaxies with comparable stellar masses can have significantly different assembly histories of their stellar content, and diverse gaseous contents. This suggests that galaxy stellar mass should be considered *neither* a robust tracer of the merging history *nor* a good tracer of the total baryonic galaxy mass.

Although the slope of the baryonic–to–total mass ratio does not significantly evolve over the redshift range which is analysed (as displayed in Fig. 4.6), Figures 4.7 and 4.8 show that, in our sample, galaxies of any given stellar mass, and at any given redshift, span a wide range of gaseous–to–stellar mass ratios. Star formation does not uniformly proceed in all galaxies: some galaxies have converted a significant fraction of their gas reservoirs into stars, whereas in others the baryonic content is still dominated by the gaseous component.

The relationship between stellar mass (within the 15 kpc central region) and total mass (within the 100 kpc central region) in the simulations is shown in Fig. 4.9, at different redshifts. Stellar and total mass in the simulations are correlated since $z \sim 1$ down to the present day, thus suggesting that galaxy stellar and dark masses grow together continuously, similarly to the results drawn from the observations in

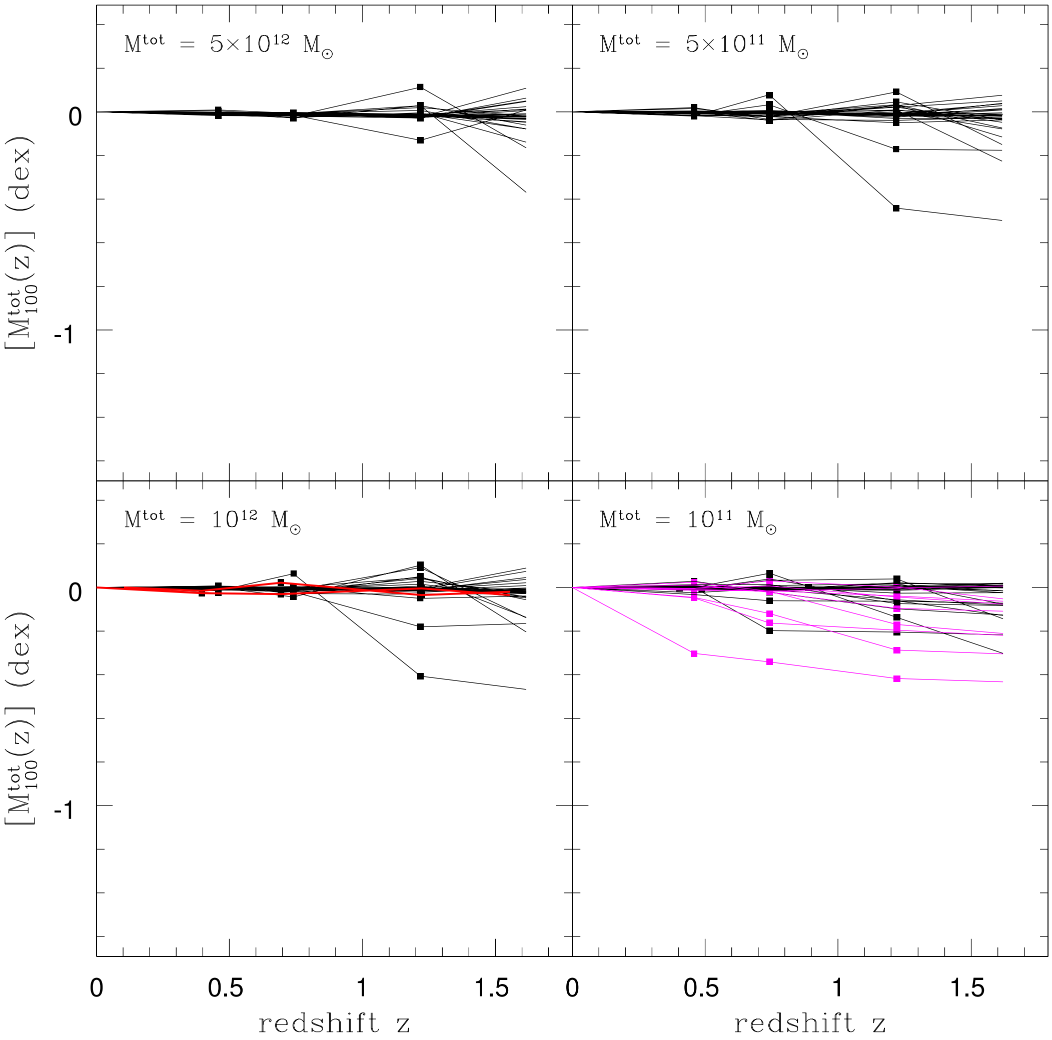

Figure 4.1: The redshift evolution of the total mass within the 100 kpc central region, normalised to the $z = 0$ value for each simulation. The semi–cosmological simulations with collapse redshift $z_c = 2$ are shown as black lines. Magenta for the collapse redshift $z_c = 1.5$ runs. The cosmological simulations are shown in red.

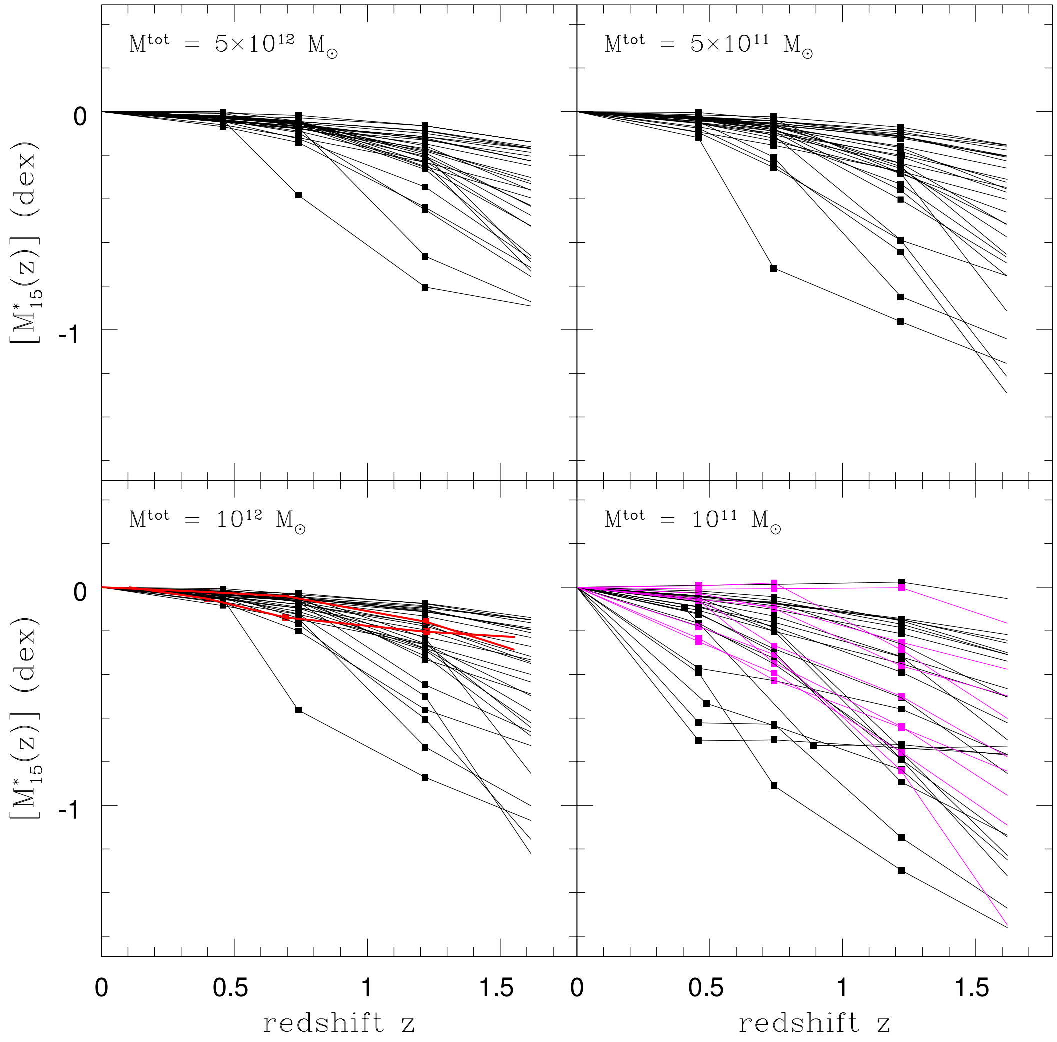

Figure 4.2: The redshift evolution of the stellar mass within the 15 kpc central region, normalised to the $z =\ 0$ value for each simulation. The semi–cosmological simulations with collapse redshift $z_c\ =\ 2$ are shown as black lines. Magenta for the collapse redshift $z_c\ =\ 1.5$ runs. The cosmological simulations are shown in red.

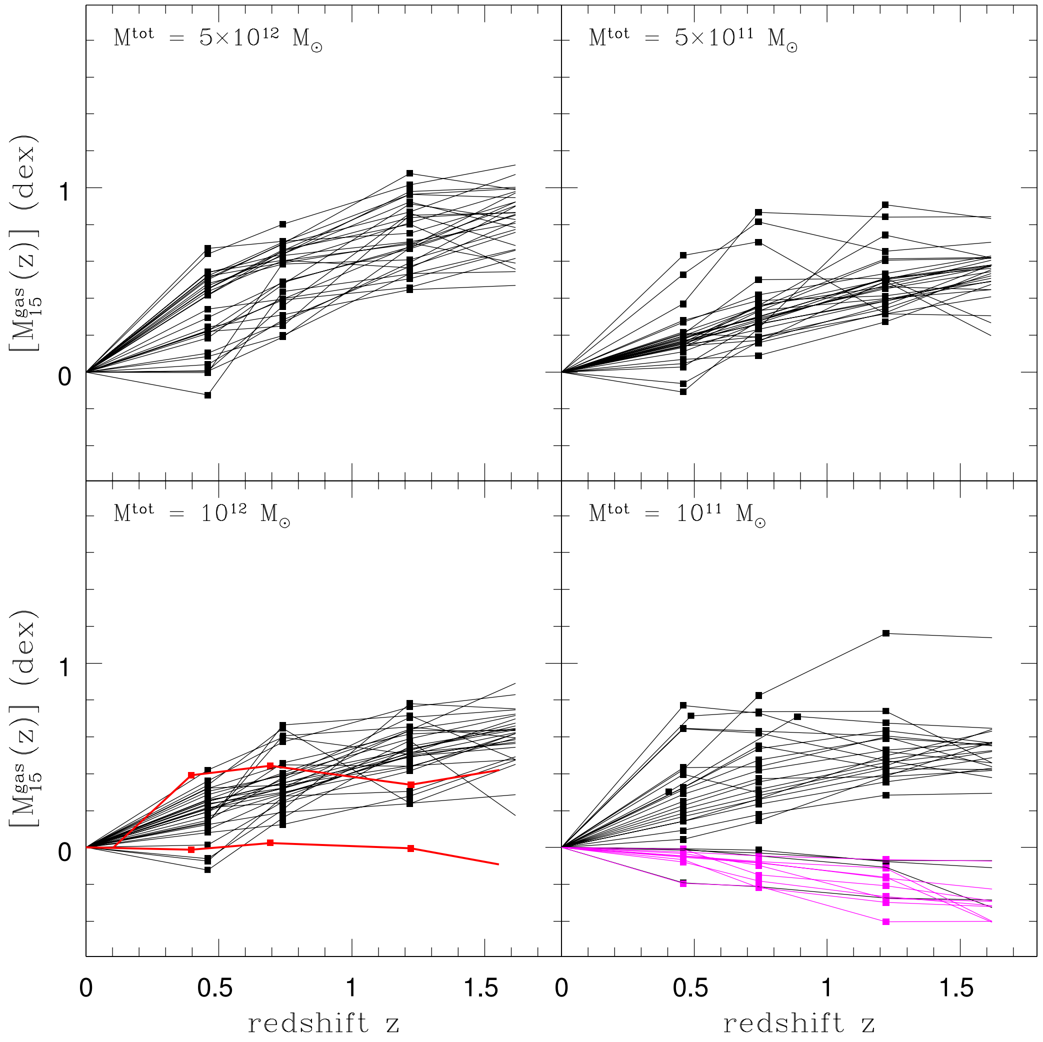

Figure 4.3: The redshift evolution of the gaseous mass within the 15 kpc central region, normalised to the z = 0 value for each simulation. The semi–cosmological simulations with collapse redshift $z_c = 2$ are shown as black lines. Magenta for the collapse redshift $z_c = 1.5$ runs. The cosmological simulations are shown in red.

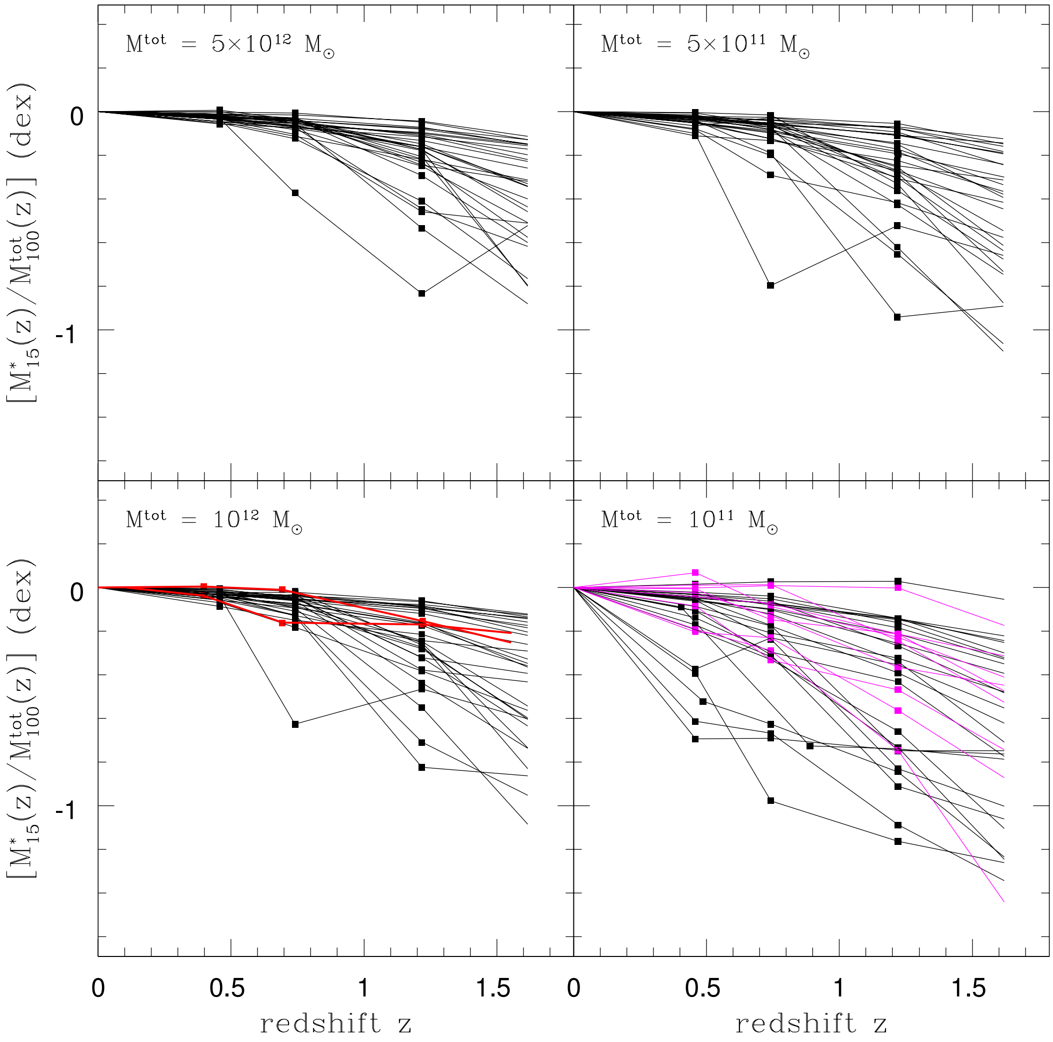

Figure 4.4: The redshift evolution of the stellar (within the 15 kpc central region) to total (within the 100 kpc central region) mass ratio, normalised to the $z = 0$ value for each simulation. The semi–cosmological simulations with collapse redshift $z_c = 2$ are shown as black lines. Magenta for the collapse redshift $z_c = 1.5$ runs. The cosmological simulations are shown in red.

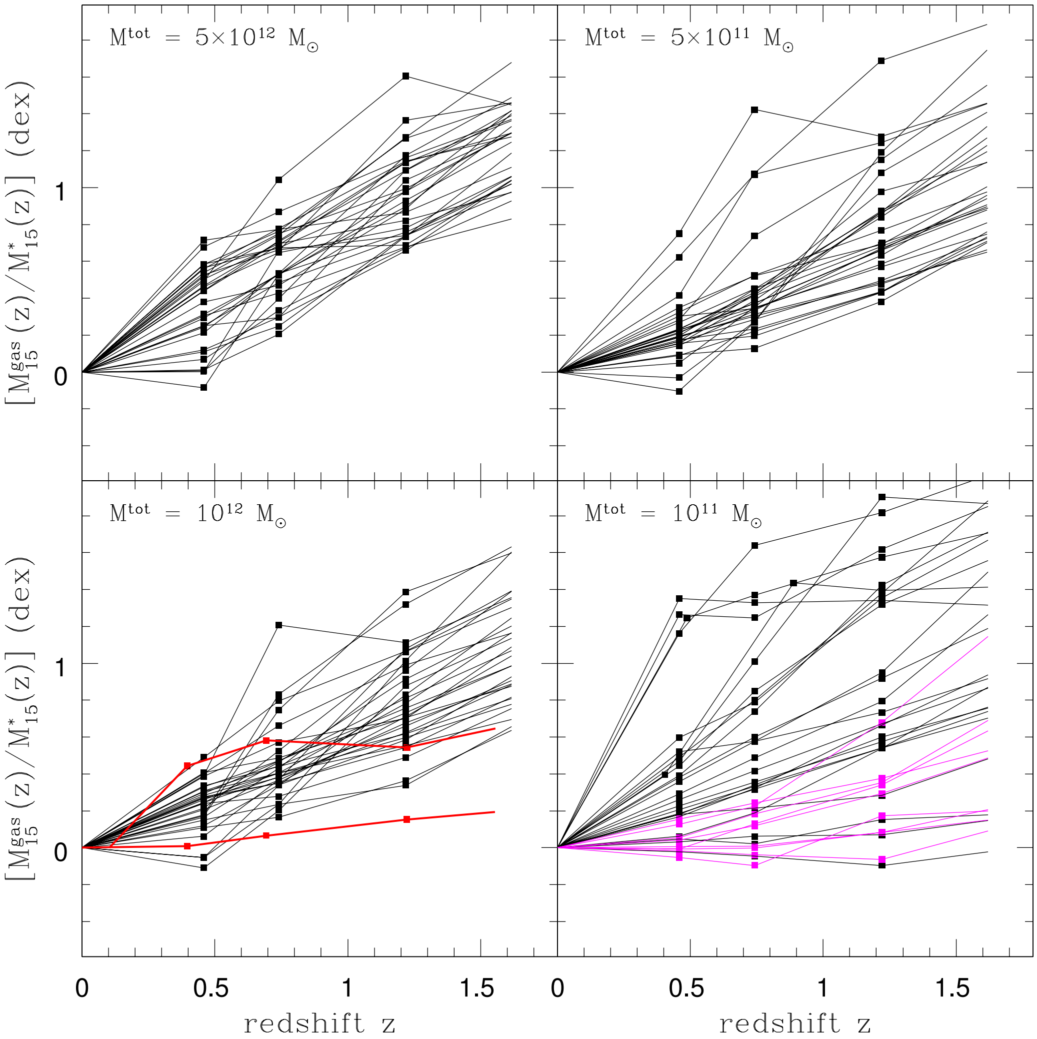

Figure 4.5: The redshift evolution of the gaseous–to–stellar mass ratio (within the 15 kpc central region), normalised to the z = 0 value for each simulation. The semi–cosmological simulations with collapse redshift $z_c = 2$ are shown as black lines. Magenta for the collapse redshift $z_c = 1.5$ runs. The cosmological simulations are shown in red.

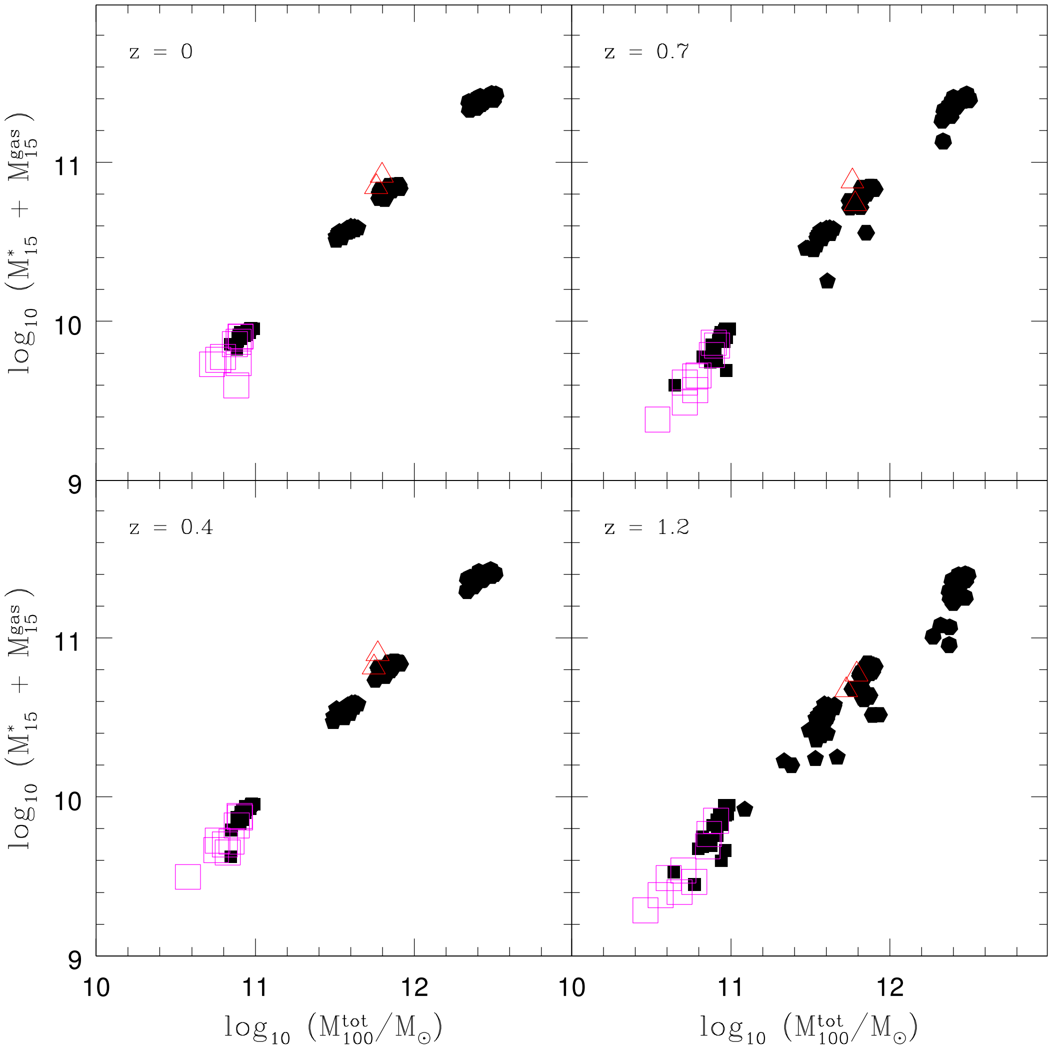

Figure 4.6: The relationship between baryonic mass (i.e. gaseous and stellar mass within the 15 kpc central region) and total mass (within the 100 kpc central region), at different redshifts. The semi–cosmological simulations with collapse redshift $z_c = 2$ are shown as filled symbols (heptagons for $M^{tot} = 5 \times 10^{12}$ $M_{\odot}$, hexagons for $M^{tot} = 10^{12}$ $M_{\odot}$, pentagons for $M^{tot} = 5 \times 10^{11}$ $M_{\odot}$, boxes for $M^{tot} = 10^{11}$ $M_{\odot}$). Larger empty boxes for the collapse redshift $z_c = 1.5$ runs. The cosmological simulations are shown as large open triangles.

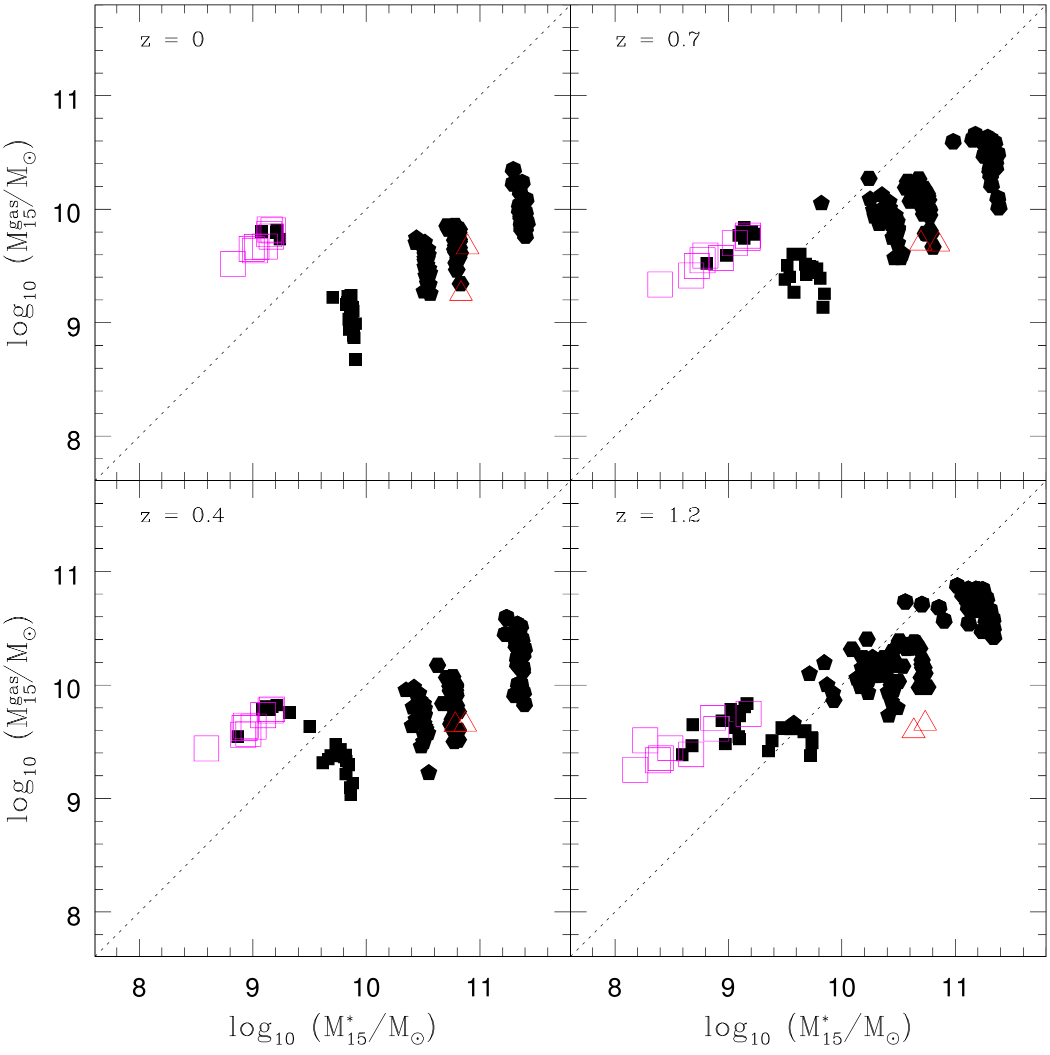

Figure 4.7: The relationship between gaseous mass and stellar mass (within the 15 kpc central region), at different redshifts. Symbols are the same as in Fig. 4.6.

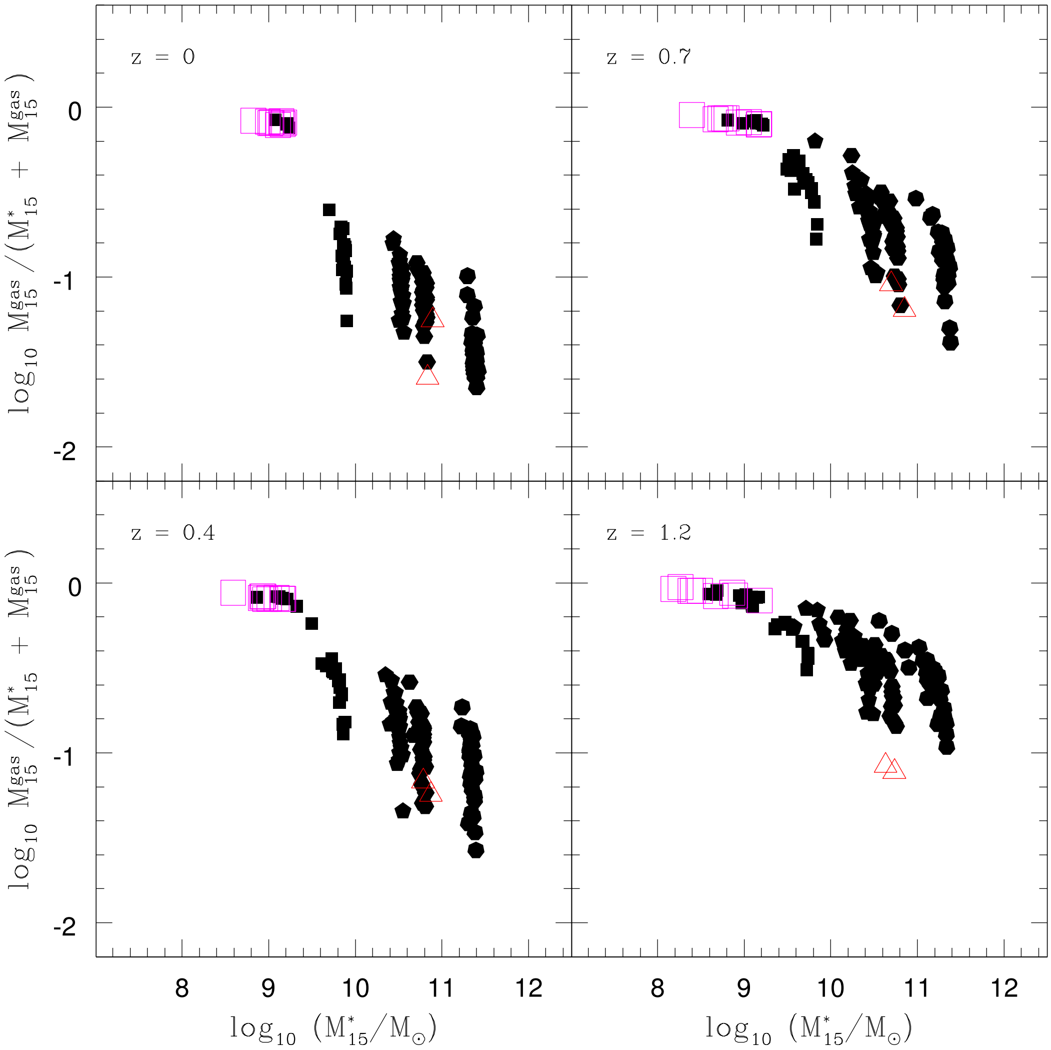

Figure 4.8: The relationship between baryonic gas fraction and stellar mass, at different redshifts. Symbols are the same as in Fig. 4.6.

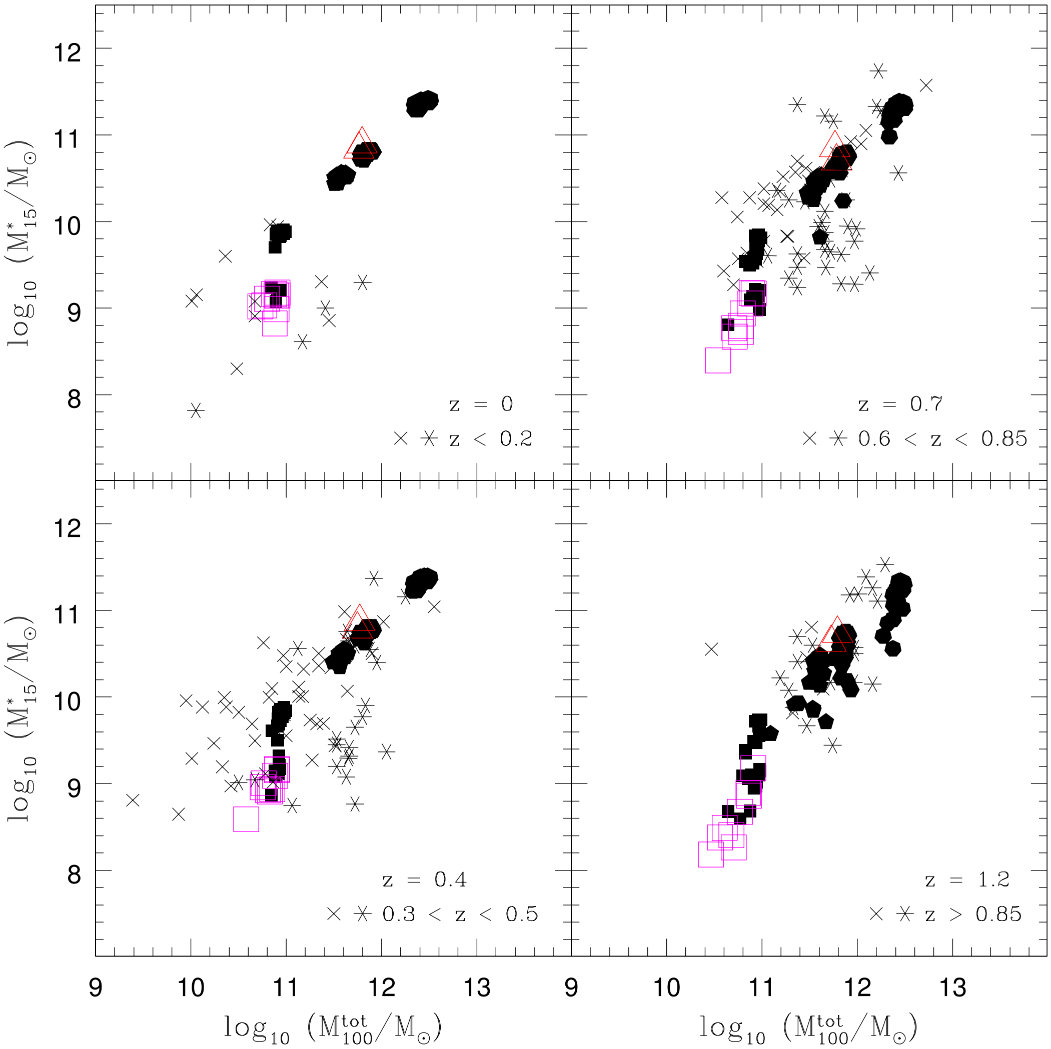

Figure 4.9: Stellar mass (within the 15 kpc central region) against total mass (within the 100 kpc central region), at different redshifts. Symbols are the same as in Fig. 4.6. The stellar–to–total mass ratio in the simulations is compared with the ratio drawn from the observations in Conselice et al. (2005) and Böhm & Ziegler (2006), displayed as six and four vertices stars, respectively.

Conselice et al. (2005) and Böhm & Ziegler (2006).

The scatter around the stellar–to–total mass ratio in the simulations increases with redshift. However, it is smaller than the dispersion around the observed relationship. The simulations analysed here are sampling neither a full range nor an a priori distribution of parameters (Section 3.2). Varying such parameters might increase the scatter in the simulations. Also, the dispersion around the observed relationship could be partially due to systematics in the observations. In fact, it is difficult to accurately estimate the dynamical mass for an intermediate redshift galaxy. The dynamical masses of these objects have been usually estimated using circular velocities obtained by long slit spectroscopy. However, Flores et al. (2006) have recently pointed out that long slit spectroscopy reveals overdispersed galaxy properties, because it tends to bias the circular velocity in galaxies with disturbed velocity fields.

As previously shown in Fig. 4.6, a tighter correlation exists between total mass and baryonic mass. Also, the baryonic–to–total mass ratio is less dispersed than the stellar–to–total mass ratio, similarly to what is observed for $z \sim 2$ galaxies (Erb et al., 2006), thus reinforcing that the galaxy stellar mass should be considered neither a robust tracer of the galaxy merging history nor a good tracer of the total baryonic galaxy mass.

4.3 Conclusions

We have presented the analysis of a sample of semi–cosmological late–type galaxy simulations with stellar mass larger than $\sim 10^9$ $M_\odot$, to explore whether hierarchical formation scenarios may account for the constraints on galaxy mass assembly over the second half of the age of the Universe.

The main results can be summarised as follows:

- Stellar, gaseous, and total masses are found to be correlated in the simulations since $z \sim 1$ down to $z = 0$, in broad agreement with the scaling relations observed in local and intermediate redshift galaxies.

- Galaxies with comparable stellar masses in the simulations can have significantly different assembly histories of their stellar content, and diverse gaseous contents. This suggests that the galaxy stellar mass should be considered neither a robust tracer of the galaxy merging history nor a good tracer of the total baryonic galaxy mass.

Chapter 5

The Mass–Metallicity Relation since z $\sim$ 1.

We analyse 112 N–body/hydrodynamical late–type galaxy simulations to study the metal enrichment of the stellar component and the interstellar medium since z $\sim$ 1, down to z = 0. The relationships between stellar mass and metallicity for both stellar and gaseous components in the simulations at z = 0 are in broad agreement with the relationships locally observed. The dispersion around these relationships in the simulations, which lies in their diverse merging histories, broadly agrees with the observed. We find that the integrated stellar populations in the simulations are dominated by stars as old as 4 – 10 Gyr. For massive simulations, the age range of the integrated stellar populations agrees with the observations. On the contrary, simulations with stellar mass $\sim$ 10^9 $M_\odot$ at z = 0 tend to be older than locally observed galaxies with comparable stellar masses.

5.1 Introduction

The correlation between galaxy metallicity and luminosity in the local universe is one of the most significant observational results in galaxy evolution. Lequeux et al. (1979) first revealed that Oxygen abundance increases with total mass for irregular galaxies. The luminosity–metallicity relation for irregulars was later confirmed by Skillman et al. (1989) among others. Subsequent studies have extended the relation to spiral galaxies (e.g.: Garnett & Shields 1987; Zaritsky et al. 1994; Garnett et al. 1997), and to elliptical galaxies (Brodie & Huchra, 1991). More recently, large samples of star–forming galaxies drawn from galaxy redshift surveys, e.g. the 2dF Galaxy Redshift Survey and the Sloan Digital Sky Survey (SDSS hereafter), have been used to confirm the luminosity–metallicity relation over a broader range (Lamareille et al. 2004; Tremonti et al. 2004). The stellar populations of local galaxies with low stellar mass are found to be generally young and metal–poor, whereas massive galaxies are found to be old and metal–rich (e.g., Gallazzi et al. 2005). Different groups have explored the properties of the interstellar gas at earlier epochs in intermediate– ($0 \lesssim z \lesssim 1$: Hammer et al. 2001; Lilly et al. 2003; Liang et al. 2004; Maier et al. 2004; Kobulnicky & Kewley 2004; Maier et al. 2005; Mouhcine et al. 2006; Lamareille et al. 2006) and high–redshift galaxies ($1.5 \lesssim z \lesssim 4$: Pettini et al. 1998; Kobulnicky & Koo 2000; Mehlert et al. 2002; Lemoine-Busserolle et al. 2003; Erb et al. 2006; Maier et al. 2006).

Here, we aim to discuss the metal enrichment histories of galactic systems in a hierarchical clustering scenario. The results of the simulations, the comparison with the data, and the implications of our results are described in Sect. 5.2. We summarise our conclusions in Sect. 5.3.

5.2 Results

We have constructed an ensemble of 112 simulated late–type galaxies in a chemo–dynamical framework (Section 3.2), spanning a factor of ∼ 50 in total mass, and sampling a range of assembly histories at a given total mass.

This sample includes the same 89 semi–cosmological `GCD+` simulations analysed in Renda et al. (2005b) and 23 more simulations, completed within the same framework, with the same parameters described in Section 3.2, and distributed among the same mass "bins". These latter simulations sample more patterns of small–scale density fluctuations, which lead to different hierarchical assembly histories. A subset of 9 simulations (with $\mathrm{M_{tot}} = 10^{11}\mathrm{M_\odot}$, collapse redshift $\mathrm{z_c} = 1.5$ and spin parameter $\lambda = 0.054$) samples more density fluctuations patterns.

As a benchmark for the semi–cosmological framework, we have also analysed 2 among the disc galaxy simulations presented in Bailin et al. (2005), which are fully cosmological `GCD+` runs and adopt a Λ–dominated CDM cosmology (Bailin et al. 2005 and references therein). The photometric properties of a stellar particle in a simulation are modeled as those of a Simple Stellar Population (SSP hereafter) with the same age and metallicity. The evolution of the SSP properties as a function of age and metallicity is taken from Mouhcine & Lançon (2003). Optical properties have been converted into the SDSS photometric system as in Fukugita et al. (1996).

In the following, the stellar mass is measured within the 15 kpc central region, at each redshift. Metallicity and age of the integrated stellar populations, and the gas–phase metallicity, are all measured within the 10 kpc central region, at each redshift.

We estimate the Oxygen abundance as $12 + \log(\mathrm{O/H})$. Caution should be taken when comparing the estimated abundances for simulated galaxies with the observed, since the latter, based on integrated spectra, may suffer from systematics (e.g., Moustakas & Kennicutt 2006).

5.2.1 Gas–phase Oxygen abundance vs. stellar mass

Fig. 5.1 shows a correlation between gas–phase Oxygen abundance and stellar mass in the simulations, at different redshifts. The consistency between semi–cosmological and cosmological simulations (see also Section 4.2) is reassuring as a robustness test for the semi–cosmological framework.

Massive galaxies with comparable stellar masses span a range of gas–phase abundances, due to their differing assembly histories, thus suggesting that stellar mass should not be considered a good tracer of gas–phase metallicity.

The results at redshift $\mathrm{z} = 0$ are compared and in broad agreement with the observed relation between stellar mass and gas–phase Oxygen abundance for a sample of SDSS galaxies at $\mathrm{z} \sim 0.1$ (Tremonti et al., 2004). The dispersion of the gas–phase metallicity at a given stellar mass at $\mathrm{z} = 0$ is similar to what is locally observed in the SDSS. This is a remarkable result, given that simulations and observations adopt different pipelines to estimate the gas–phase metallicity: for example, the SDSS fibre spectra preferentially sample the inner $\sim 25\%$ of a galaxy (e.g., Tremonti et al. 2004 and references therein) whereas we are considering the Oxygen abundance within the inner 10 kpc in the simulations.

The collapse–redshift $\mathrm{z_c} = 1.5$ runs at $\mathrm{M_{tot}} = 10^{11}\ \mathrm{M_\odot}$ are broadly as evolved as the most metal–poor $\mathrm{z_c} = 2.0$ simulations at the same $\mathrm{M_{tot}}$. If the semi–cosmological simulations were constrained to agree with the observations at redshift $\mathrm{z} \sim 0$, the collapse–redshift range at $\mathrm{M_{tot}} = 10^{11}\ \mathrm{M_\odot}$ would then be $1.5 \lesssim \mathrm{z_c} \lesssim 2.0$, thus suggesting that the observed low stellar mass galaxies may

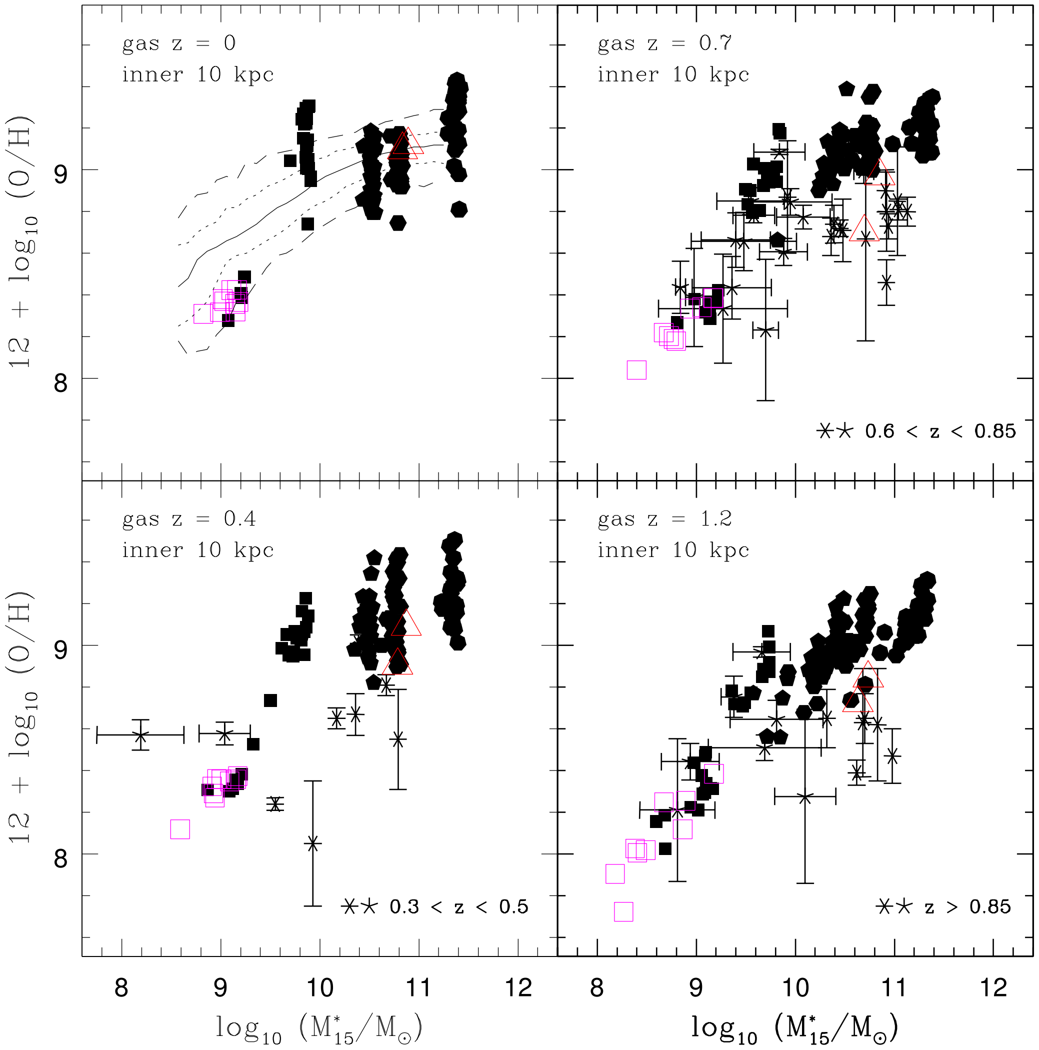

Figure 5.1: Gas–phase Oxygen abundance against integrated stellar mass in the simulations, at different redshifts. The semi–cosmological simulations with collapse redshift $z_c = 2$ are shown as filled symbols (heptagons for $M^{tot} = 5 \times 10^{12}$ $M_\odot$, hexagons for $M^{tot} = 10^{12}$ $M_\odot$, pentagons for $M^{tot} = 5 \times 10^{11}$ $M_\odot$, boxes for $M^{tot} = 10^{11}$ $M_\odot$). Larger empty boxes for collapse redshift $z_c = 1.5$ runs. The cosmological simulations are shown as large empty triangles. The $z = 0$ gas–phase Oxygen abundance in the simulations is compared with $z \sim 0.1$ galaxies in the SDSS (Tremonti et al., 2004): solid line for the median; dotted line for 16 and 84 percentile; dashed line for 2.5 and 97.5 percentile. The results at low and intermediate redshifts are compared with the samples observed in Savaglio et al. (2005) and Liang et al. (2006), shown as five and six vertices stars, respectively.

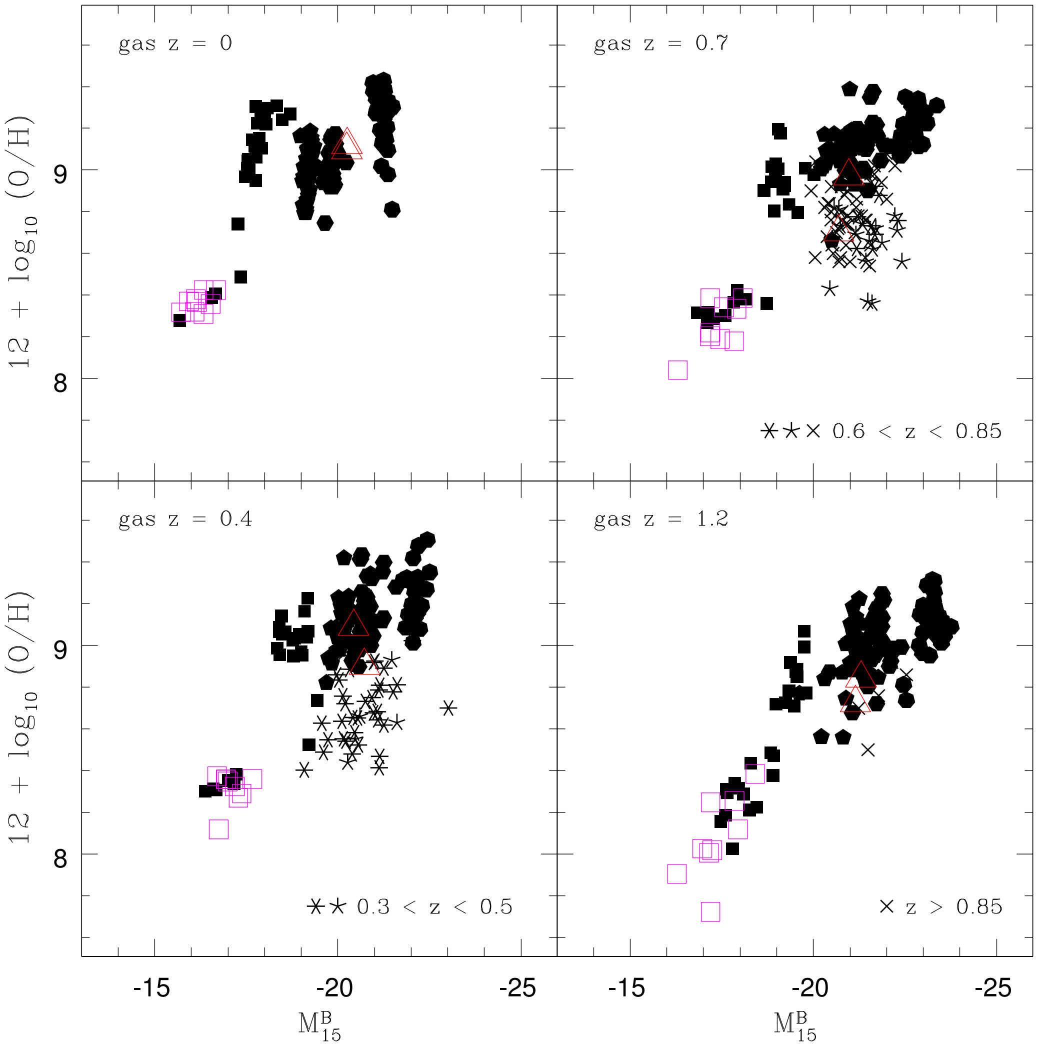

Figure 5.2: Gas–phase Oxygen abundance against B–band luminosity. Symbols are the same as in Fig. 5.1. The redshift evolution in the simulations is compared with the relationship between the observed luminosity and the gas–phase metallicity at intermediate redshifts in Lilly et al. (2003), Liang et al. (2004), and Mouhcine et al. (2006), shown as four, five and six vertices stars, respectively.

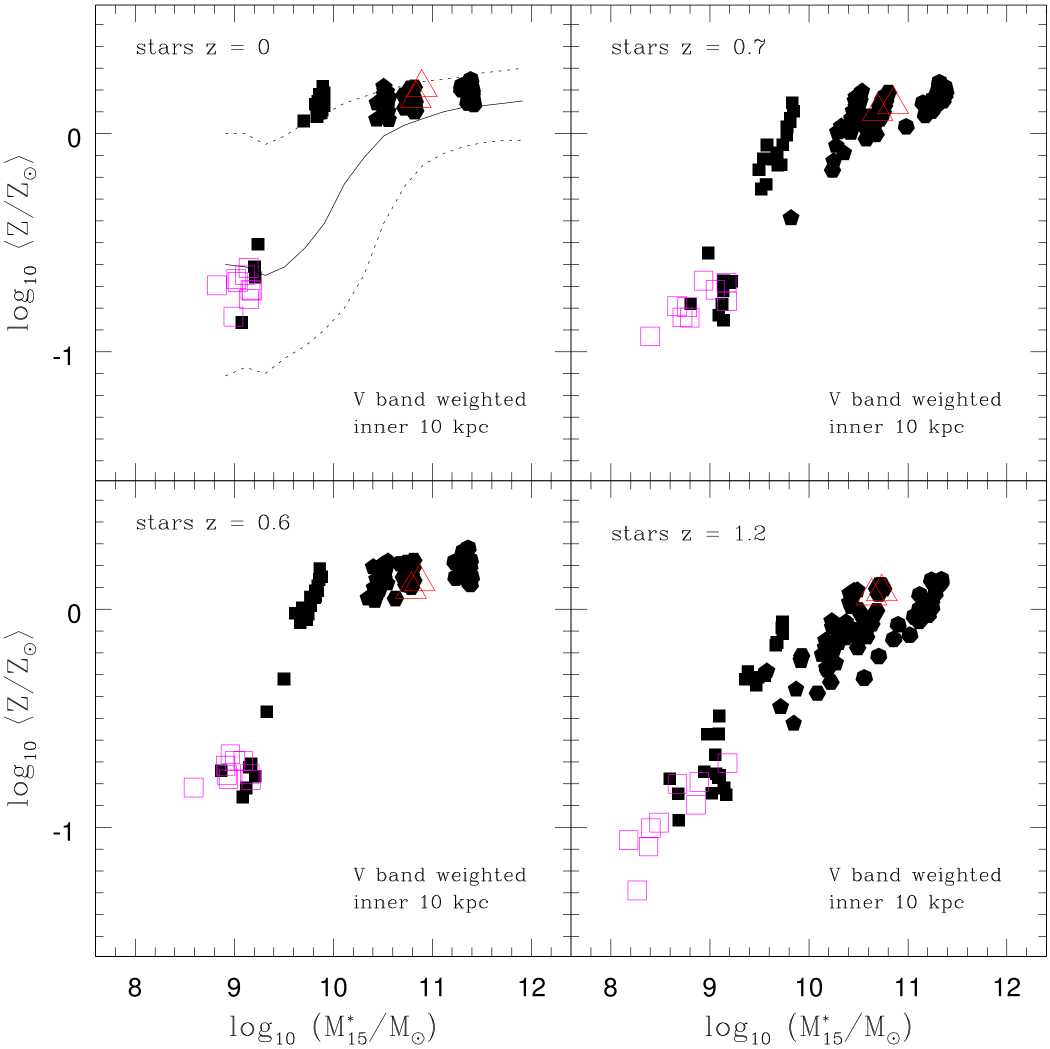

Figure 5.3: The V–band luminosity–weighted metallicity of the integrated stellar populations against the integrated stellar mass, at different cosmic epochs. Symbols are the same as in Fig. 5.1. The results at z = 0 are compared with the z ∼ 0.1 relation between stellar mass and metallicity in the SDSS (Gallazzi et al., 2005): solid line for the median; dotted line for 16 and 84 percentile.

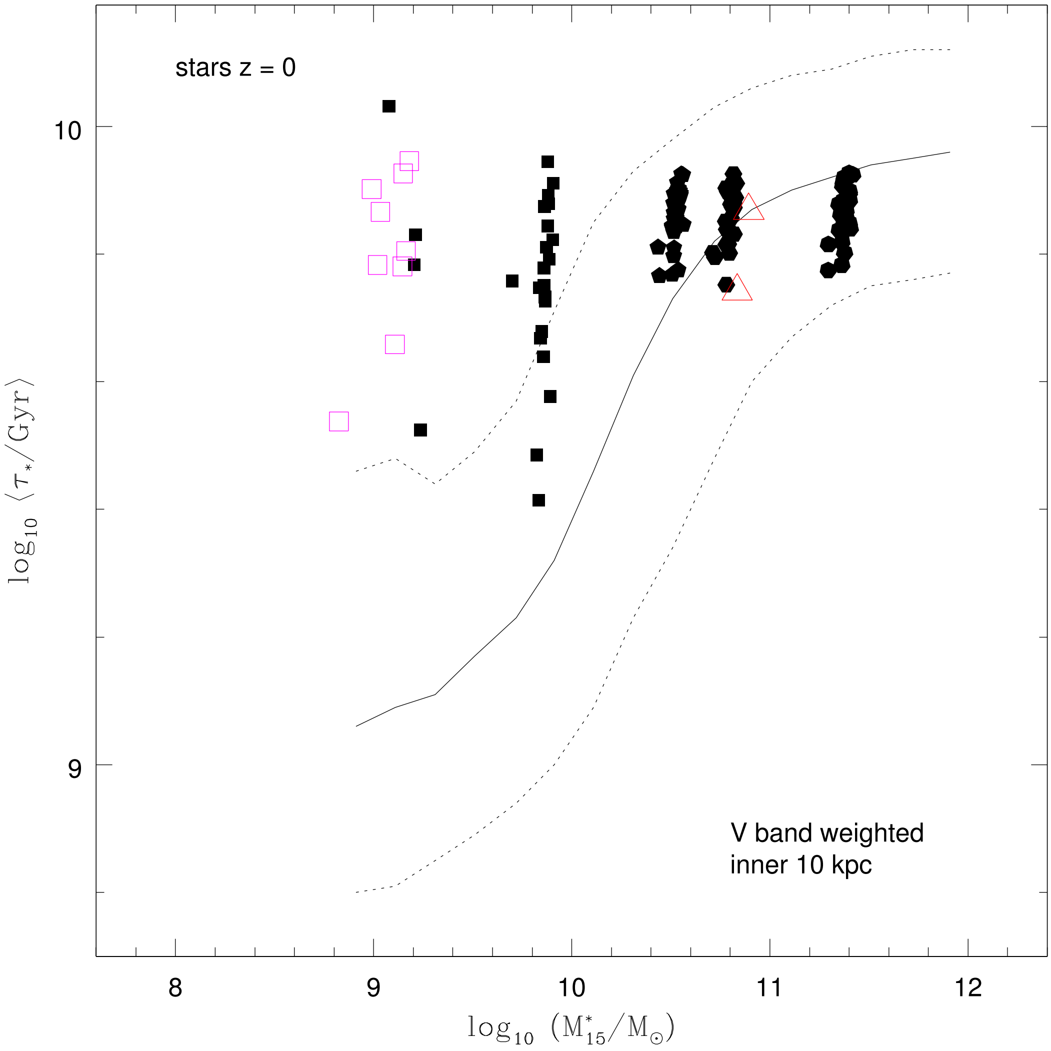

Figure 5.4: The V–band luminosity–weighted age of the integrated stellar populations, against the stellar mass at redshift z = 0. Symbols are the same as in Fig. 5.1. The results are compared with the z ∼ 0.1 relation between stellar mass and age in the SDSS (Gallazzi et al., 2005): solid line for the median; dotted line for 16 and 84 percentile.

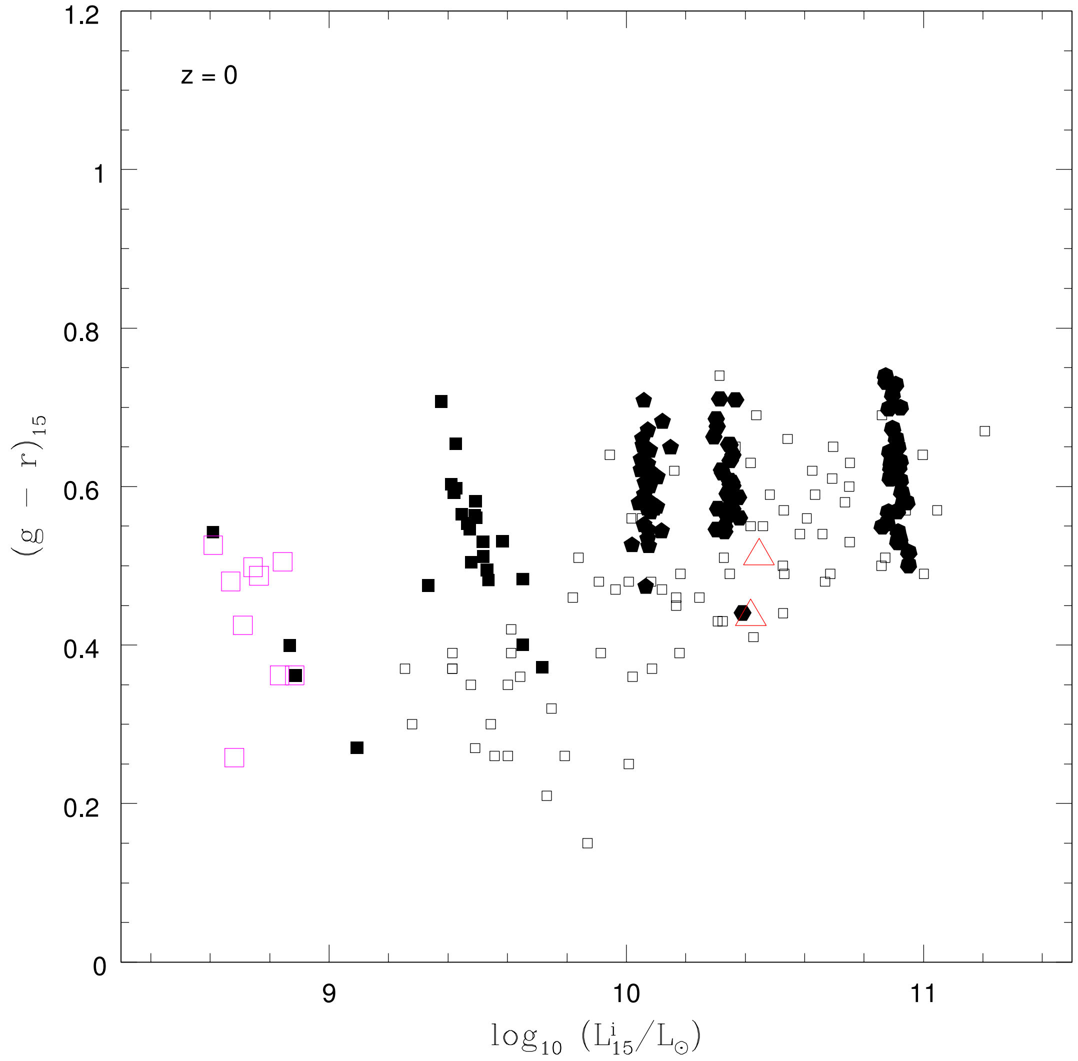

Figure 5.5: The z = 0 Colour–Magnitude relation in the simulations. Symbols are the same as in Fig. 5.1. The CMR in the simulations is compared with the local CMR for a sample of disc–dominated SDSS galaxies selected by Pizagno et al. (2005), shown as empty boxes.

have collapsed out of density peaks with smaller values of δ_i (see also Section 3.2).

Fig. 5.1 shows that the redshift evolution of the mass–metallicity relationship depends on galaxy mass. Gas–phase abundances do not significantly evolve in simulations with stellar mass larger than $\sim 10^{10}$ $M_\odot$, and the mass–metallicity relationship remains nearly as flat as it is at z $\sim$ 1. On the contrary, there is a systematic metal enrichment for low stellar mass simulations, which increase their stellar contents by a large factor, migrating from stellar masses of $\sim 10^9$ $M_\odot$ to $\sim 10^{10}$ $M_\odot$. Such behaviour is consistent with a scenario where massive galaxies have burnt a significant fraction of their gas reservoirs and are dominated by stars early on, thus leaving their metal enrichment almost unchanged since z $\sim$ 1. Low stellar mass galaxies would rather form stars in a more extended fashion, and a sizeable fraction of their baryons would still be gaseous at the present epoch.

For intermediate redshifts, the mass–metallicity relation in the simulations is compared and in broad agreement with that reported at $0.4 \lesssim z \lesssim 1$ in Savaglio et al. (2005) and Liang et al. (2006), which too support a flat mass–metallicity relation for massive galaxies since z $\sim$ 1 down to z $\sim$ 0.

The gas–phase Oxygen abundances for low stellar masses in the simulations agree with the observed values, whereas the metallicity for more massive simulations tend to be systematically higher than the observed abundances. Part of the offset could be explained by systematics affecting the measurements, especially at the high–metallicity end (e.g.: Ellison & Kewley 2005; Kennicutt et al. 2003).

5.2.2 Gas–phase Oxygen abundance vs. galaxy luminosity

As a reflection of the relationship between stellar mass and gas–phase metallicity, the relationship between gas metallicity and galaxy luminosity is displayed in Fig. 5.2.

The luminosity–metallicity relationship is compared and in broad agreement with observations at intermediate redshift: Lilly et al. (2003) at $0.5 \lesssim z \lesssim 0.9$; Liang et al. (2004) at $0 \lesssim z \lesssim 1.2$; Mouhcine et al. (2006) at $0.2 \lesssim z \lesssim 0.8$. As previously noted, this is a remarkable result, given that simulations and observations adopt different pipelines to estimate the gas–phase metallicity.

The Oxygen abundances of luminous galaxies in the simulations, i.e. B–band magnitude brighter than -20, are larger than what is observed at $0.4 \lesssim z \lesssim 0.7$. Systematics in the observations may play a role here too, as discussed above in connection with the mass–metallicity relationship for massive galaxies.

5.2.3 Stellar metallicity/age vs. stellar mass

Age and metallicity of integrated stellar populations are powerful tracers of galaxy star formation and metal enrichment histories. Fig. 5.3 shows the relationship between stellar mass and V–band luminosity–weighted metallicity, at different redshifts.

The general behaviour is similar to that of the gas–phase Oxygen abundance as a function of stellar mass (Fig. 5.1), although stellar metallicities are less dispersed than gas–phase Oxygen abundances at a given stellar mass.

The results at redshift $z = 0$ in the simulations are compared with the observed relation for a large sample of SDSS galaxies at $0.005 \lesssim z \lesssim 0.22$ as reported in Gallazzi et al. (2005), whose sample includes both quiescent early–type and actively star–forming galaxies, which might explain the smaller stellar metallicity dispersion at a given stellar mass in the simulations (which have late–type morphologies) compared with the dispersion observed in the more heterogeneous SDSS sample.

Fig. 5.4 shows the $z = 0$ relationship between stellar mass and V–band luminosity–weighted age of the integrated stellar populations in the simulations, compared with the observed relationship. We find no relation between age and stellar mass. Massive galaxies with stellar mass larger than $\sim 10^{10}$ $M_\odot$ have age ranging from $\sim$ 6.5 Gyr to $\sim$ 9 Gyr, in broad agreement with the age derived for SDSS galaxies with comparable stellar masses. For less massive galaxies in the simulations, the age range is broader, going from $\sim$ 3 to $\sim$ 10 Gyr, thus older than in Gallazzi et al. (2005), whose sample is however much less populated and thus less robust at stellar masses $M_* < 10^{10}$ $M_\odot$ (see Fig. 6 in Gallazzi et al. 2005).

The age issue in the simulations as outlined above signals that feedback should more effectively prevent gas from collapsing and cooling in the early stages of the hierarchy in order to ensure that most of the stellar content in low stellar mass galaxies is not formed early on. This has been already invoked in previous studies (e.g.: Steinmetz & Navarro 1999).

5.2.4 The Colour–Magnitude Relation

Another signature of feedback–related problems in our sample, Fig. 5.5 shows the $z = 0$ relationship between the (g - r) colour and the i–band luminosity in the simulations, compared[1] with a sample of disc–dominated local galaxies in the SDSS, selected by Pizagno et al. (2005).

The integrated stellar population colours of luminous galaxies in the simulations are in good agreement with the observed colours at comparable luminosities, which is expected due to the agreement, in massive simulations, of age and stellar metallicity with the observations. The colour dispersion in the simulations - which reflects the diverse formation histories which have been sampled - agrees with the observed dispersion. This is a remarkable result, given that the observed sample has explicitly been selected to include disc–dominated galaxies with a disc–to–total luminosity ratio $\mathrm{f_d} \geq 0.9$ (see Pizagno et al. 2005), whereas the simulated sample consists of late–type galaxy simulations which have not been morphologically selected.

Although the colour dispersion for less massive simulations is comparable with the observed dispersion, fainter simulations show integrated (g - r) colours generally redder than the observed, i.e. the simulated CMR is shallower than the observed. The discrepancy between observed and simulated colours for faint galaxies is due to the age discrepancy for faint galaxies between observations and simulations. Although faint simulations in our sample agree with stellar and gaseous metallicities for locally observed galaxies with comparable luminosities and/or stellar masses, the former are older, resulting in redder colours.

5.3 Conclusions

We have presented the analysis of a sample of semi–cosmological late–type galaxy simulations with stellar mass larger than $\sim 10^9$ $\mathrm{M}_\odot$, to explore galaxy metal enrichment over the last half of the age of the Universe. A particular emphasis has been placed upon the relationship between stellar mass and metallicity of both gaseous and stellar components.

The main results can be summarised as follows.

- A correlation between gas–phase Oxygen abundance and stellar mass is present at all redshifts since $z \sim 1$ down to $z = 0$.

---

[1] Since dust–correction has not been implemented in our code, we have compared the colour–magnitude relation (CMR hereafter) with the sample of Pizagno et al. (2005), whose internal dust reddening was corrected for as in Tully et al. (1998), rather than comparing the CMR in the simulations with the low redshift New York University Value–Added Galaxy Catalogue of Blanton et al. (2005), which do not take into account extinction but the Galactic extinction as in Schlegel et al. (1998).

- The $z = 0$ relationship between stellar mass and gas–phase metallicity in the simulations is in broad agreement with the $z \sim 0.1$ correlation observed in SDSS galaxies.

- The $z = 0$ dispersion of the gas–phase Oxygen abundances for simulations with comparable masses and diverse merging histories is in broad agreement with the $z \sim 0.1$ dispersion observed in SDSS galaxies. This suggests that the latter could be due to the differing formation histories of galaxies with comparable masses.

- The mass–metallicity relationship for massive simulations is $\sim$ flat since $z \sim 1$ down to $z = 0$, thus suggesting that they experience substantial metal enrichment early on.

- No relationship is found in the simulations between age and stellar mass. The age range for massive simulations is similar to that observed for comparable mass $z \sim 0$ galaxies. However, the $z = 0$ stellar populations of less massive simulations tend to be dominated by stars older than the observed. A mechanism to delay star formation seems necessary to solve the discrepancy, as also suggested by the $z = 0$ Colour–Magnitude Relation in the simulations, which is shallower than the observed.

Chapter 6

Conclusions and Future Directions

Which is "normal"?...Is the Milky Way an outlier? Is there any stellar halo–galaxy formation symbiosis? These driving questions in mind, we have tried to face the challenge they pose and undertaken the path which has led to this PhD Thesis. Here we summarise what (we think that) we see from our point of view.

We have presented in Chapter 3 (which synthesises the background which is in Appendices B – H; see also Renda et al. 2005b) an analysis of several late–type galaxy stellar halos within a grid of semi–cosmological simulations, with particular emphasis placed upon the relationship between stellar halo metallicity and galactic luminosity. It helps to stress here that "Halo Semantics" is currently a controversial topic (e.g., Ibata et al. 2007 and references therein): we have labelled as "topographical halo" the ensemble of stellar particles in a simulation at a projected radius R $>$ 15 kpc, at z = 0. Although future analysis of simulations at resolutions higher than the current would further improve the study we have undertaken, we have shown that - at any given galaxy luminosity or, conversely, galaxy dynamical mass - halo metallicities in the simulations span a range in excess of $\sim$ 1 dex, a result which is strengthened by the robustness tests we have performed.

We suggest that the underlying driver of the halo metallicity dispersion can be traced to the diversity of galactic mass assembly histories inherent within the hierarchical clustering paradigm. Galaxies with a more protracted assembly history possess more metal–rich and younger stellar halos, with an associated greater dispersion in age, than galaxies which experience more of a monolithic collapse.

For a given galaxy luminosity (or dynamical mass), those galaxies with more extended assembly histories also possess more massive stellar halos, which in turn leads to a direct correlation between the stellar halo metallicity and its surface brightness (as anticipated by earlier semi–analytical models - e.g.: Chapter 2; Renda et al. 2005). By extension, such a correlation may prove to be a useful diagnostic tool for disentangling the formation history of late–type galaxies.

Recently, Mouhcine et al. (2005) have presented an observed correlation between stellar halo metallicity and galactic luminosity. The observed halo metallicity dispersion at a given galactic luminosity is *smaller* than what we find in our simulations. *However* the latter can account for the outliers in the observed trend. Since our motivation has been to study which is the effect of the pattern of the initial density fluctuations *alone* on the stellar halo features at redshift $z = 0$ in late–type galaxy simulations, it helps to note that galaxy formation, as it is observed, is an ongoing process which is the result of the interplay among different parameters, of which the pattern of the initial density fluctuations (thus the merging history) is one. We have shown that the merging history *alone* may be held responsible of the dispersion in halo metallicity at comparable galactic luminosities.

We have then analysed the stellar mass assembly, and the relationships between stellar, gaseous and total mass since $z \sim 1$ down to $z = 0$ in the simulations, to explore whether hierarchical formation scenarios may account for the constraints on galaxy mass assembly over the second half of the age of the Universe (Chapter 4).

The redshift evolution of the stellar mass in simulations with comparable luminosities at $z = 0$ shows a large dispersion, which lies in their differing merging histories. This contrasts with the redshift evolution of the total mass within the central 100 kpc, which is already assembled by $z \sim 1.5$. The stellar–to–total mass ratio in the simulations is in broad agreement with the observed (e.g., Conselice et al. 2005). We find that massive simulations are generally more evolved than their lower mass counterparts. Galaxies with comparable luminosities/stellar masses at $z = 0$ in the simulations can have significantly different assembly histories of their stellar content, and diverse gaseous contents. This suggests that stellar mass should not be considered neither a robust tracer of the galaxy merging history nor a good tracer of the total baryonic galaxy mass.

We have finally analysed the metal enrichment of the stellar and gaseous components in the simulations (Chapter 5). A correlation between gas–phase Oxygen abundance and stellar mass is present since $z \sim 1$ down to $z = 0$. The $z = 0$ relationship between stellar mass and gas–phase metallicity in the simulations is in broad agreement with the $z \sim 0.1$ correlation observed in SDSS galaxies (Tremonti et al., 2004). The z = 0 dispersion of the gas–phase Oxygen abundances for simulations with comparable masses and diverse merging histories is in broad agreement with the dispersion observed at z ∼ 0.1 in SDSS galaxies. This suggests that the latter could be due to the differing formation histories of galaxies with comparable masses. The mass–metallicity relationship for massive simulations is ∼ flat since z ∼ 1 down to z = 0, thus suggesting that they experience substantial metal enrichment early on. No relationship is found in the simulations between age and stellar mass. The age range for massive simulations is similar to that observed for comparable mass z ∼ 0 galaxies. However, the z = 0 stellar populations of less massive simulations tend to be dominated by stars older than the observed. A mechanism to delay star formation seems necessary to solve the discrepancy, as also suggested by the z = 0 Colour–Magnitude Relation in the simulations, which is shallower than the observed.

Where do we go from here? However promising they are, chemo–dynamical simulations still suffer from feedback related issues (e.g.: Steinmetz & Navarro 1999; Thacker & Couchman 2000; Abadi et al. 2003; Robertson et al. 2006; Stinson et al. 2006; Kaufmann et al. 2007) which are reflected here in the mass–metallicity relationship and in the Colour–Magnitude Relation (Chapter 5). It is reassuring though - as a robustness test for the semi–cosmological framework - that there is consistency between the results of semi–cosmological and cosmological simulations, as shown in Chapters 4 and 5.

We have focused here in this PhD Thesis on the formation of stellar halos in late–type galaxies. We have shown that the diverse galaxy merging histories may be held responsible of the observed dispersion in halo metallicity at comparable galactic luminosities (Chapter 3). Higher resolution simulations, a deeper understanding of the role of feedback processes in galaxy formation, and further observations are all together needed to take the next step on this research path.

Appendices

Appendix A

On the origin of fluorine in the Milky Way

The main astrophysical factories of fluorine (^{19}F) are thought to be Type II supernovae, Wolf–Rayet stars, and the Asymptotic Giant Branch (AGB) of intermediate mass stars. We present a model for the chemical evolution of fluorine in the Milky Way in a semi–analytic multi–zone chemical evolution framework. For the first time, we quantitatively demonstrate the impact of fluorine nucleosynthesis in Wolf–Rayet and AGB stars. The inclusion of these latter two fluorine production sites provides a possible solution to the long–standing discrepancy between model predictions and the fluorine abundances observed in Milky Way giants. Finally, fluorine is discussed as a possible probe of the role of supernovae and intermediate mass stars in the chemical evolution history of the globular cluster ω Centauri.

A.1 Introduction

The three primary astrophysical factories for fluorine (^{19}F) production have long been thought to be Type II Supernovae (SNe II), Wolf–Rayet (WR) stars, and Asymptotic Giant Branch (AGB) stars (e.g., respectively: Woosley & Weaver 1995; Meynet & Arnould 2000; Forestini et al. 1992; Mowlavi, Jorissen & Arnould 1998). Previous attempts to model the Galactic production and evolution of ^{19}F have been restricted to explore the role of SNe II alone (e.g.: Timmes, Woosley & Weaver 1995; Alibés, Labay & Canal 2001).

The above problem has now been ameliorated by the release of the first detailed yield predictions for fluorine production from WR and AGB stars. We are now in a position to incorporate these yields into a Galactic chemical evolution framework, in order to assess the respective contributions of the three putative fluorine production sites. To do so, we will make use of `GEtool`, a semi–analytical multi–zone Galactic chemical evolution package which has been calibrated with extant observational data for the Milky Way (Fenner & Gibson 2003; Gibson et al. 2003).

Specifically, in what follows, we compare the model fluorine distribution in the Milky Way with the abundances observed by Jorissen, Smith & Lambert (1992) in near–solar metallicity giants. Further, our model predictions are contrasted with new fluorine determinations for giants in the Large Magellanic Cloud (LMC) and ω Centauri (Cunha et al., 2003). In addition, new results for more ω Centauri giants from Smith et al. (2004) are included. The latter two systems are likely to have had *very* different star formation and chemical evolution histories from those of the Milky Way, but despite these obvious differences, a comparison against these new data can be valuable. In Section A.2, we provide a cursory overview of the three traditional ^{19}F nucleosynthesis sites; the chemical evolution code in which the nucleosynthesis products from these factories have been implemented is described in Section A.3. Our results are then presented and summarised in Sections A.4 and A.5, respectively.

A.2 Nucleosynthesis of ^{19}F

A.2.1 Type II Supernovae

The massive star progenitors to SNe II produce fluorine primarily as the result of spallation of ^{20}Ne by μ and τ neutrinos near the collapsed core (Woosley & Haxton 1988; Woosley et al. 1990). A fraction of the ^{19}F thus created is destroyed by the subsequent shock but most is returned to the ambient Interstellar Medium (ISM). The fluorine yields by neutrino spallation are very sensitive to the assumed spectra of μ and τ neutrinos (Woosley et al., 2002), which could be nonthermal and deficient on their high–energy tails, lowering the equivalent temperature of the neutrinos in the supernova model (Myra & Burrows, 1990). An additional source of ^{19}F derives from pre–explosive CNO burning in helium shell. However, fluorine production by neutrino spallation is largely dominant, as evident by comparing the models in Woosley & Weaver (1995), and recent models which do not include neutrino nucleosynthesis of fluorine (Limongi & Chieffi, 2003). Most recently, Heger et al. (2004) suggest that the relevant neutrino cross sections need to be revised downwards; if confirmed, the associated SNe II ^{19}F yield would decrease by $\sim 50\%$. In light of the preliminary nature of the Heger et al. claim, we retain the conservative choice offered by the Woosley & Weaver (1995) compilation.

A.2.2 Asymptotic Giant Branch stars

The nucleosynthesis pathways for fluorine production within AGB stars involve both helium burning and combined hydrogen–helium burning phases (e.g.: Forestini et al. 1992; Jorissen et al. 1992; Mowlavi et al. 1998) and are companions for the nucleosynthesis by slow neutron accretion (s–process) (Mowlavi et al., 1998). Provided a suitable source of protons is available, fluorine can be synthesised via ^{14}N(α,γ)^{18}F (β^+) ^{18}O(p,α) ^{15}N(α,γ) ^{19}F. Primary sources of uncertainty in predicting fluorine nucleosynthesis in AGB stars relate to the adopted reaction rates, especially ^{14}C(α, γ)^{18}O and ^{19}F(α, p)^{22}Ne, and the treatment of the nucleosynthesis occurring during the convective thermal pulses. Nucleosynthesis during the interpulse periods can also be important if protons from the envelope are partially mixed in the top layers of the He intershell (partial mixing zone), as Lugaro et al. (2004) have recently demonstrated. Nucleosynthesis in this zone may result in a significant increase in the predicted ^{19}F yields. The magnitude of these systematic uncertainties for stellar models with mass $\sim$ 3 M$_\odot$ and metallicities Z = 0.004 – 0.02 are $\sim$ 50 %, while for stellar models with mass M = 5 M$_\odot$ and metallicity Z = 0.02 the uncertainty is a factor of $\sim$ 5, due to the uncertain ^{19}F(α, p)^{22}Ne reaction rate. Characterising the mass– and metallicity– dependence of the partial mixing zone–^{19}F relationship needs to be completed before we can assess its behaviour self–consistently within our chemical evolution model of the Milky Way. For the present study, we have adopted the yields presented in Renda et al. (2004), based upon the Karakas & Lattanzio (2003, and references therein) models, which themselves do not include ^{19}F nucleosynthesis via partial mixing. This choice is a conservative one, and thus should be considered as a lower limit to the production of ^{19}F from AGB stars.

For stars more massive than $\approx$ 4 M$_\odot$, the convective envelope is so deep that it penetrates into the top of the hydrogen–burning shell so that nucleosynthesis actually occurs in the envelope of the star. Such "hot–bottom–burning" acts to destroy ^{19}F, and should be treated self–consistently within the AGB models considered.

A.2.3 Wolf–Rayet stars

Fluorine production in WR stars is tied to its nucleosynthesis during the helium–burning phase. At the end of this phase though, significant fluorine destruction occurs via $^{19}\mathrm{F}(\alpha, \mathrm{p})^{22}\mathrm{Ne}$. Any earlier synthesised $^{19}\mathrm{F}$ must be removed from the stellar interior in order to avoid destruction. For massive stars to be significant contributors to net fluorine production, they must experience mass loss on a timescale that allows the removal of $^{19}\mathrm{F}$ before its destruction. This requirement is met by WR stars.

Recently, Meynet & Arnould (2000) studied the role that such stars can play in the chemical evolution of fluorine by adopting updated reaction rates coupled with extreme mass–loss rates in not–rotating stellar models. They pointed out that WR mass–loss is strongly metallicity–dependent, and that the number of WR stars at low metallicities is very small. Their WR yields reflect such metallicity–dependence, with minimal fluorine returned to the ISM at low metallicities, but significant $^{19}\mathrm{F}$ returned at solar and super–solar metallicities. The WR yields are sensitive to the adopted reaction and mass–loss rates, while rotating models could favour an early entrance into the WR phase for a given mass, decrease the minimum initial mass for a star to go through a WR phase at a given metallicity, and open more nucleosynthetic channels because of the mixing induced by rotation. Therefore, after Meynet & Arnould (2000), we consider the aforementioned WR yields as lower limits.

A.3 The model

In this study we employ `GEtool`, our semi–analytical multi–zone chemical evolution package to model a sample Milky Way–like disk galaxy (Fenner & Gibson 2003; Gibson et al. 2003). A dual–infall framework is constructed in which the first infall episode corresponds to the formation of the halo, and the second to the inside–out formation of the disk.

A Kroupa, Tout & Gilmore (1993) initial mass function (IMF) has been assumed, with lower and upper mass limits of 0.08 $\mathrm{M}_\odot$ and 120 $\mathrm{M}_\odot$, respectively. Stellar yields are one of the most important features in galactic chemical evolution models, yet questions remain concerning the precise composition of stellar ejecta, due to the uncertain role played by processes including mass loss, rotation, fall–back, and the location of the mass cut, which separates the remnant from the ejected material in SNe. The SNe II yields are from Woosley & Weaver (1995); for stars more massive than 60 $M_\odot$, the yields are assumed to be mass–independent. Such assumption is made to avoid extreme extrapolation from the most massive star in the Woosley & Weaver models (40 $M_\odot$) to the upper end of the IMF (120 $M_\odot$), and has negligible effect on the results, given the shape of the adopted IMF.

We have halved the iron yields shown in Woosley & Weaver (1995), as suggested by Timmes et al. (1995). The Type Ia (SNe Ia) yields of Iwamoto et al. (1999) were also employed. We adopted the metallicity–dependent yields of Renzini & Voli (1981) for single stars in the mass range 1 – 8 $M_\odot$. For the purposes of this work, which focuses on fluorine, the choice of the Renzini & Voli yields set does not affect the results. Metalllicity–dependent stellar lifetimes have been taken from Schaller et al. (1992).

We have constructed three Milky Way (MW) model variants that differ only in their respective treatments of ^{19}F production: 1) MWa assumes that SNe II are the only source of ^{19}F; 2) MWb includes yields from both SNe II *and* WR stars; 3) MWc includes all three sources of fluorine - SNe II, WR, and AGB stars.

We end by noting that within our adopted dual–infall framework for the chemical evolution of the Milky Way, our model is constrained by an array of observational boundary conditions, including the present–day star and gas distributions (both in density and metallicity), abundance ratio patterns, age–metallicity relation, and G–dwarf distribution (Gibson et al., 2003). While the modification of any individual ingredient within the model framework will have an impact, to some degree, upon the predicted chemical evolution, this can only eventuate at the expense of one or more of the aforementioned boundary conditions that we require our model to adhere to. Within our framework, yield uncertainties will dominate the systematic uncertainties for the predicted evolution of ^{19}F.

A.3.1 Fluorine yields

We now summarise the ^{19}F yields employed in our three "Milky Way" models.

1) SNe II ^{19}F yields are taken from Woosley & Weaver (1995) and assumed to be mass–independent for stellar masses in excess of 60 $M_\odot$.

2) WR ^{19}F yields are taken from Meynet & Arnould (2000) for stellar masses in the range 25 – 120 $M_\odot$: each star within this range is assumed to evolve through the

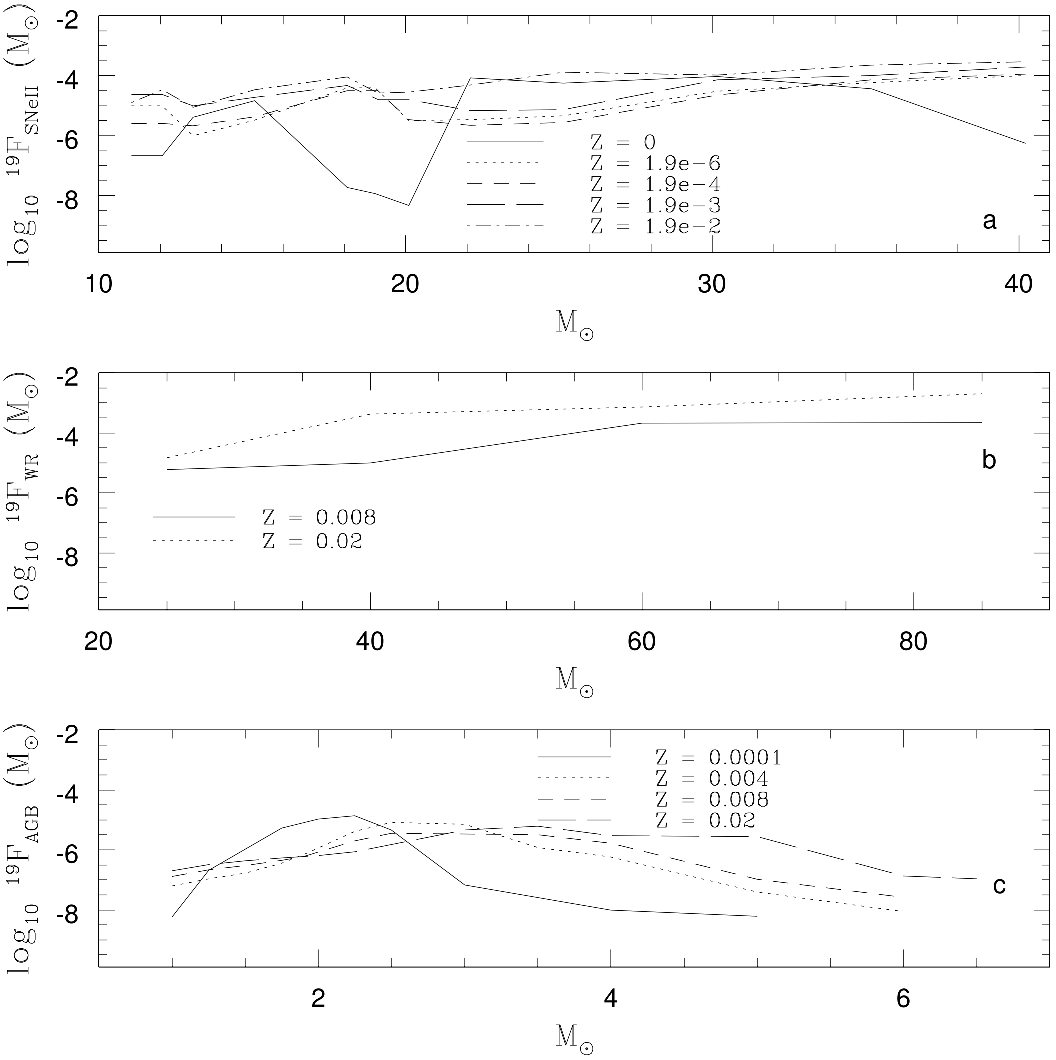

Figure A.1: Fluorine yields from: “a”, SNe II (Woosley & Weaver 1995); “b”, WR (Meynet & Arnould 2000); “c”, AGB stars.

WR stage. Such simplifying assumption could overestimate the WR contribution to fluorine, even though the adopted WR yields are themselves lower limits (Section A.2.3). The WR fluorine contribution has been added to the corresponding SNe II contribution (which comes from a different stage of the stellar evolution).

3) AGB ^{19}F and oxygen yields in the mass range 1 – 6.5 $M_\odot$ have been derived from stellar models constructed with the Mount Stromlo Stellar Structure Code (Frost & Lattanzio 1996; Karakas et al. 2002), and are presented in Renda et al. (2004). The post–processing nucleosynthesis models with 74 species and time–dependent diffusive convective mixing are described in detail in Frost et al. (1998) and Karakas & Lattanzio (2003).

To ensure internal consistency, we have also employed the AGB oxygen yields *in lieu* of those of Renzini & Voli (1981), within this mass range.

The above fluorine yields are shown in Figure A.1. In Figure A.2, the yields are expressed as [F/O][1] and $\langle[\mathrm{F/O}]\rangle_{IMF}$, the latter corresponding to the mean [F/O] yields for SNe II and AGB stars, weighted by the IMF over the SNe II and AGB mass range, respectively. We have not shown a comparable entry for the WR stars as a self–consistent treatment of the oxygen production was not included in Meynet & Arnould (2000). Here, oxygen has been used as the normalisation to make easier the comparison with the observations, especially in ω Centauri, though oxygen can be synthesised in various stellar sites, and its yields can be affected by different reaction rates and modeling of helium cores, semi–convection, convective boundary layers, and mass–loss (e.g.: Woosley et al. 2002; Dray et al. 2003).

A.4 Results

In Figure A.3, the evolution of [F/O], A(O), the gas infall rate $\dot{\sigma}_{infall}$, the star formation rate (SFR), the SNe II rate and the gas–phase global metallicity Z of the three models at the solar neighbourhood are summarised. The empirical SFR history derived by Bertelli & Nasi (2001) is shown as a thick solid line in panel “d” of Figure A.3, while the shaded region corresponds to the range of values suggested by Rana (1991). A conservative range of estimated SNe II rates is also shown

---

[1] Hereafter, $[\mathrm{X/Y}] = \log_{10}(\mathrm{X/Y}) - \log_{10}(\mathrm{X/Y})_\odot$ and $\mathrm{A(X)} = 12 + \log_{10}(\mathrm{n_X/n_H})$. An accurate determination of photospheric solar abundances requires detailed modeling of the solar granulation and accounting for departures from local thermodynamical equilibrium (e.g., Allende Prieto, Lambert & Asplund 2001). We adopt the solar fluorine abundance suggested by Cunha et al. (2003), and the solar iron and oxygen abundances from Holweger (2001).

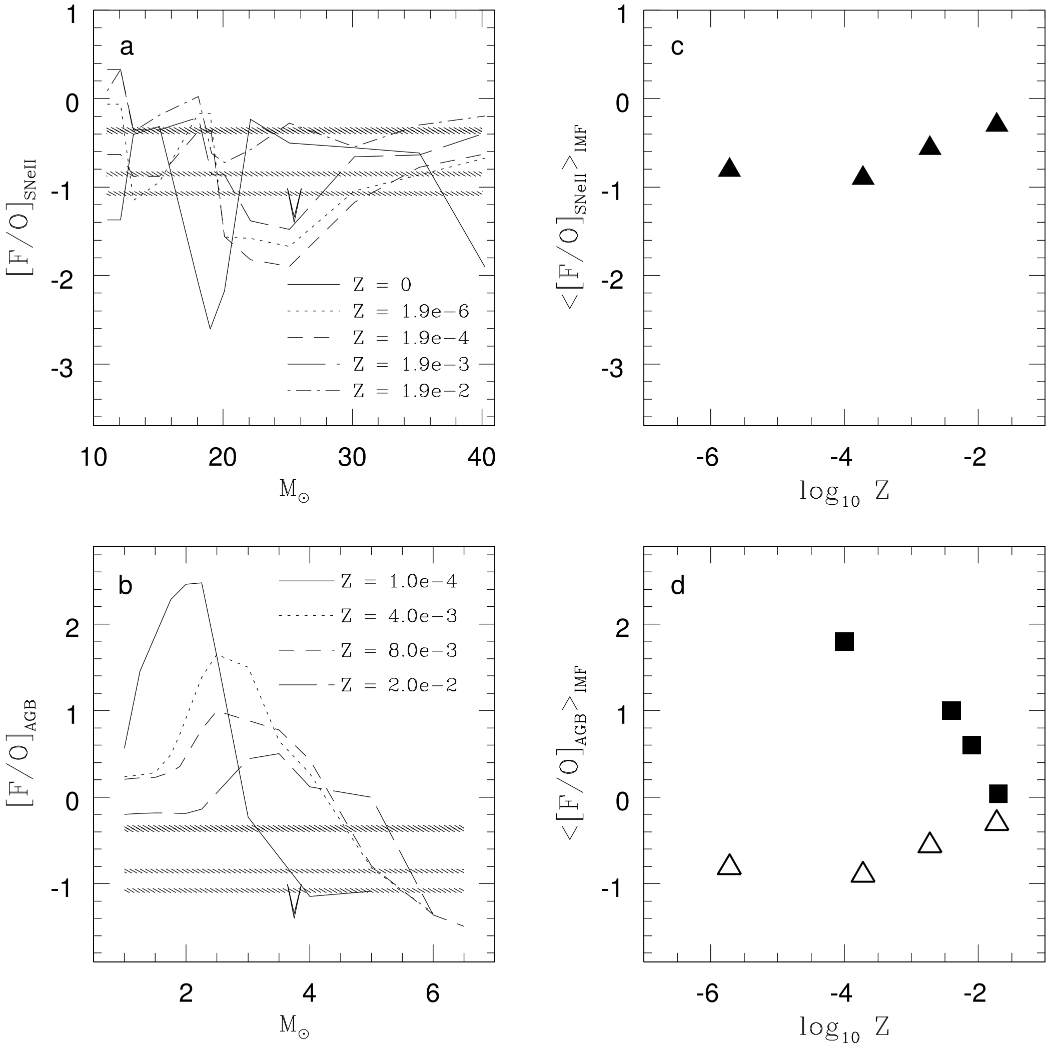

Figure A.2: [F/O] and $\langle[F/O]\rangle_{IMF}$ for SNe II and AGB yields (upper and lower panels, respectively). Here, $A(^{19}F)_\odot = 4.55$ (see discussion in Cunha et al. 2003) and $A(O)_\odot = 8.736$ (e.g., Holweger 2001). The shaded regions in panels "a" and "b" show the observed [F/O] in ω Cen giants (Cunha et al. 2003). The $\langle[F/O]\rangle_{IMF}$ are weighted by the IMF over the SNe II (11 – 40 $M_\odot$) and AGB (1 – 6.5 $M_\odot$) mass range, respectively. In panel "d", both $\langle[F/O]_{AGB}\rangle_{IMF}$ and $\langle[F/O]_{SNe\ II}\rangle_{IMF}$ are shown (closed boxes and open triangles, respectively).

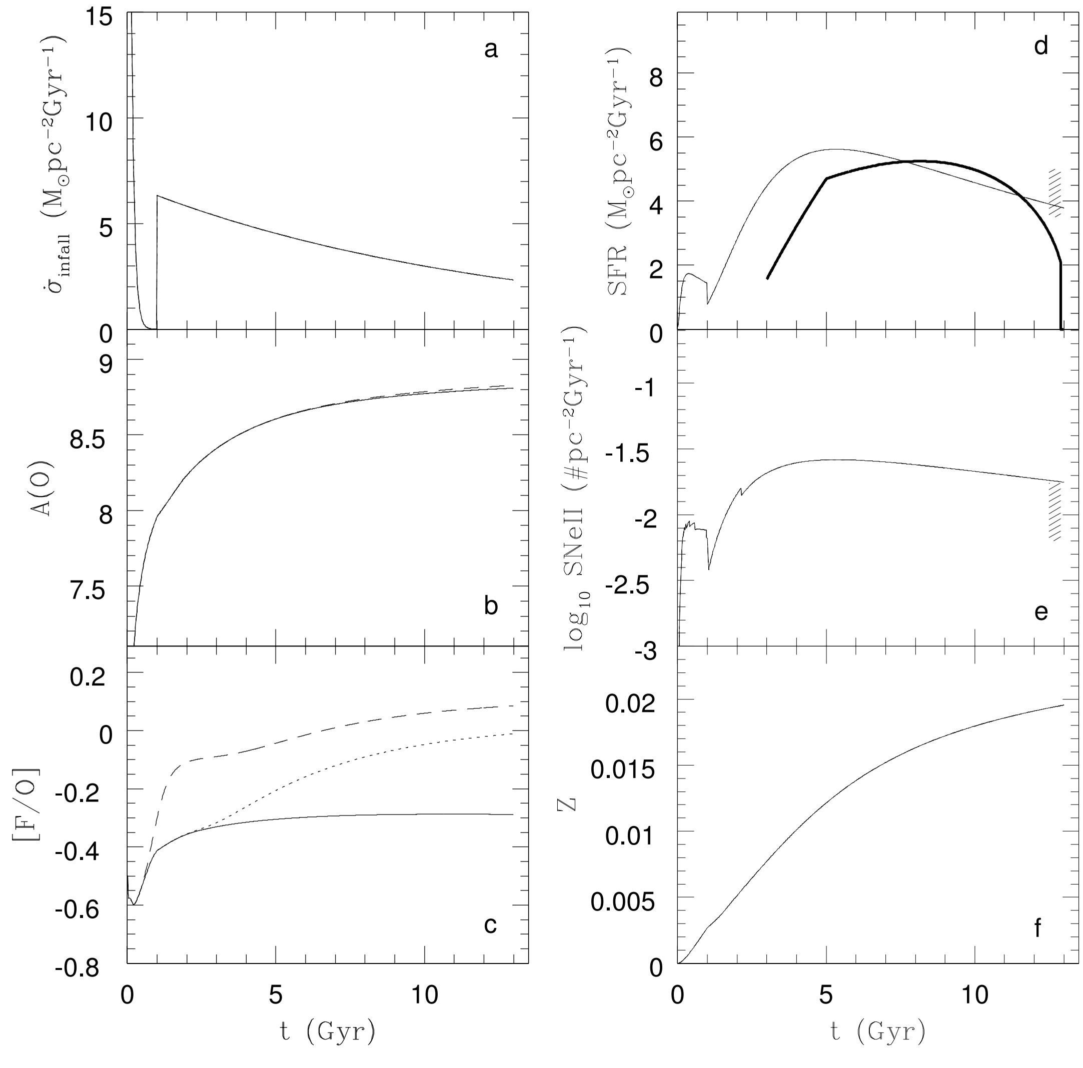

Figure A.3: Predicted evolution in the solar neighbourhood of: "a", the gas infall rate $\dot{\sigma}_{infall}$; "b", A(O); "c", [F/O]; "d", the star formation rate (SFR); "e", the SNe II rate; "f", the metallicity Z (MWa, solid line; MWb, dotted; MWc, short–dashed). The SFR history at the solar neighbourhood obtained by Bertelli & Nasi (2001) is also shown as a thick solid line in panel "d", while the shaded region shows the range of values suggested by Rana (1991). A range of values corresponding to the estimated SNe II rate is shown in panel "e" (Cappellaro et al. 1999).

in panel "e" (Cappellaro, Evans & Turatto 1999).[2]. Figure A.4 then shows the the evolution of [F/O] versus A(O) (panel "a"), and the evolution of [F/O] versus [O/Fe] (panel "b"), compared against the IMF–weighted SNe II yields (recall Figure A.2).

The MWa model provides a satisfactory reproduction of the estimated star formation history and SNe II rate in the solar neighbourhood (Figure A.3, panels "d" and "e"). This model, whose only fluorine source is SNe II, underproduces fluorine with respect to the abundances measured in K and M Milky Way giants observed by Jorissen et al. (1992) and reanalysed by Cunha et al. (2003) (Fig. A.4, panel "a"). Fig. A.4, panel "a" does not show the s–process enriched AGB stars of spectral types MS, S, or C in Jorissen et al. (1992), where freshly synthesised fluorine could be mixed to the stellar surface. Such inclusion of self–polluted ^{19}F–rich stars could obscure any metallicity trend. The results of the MWa and MWb models show that the additional contribution from WR stars increases [F/O] by up to factor of 2 by the present–day, but it is negligible in excess of $\sim$ 9 Gyr ago (Figure A.3, panel "c").

The addition of both WR *and* AGB sources within the MWc model leads to a present–day [F/O] that is $\sim$ 0.4 dex greater than in the MWa case. Further, and perhaps more important, AGB stars are now shown to deliver significant amounts of fluorine to the ISM during the early epochs of the Milky Way's evolution. Such a result is entirely consistent (and expected) given the metallicity–dependence of the AGB yields; said yields possess [F/O] ratios which are greater at lower metallicities (recall Figure A.2). We can conclude that it is only the addition of *both* the WR and the AGB contributions which allow for a significant improvement in the comparison between galactic models incorporating fluorine evolution and the observational data.

A.5 Discussion

We have studied the Galactic chemical evolution of fluorine, for the first time using new grids of stellar models which provide self–consistent predictions of fluorine nucleosynthesis for stars in both the WR and AGB phases of stellar evolution. We have shown that the WR contribution is significant at solar and super–solar metallicities because of the adopted metallicity–dependent mass–loss prescription employed

---

[2] The range of values shown in panel "e" of Figure A.3 is derived from the sample of S0a – Sb galaxies in Cappellaro et al. (1999) - 0.42 ± 0.19 SNu, where 1 SNu= 1 SN(100 yr)$^{-1}$(10^{10} L$^{B}_{\odot}$)$^{-1}$, assuming $L^{B}_{MW} = 2 \times 10^{10}$ L$^{B}_{\odot}$ and a galactic radial extent of 15 kpc. Given these assumptions, the estimated SNe II rate at the solar neighbourhood is necessarily uncertain.

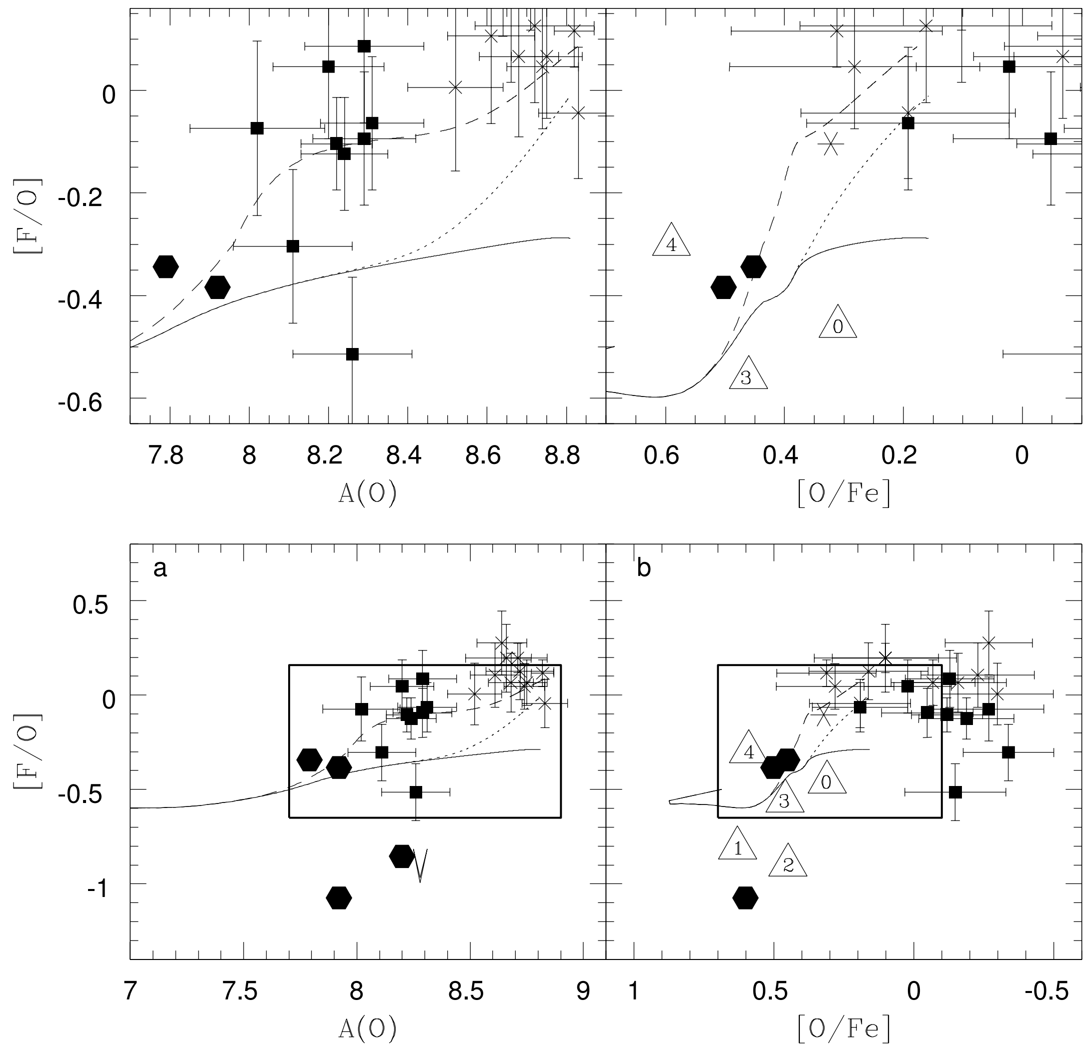

Figure A.4: In panel "a", [F/O] as a function of A(O) for the MW models (MWa, solid line; MWb, dotted; MWc, short–dashed). Also shown are the values observed in Milky Way, LMC, and ω Cen giants (crosses, boxes and hexagons, respectively). In panel "b": [F/O] as a function of [O/Fe], compared with the IMF–weighted $\langle[\mathrm{F/O}]_{\mathrm{SNe\ II}}\rangle_{\mathrm{IMF}}$ and $\langle[\mathrm{O/Fe}]_{\mathrm{SNe\ II}}\rangle_{\mathrm{IMF}}$ yields for SNe II (open triangles). Within the open triangles: "0" corresponds to Z=0; "1", to Z=1.9×10^{-6}; "2", to Z=1.9×10^{-4}; "3", to Z=1.9×10^{-3}; "4", to Z=1.9×10^{-2}. The upper panels represent enlargements of the framed regions delineated in the corresponding bottom panels.

in the stellar models. In contrast, the contribution of AGB stars to fluorine production peaks during the early epochs of the Galaxy's evolution (again due to the metallicity–dependent behaviour of the AGB models). In combination, the addition of the WR and AGB yields leads to a significant improvement in the galactic chemical evolution models when compared against observations.

The comparison between our MW models and the fluorine abundances in LMC and ω Cen giants (Cunha et al., 2003) is not straightforward, as the latter two have star formation (and therefore chemical evolution) histories different from that of the MW. However, it is interesting to speculate on the possible origin of fluorine in ω Cen, given the unique nature of this "globular cluster" (e.g., Smith 2003). Specifically, ω Cen is the most massive Galactic cluster, and unlike most globulars, possesses a significant spread in metallicity (~ 1.5 dex) amongst its stellar population. It has been suggested that ω Cen is actually the remnant core of a tidally–disrupted dwarf galaxy (Bekki & Freeman, 2003). Such a scenario could naturally drive radial gas inflows to the dwarf nucleus, potentially triggering starbursts.

Interestingly, SNe II ejecta are characterised by low $\langle[\mathrm{F/O}]\rangle_{IMF}$ (Figure A.2 panel "c") and high $\langle[\mathrm{O/Fe}]\rangle_{IMF}$ (Figure A.4 panel "b"), whereas AGB ejecta have higher $\langle[\mathrm{F/O}]\rangle_{IMF}$ (Figure A.2 panel "d"). The observed ω Cen giants have primarily low [F/O] (Figures: A.2, panels "a" – "b"; A.4, panels "a" – "b ") and high [O/Fe] (Figure A.4, panel "b") values, consistent with a picture in which their interiors have been polluted by the ejecta of an earlier generation of SNe II, but not from a comparable generation of AGB. Given that the observed oxygen abundance in such ω Cen giants is similar to that seen in comparable LMC and MW giants, as in Figure A.4, panel "a", this would suggest that the chemical enrichment of ω Cen proceeded on a short timescale (to avoid pollution from the lower mass progenitors to the AGB stars) and in an inhomogeneous manner (given the significant scatter in observed fluorine abundances), as previously discussed by Cunha et al. (2003). Should the (downward) revised neutrino cross sections alluded to in Section A.2.1 be confirmed (Heger et al. 2004), the concurrent factor of ~ 2 reduction in SNe II ^{19}F production would improve the agreement of the model with the observed [F/O] ratio in ω Cen giants. This would consequently strengthen our conclusions which already support a picture whereby these giants have been polluted by earlier generations of SNe II ejecta.

Appendix B

Stellar Halo Metallicity Distributions

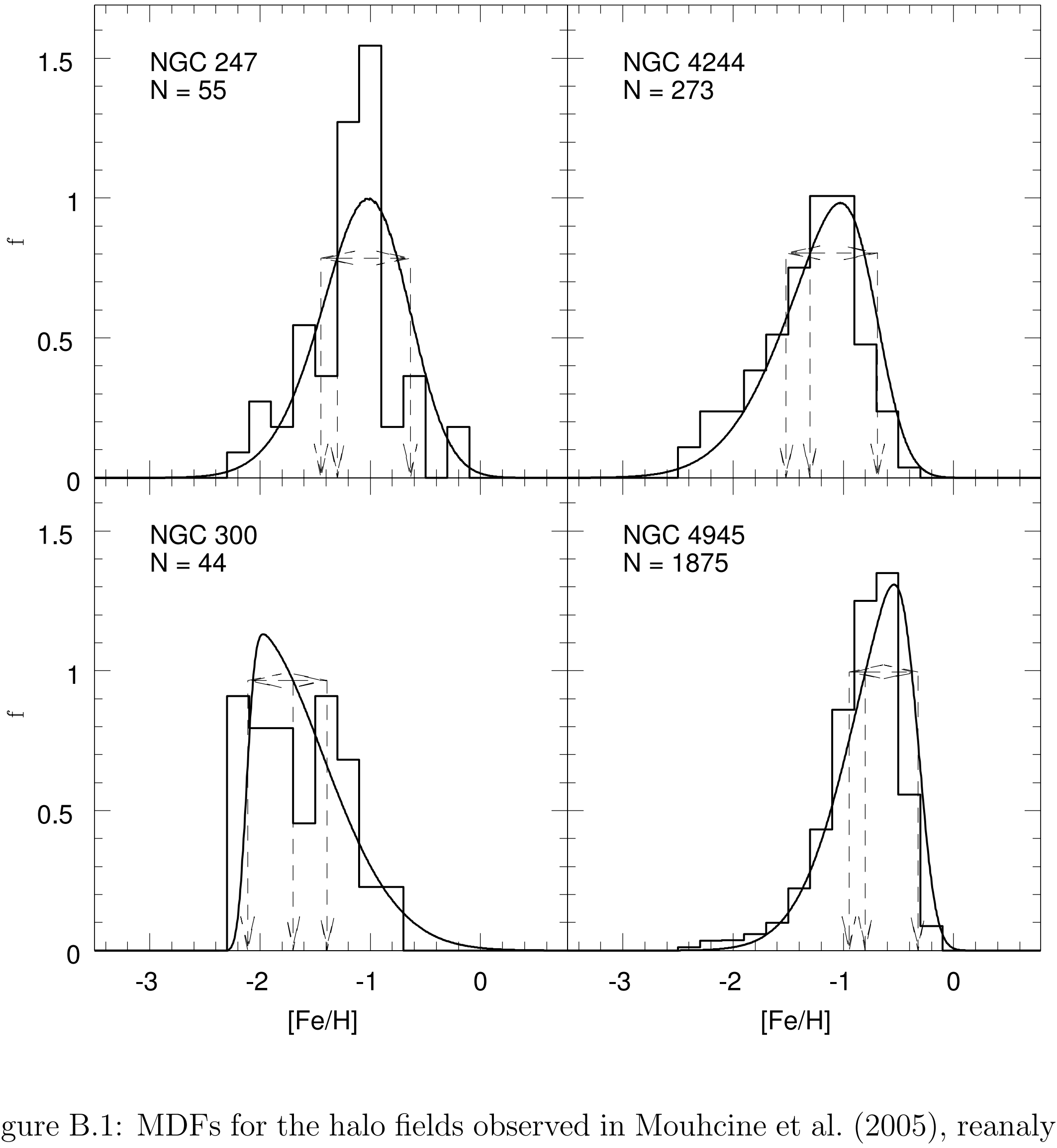

Figure B.1: MDFs for the halo fields observed in Mouhcine et al. (2005), reanalysed by the same pipeline as in Renda et al. (2005b). The 68% Confidence Level range and the number of stellar particles each MDF refers to are also shown.

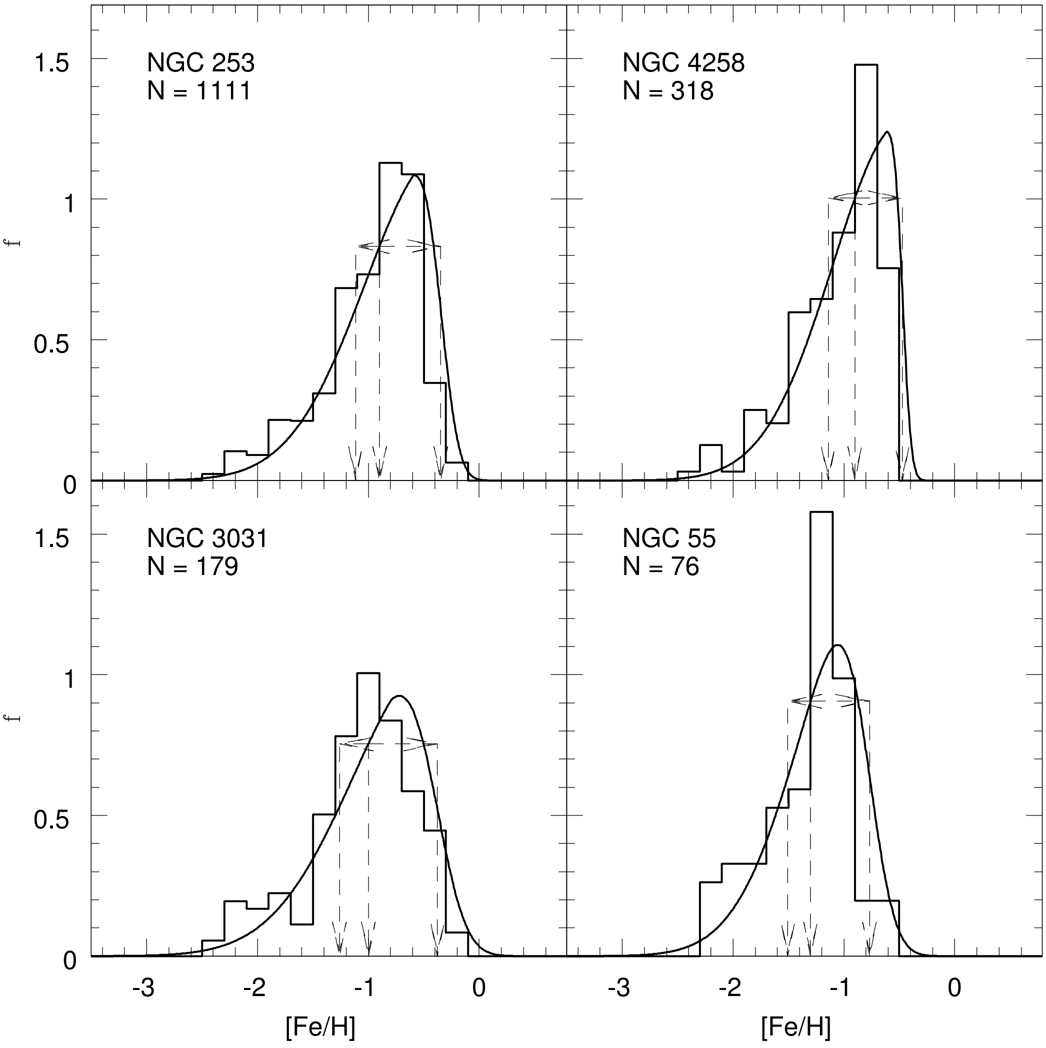

Figure B.2: (continued) MDFs for the halo fields observed in Mouhcine et al. (2005), reanalysed by the same pipeline as in Renda et al. (2005b). The 68% Confidence Level range and the number of stellar particles each MDF refers to are also shown.

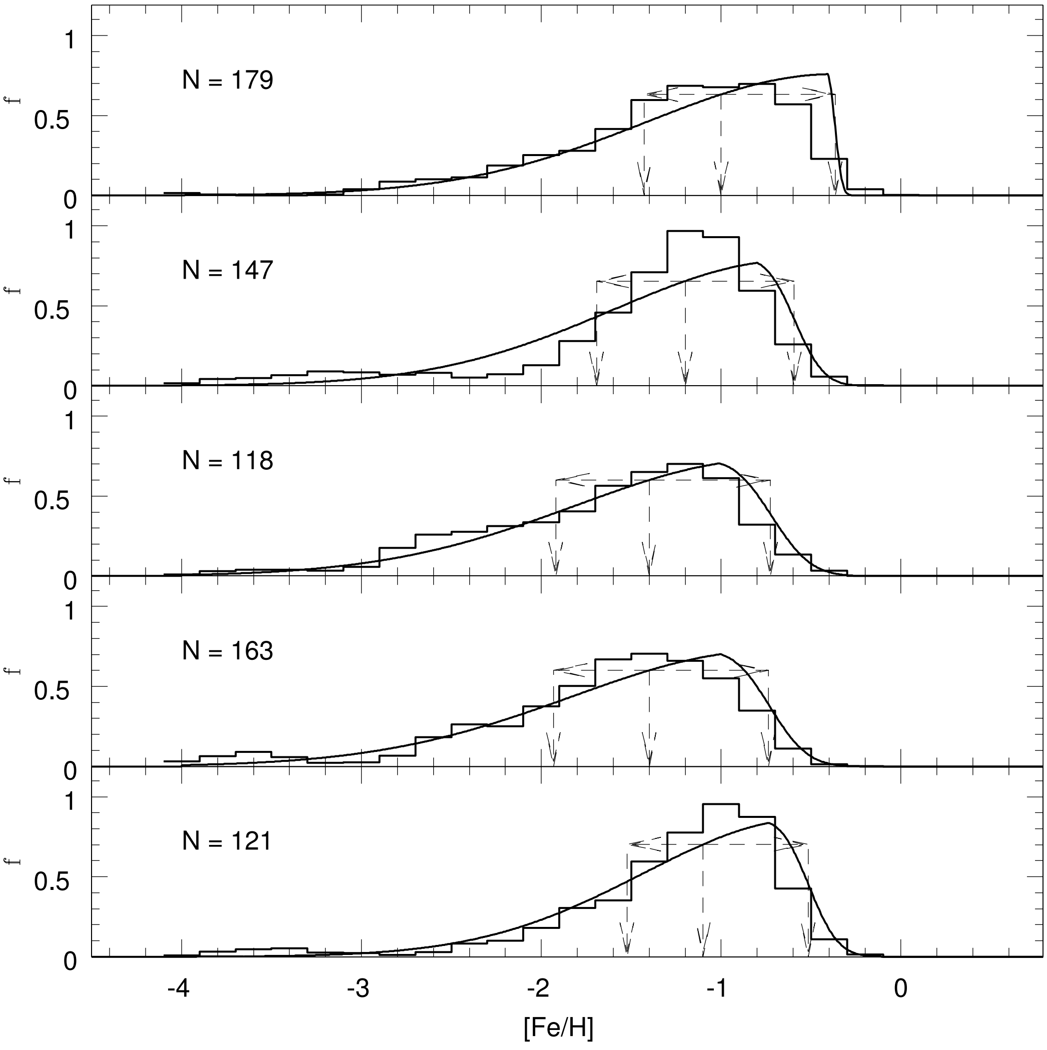

Figure B.3: Halo stellar particle MDFs for the $M_{tot} = 10^{11}$ $M_{\odot}$ semi–cosmological simulations in Renda et al. (2005b). The 68% Confidence Level range and the number of stellar particles each MDF refers to are also shown.

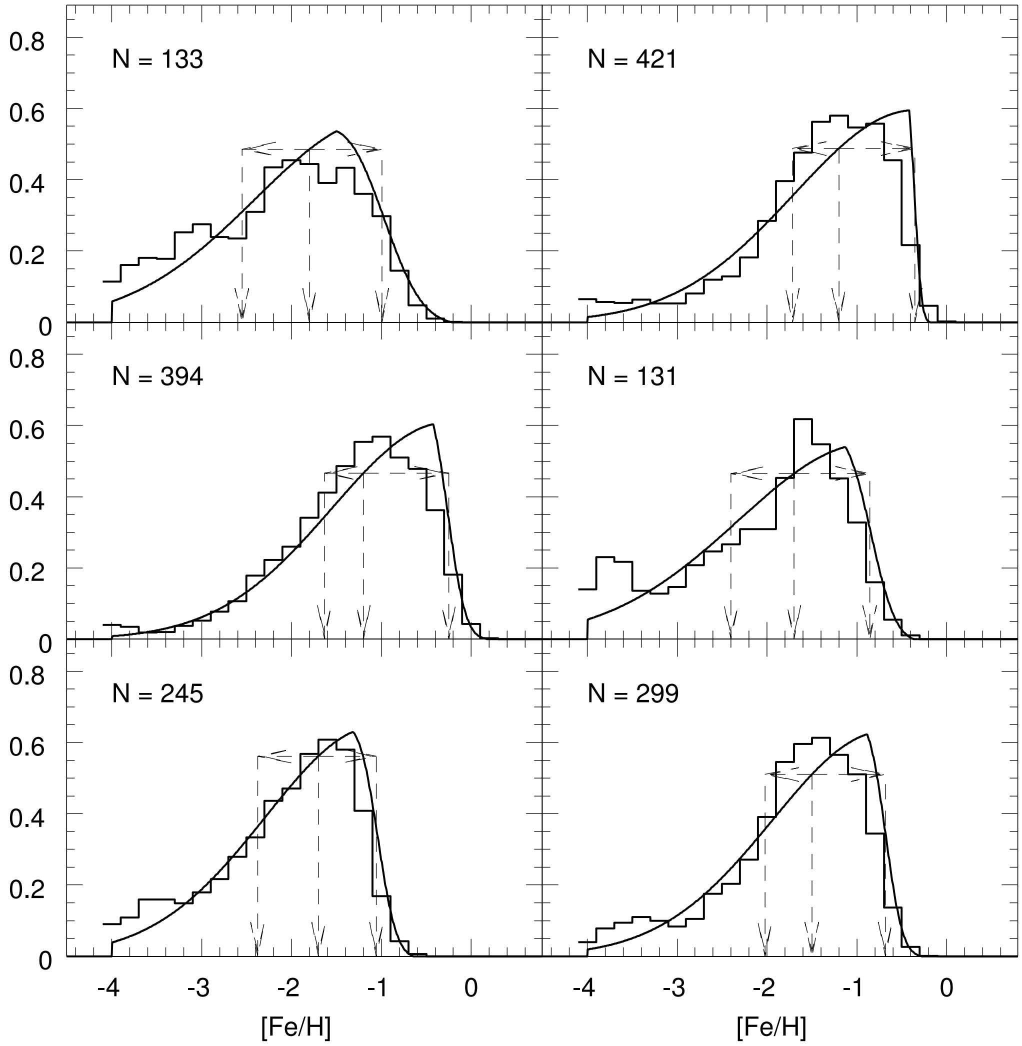

Figure B.4: Halo stellar particle MDFs for the $M_{tot} = 5{\times}10^{11}\ M_{\odot}$ semi–cosmological simulations in Renda et al. (2005b). The 68% Confidence Level range and the number of stellar particles each MDF refers to are also shown.

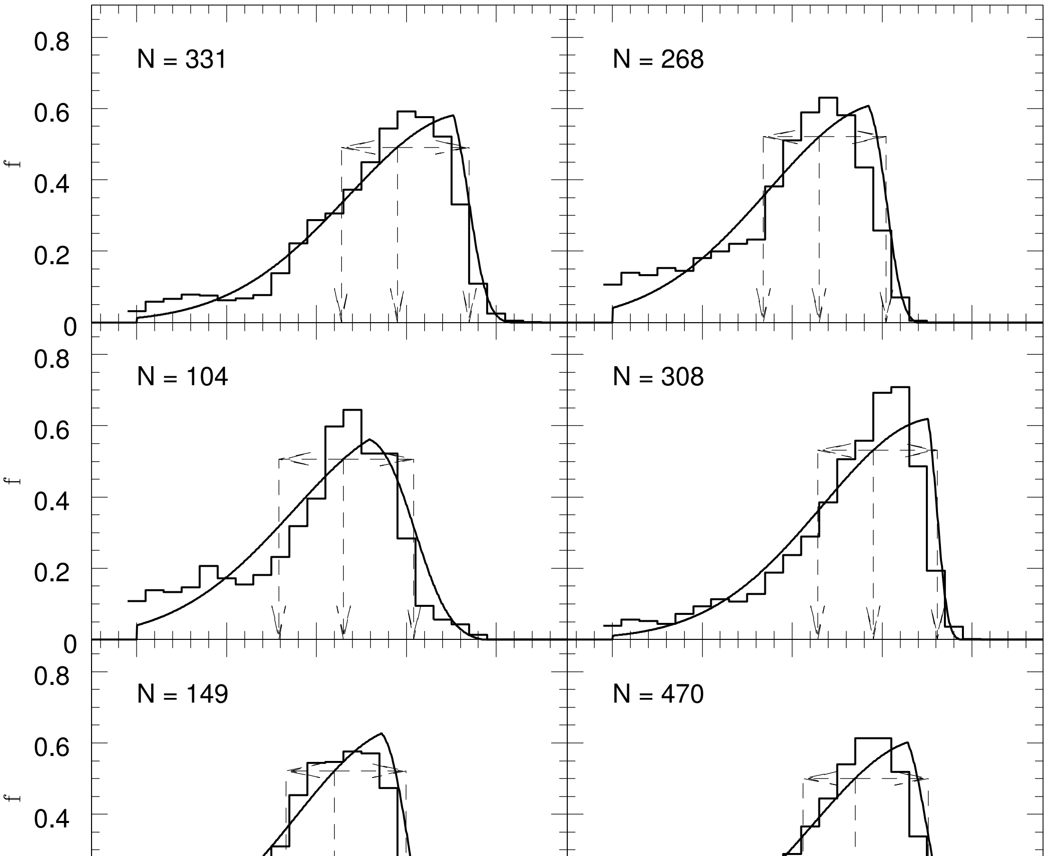

Figure B.5: (continued) Halo stellar particle MDFs for the $M_{tot} = 5 \times 10^{11}$ $M_\odot$ semi–cosmological simulations in Renda et al. (2005b). The 68% Confidence Level range and the number of stellar particles each MDF refers to are also shown.

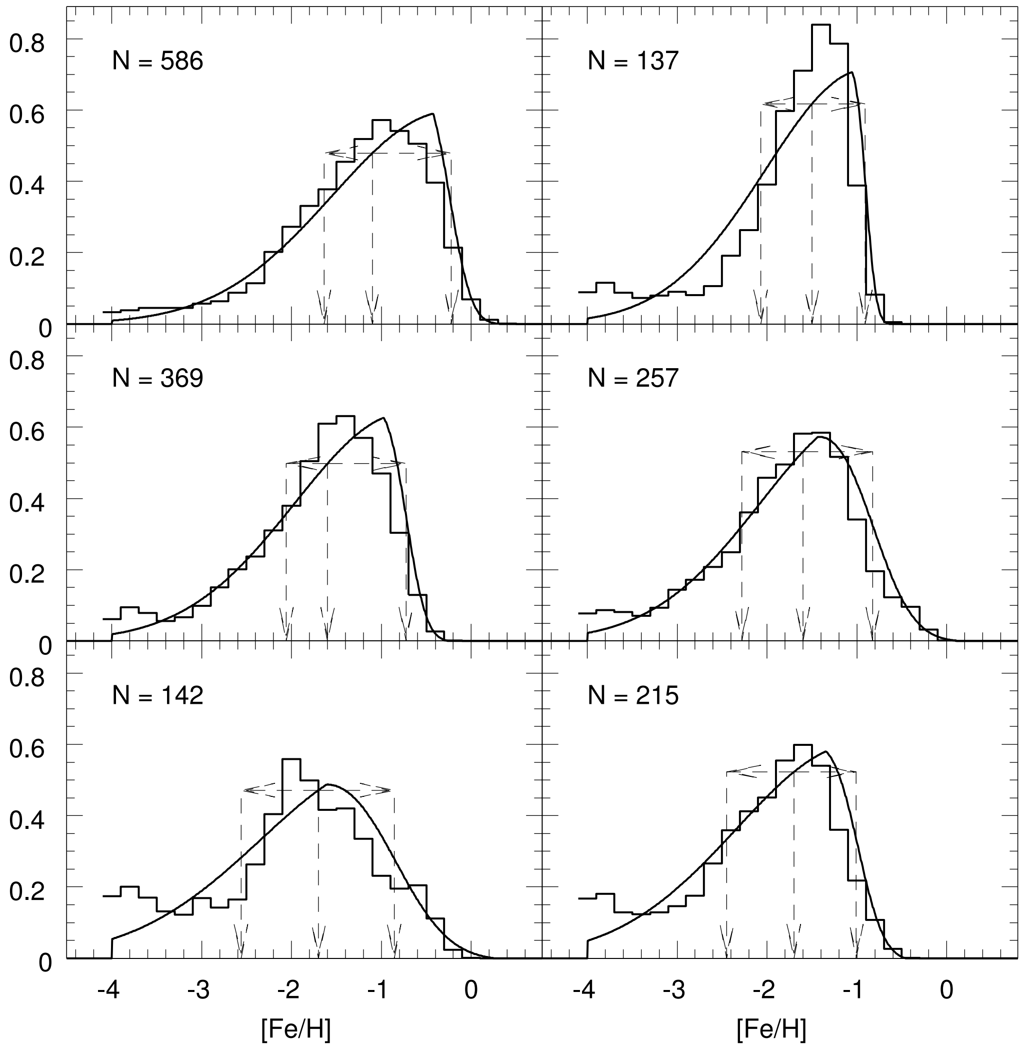

Figure B.6: (continued) Halo stellar particle MDFs for the $M_{tot} = 5\times10^{11}\ M_{\odot}$ semi–cosmological simulations in Renda et al. (2005b). The 68% Confidence Level range and the number of stellar particles each MDF refers to are also shown.

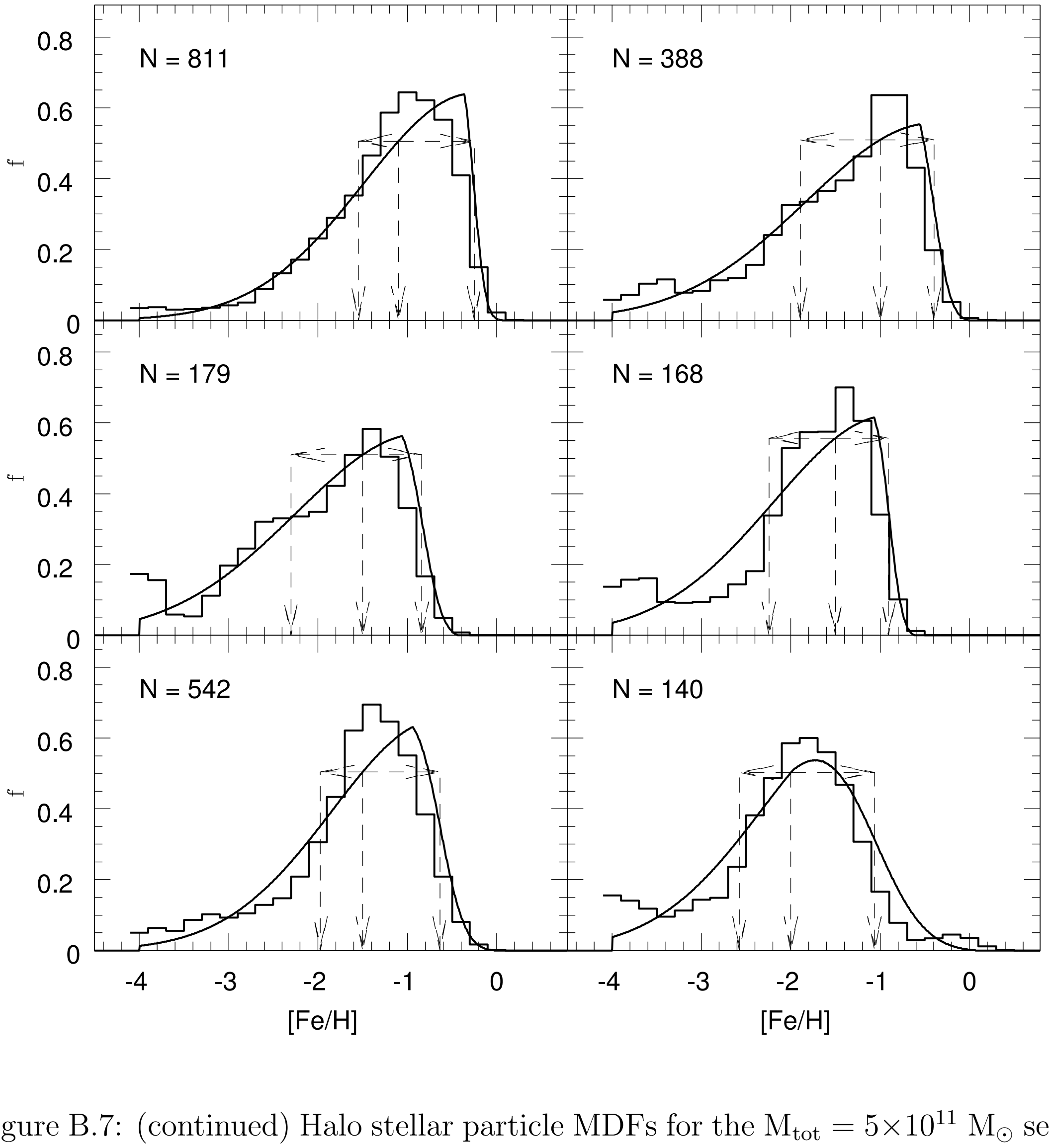

Figure B.7: (continued) Halo stellar particle MDFs for the $M_{tot} = 5\times10^{11}$ $M_{\odot}$ semi–cosmological simulations in Renda et al. (2005b). The 68% Confidence Level range and the number of stellar particles each MDF refers to are also shown.

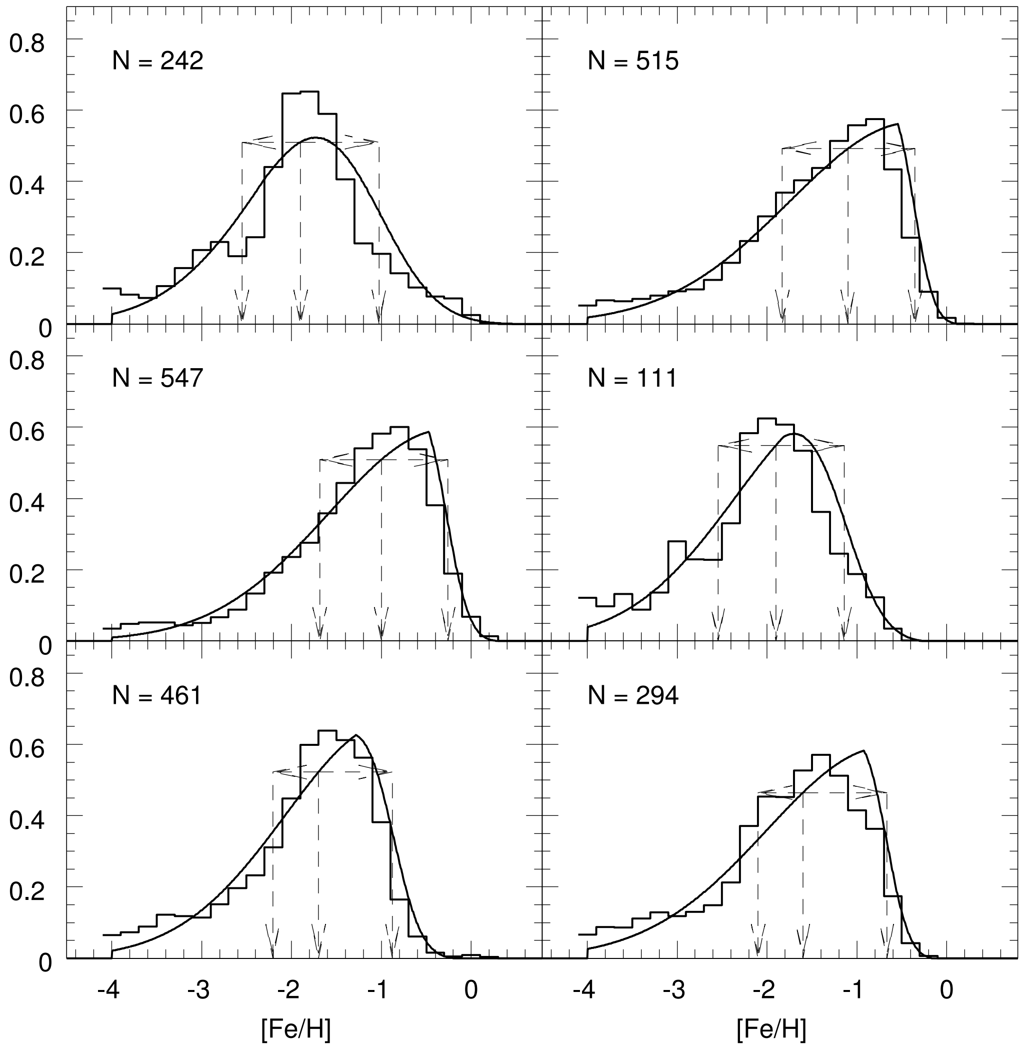

Figure B.8: Halo stellar particle MDFs for the $M_{tot} = 10^{12}\ M_{\odot}$ semi–cosmological simulations in Renda et al. (2005b). The 68% Confidence Level range and the number of stellar particles each MDF refers to are also shown.

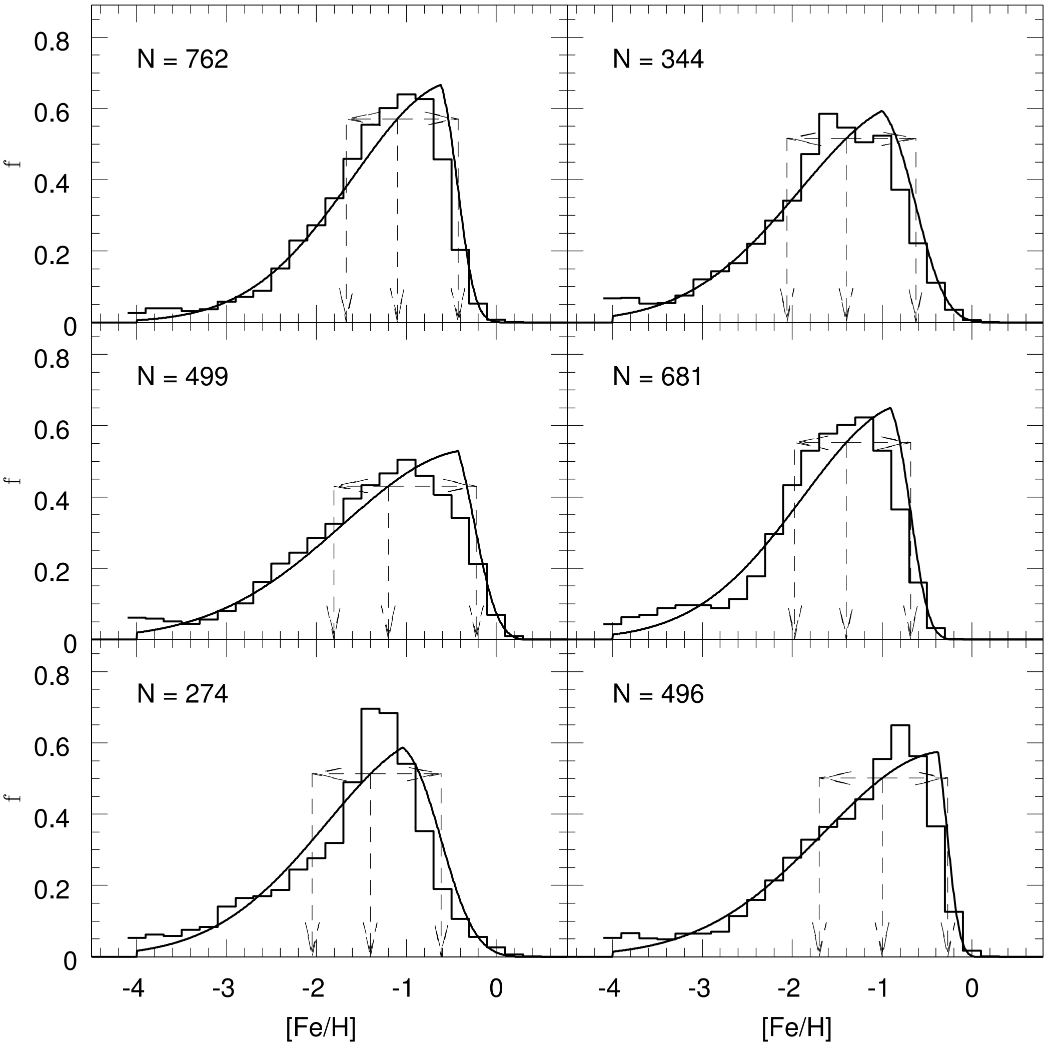

Figure B.9: (continued) Halo stellar particle MDFs for the $M_{tot} = 10^{12}$ $M_{\odot}$ semi–cosmological simulations in Renda et al. (2005b). The 68% Confidence Level range and the number of stellar particles each MDF refers to are also shown.

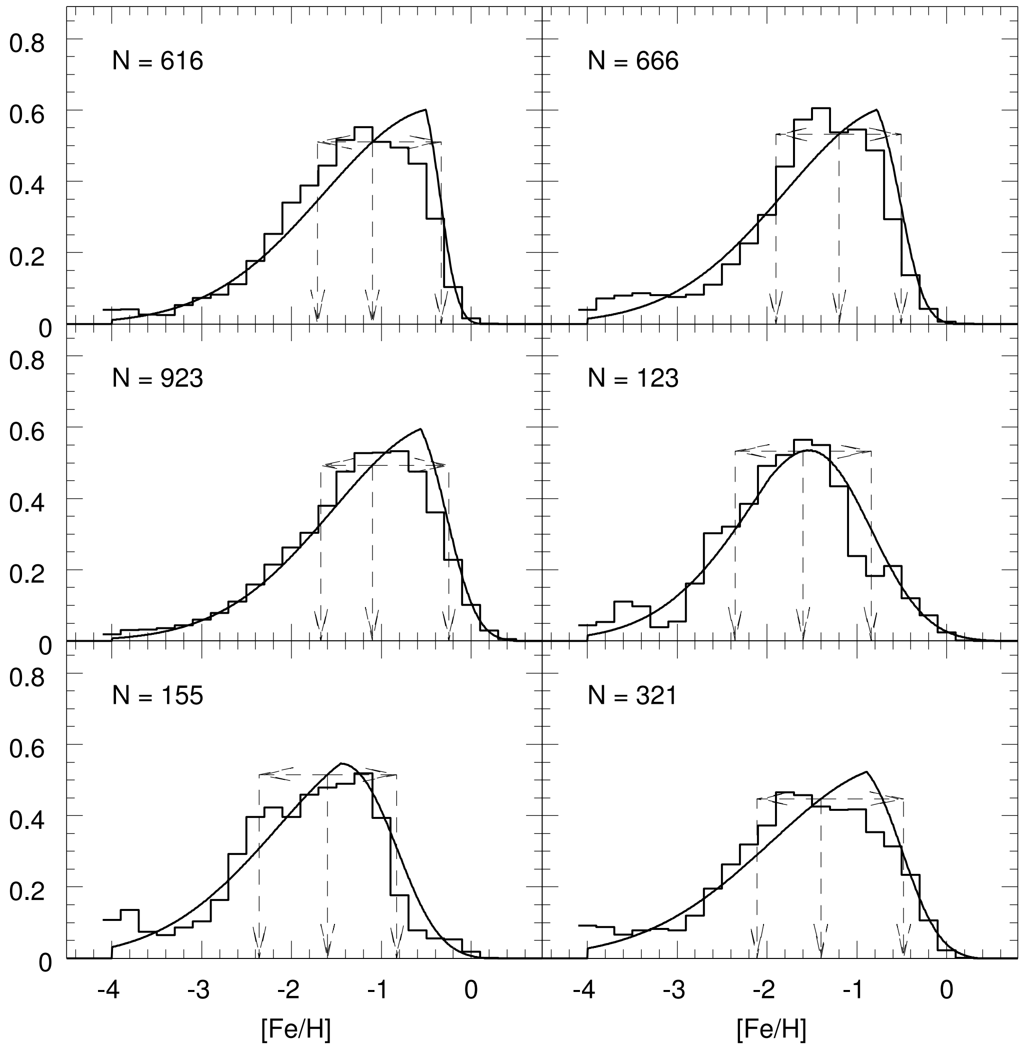

Figure B.10: (continued) Halo stellar particle MDFs for the $M_{tot} = 10^{12}$ $M_{\odot}$ semi–cosmological simulations in Renda et al. (2005b). The 68% Confidence Level range and the number of stellar particles each MDF refers to are also shown.

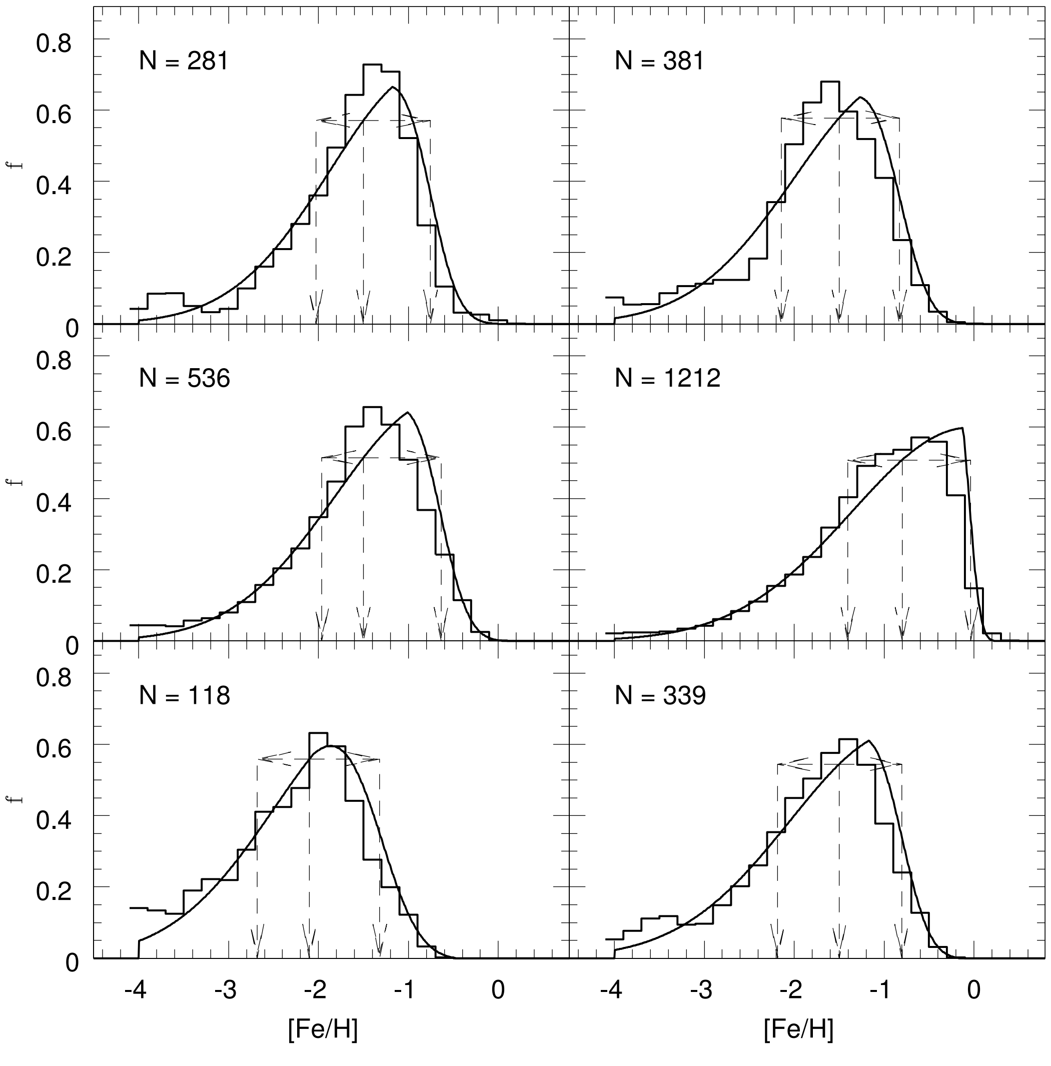

Figure B.11: (continued) Halo stellar particle MDFs for the $M_{tot} = 10^{12}$ $M_{\odot}$ semi–cosmological simulations in Renda et al. (2005b). The 68% Confidence Level range and the number of stellar particles each MDF refers to are also shown.

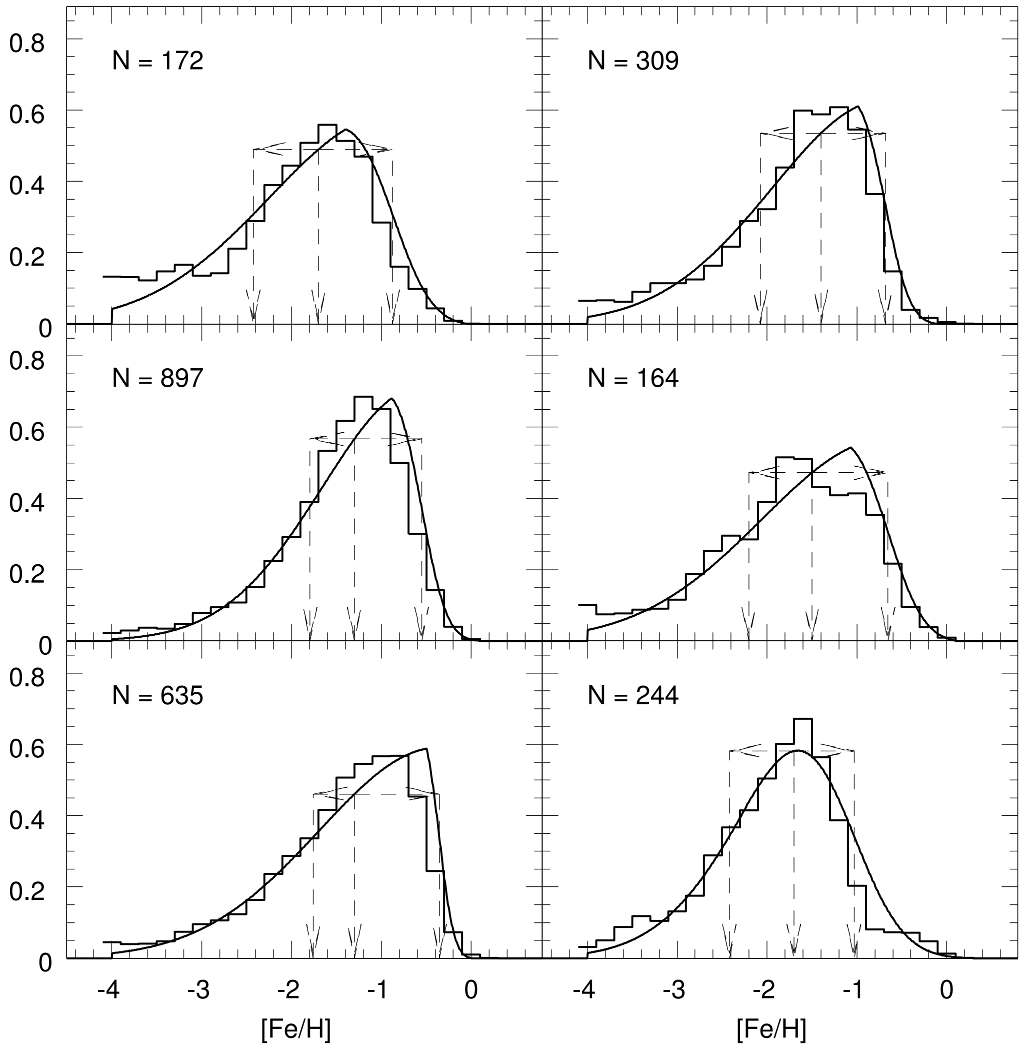

Figure B.12: (continued) Halo stellar particle MDFs for the $M_{tot} = 10^{12}$ $M_\odot$ semi–cosmological simulations in Renda et al. (2005b). The 68% Confidence Level range and the number of stellar particles each MDF refers to are also shown.

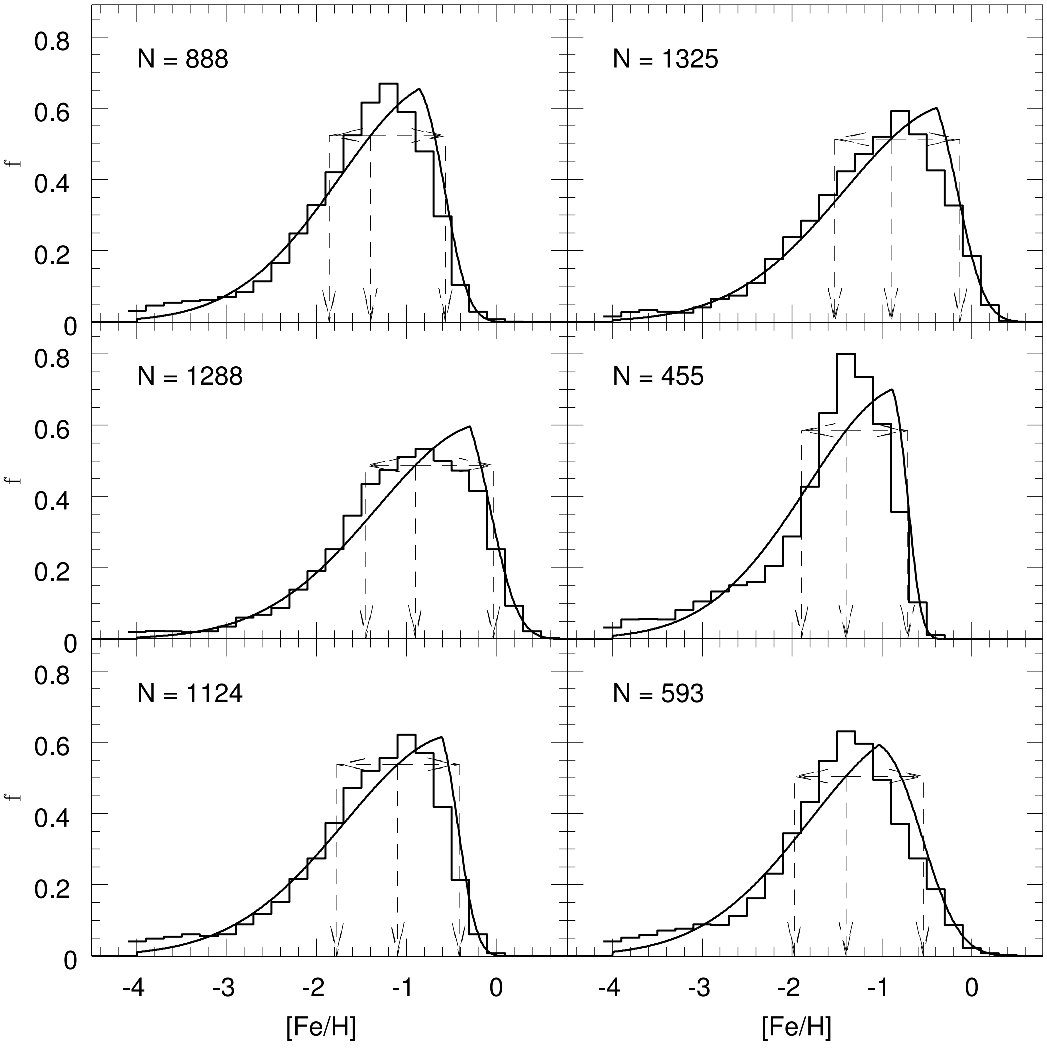

Figure B.13: Halo stellar particle MDFs for the $M_{tot} = 5 \times 10^{12}$ $M_\odot$ semi–cosmological simulations in Renda et al. (2005b). The 68% Confidence Level range and the number of stellar particles each MDF refers to are also shown.

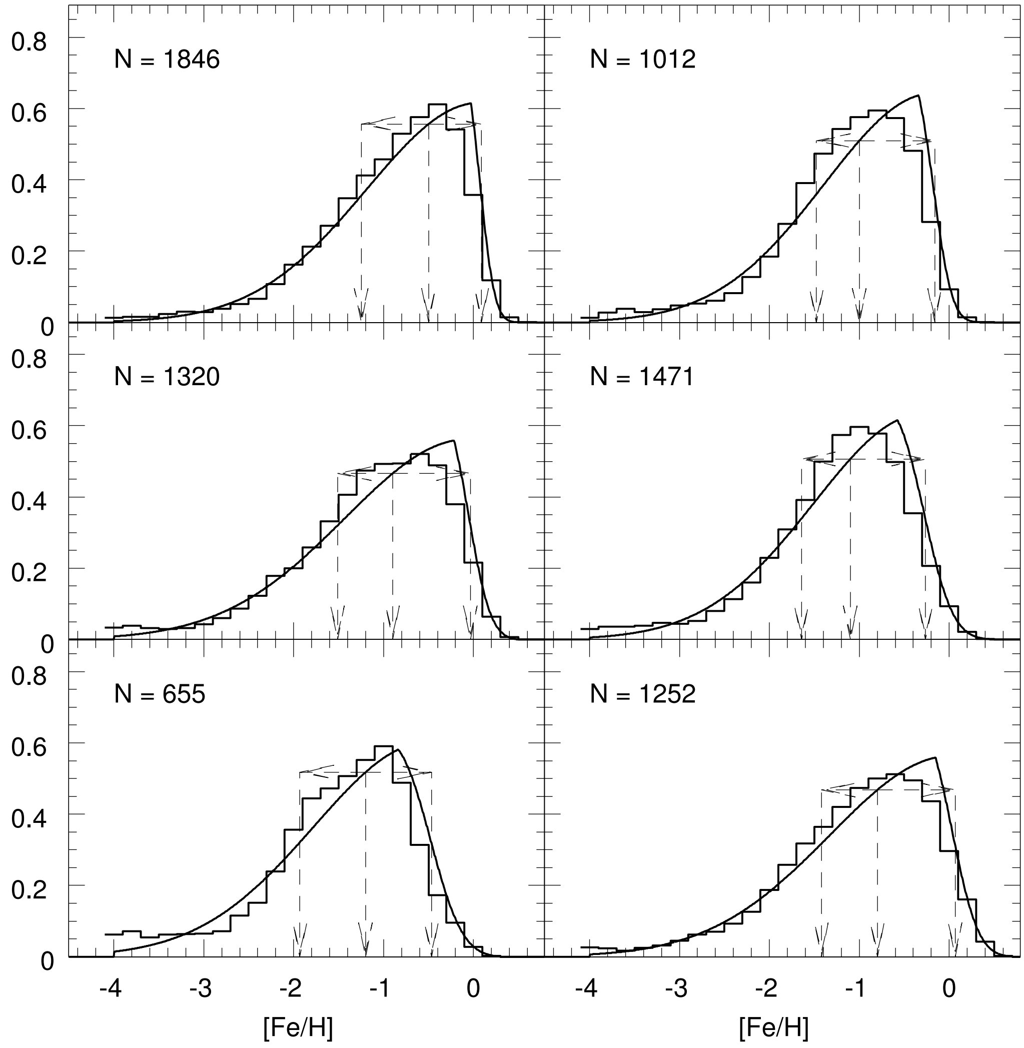

Figure B.14: (continued) Halo stellar particle MDFs for the $M_{tot} = 5 \times 10^{12}$ $M_\odot$ semi–cosmological simulations in Renda et al. (2005b). The 68% Confidence Level range and the number of stellar particles each MDF refers to are also shown.

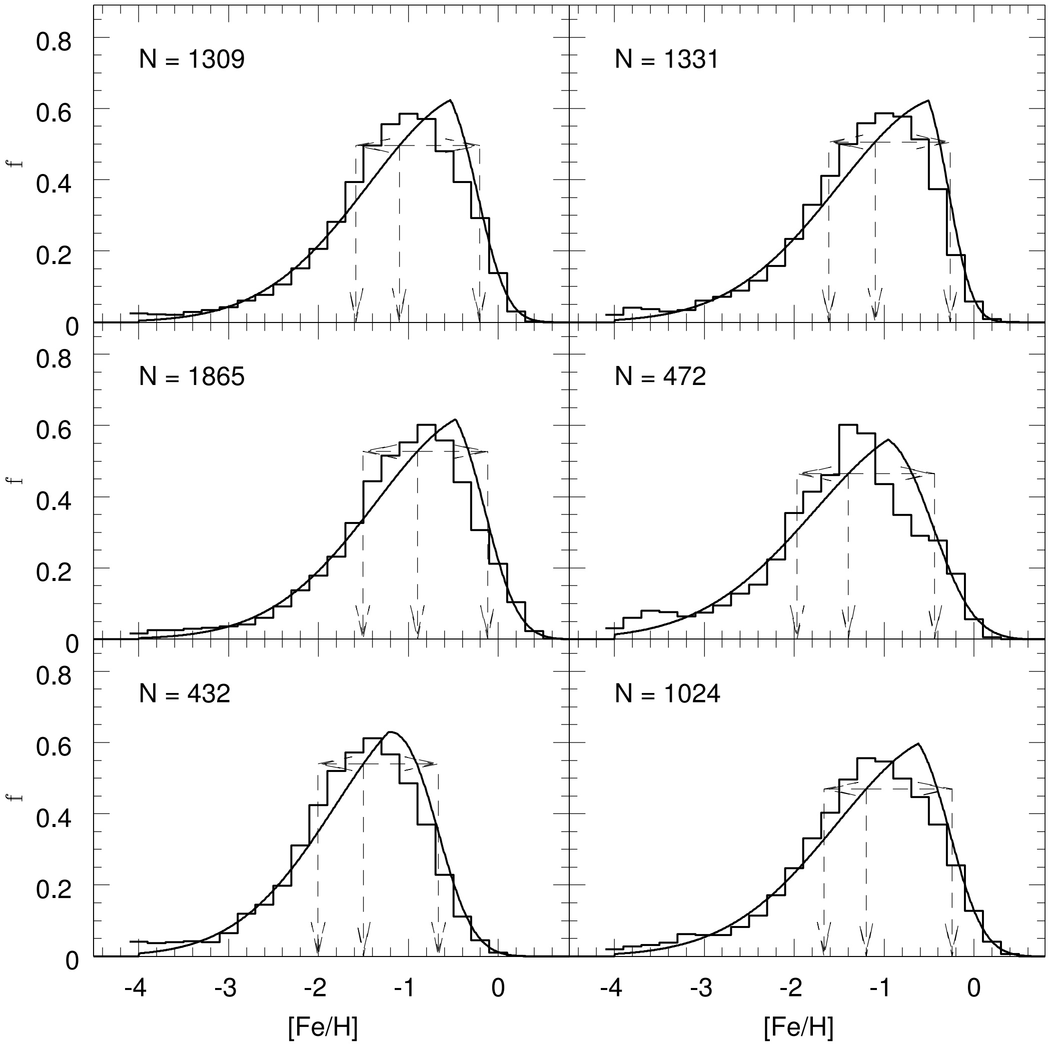

Figure B.15: (continued) Halo stellar particle MDFs for the $M_{tot} = 5{\times}10^{12}\ M_{\odot}$ semi–cosmological simulations in Renda et al. (2005b). The 68% Confidence Level range and the number of stellar particles each MDF refers to are also shown.

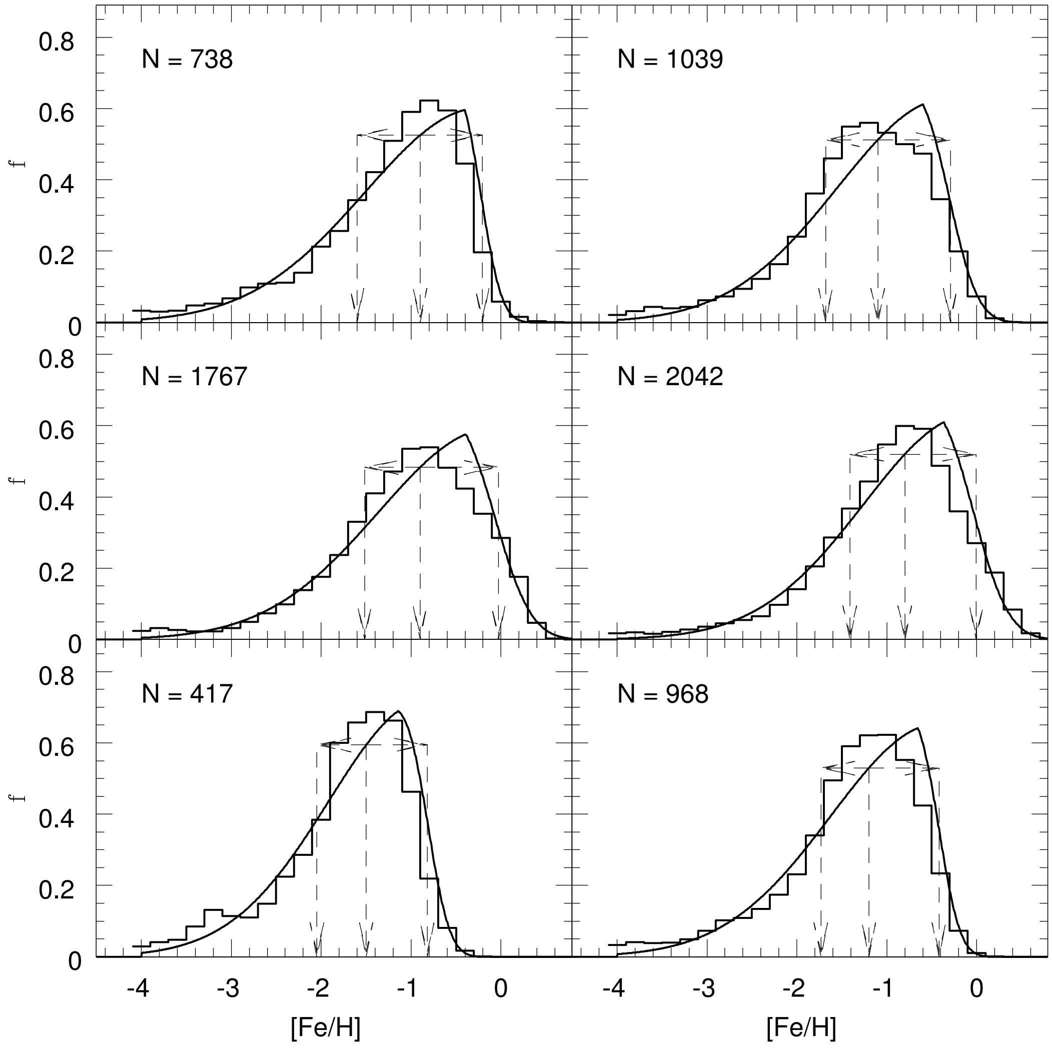

Figure B.16: (continued) Halo stellar particle MDFs for the $M_{tot} = 5\times10^{12}$ $M_\odot$ semi–cosmological simulations in Renda et al. (2005b). The 68% Confidence Level range and the number of stellar particles each MDF refers to are also shown.

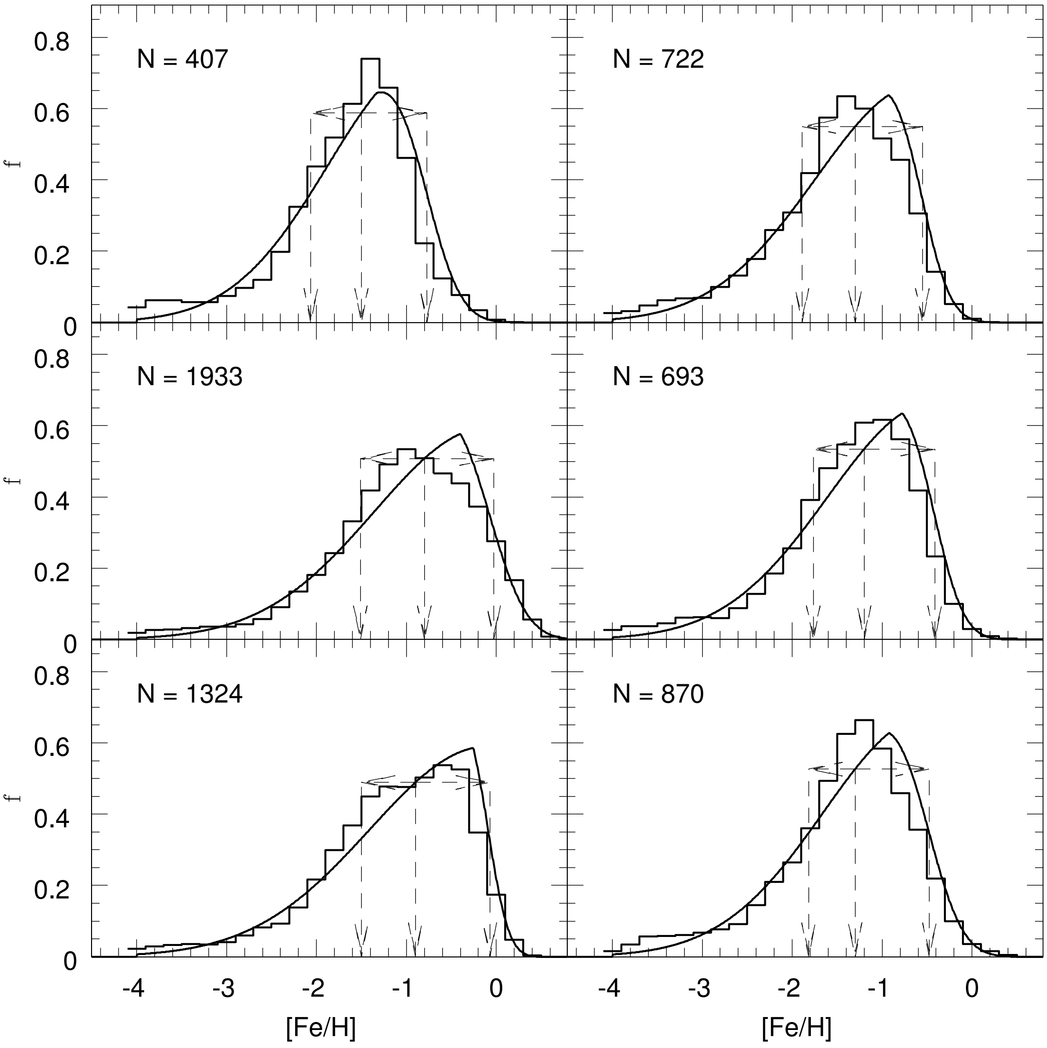

Figure B.17: (continued) Halo stellar particle MDFs for the $M_{tot} = 5\times10^{12}\ M_\odot$ semi–cosmological simulations in Renda et al. (2005b). The 68% Confidence Level range and the number of stellar particles each MDF refers to are also shown.

Appendix C

Stellar Halo [O/Fe] Distributions

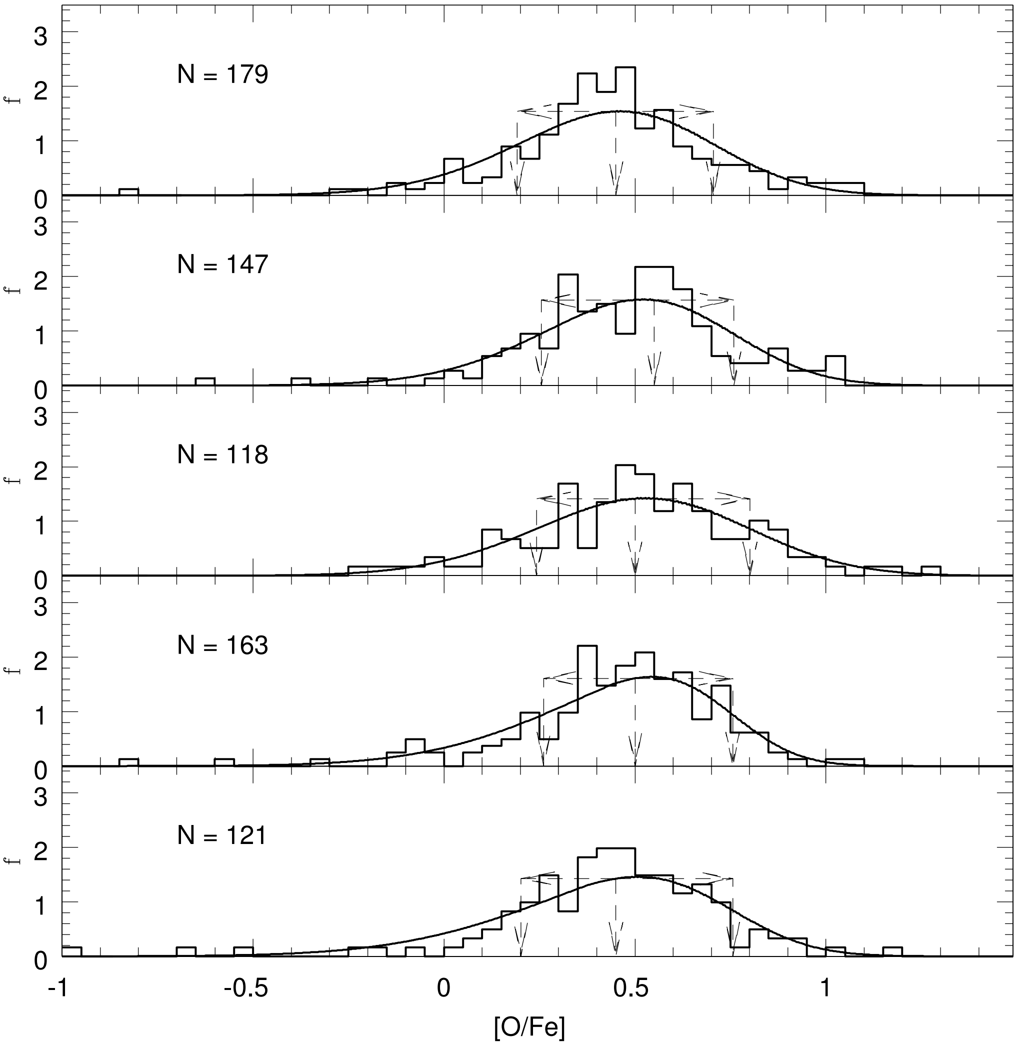

Figure C.1: Halo stellar particle [O/Fe] distribution for the $M_{tot} = 10^{11}$ $M_{\odot}$ semi–cosmological simulations in Renda et al. (2005b). The 68% Confidence Level range and the number of stellar particles each distribution refers to are also shown.

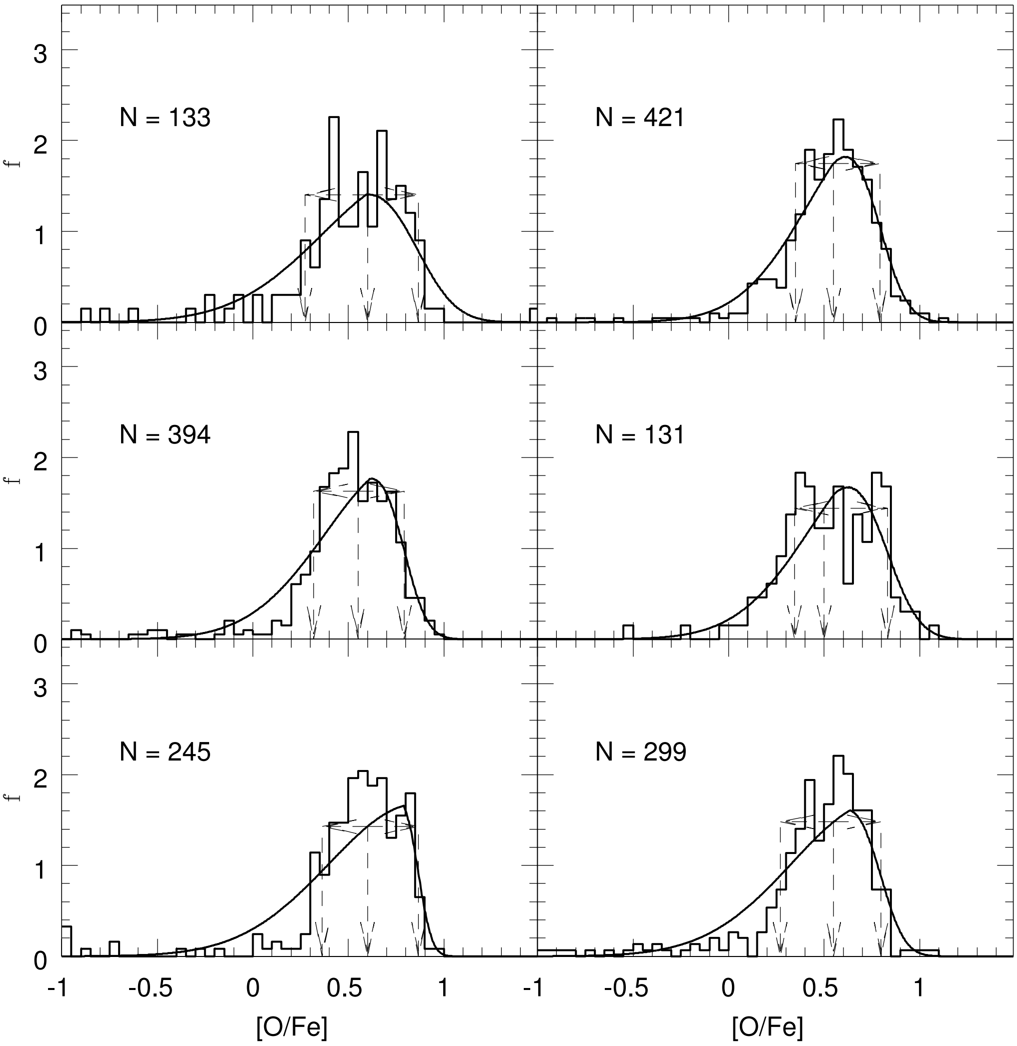

Figure C.2: Halo stellar particle [O/Fe] distribution for the $M_{tot} = 5 \times 10^{11}$ $M_\odot$ semi–cosmological simulations in Renda et al. (2005b). The 68% Confidence Level range and the number of stellar particles each distribution refers to are also shown.

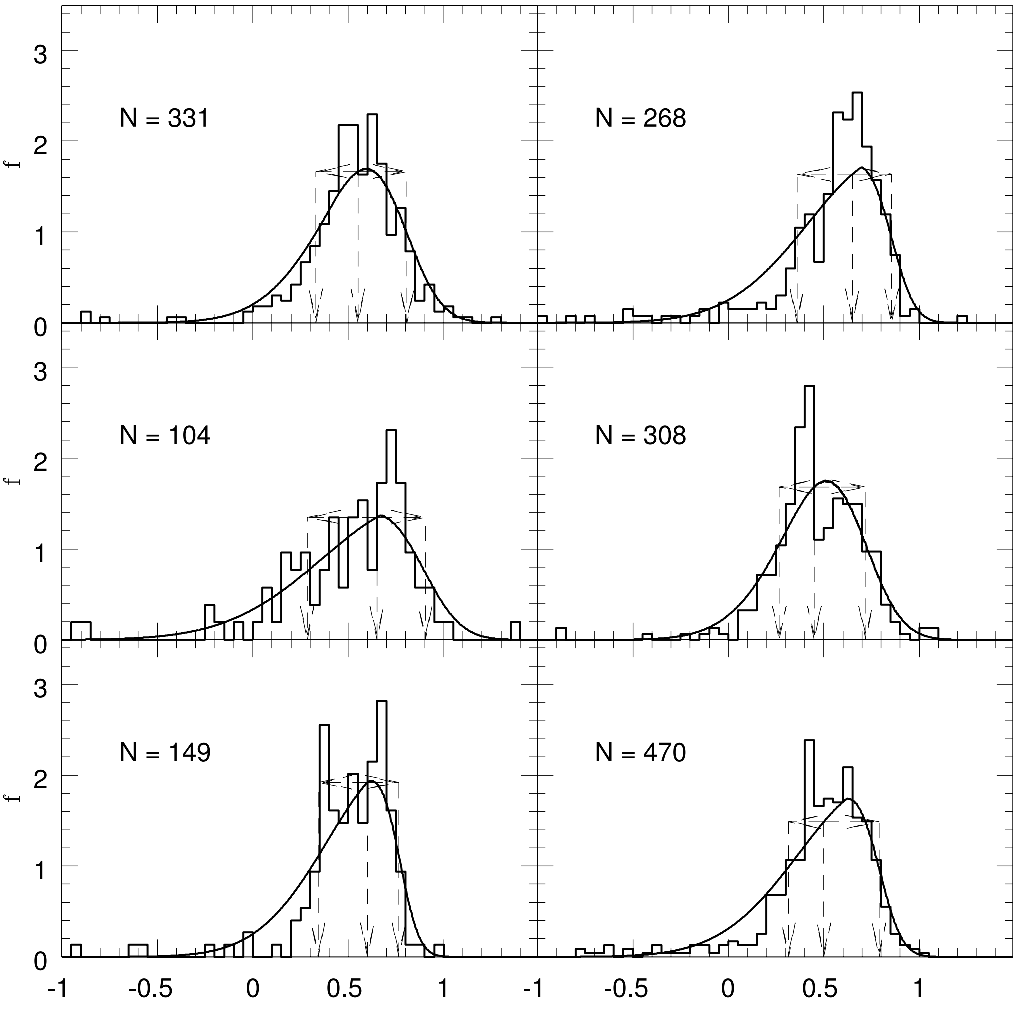

Figure C.3: (continued) Halo stellar particle [O/Fe] distribution for the $M_{tot} = 5\times10^{11}\ M_{\odot}$ semi–cosmological simulations in Renda et al. (2005b). The 68% Confidence Level range and the number of stellar particles each distribution refers to are also shown.

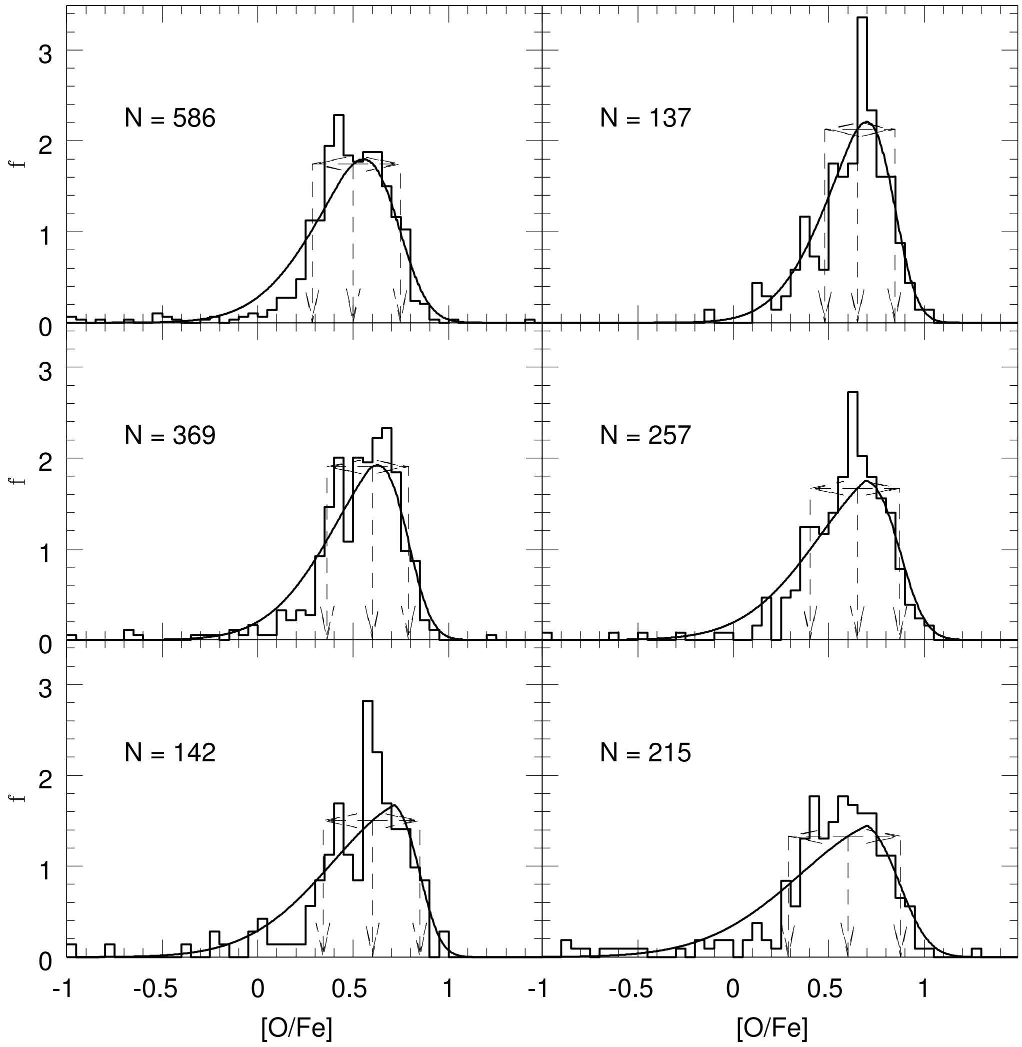

Figure C.4: (continued) Halo stellar particle [O/Fe] distribution for the $M_{tot} = 5{\times}10^{11}\ M_{\odot}$ semi–cosmological simulations in Renda et al. (2005b). The 68% Confidence Level range and the number of stellar particles each distribution refers to are also shown.

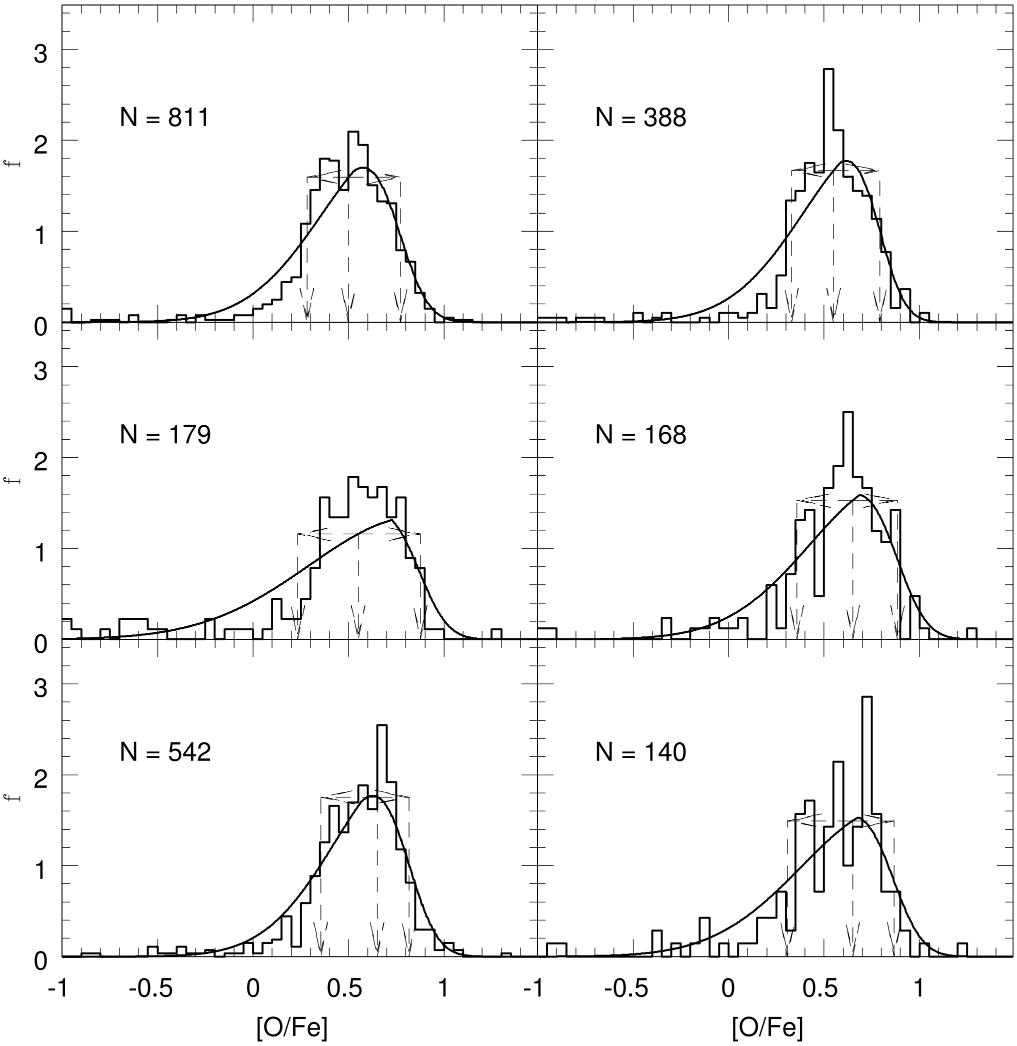

Figure C.5: (continued) Halo stellar particle [O/Fe] distribution for the $M_{tot} = 5 \times 10^{11}$ $M_{\odot}$ semi–cosmological simulations in Renda et al. (2005b). The 68% Confidence Level range and the number of stellar particles each distribution refers to are also shown.

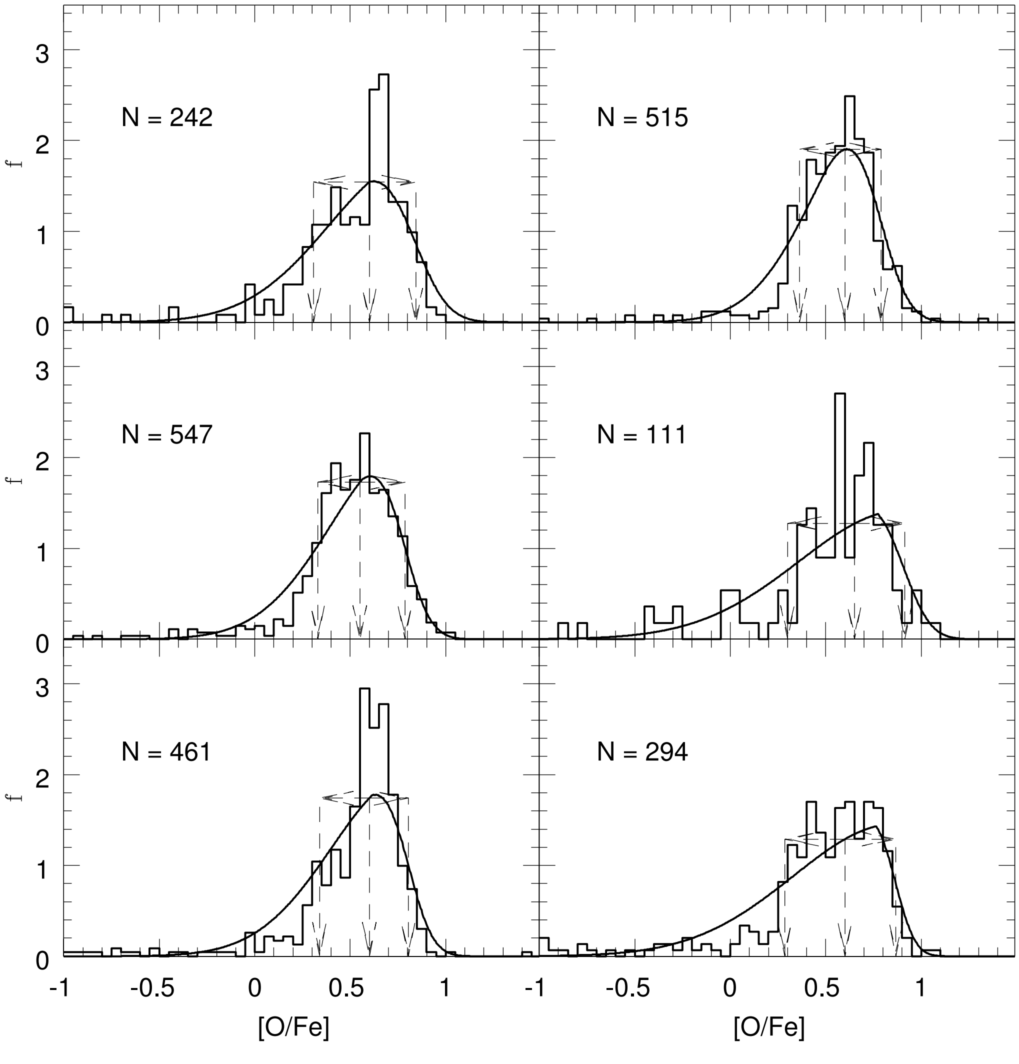

Figure C.6: Halo stellar particle [O/Fe] distribution for the $M_{tot} = 1\times10^{12}$ $M_\odot$ semi–cosmological simulations in Renda et al. (2005b). The 68% Confidence Level range and the number of stellar particles each distribution refers to are also shown.

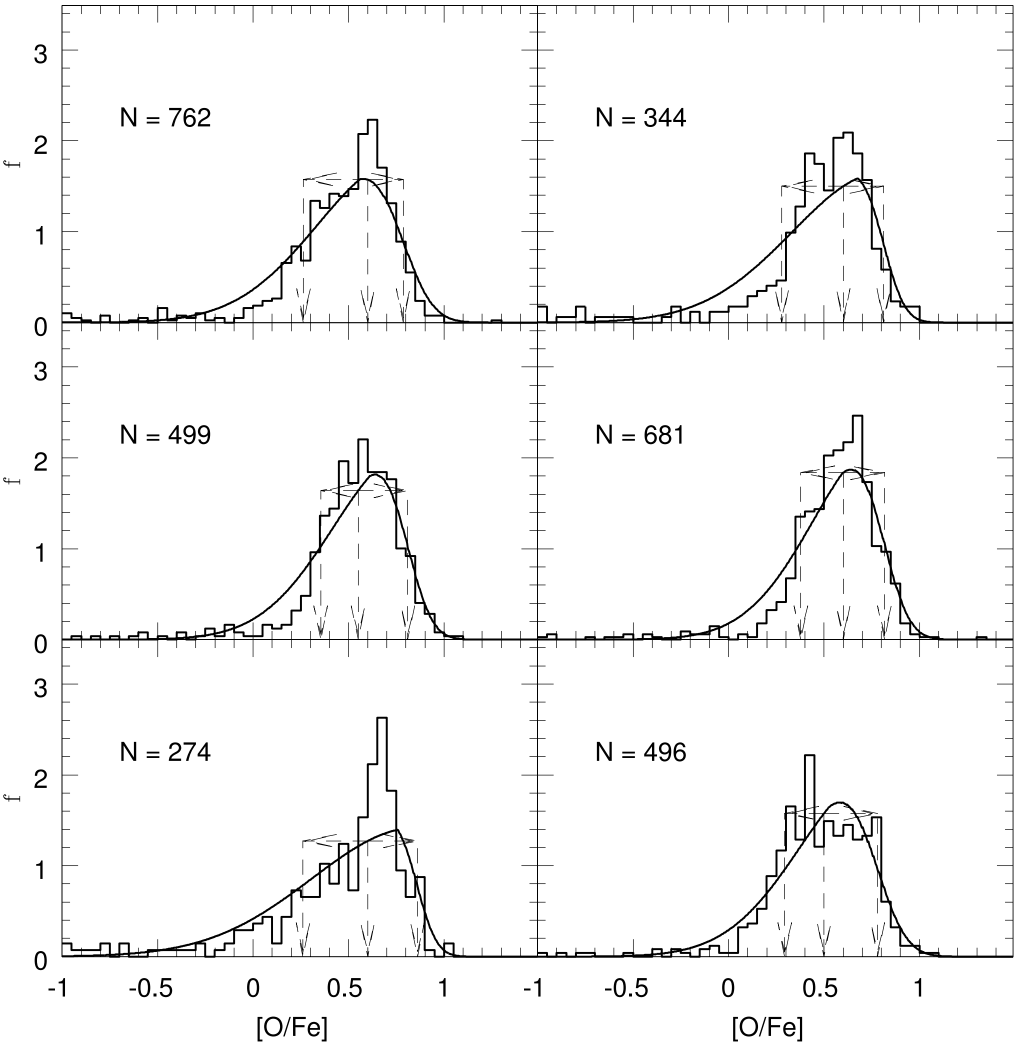

Figure C.7: (continued) Halo stellar particle [O/Fe] distribution for the $M_{tot} = 10^{12}$ $M_{\odot}$ semi–cosmological simulations in Renda et al. (2005b). The 68% Confidence Level range and the number of stellar particles each distribution refers to are also shown.

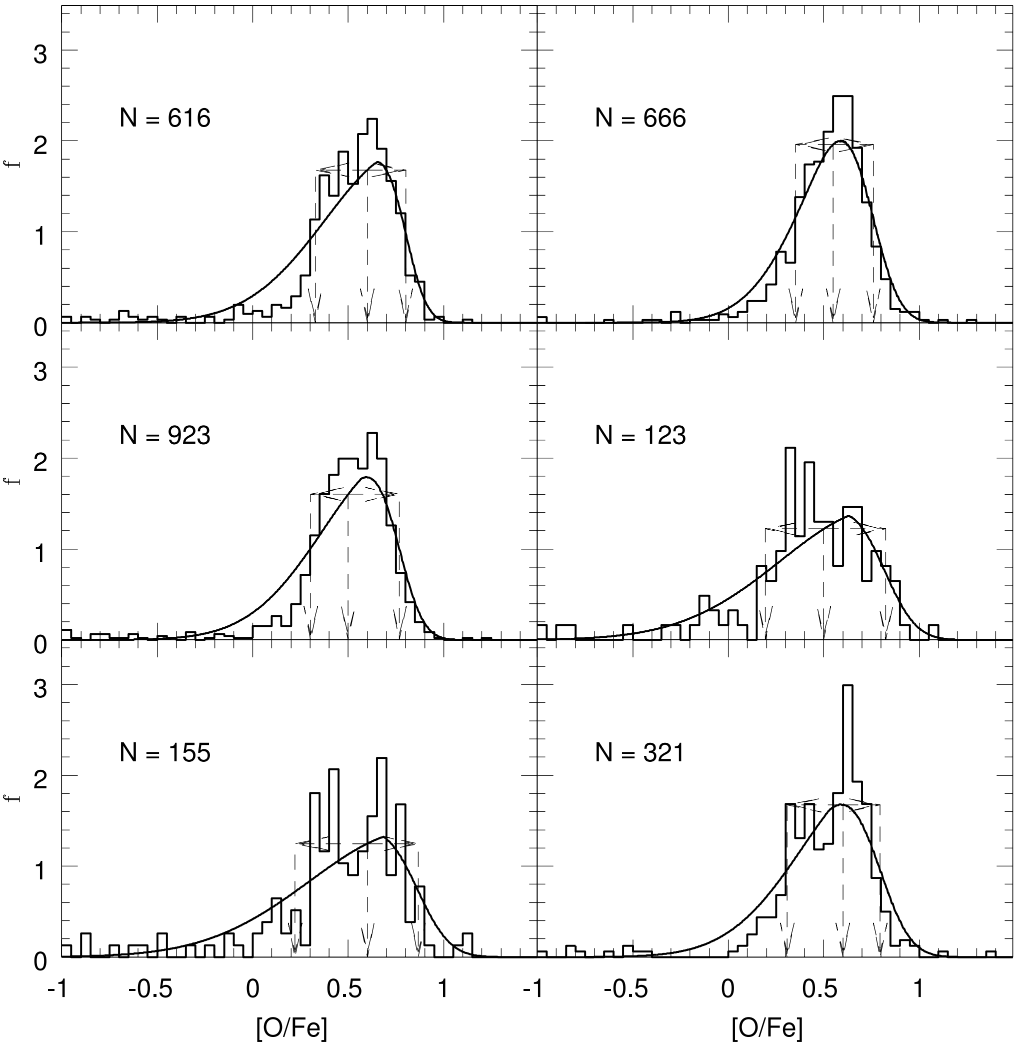

Figure C.8: (continued) Halo stellar particle [O/Fe] distribution for the $M_{tot} = 10^{12}$ $M_{\odot}$ semi–cosmological simulations in Renda et al. (2005b). The 68% Confidence Level range and the number of stellar particles each distribution refers to are also shown.

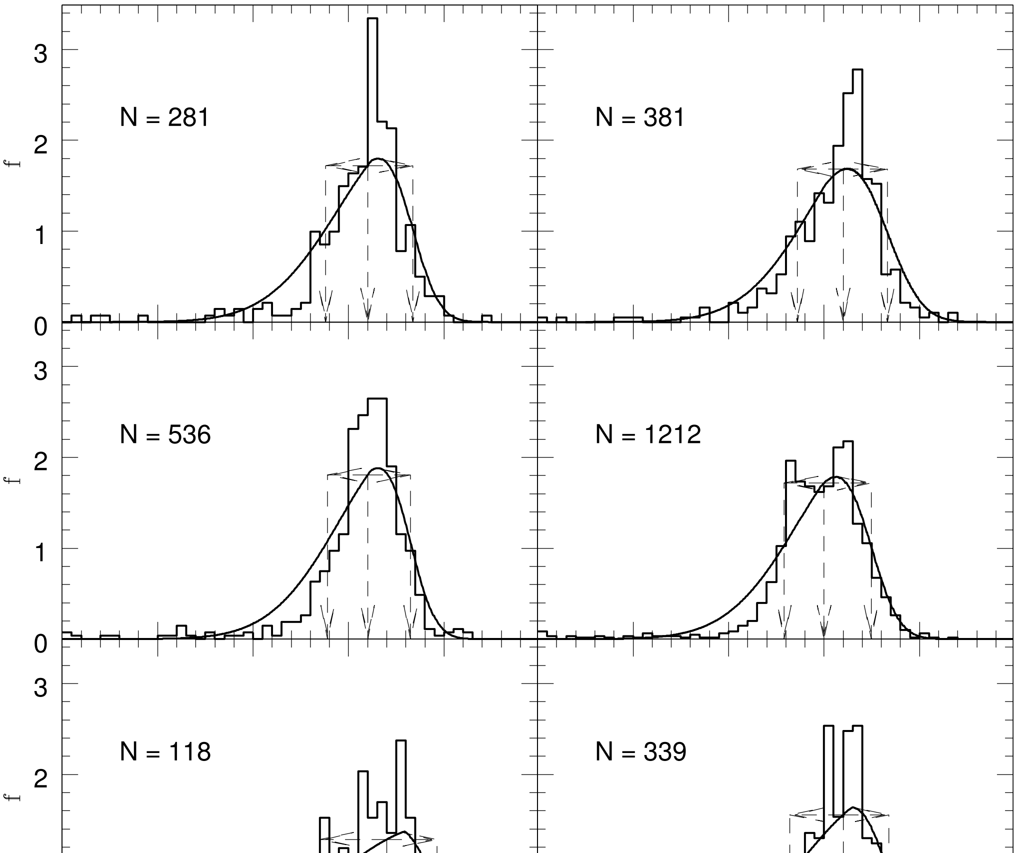

Figure C.9: (continued) Halo stellar particle [O/Fe] distribution for the $M_{tot} = 10^{12}\ M_{\odot}$ semi–cosmological simulations in Renda et al. (2005b). The 68% Confidence Level range and the number of stellar particles each distribution refers to are also shown.

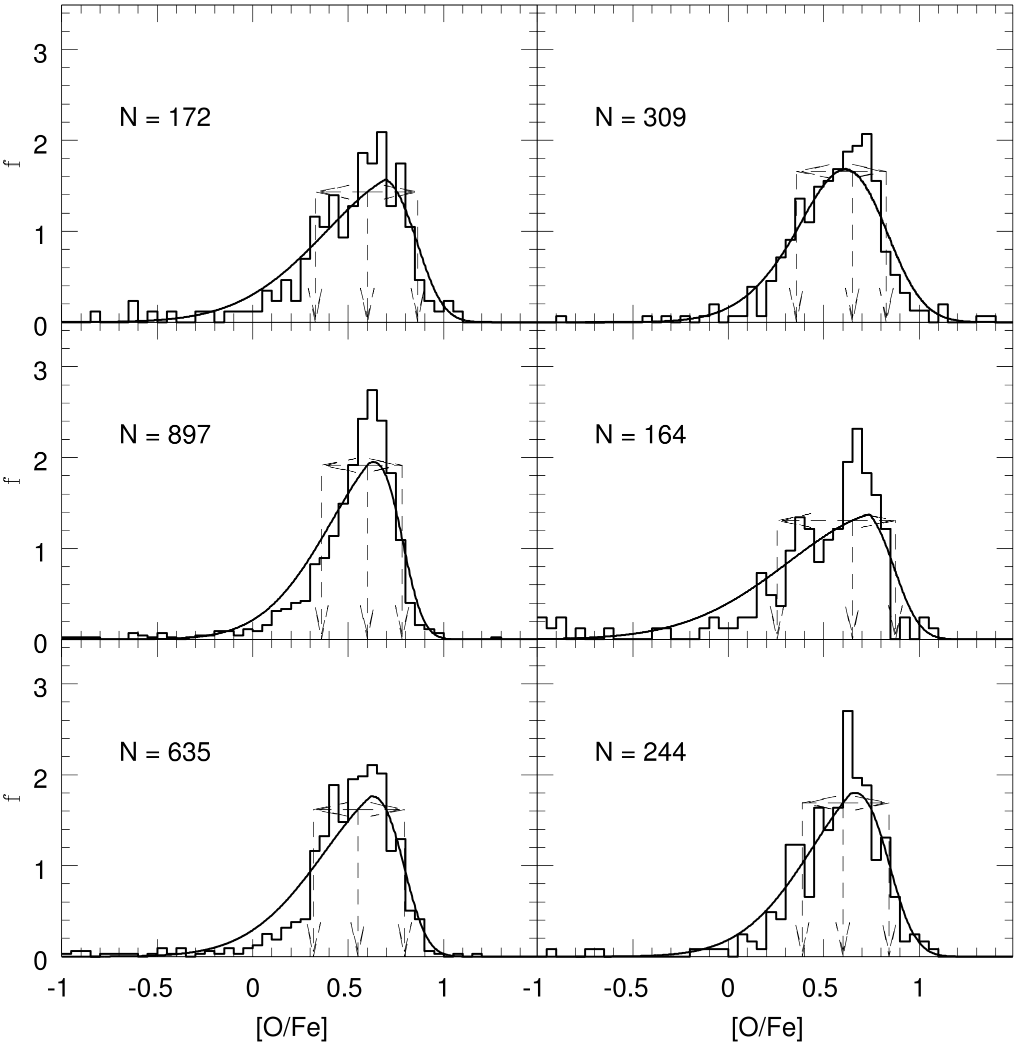

Figure C.10: (continued) Halo stellar particle [O/Fe] distribution for the $M_{tot} = 10^{12} M_\odot$ semi–cosmological simulations in Renda et al. (2005b). The 68% Confidence Level range and the number of stellar particles each distribution refers to are also shown.

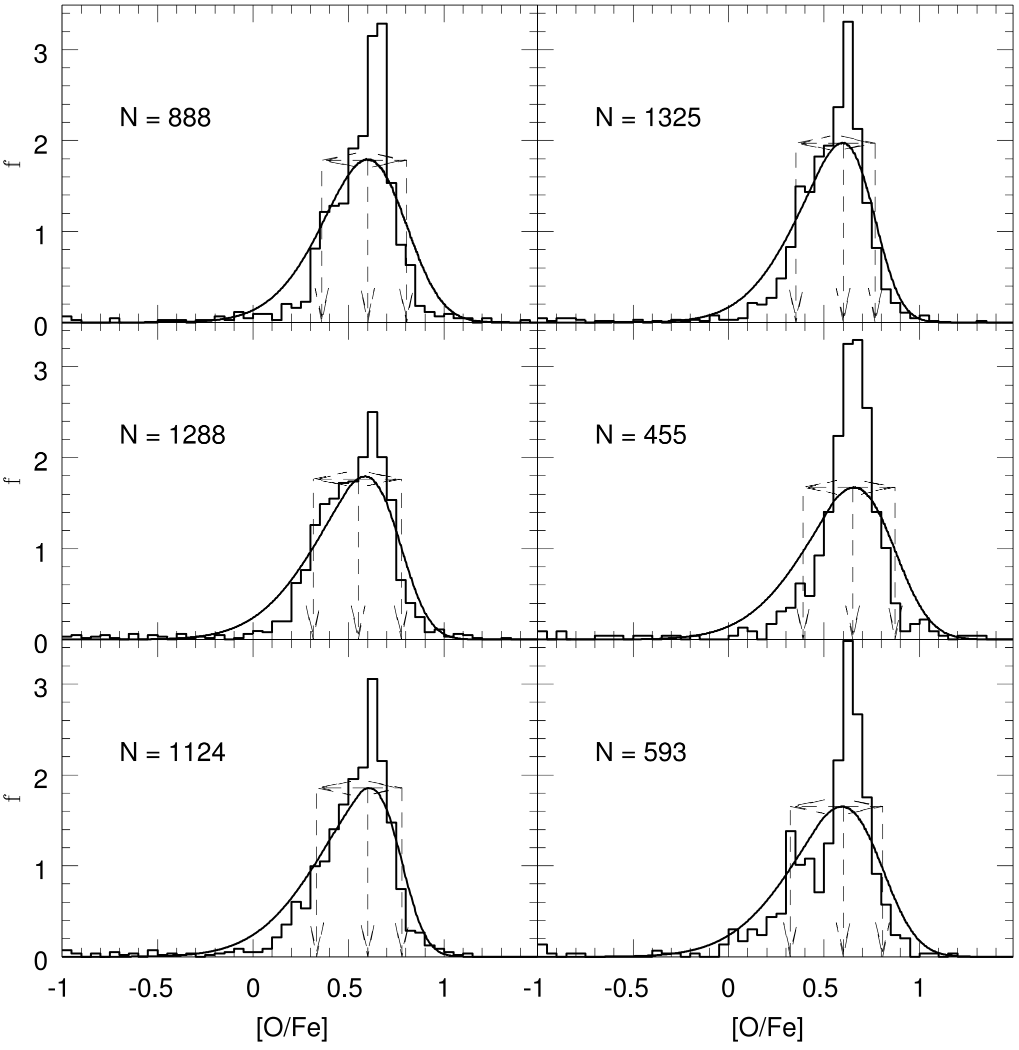

Figure C.11: Halo stellar particle [O/Fe] distribution for the $M_{tot} = 5 \times 10^{12}\ M_{\odot}$ semi–cosmological simulations in Renda et al. (2005b). The 68% Confidence Level range and the number of stellar particles each distribution refers to are also shown.

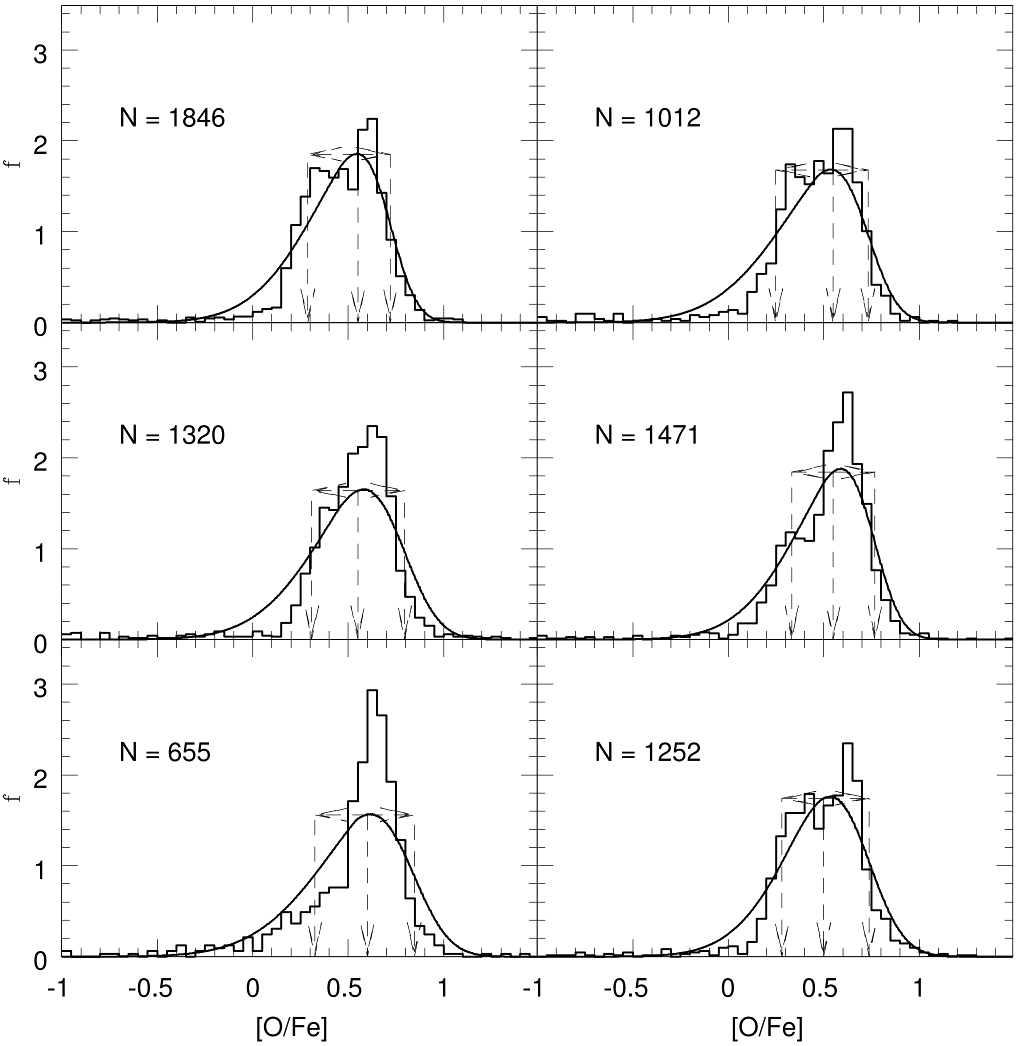

Figure C.12: (continued) Halo stellar particle [O/Fe] distribution for the $M_{tot} = 5\times10^{12}\ M_{\odot}$ semi–cosmological simulations in Renda et al. (2005b). The 68% Confidence Level range and the number of stellar particles each distribution refers to are also shown.

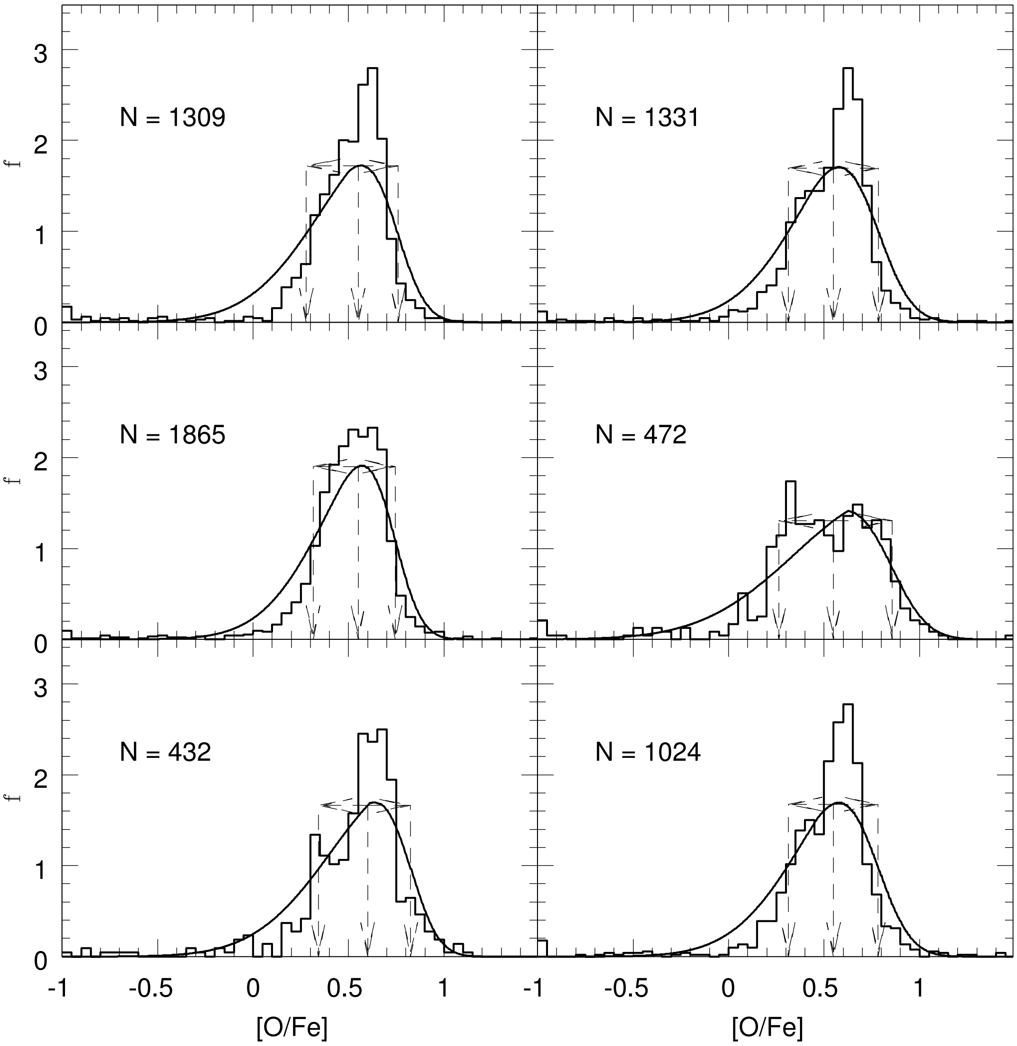

Figure C.13: (continued) Halo stellar particle [O/Fe] distribution for the $M_{tot} = 5\times10^{12}$ $M_\odot$ semi–cosmological simulations in Renda et al. (2005b). The 68% Confidence Level range and the number of stellar particles each distribution refers to are also shown.

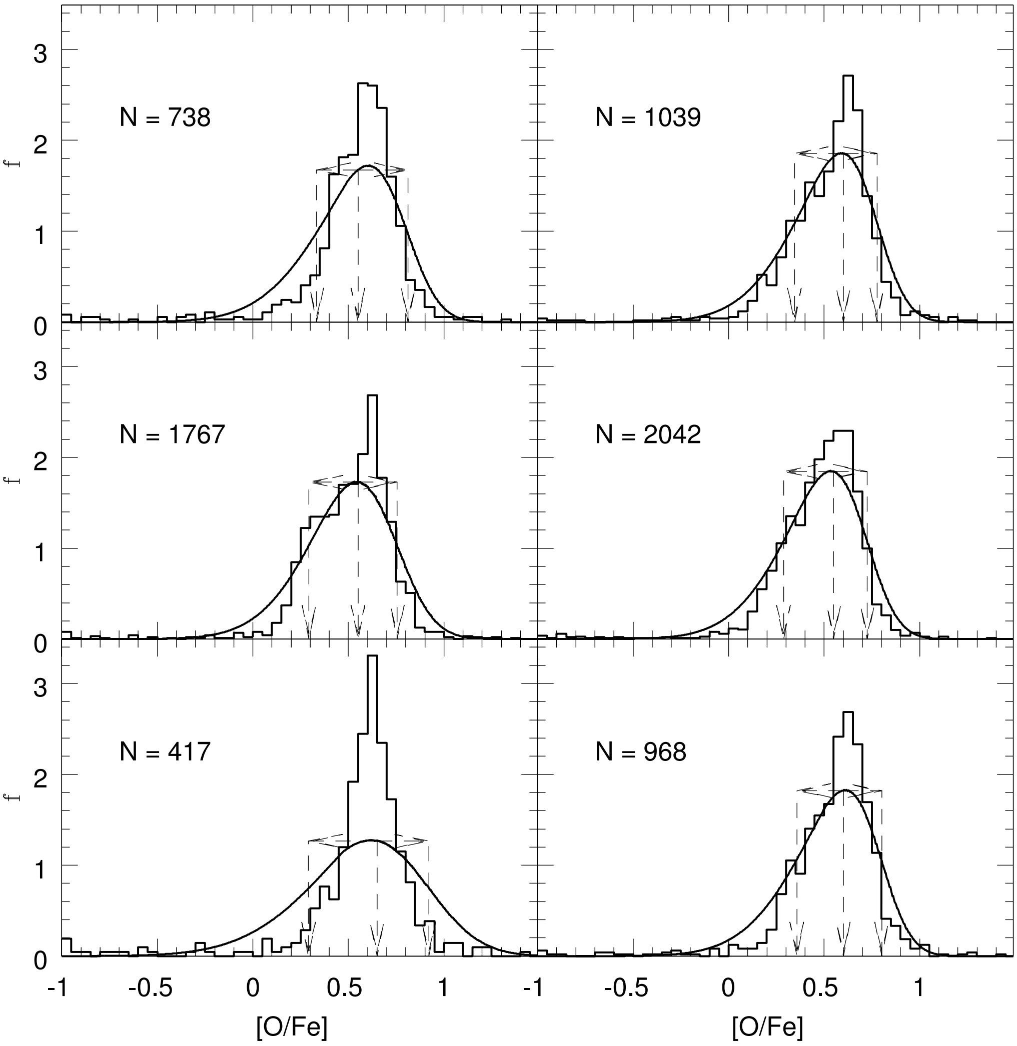

Figure C.14: (continued) Halo stellar particle [O/Fe] distribution for the $M_{tot} = 5 \times 10^{12}$ $M_\odot$ semi–cosmological simulations in Renda et al. (2005b). The 68% Confidence Level range and the number of stellar particles each distribution refers to are also shown.

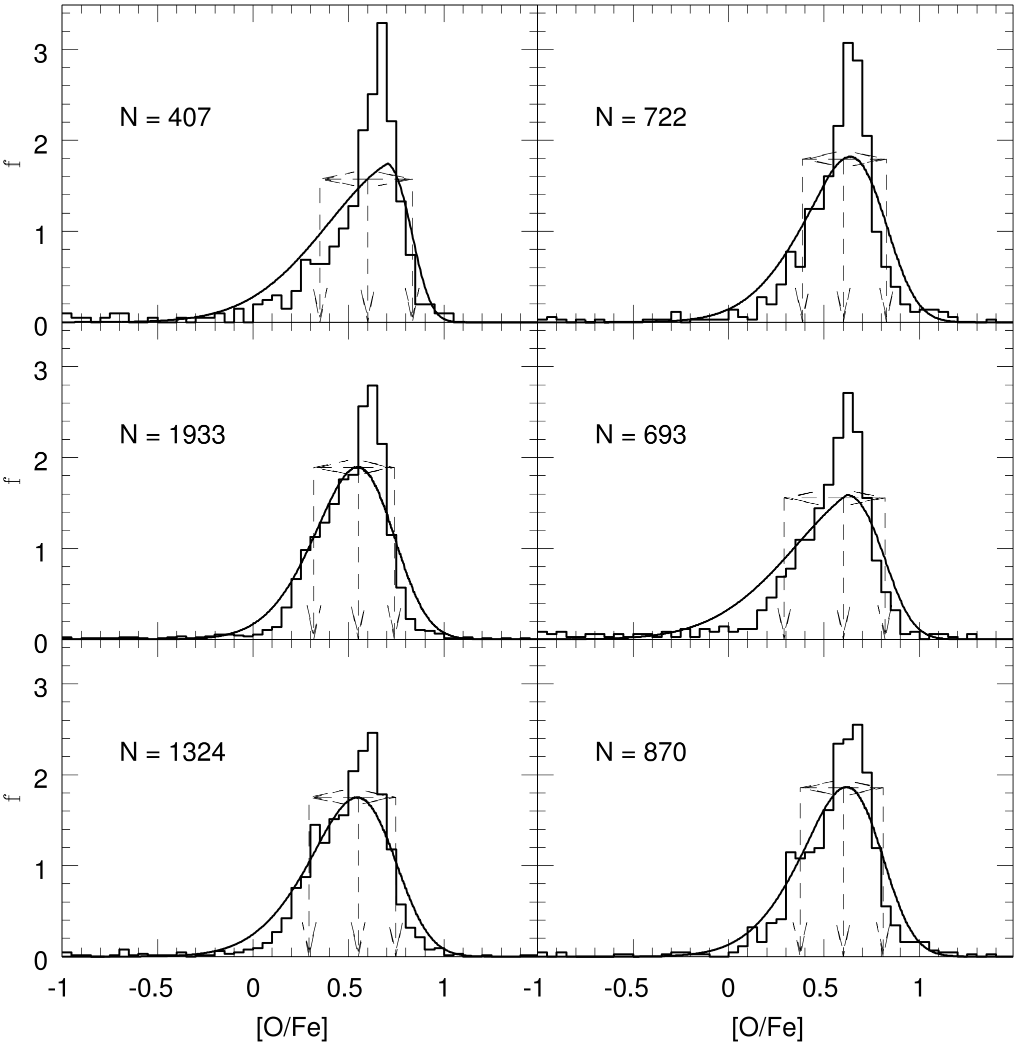

Figure C.15: (continued) Halo stellar particle [O/Fe] distribution for the $M_{tot} = 5{\times}10^{12}$ $M_\odot$ semi–cosmological simulations in Renda et al. (2005b). The 68% Confidence Level range and the number of stellar particles each distribution refers to are also shown.

Appendix D

Stellar Halo Age Distributions

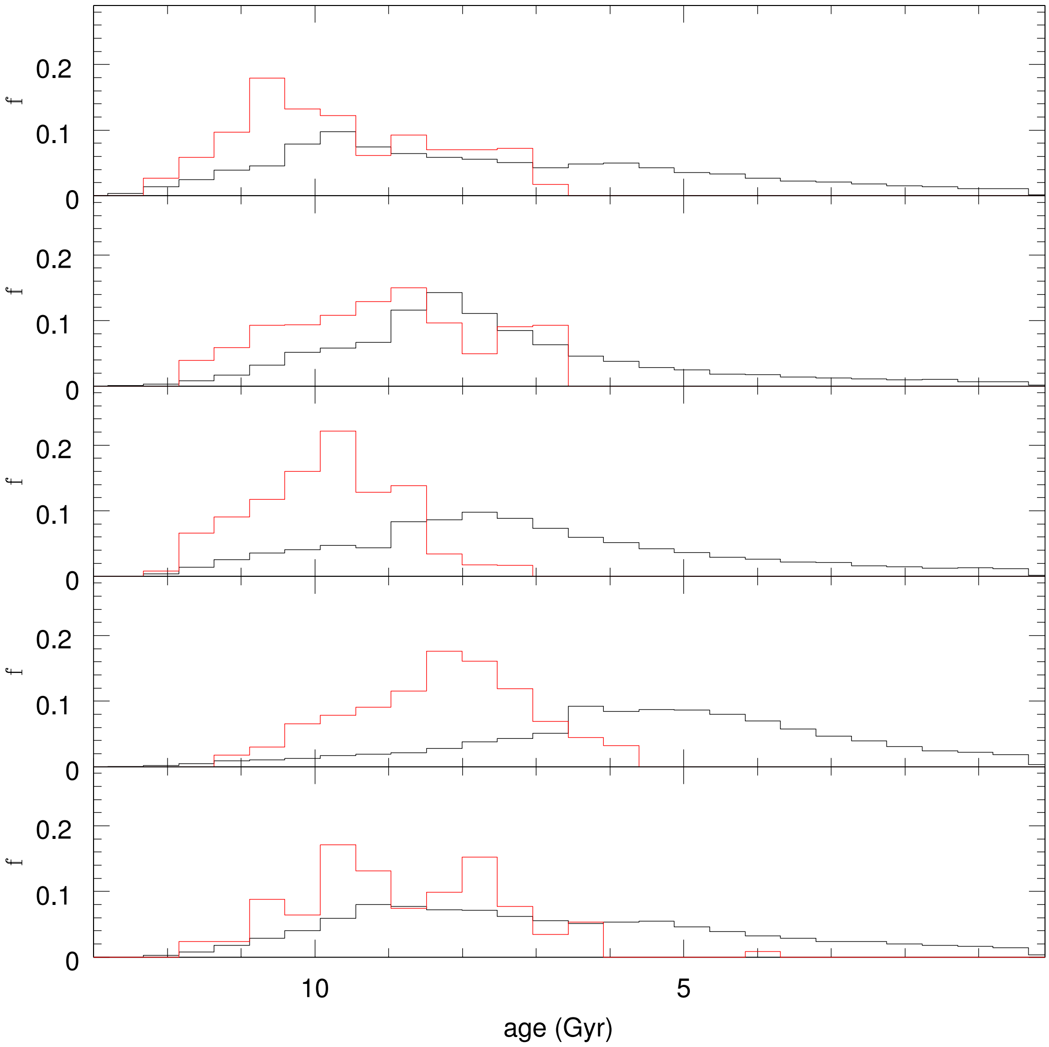

Figure D.1: Halo (red) and galaxy (black) age distributions for the $M_{tot} = 10^{11}$ $M_{\odot}$ semi–cosmological simulations in Renda et al. (2005b).

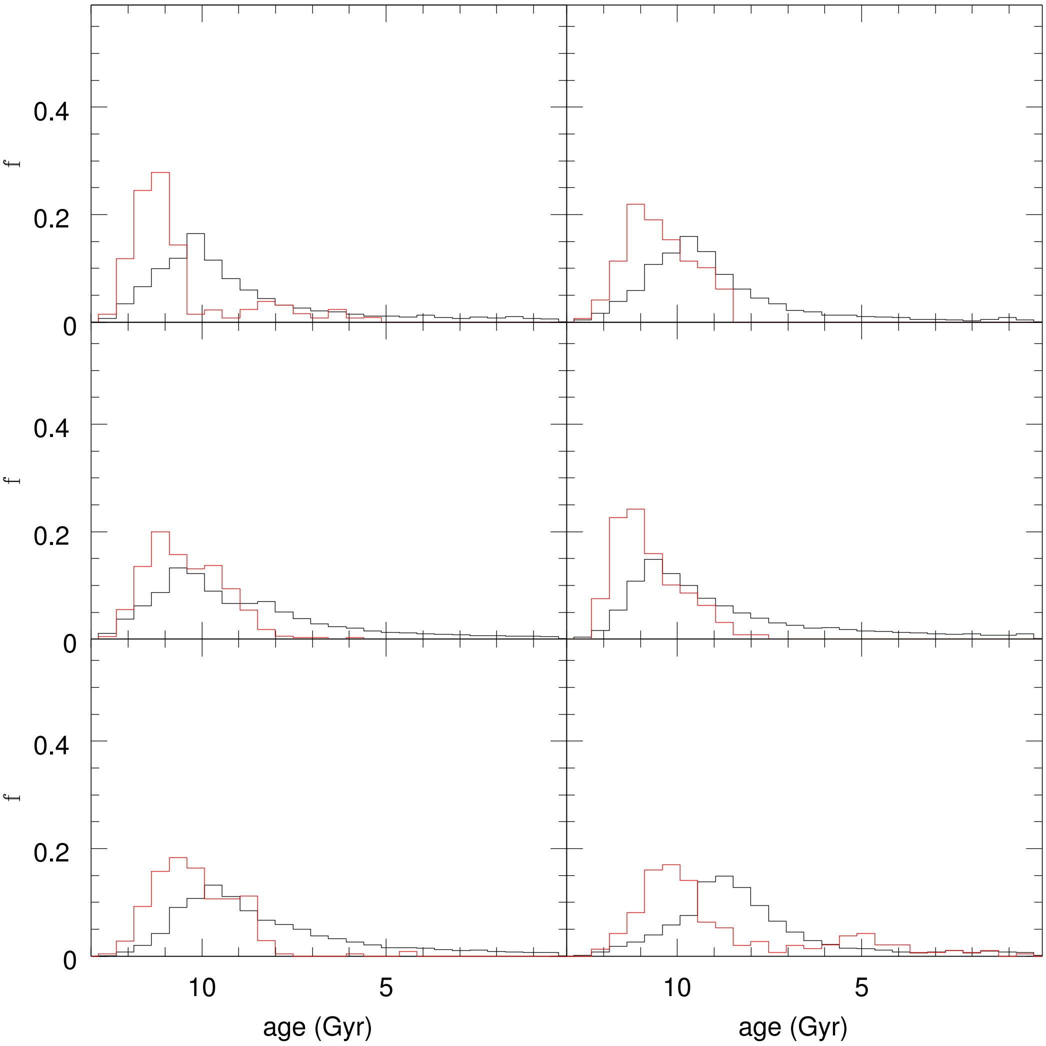

Figure D.2: Halo (red) and galaxy (black) age distributions for the $M_{tot} = 5\times10^{11}$ $M_\odot$ semi–cosmological simulations in Renda et al. (2005b).

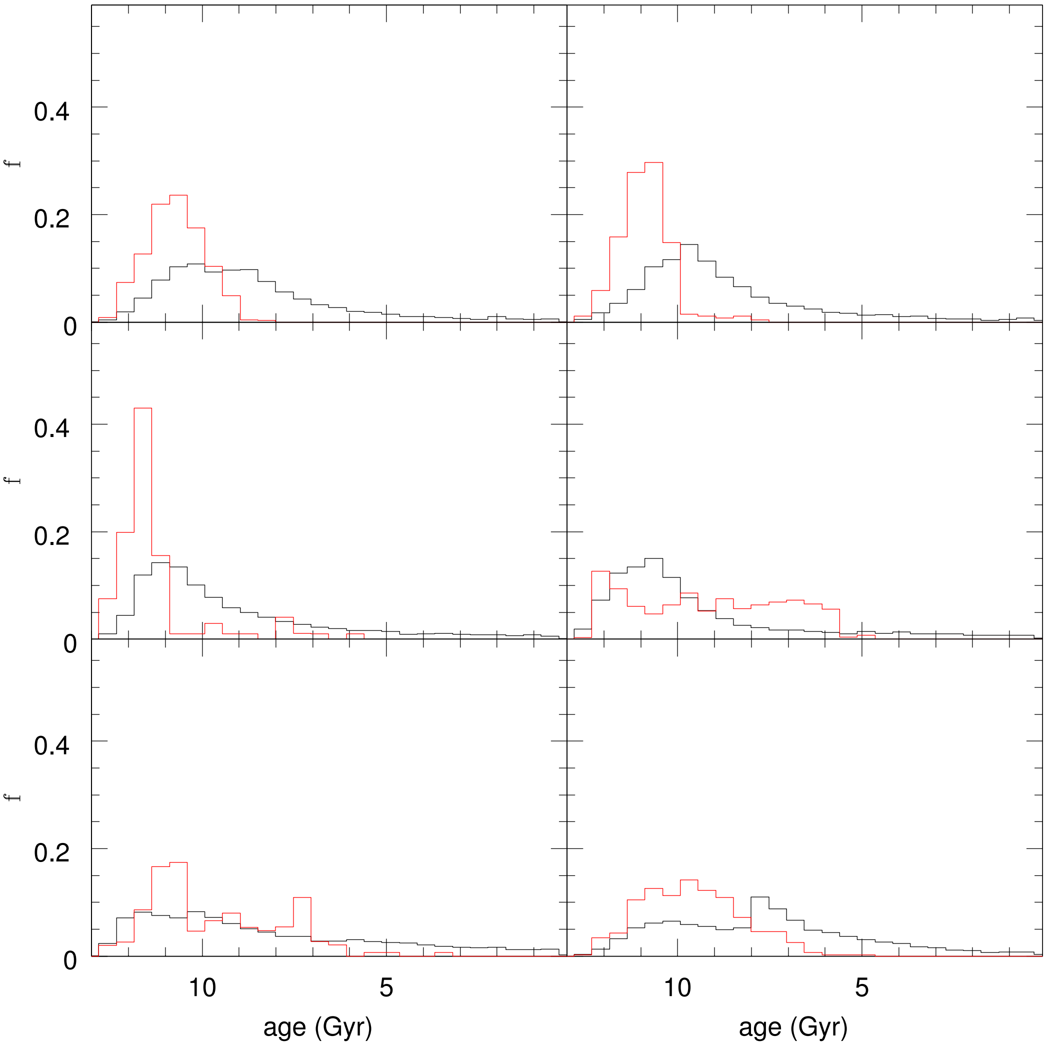

Figure D.3: (continued) Halo (red) and galaxy (black) age distributions for the $M_{tot} = 5\times10^{11}$ $M_\odot$ semi–cosmological simulations in Renda et al. (2005b).

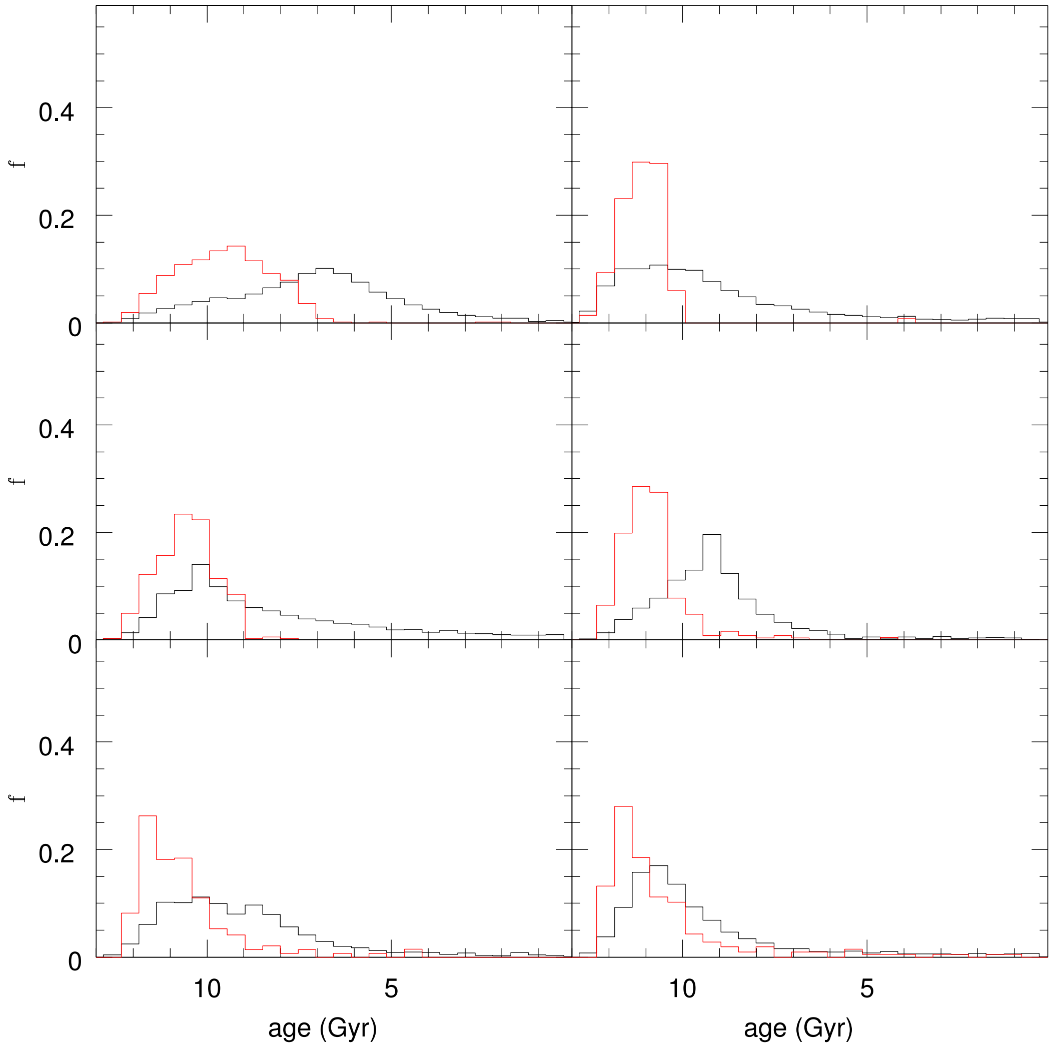

Figure D.4: (continued) Halo (red) and galaxy (black) age distributions for the $M_{tot} = 5\times10^{11}\ M_\odot$ semi–cosmological simulations in Renda et al. (2005b).

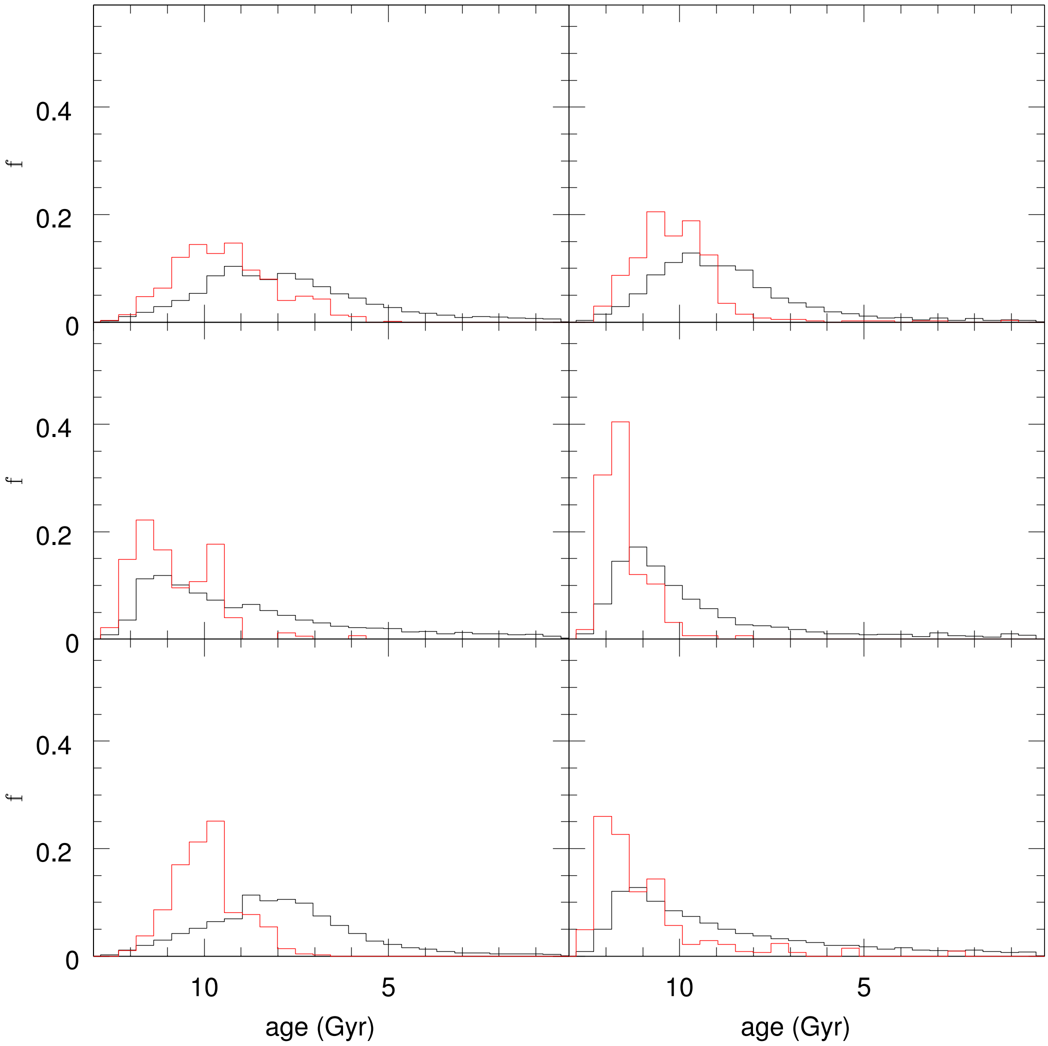

Figure D.5: (continued) Halo (red) and galaxy (black) age distributions for the $M_{tot} = 5{\times}10^{11}\ M_{\odot}$ semi–cosmological simulations in Renda et al. (2005b).

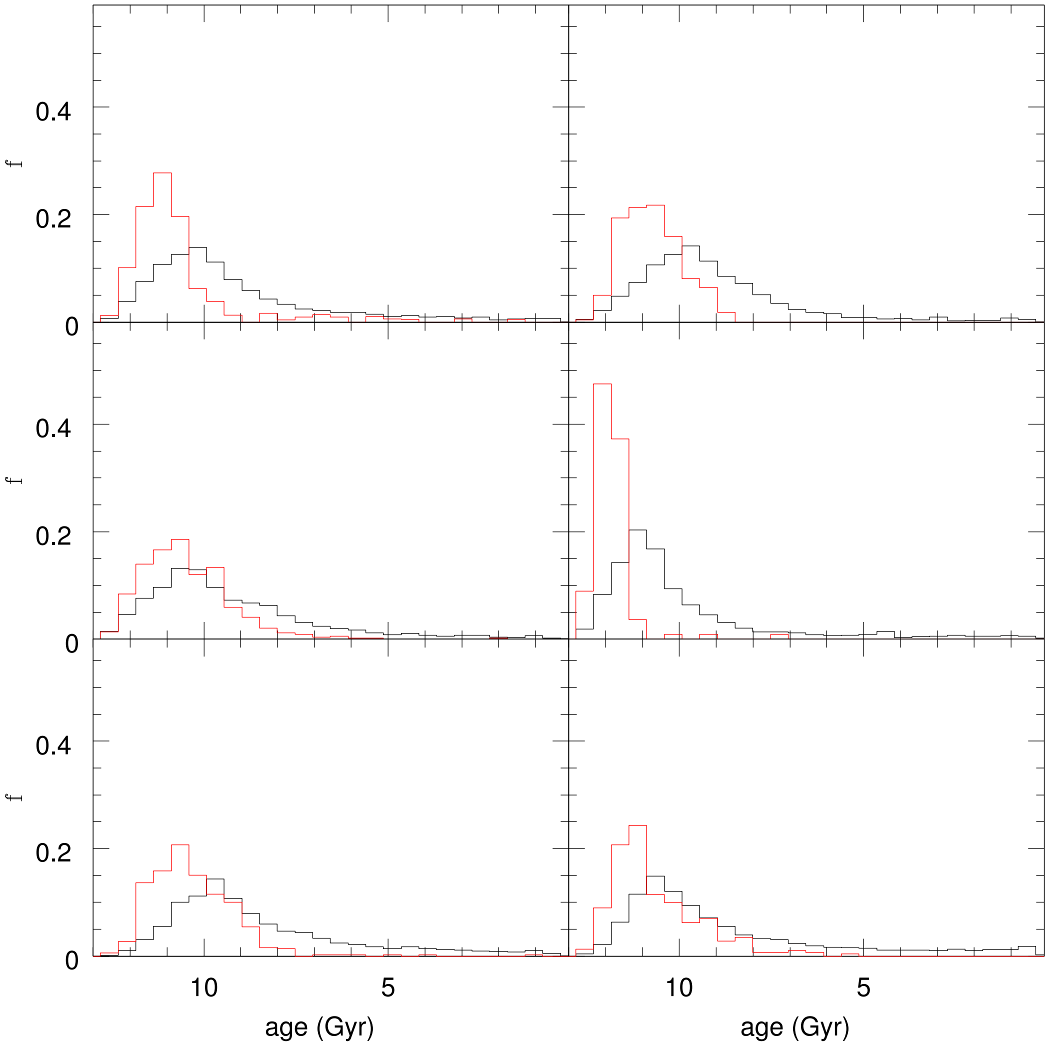

Figure D.6: Halo (red) and galaxy (black) age distributions for the $M_{tot} = 10^{12}\ M_\odot$ semi–cosmological simulations in Renda et al. (2005b).

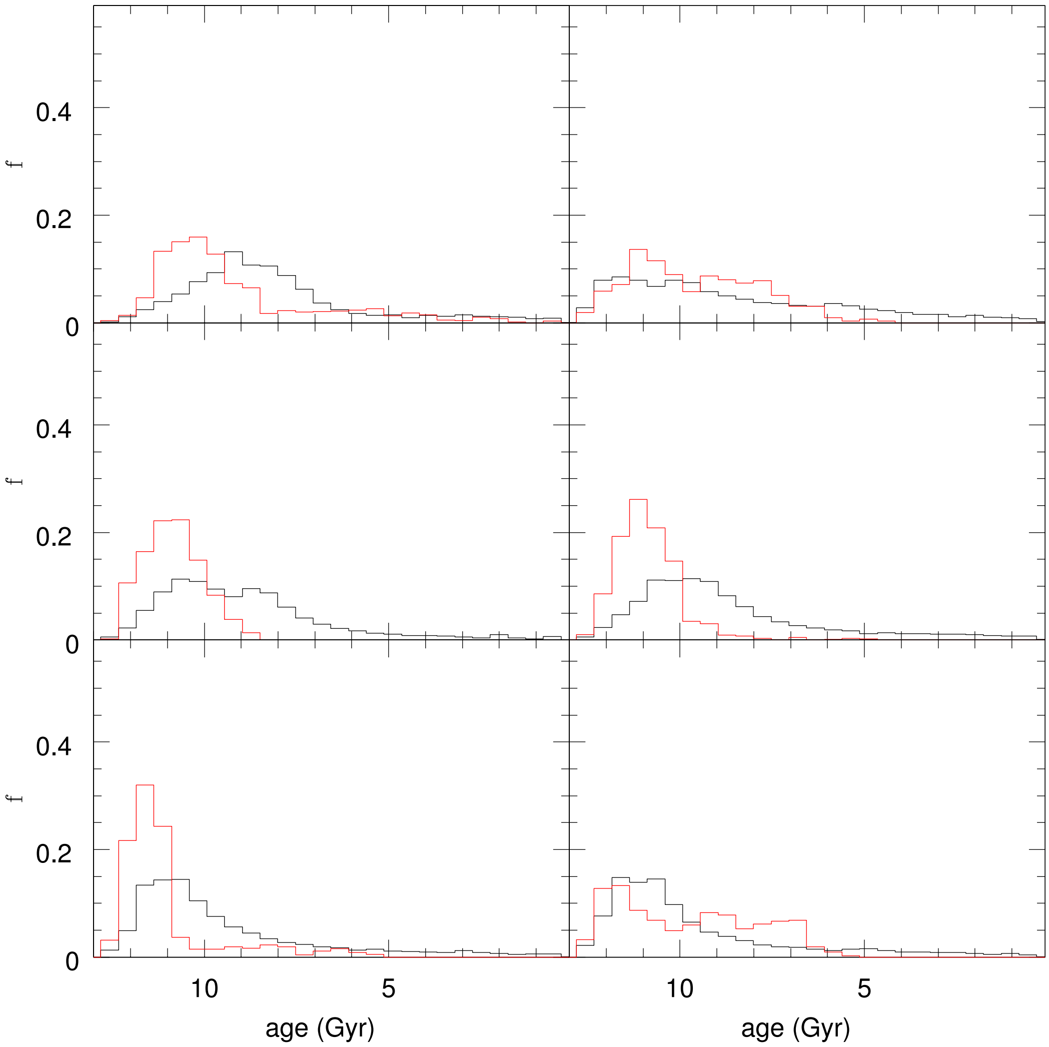

Figure D.7: (continued) Halo (red) and galaxy (black) age distributions for the $M_{tot} = 10^{12}$ $M_\odot$ semi–cosmological simulations in Renda et al. (2005b).

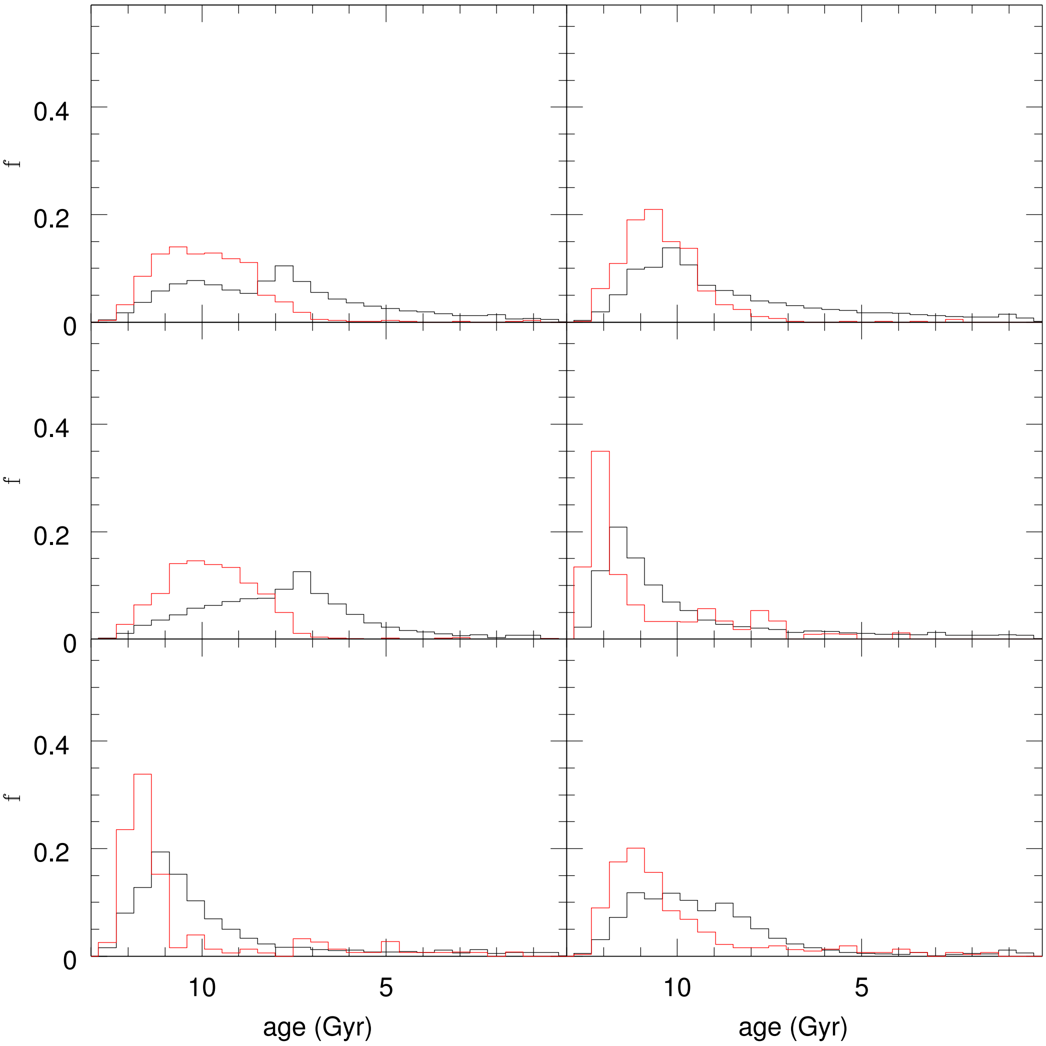

Figure D.8: (continued) Halo (red) and galaxy (black) age distributions for the $M_{tot} = 10^{12}\ M_\odot$ semi–cosmological simulations in Renda et al. (2005b).

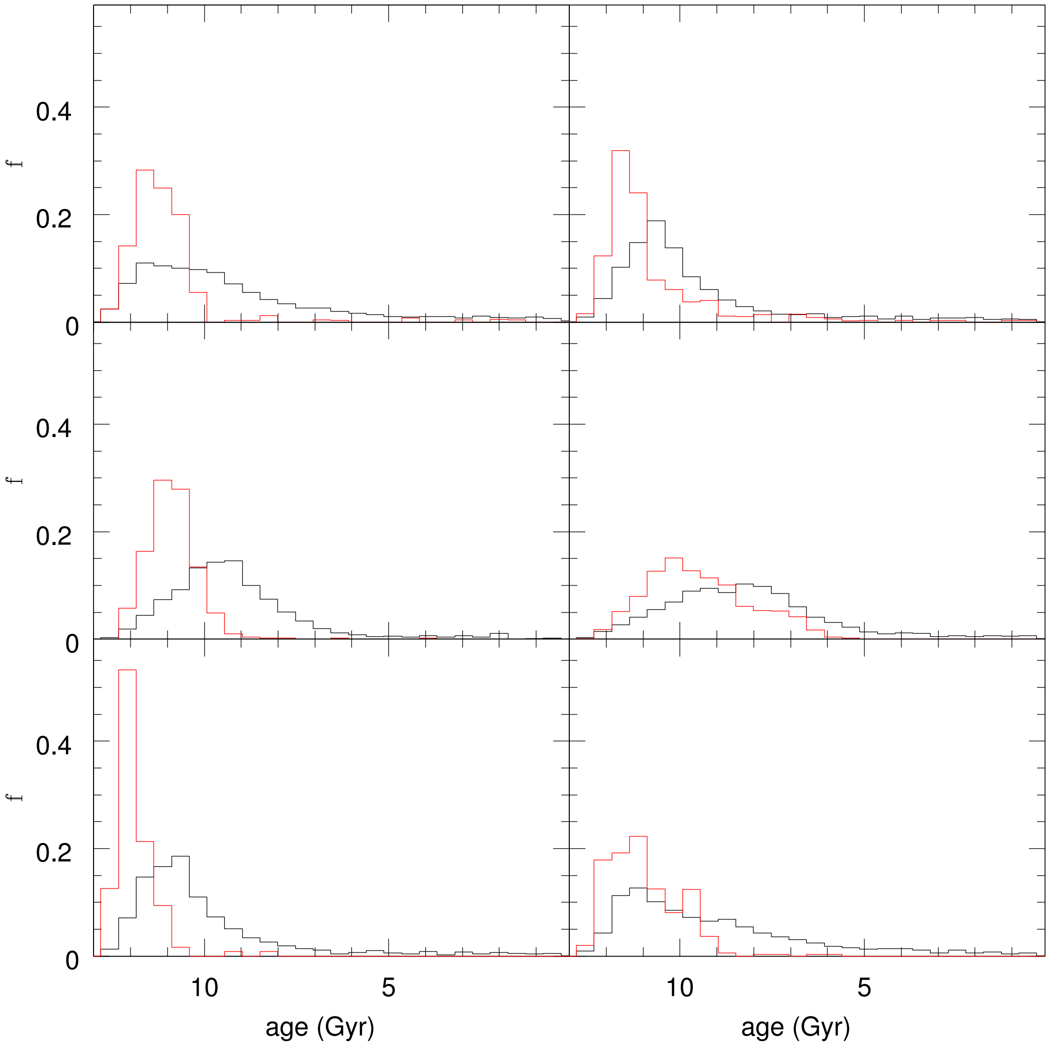

Figure D.9: (continued) Halo (red) and galaxy (black) age distributions for the $M_{tot} = 10^{12}\ M_{\odot}$ semi–cosmological simulations in Renda et al. (2005b).

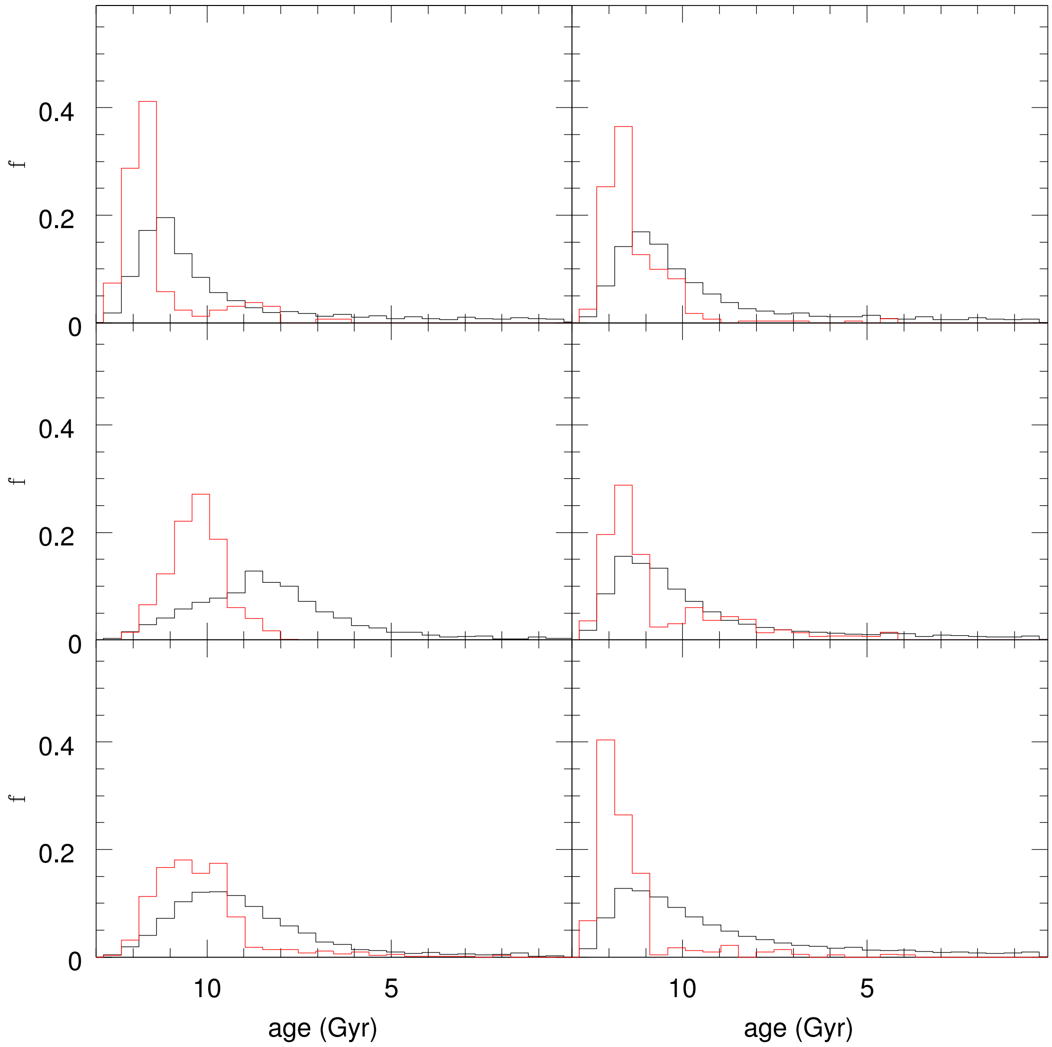

Figure D.10: (continued) Halo (red) and galaxy (black) age distributions for the $M_{tot} = 10^{12}$ $M_{\odot}$ semi–cosmological simulations in Renda et al. (2005b).

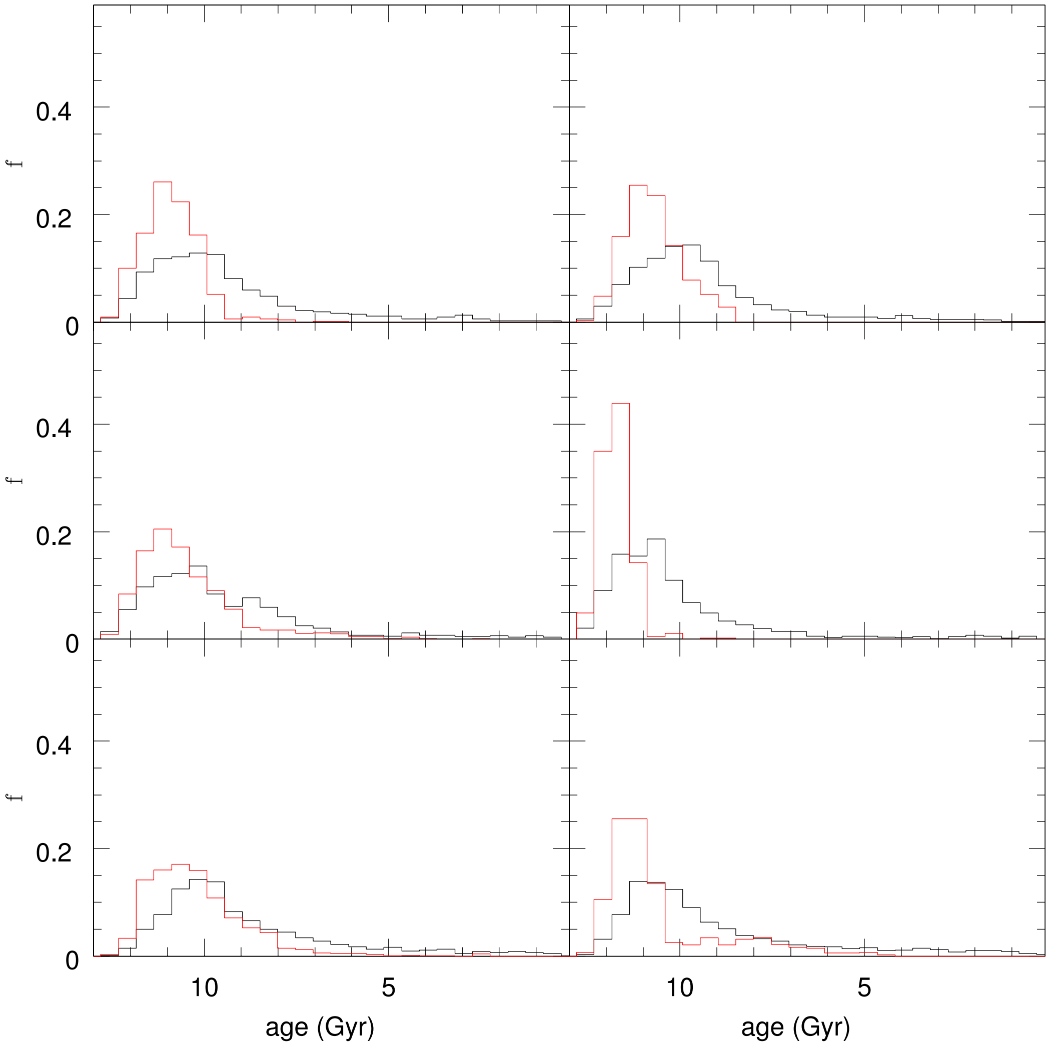

Figure D.11: Halo (red) and galaxy (black) age distributions for the $M_{tot} = 5\times10^{12}$ $M_\odot$ semi–cosmological simulations in Renda et al. (2005b).

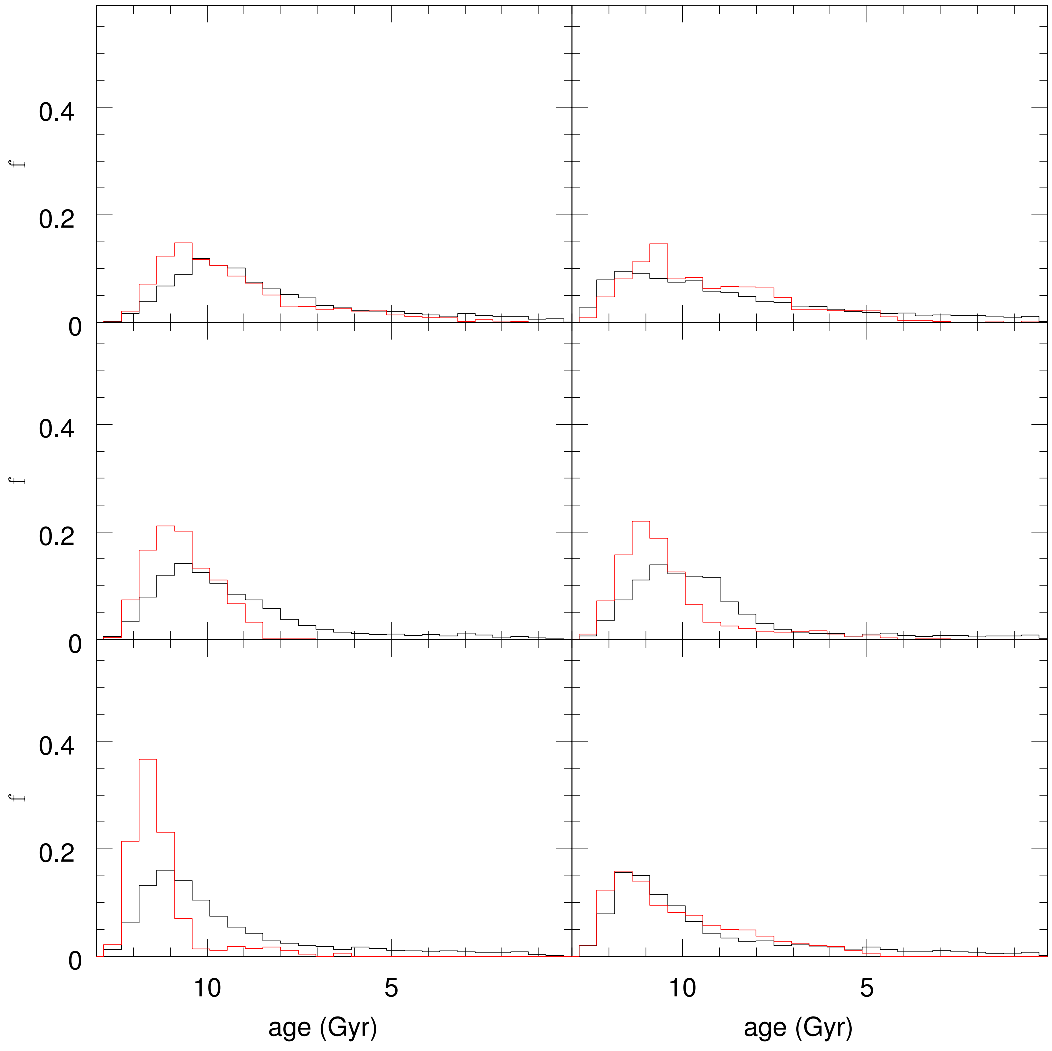

Figure D.12: (continued) Halo (red) and galaxy (black) age distributions for the $M_{tot} = 5 \times 10^{12}$ $M_{\odot}$ semi–cosmological simulations in Renda et al. (2005b).

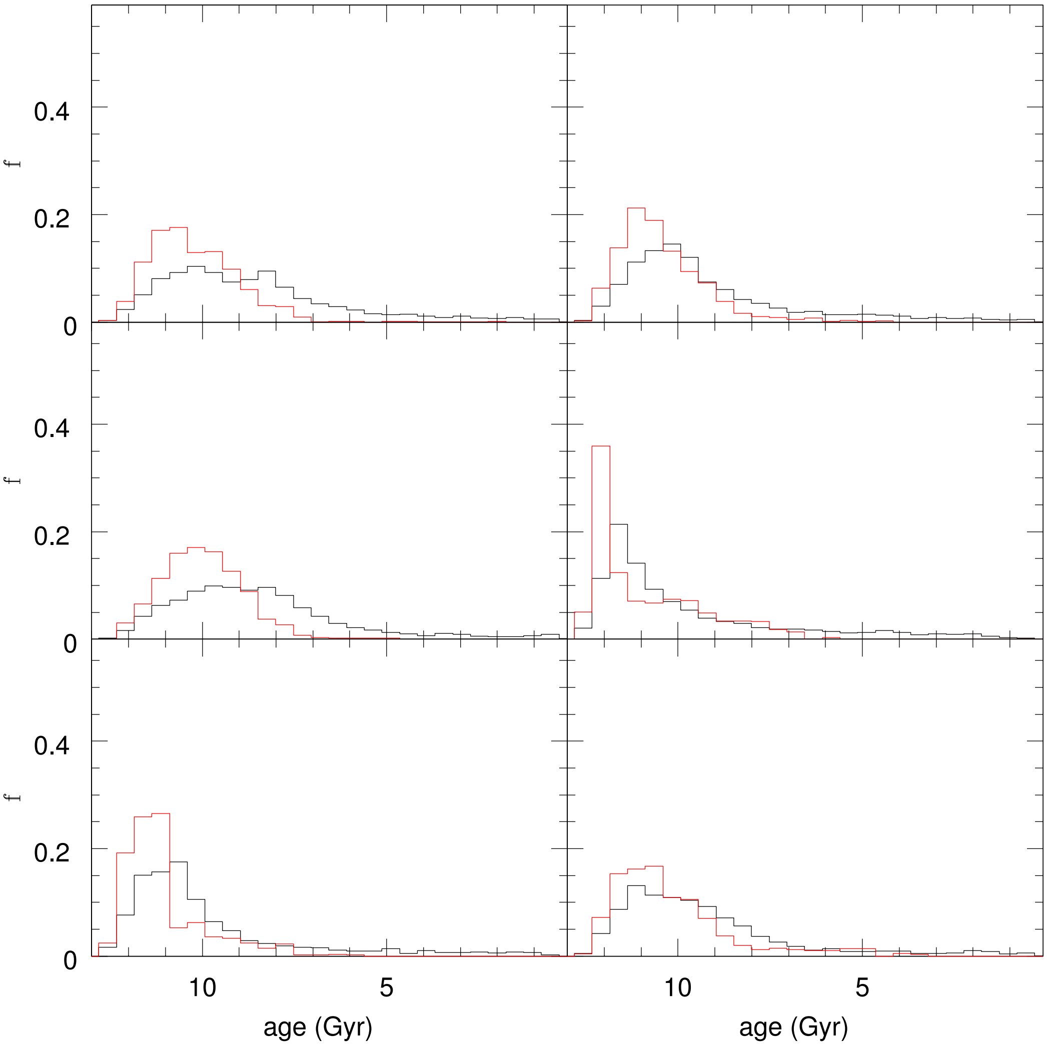

Figure D.13: (continued) Halo (red) and galaxy (black) age distributions for the $M_{tot} = 5\times10^{12}$ $M_{\odot}$ semi–cosmological simulations in Renda et al. (2005b).

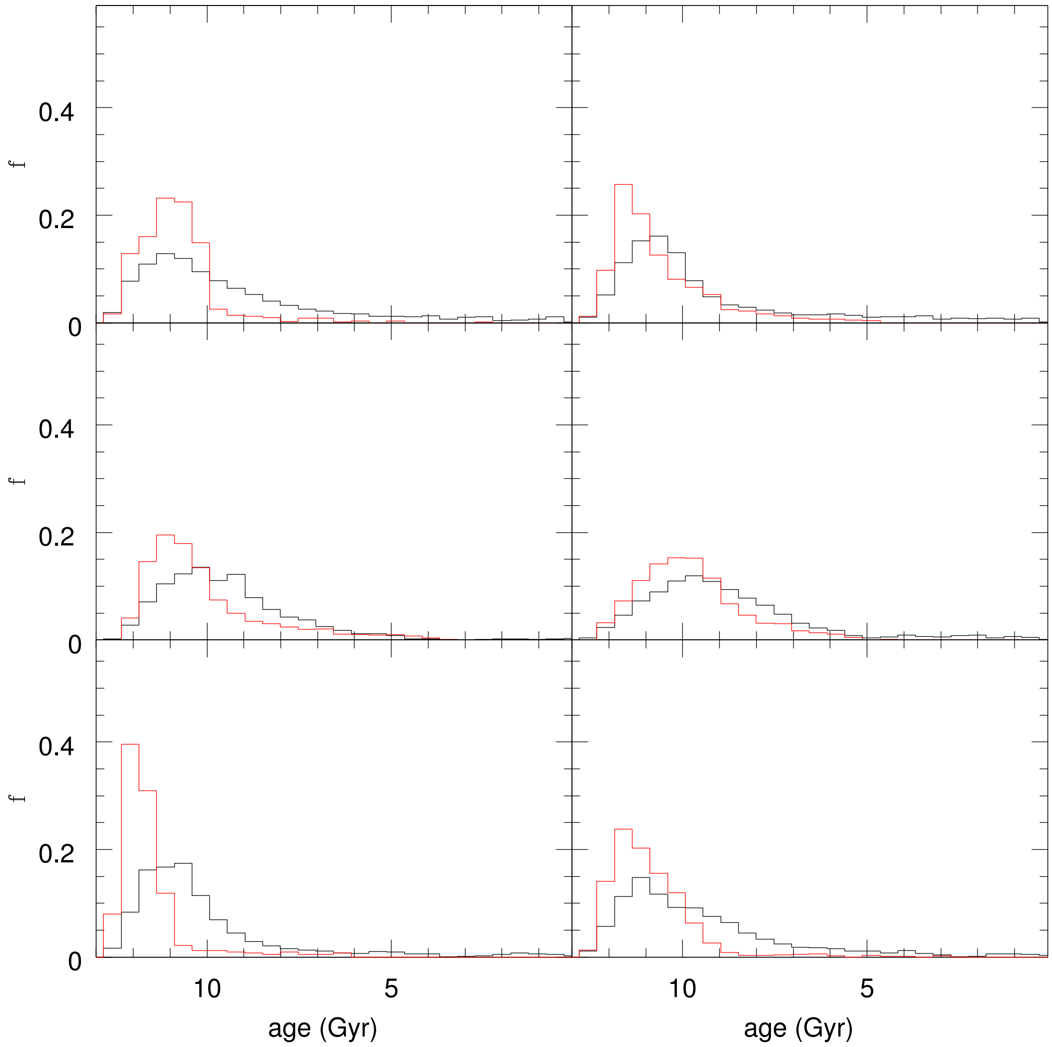

Figure D.14: (continued) Halo (red) and galaxy (black) age distributions for the $M_{tot} = 5{\times}10^{12}$ $M_{\odot}$ semi–cosmological simulations in Renda et al. (2005b).

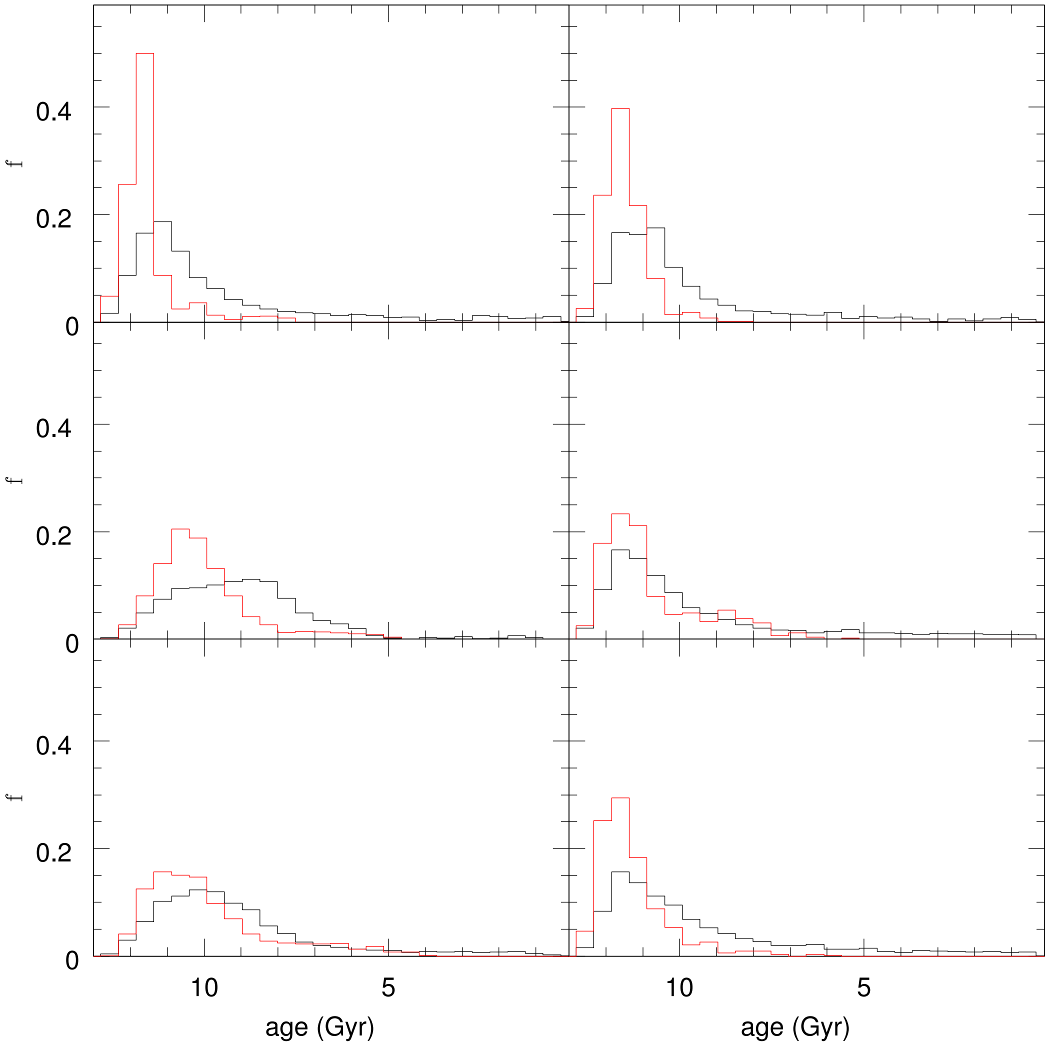

Figure D.15: (continued) Halo (red) and galaxy (black) age distributions for the $M_{tot} = 5 \times 10^{12}\ M_{\odot}$ semi–cosmological simulations in Renda et al. (2005b).

Appendix E

Galaxy Rotation Curves

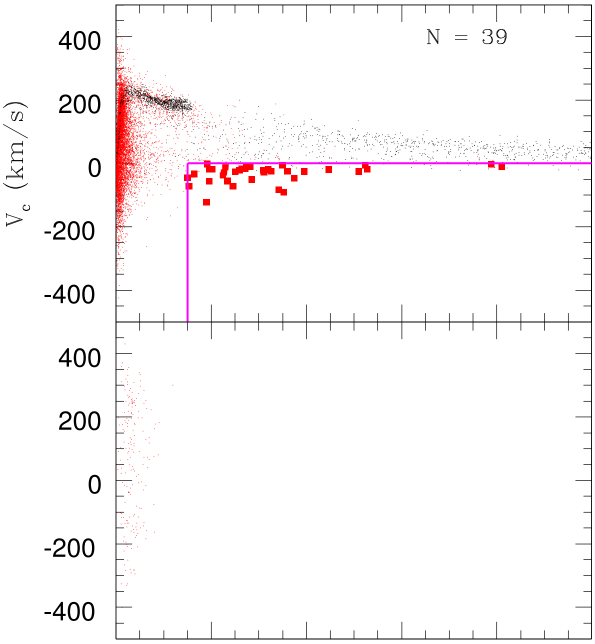

Figure E.1: Galaxy rotation curves for the $M_{tot} = 5\times10^{11}$ $M_\odot$ semi–cosmological simulations in Renda et al. (2005b). Black dots for the gaseous particles. Red dots for the stellar particles; red boxes for the ensemble of stellar particles (enclosed within the magenta frame) which are counter–rotating with $v_\theta < 0$ within each topographical halo at a projected radius $R > 15$ kpc. The size of such ensemble is also shown in each panel.

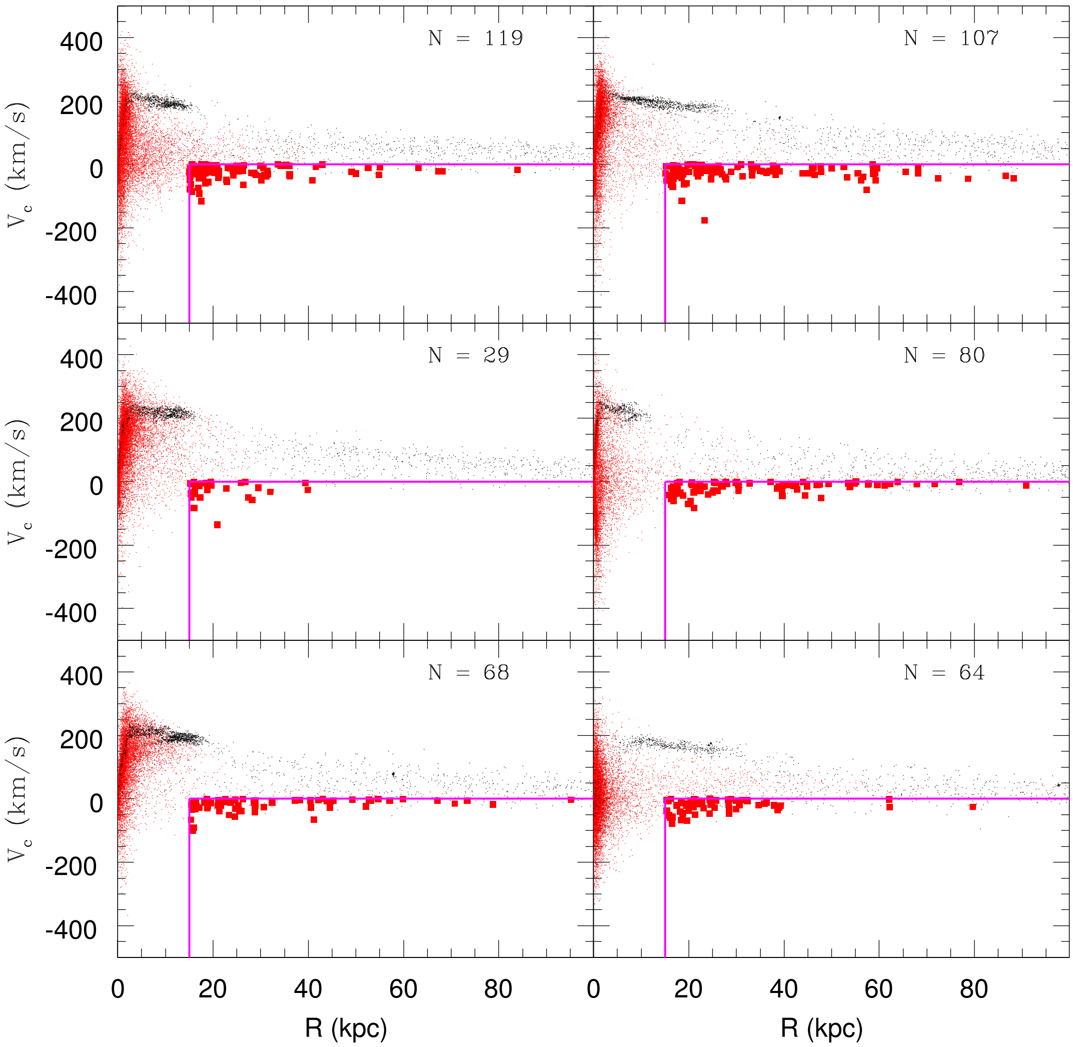

Figure E.2: (continued) Galaxy rotation curves for the $M_{tot} = 5 \times 10^{11}$ $M_\odot$ semi–cosmological simulations in Renda et al. (2005b). Black dots for the gaseous particles. Red dots for the stellar particles; red boxes for the ensemble of stellar particles (enclosed within the magenta frame) which are counter–rotating with $v_\theta < 0$ within each topographical halo at a projected radius $R > 15$ kpc. The size of such ensemble is also shown in each panel.

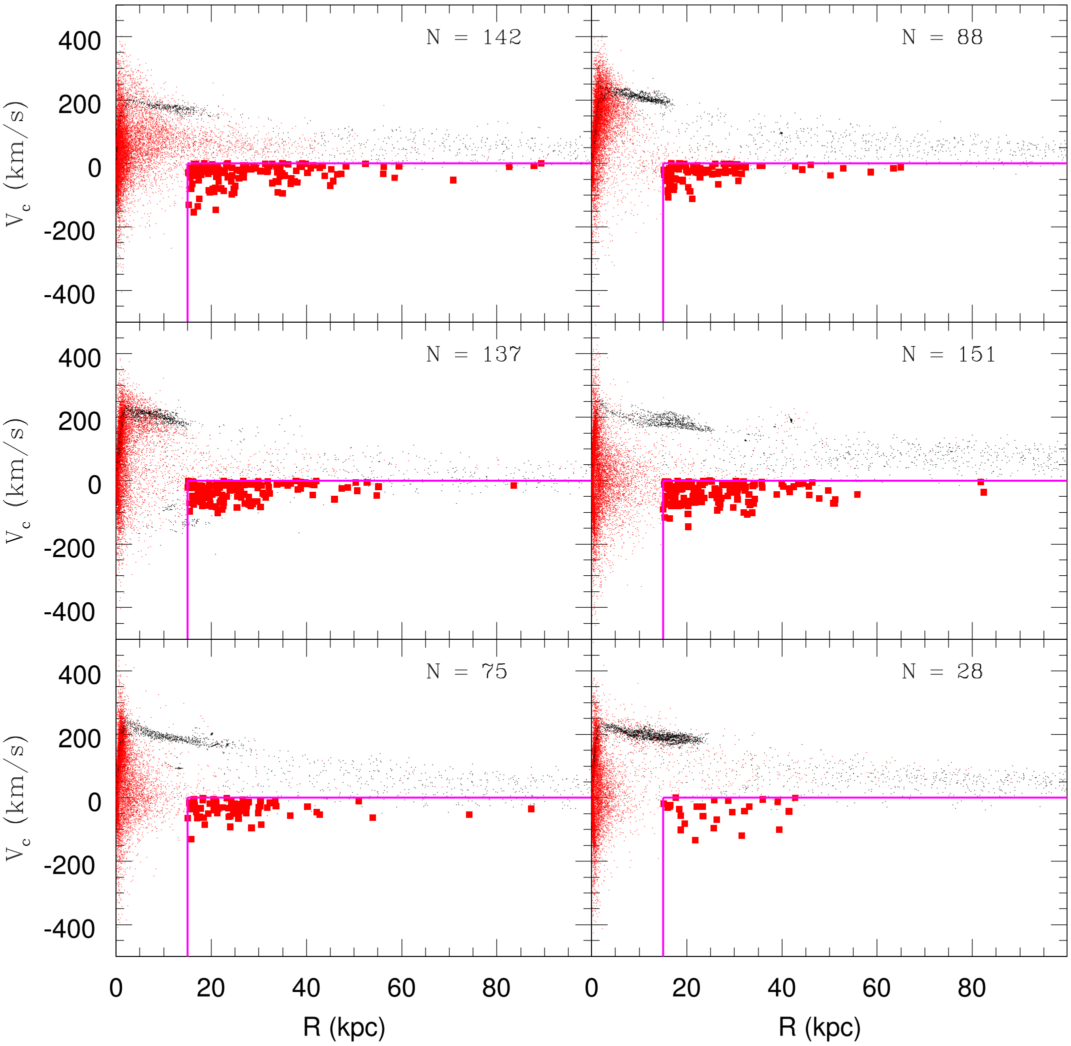

Figure E.3: (continued) Galaxy rotation curves for the $M_{tot} = 5 \times 10^{11}\ M_\odot$ semi–cosmological simulations in Renda et al. (2005b). Black dots for the gaseous particles. Red dots for the stellar particles; red boxes for the ensemble of stellar particles (enclosed within the magenta frame) which are counter–rotating with $v_\theta < 0$ within each topographical halo at a projected radius $R > 15$ kpc. The size of such ensemble is also shown in each panel.

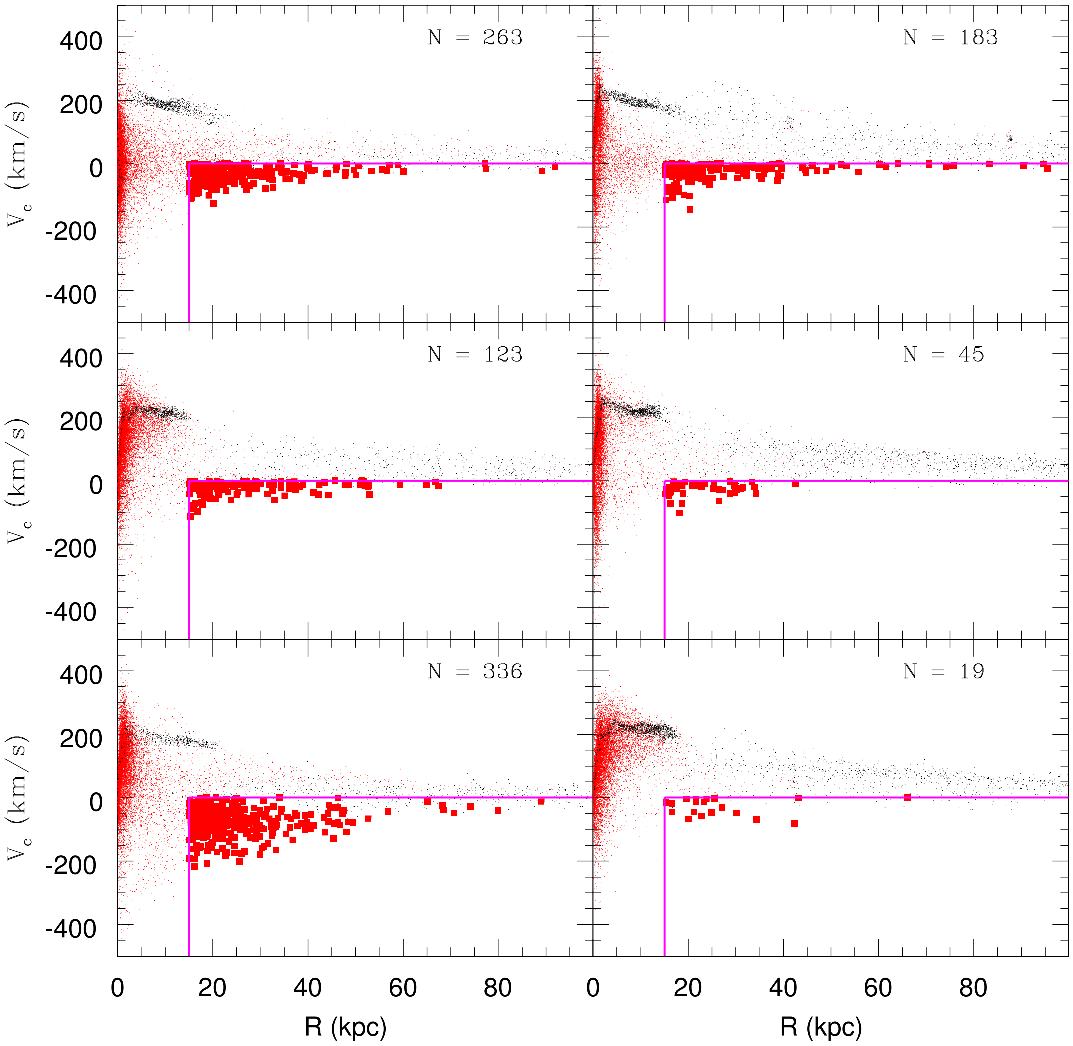

Figure E.4: (continued) Galaxy rotation curves for the $M_{tot} = 5\times10^{11}$ $M_{\odot}$ semi–cosmological simulations in Renda et al. (2005b). Black dots for the gaseous particles. Red dots for the stellar particles; red boxes for the ensemble of stellar particles (enclosed within the magenta frame) which are counter–rotating with $v_\theta < 0$ within each topographical halo at a projected radius $R > 15$ kpc. The size of such ensemble is also shown in each panel.

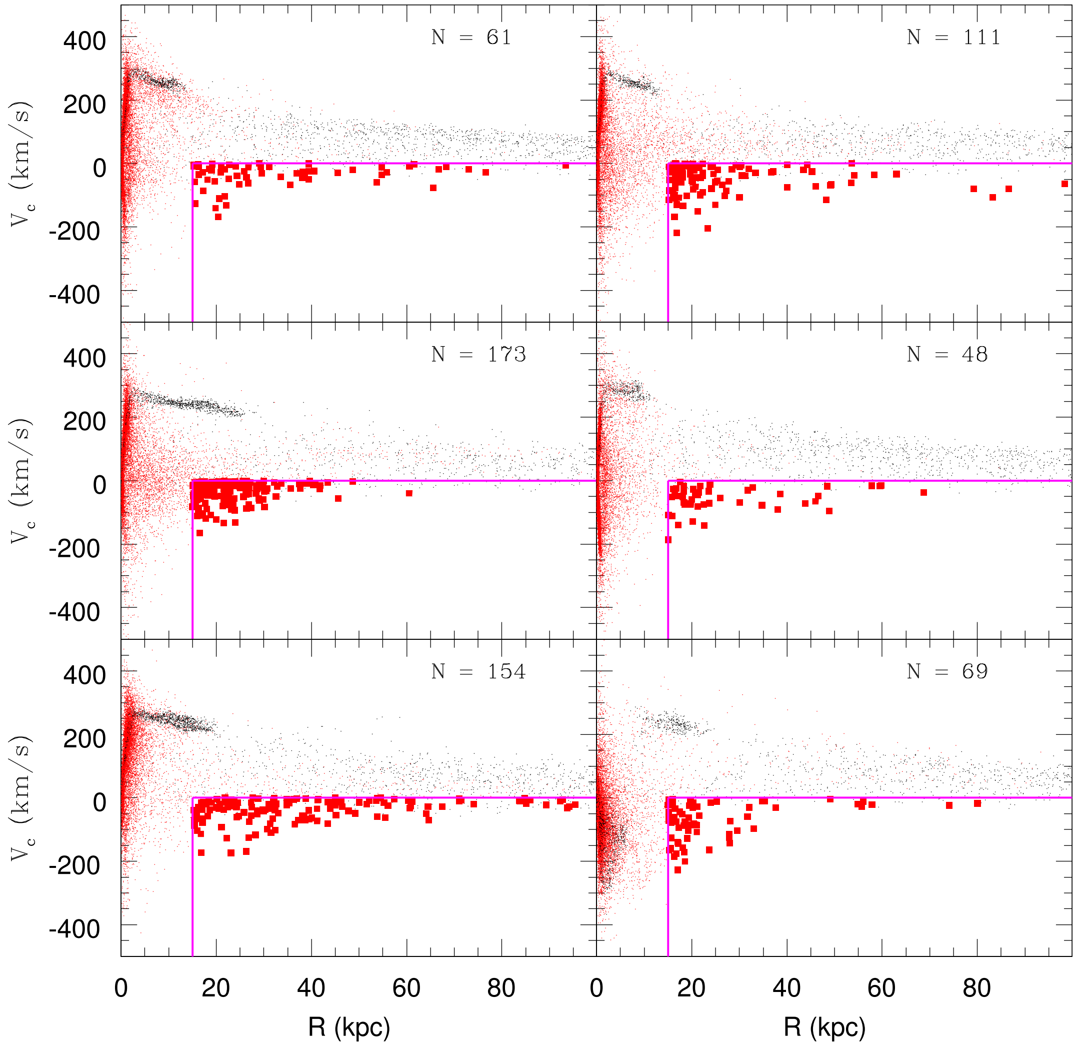

Figure E.5: Galaxy rotation curves for the $M_{tot} = 10^{12}$ $M_\odot$ semi–cosmological simulations in Renda et al. (2005b). Black dots for the gaseous particles. Red dots for the stellar particles; red boxes for the ensemble of stellar particles (enclosed within the magenta frame) which are counter–rotating with $v_\theta < 0$ within each topographical halo at a projected radius $R > 15$ kpc. The size of such ensemble is also shown in each panel.

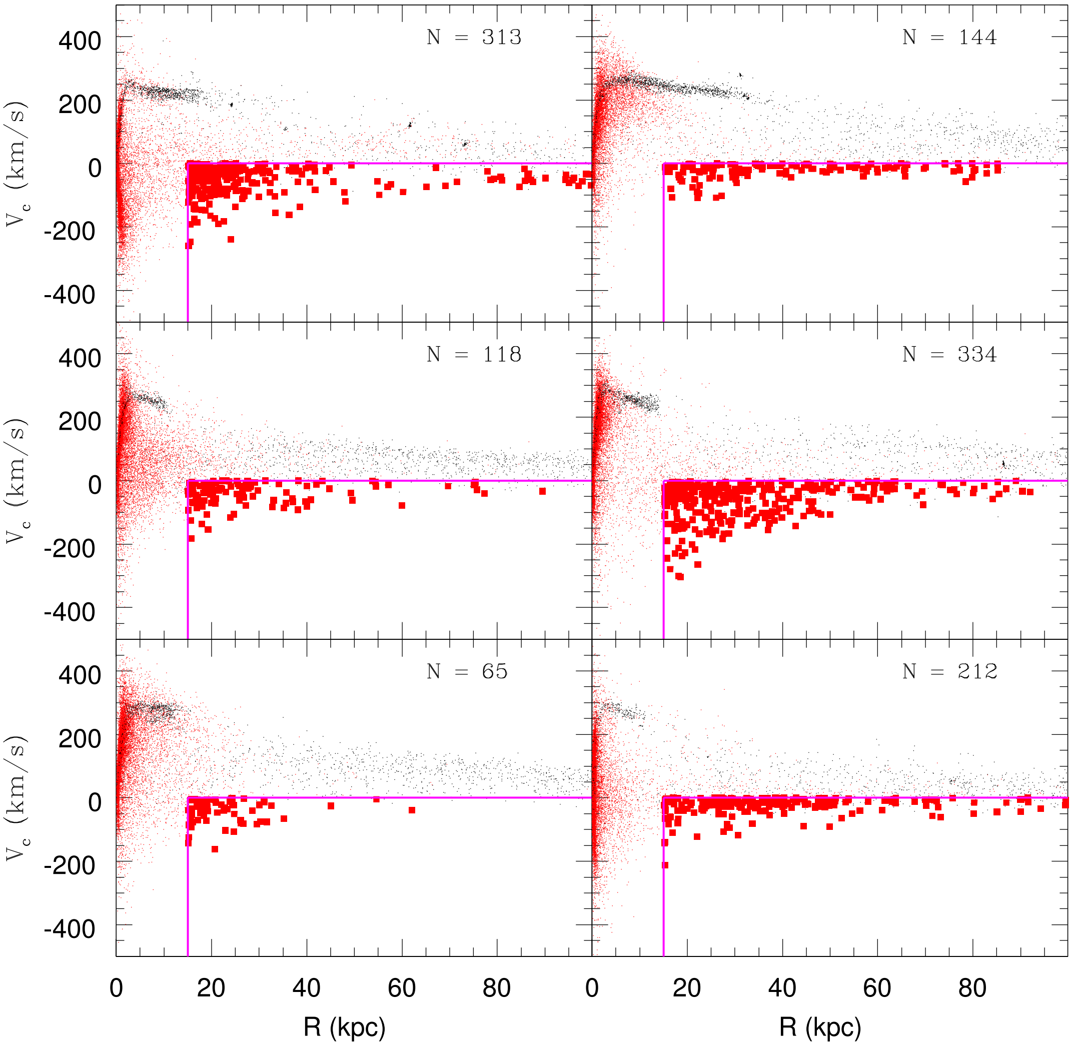

Figure E.6: (continued) Galaxy rotation curves for the $M_{tot} = 10^{12}$ $M_{\odot}$ semi–cosmological simulations in Renda et al. (2005b). Black dots for the gaseous particles. Red dots for the stellar particles; red boxes for the ensemble of stellar particles (enclosed within the magenta frame) which are counter–rotating with $v_{\theta} < 0$ within each topographical halo at a projected radius $R > 15$ kpc. The size of such ensemble is also shown in each panel.

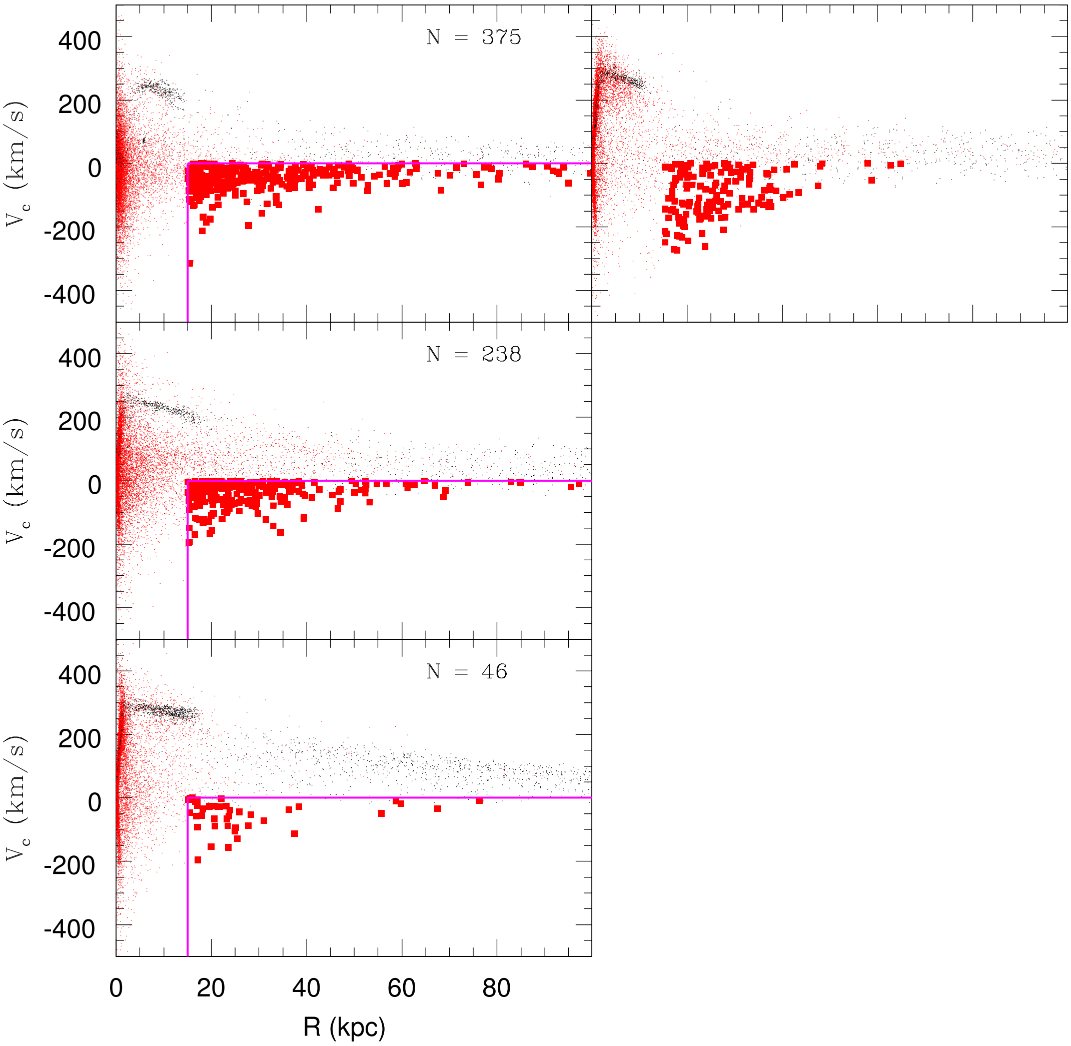

Figure E.7: (continued) Galaxy rotation curves for the $M_{tot} = 10^{12}\ M_\odot$ semi–cosmological simulations in Renda et al. (2005b). Black dots for the gaseous particles. Red dots for the stellar particles; red boxes for the ensemble of stellar particles (enclosed within the magenta frame) which are counter–rotating with $v_\theta < 0$ within each topographical halo at a projected radius $R > 15$ kpc. The size of such ensemble is also shown in each panel.

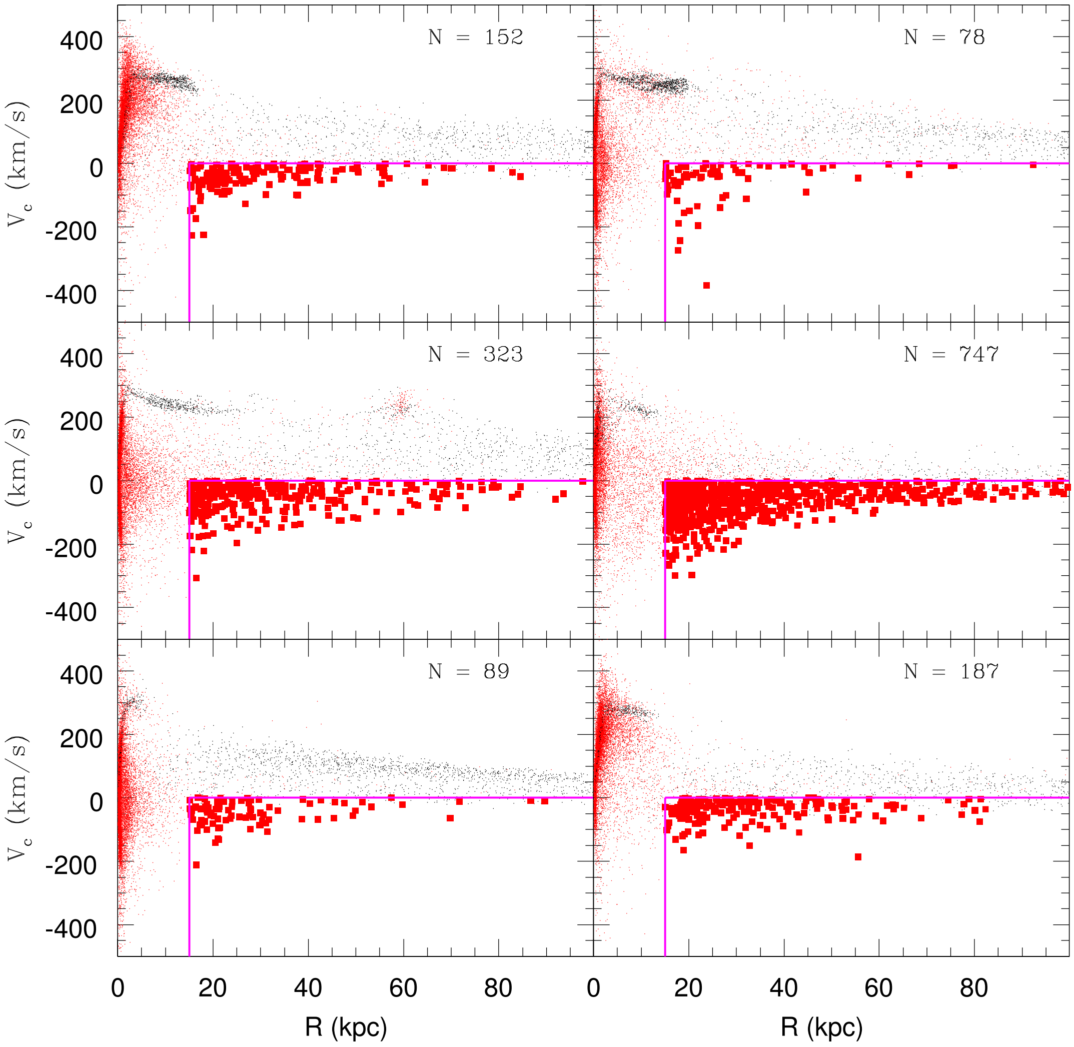

Figure E.8: (continued) Galaxy rotation curves for the $M_{tot} = 10^{12}$ $M_\odot$ semi–cosmological simulations in Renda et al. (2005b). Black dots for the gaseous particles. Red dots for the stellar particles; red boxes for the ensemble of stellar particles (enclosed within the magenta frame) which are counter–rotating with $v_\theta < 0$ within each topographical halo at a projected radius $R > 15$ kpc. The size of such ensemble is also shown in each panel.

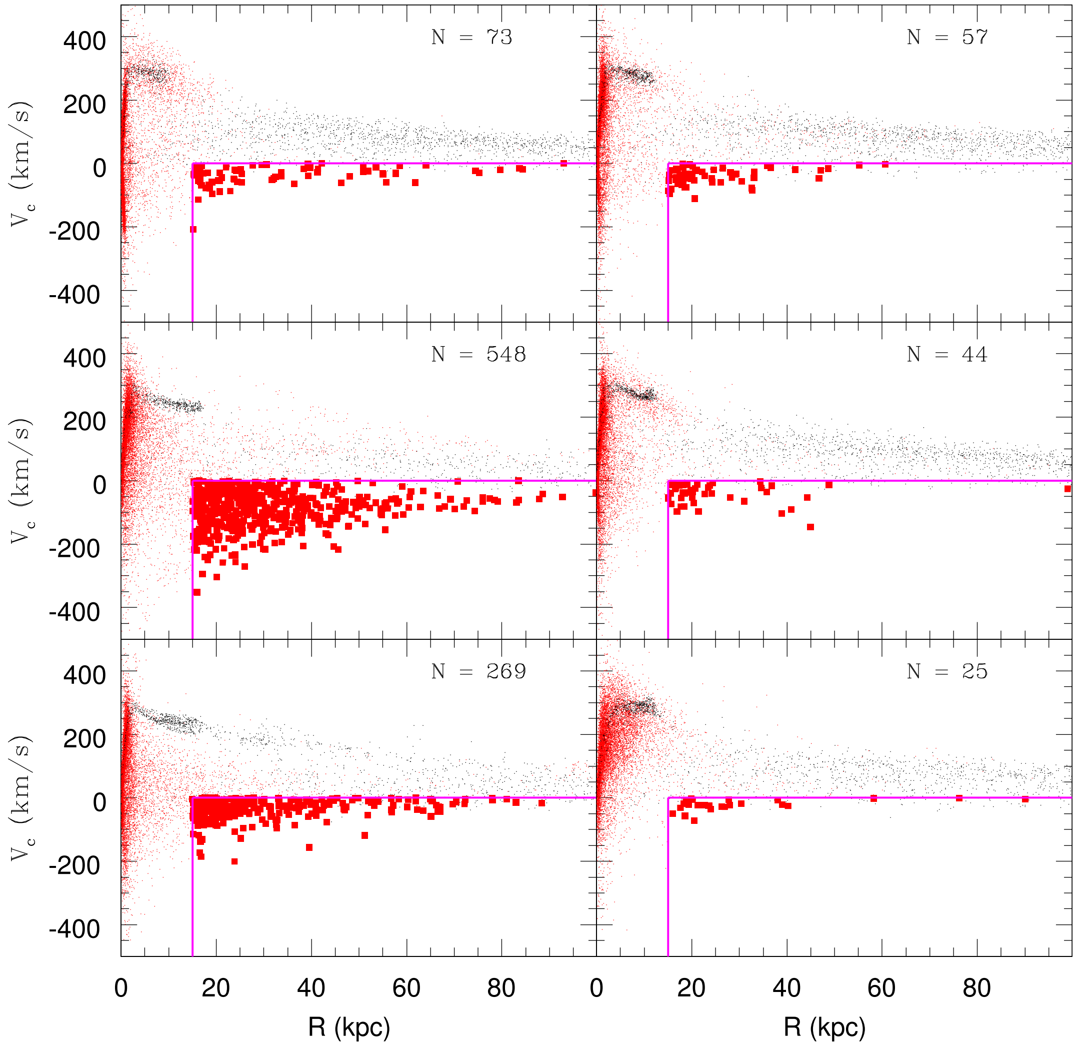

Figure E.9: (continued) Galaxy rotation curves for the $M_{tot} = 10^{12}\ M_\odot$ semi–cosmological simulations in Renda et al. (2005b). Black dots for the gaseous particles. Red dots for the stellar particles; red boxes for the ensemble of stellar particles (enclosed within the magenta frame) which are counter–rotating with $v_\theta < 0$ within each topographical halo at a projected radius $R > 15$ kpc. The size of such ensemble is also shown in each panel.

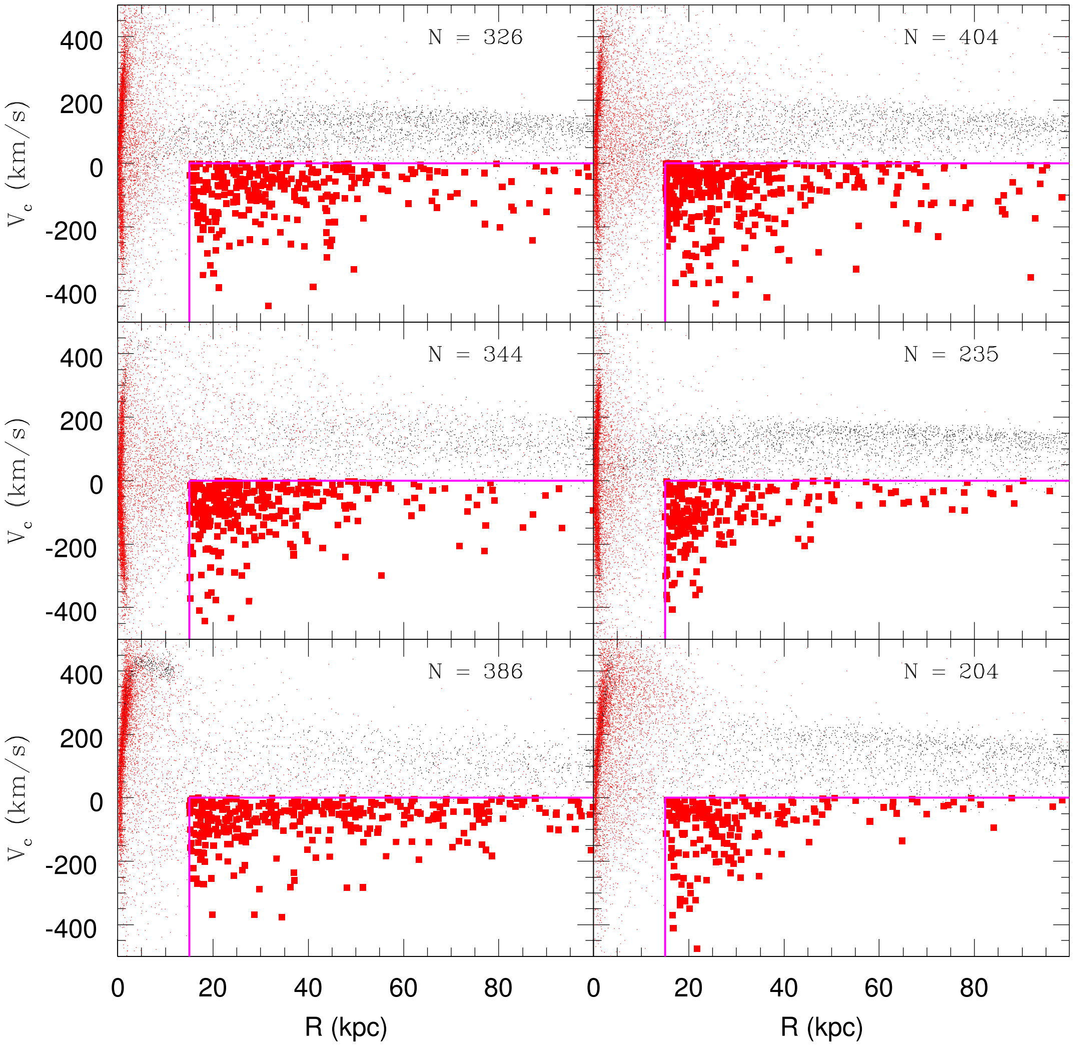

Figure E.10: Galaxy rotation curves for the $M_{tot} = 5 \times 10^{12}$ $M_\odot$ semi–cosmological simulations in Renda et al. (2005b). Black dots for the gaseous particles. Red dots for the stellar particles; red boxes for the ensemble of stellar particles (enclosed within the magenta frame) which are counter–rotating with $v_\theta < 0$ within each topographical halo at a projected radius $R > 15$ kpc. The size of such ensemble is also shown in each panel.

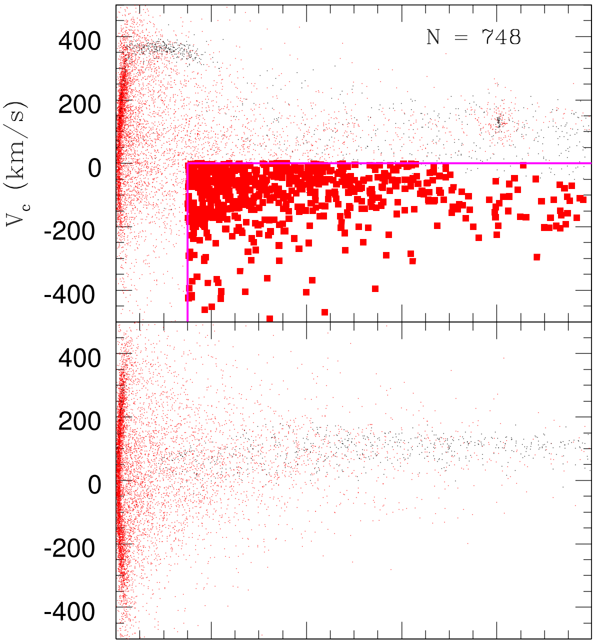

Figure E.11: (continued) Galaxy rotation curves for the $M_{tot} = 5\times10^{12}$ $M_\odot$ semi–cosmological simulations in Renda et al. (2005b). Black dots for the gaseous particles. Red dots for the stellar particles; red boxes for the ensemble of stellar particles (enclosed within the magenta frame) which are counter–rotating with $v_\theta < 0$ within each topographical halo at a projected radius $R > 15$ kpc. The size of such ensemble is also shown in each panel.

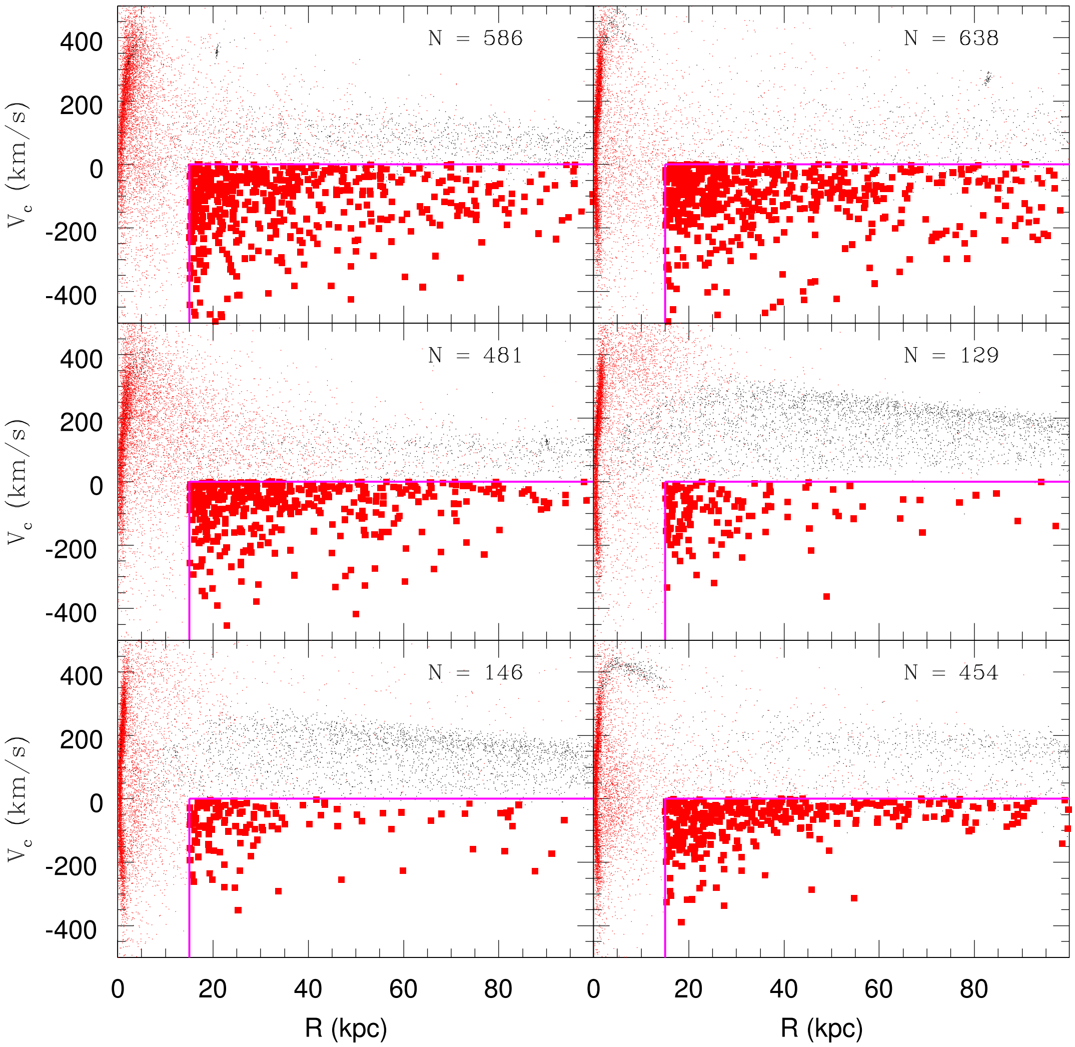

Figure E.12: (continued) Galaxy rotation curves for the $M_{tot} = 5\times10^{12}\ M_\odot$ semi–cosmological simulations in Renda et al. (2005b). Black dots for the gaseous particles. Red dots for the stellar particles; red boxes for the ensemble of stellar particles (enclosed within the magenta frame) which are counter–rotating with $v_\theta < 0$ within each topographical halo at a projected radius $R > 15$ kpc. The size of such ensemble is also shown in each panel.

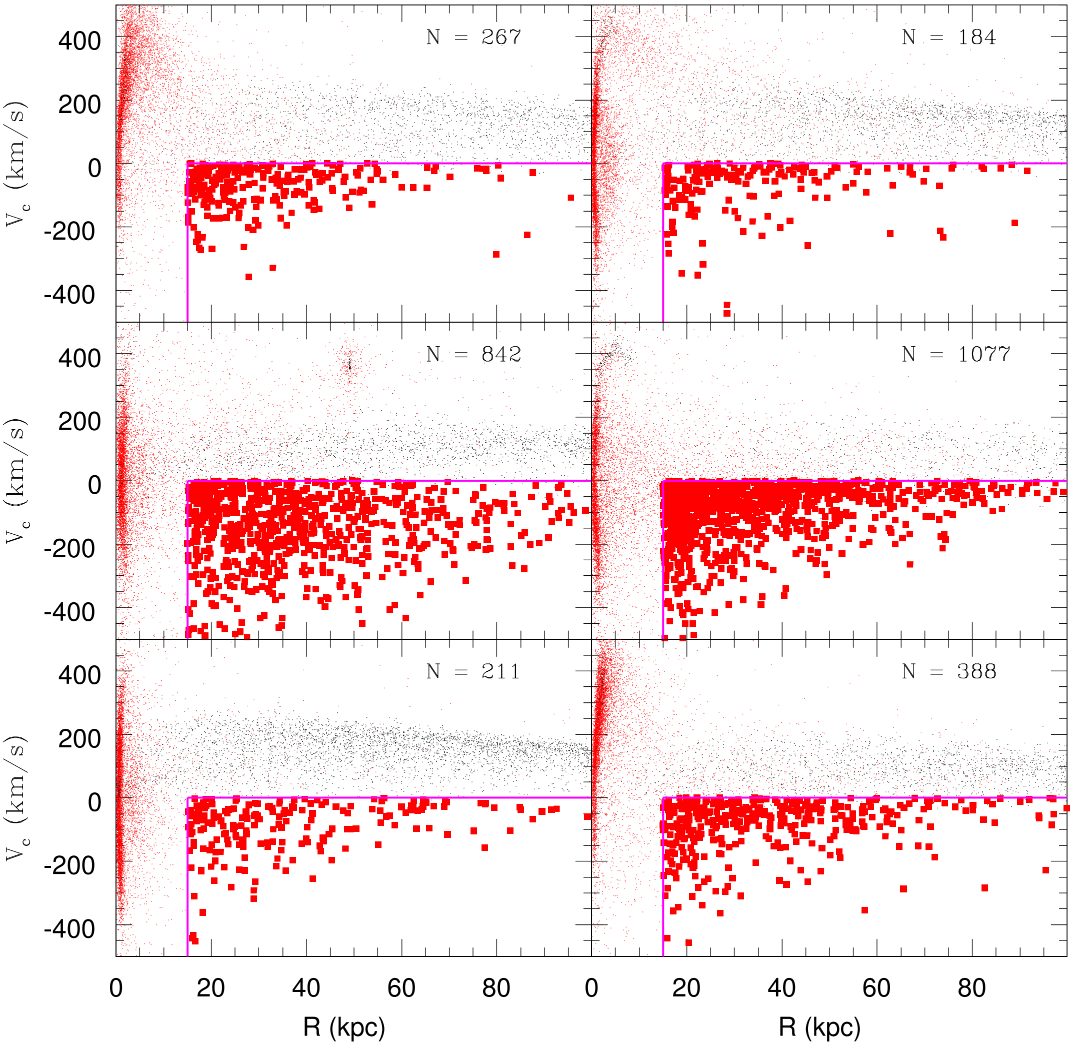

Figure E.13: (continued) Galaxy rotation curves for the $M_{tot} = 5\times10^{12}\ M_\odot$ semi–cosmological simulations in Renda et al. (2005b). Black dots for the gaseous particles. Red dots for the stellar particles; red boxes for the ensemble of stellar particles (enclosed within the magenta frame) which are counter–rotating with $v_\theta < 0$ within each topographical halo at a projected radius $R > 15$ kpc. The size of such ensemble is also shown in each panel.

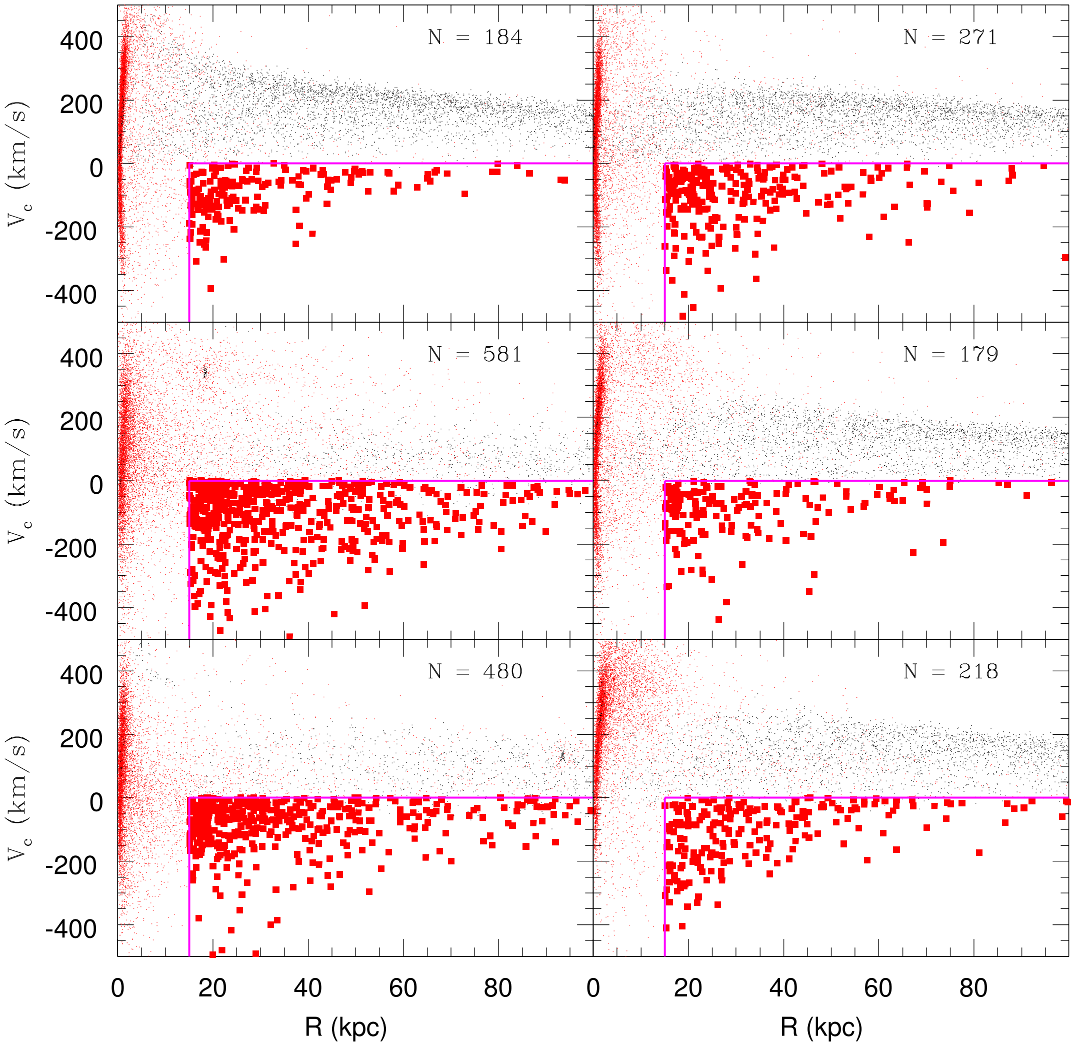

Figure E.14: (continued) Galaxy rotation curves for the $M_{tot} = 5\times10^{12}$ $M_\odot$ semi–cosmological simulations in Renda et al. (2005b). Black dots for the gaseous particles. Red dots for the stellar particles; red boxes for the ensemble of stellar particles (enclosed within the magenta frame) which are counter–rotating with $v_\theta < 0$ within each topographical halo at a projected radius $R > 15$ kpc. The size of such ensemble is also shown in each panel.

Appendix F

(Once More) Stellar Halo Metallicity Distributions

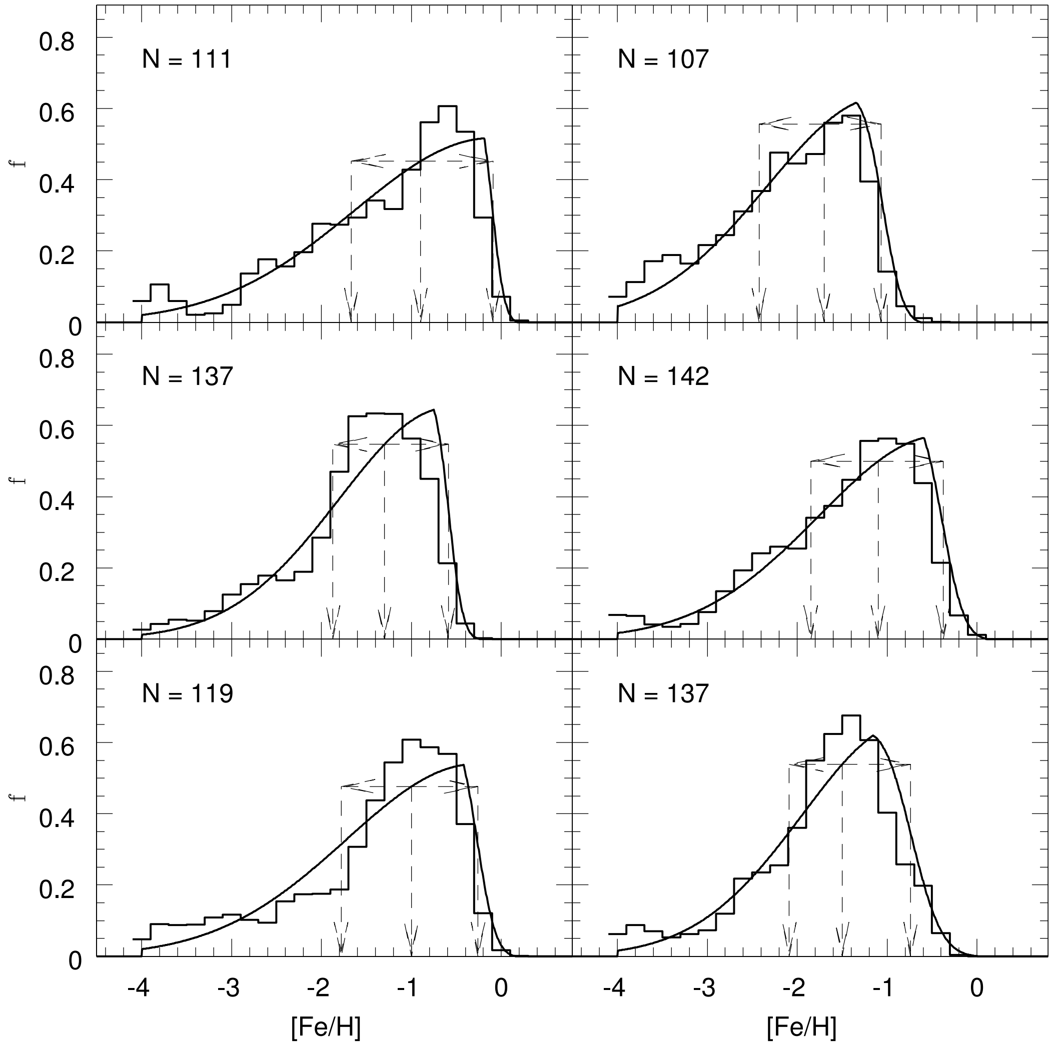

Figure F.1: Kinematically selected halo MDFs for the $M_{tot} = 5\times10^{11}$ $M_{\odot}$ semi–cosmological simulations in Renda et al. (2005b). The 68% Confidence Level range and the number of stellar particles each MDF relates to are also shown. Each MDF refers to the stellar particles in the simulation which are counter–rotating with $v_\theta < 0$ at a projected radius $R > 15$ kpc.

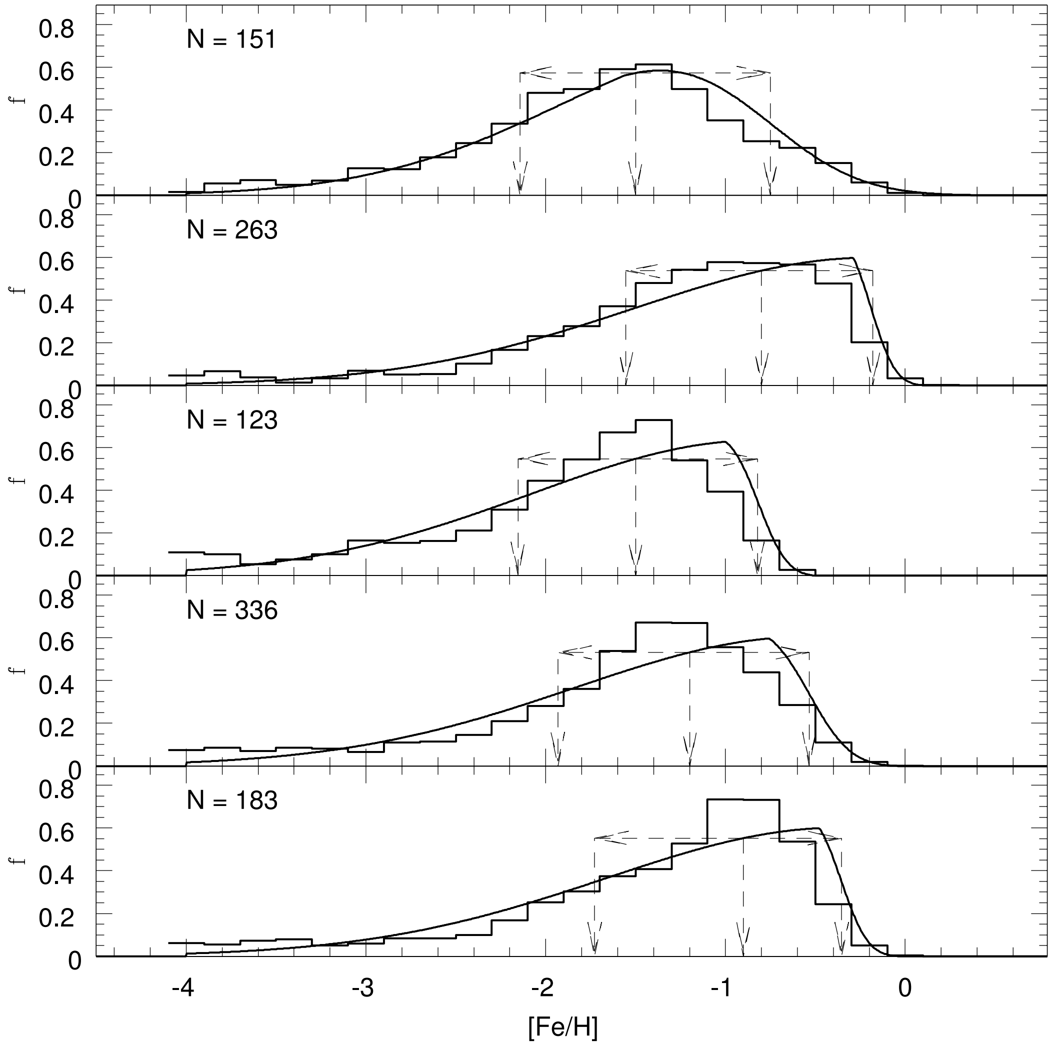

Figure F.2: (continued) Kinematically selected halo MDFs for the $M_{tot} = 5\times10^{11}$ $M_{\odot}$ semi–cosmological simulations in Renda et al. (2005b). The 68% Confidence Level range and the number of stellar particles each MDF relates to are also shown. Each MDF refers to the stellar particles in the simulation which are counter–rotating with $v_{\theta} < 0$ at a projected radius $R > 15$ kpc.

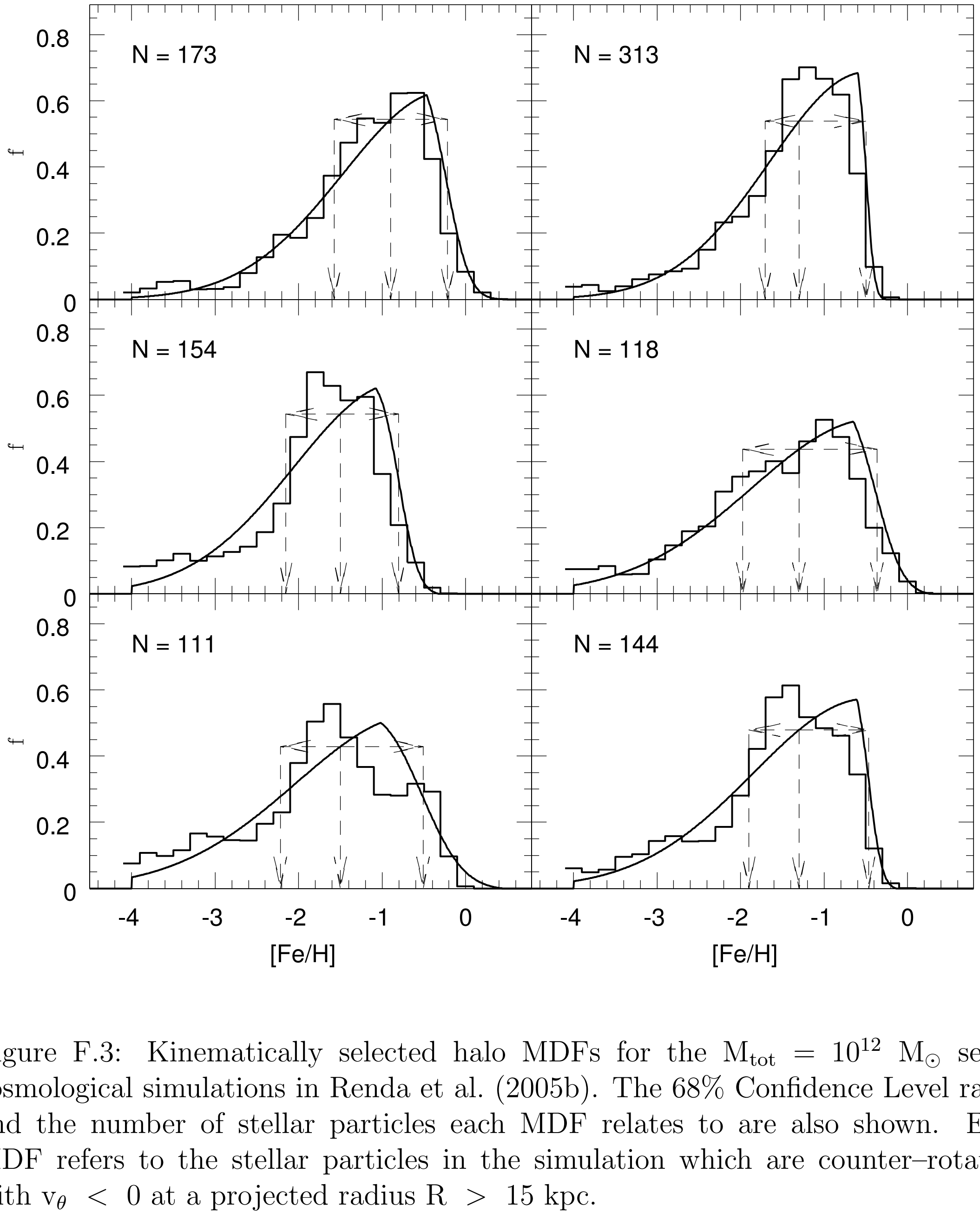

Figure F.3: Kinematically selected halo MDFs for the $M_{tot} = 10^{12}$ $M_\odot$ semi–cosmological simulations in Renda et al. (2005b). The 68% Confidence Level range and the number of stellar particles each MDF relates to are also shown. Each MDF refers to the stellar particles in the simulation which are counter–rotating with $v_\theta < 0$ at a projected radius $R > 15$ kpc.

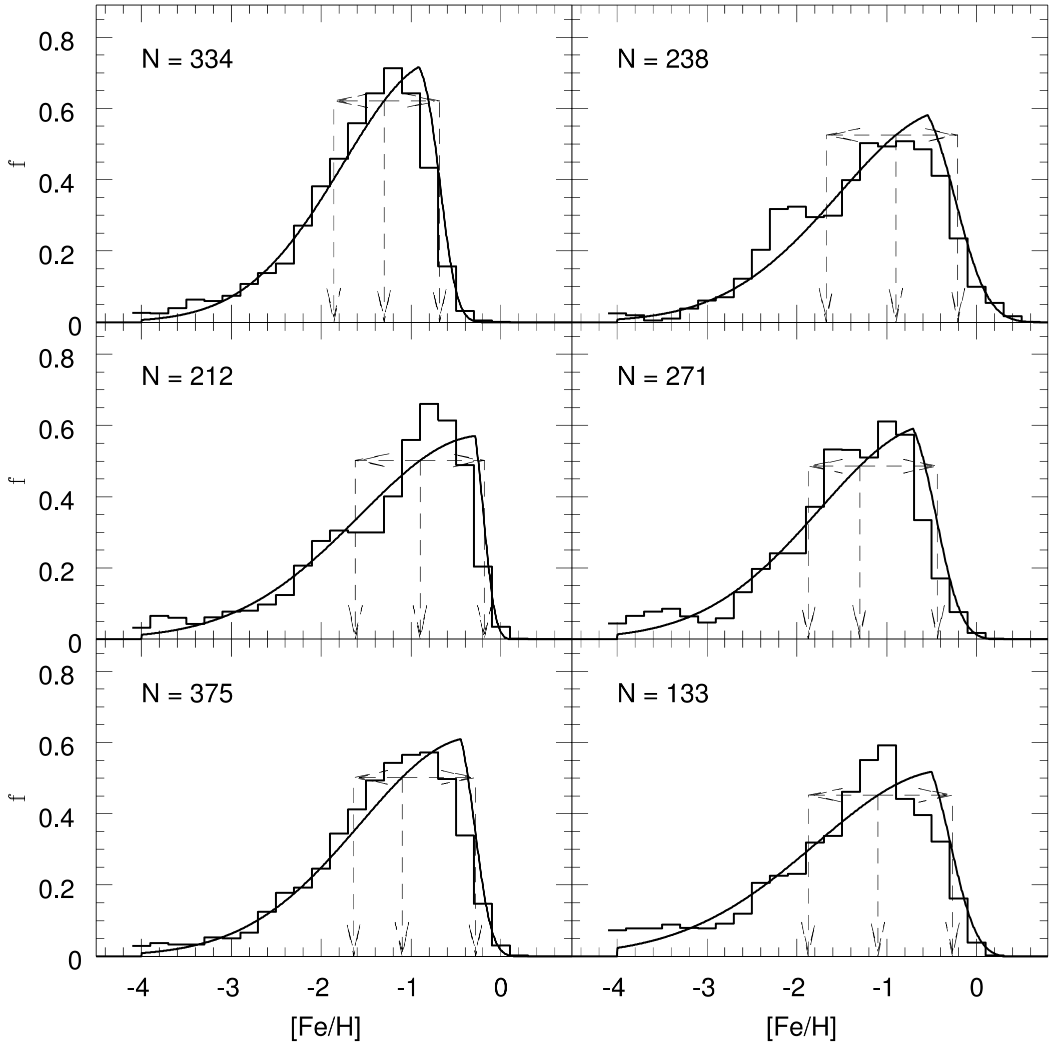

Figure F.4: (continued) Kinematically selected halo MDFs for the $M_{tot} = 10^{12}\ M_{\odot}$ semi–cosmological simulations in Renda et al. (2005b). The 68% Confidence Level range and the number of stellar particles each MDF relates to are also shown. Each MDF refers to the stellar particles in the simulation which are counter–rotating with $v_{\theta} < 0$ at a projected radius $R > 15$ kpc.

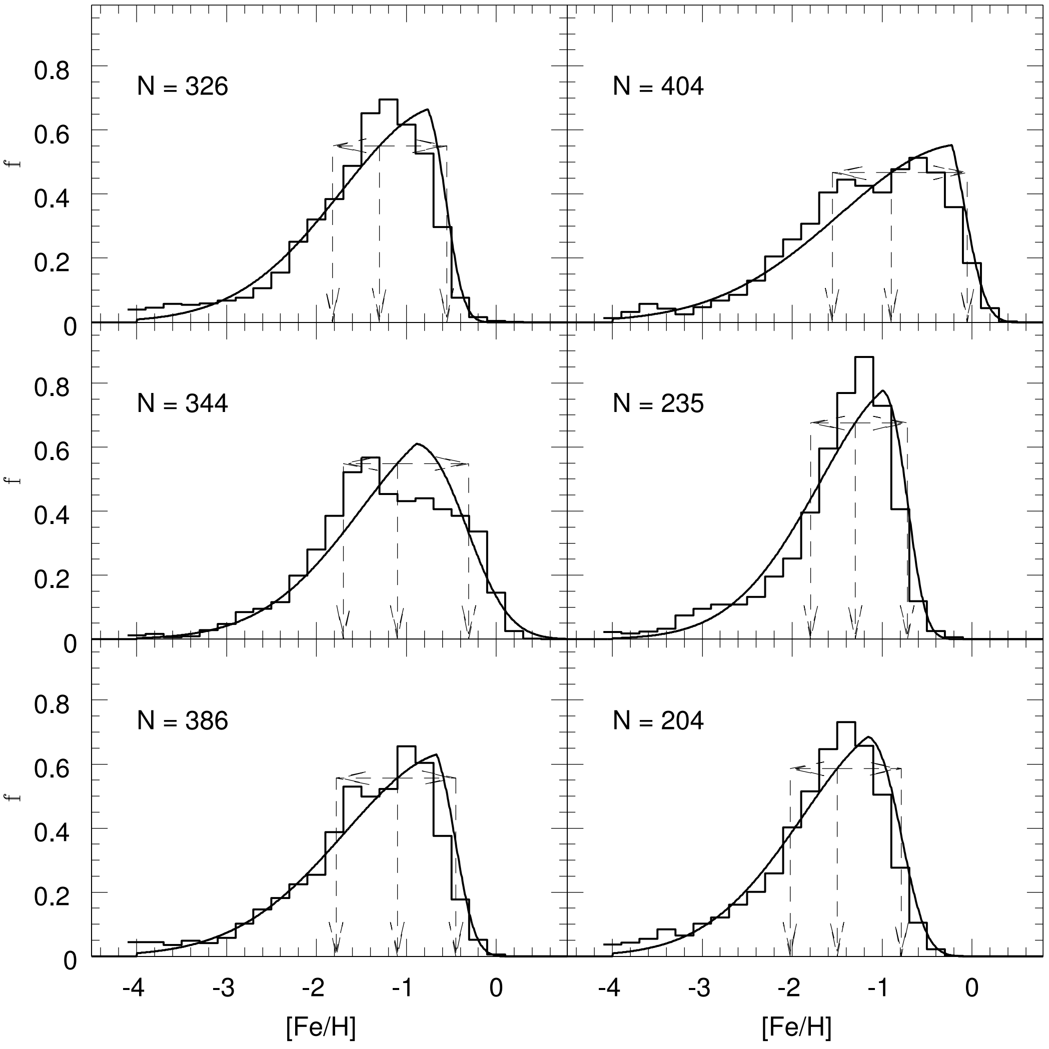

Figure F.5: Kinematically selected halo MDFs for the $M_{tot} = 5\times10^{12}$ $M_\odot$ semi–cosmological simulations in Renda et al. (2005b). The 68% Confidence Level range and the number of stellar particles each MDF relates to are also shown. Each MDF refers to the stellar particles in the simulation which are counter–rotating with $v_\theta < 0$ at a projected radius $R > 15$ kpc.

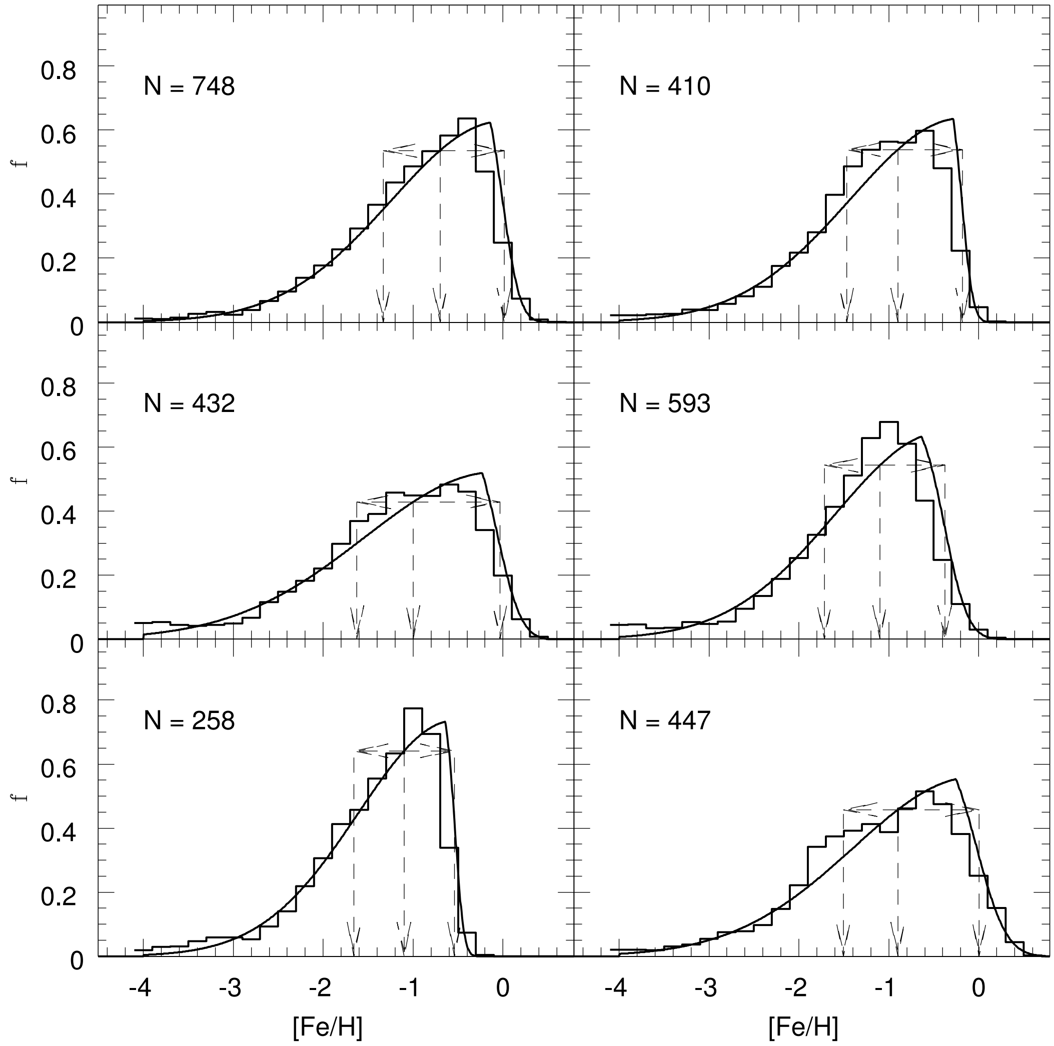

Figure F.6: (continued) Kinematically selected halo MDFs for the $M_{tot} = 5 \times 10^{12}$ $M_\odot$ semi–cosmological simulations in Renda et al. (2005b). The 68% Confidence Level range and the number of stellar particles each MDF relates to are also shown. Each MDF refers to the stellar particles in the simulation which are counter–rotating with $v_\theta < 0$ at a projected radius $R > 15$ kpc.

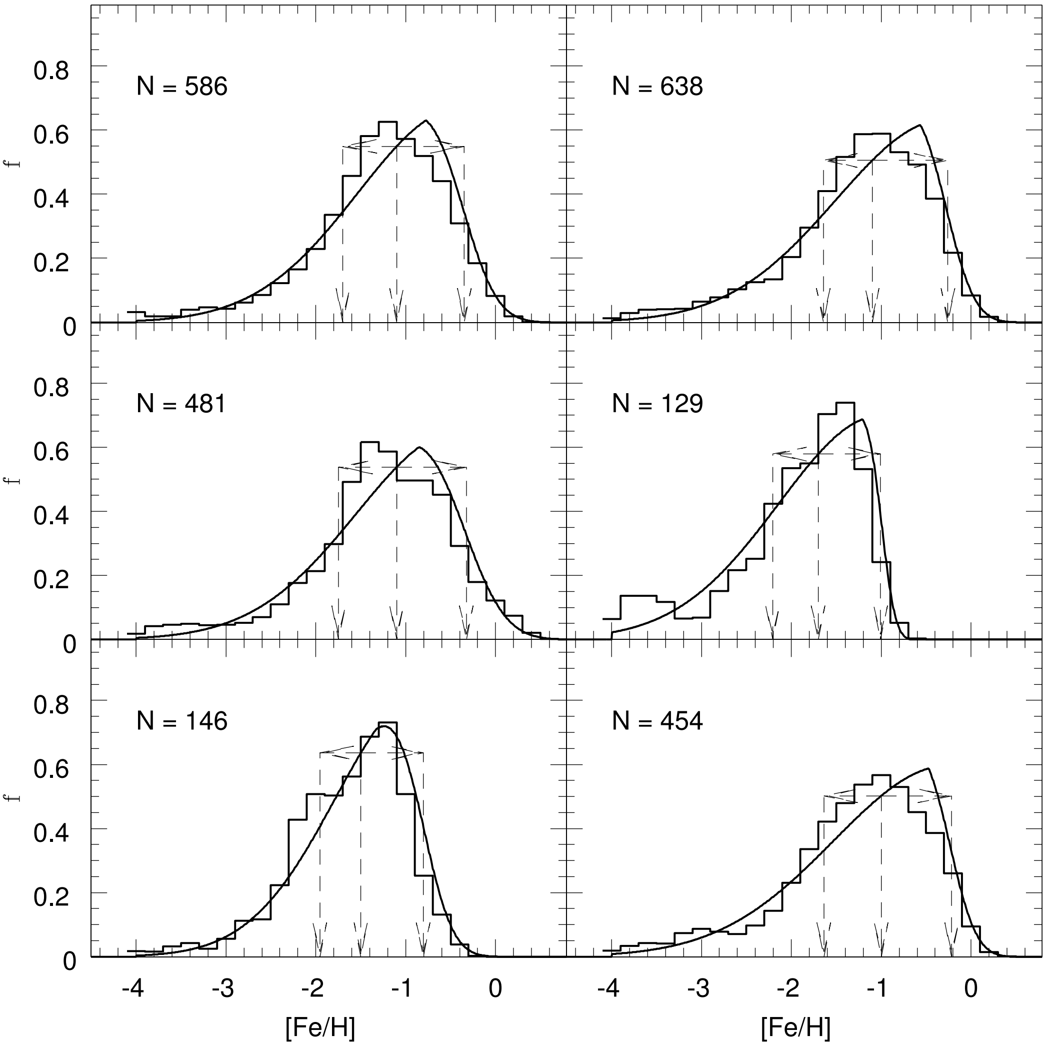

Figure F.7: (continued) Kinematically selected halo MDFs for the $M_{tot} = 5\times10^{12}$ $M_\odot$ semi–cosmological simulations in Renda et al. (2005b). The 68% Confidence Level range and the number of stellar particles each MDF relates to are also shown. Each MDF refers to the stellar particles in the simulation which are counter–rotating with $v_\theta < 0$ at a projected radius $R > 15$ kpc.

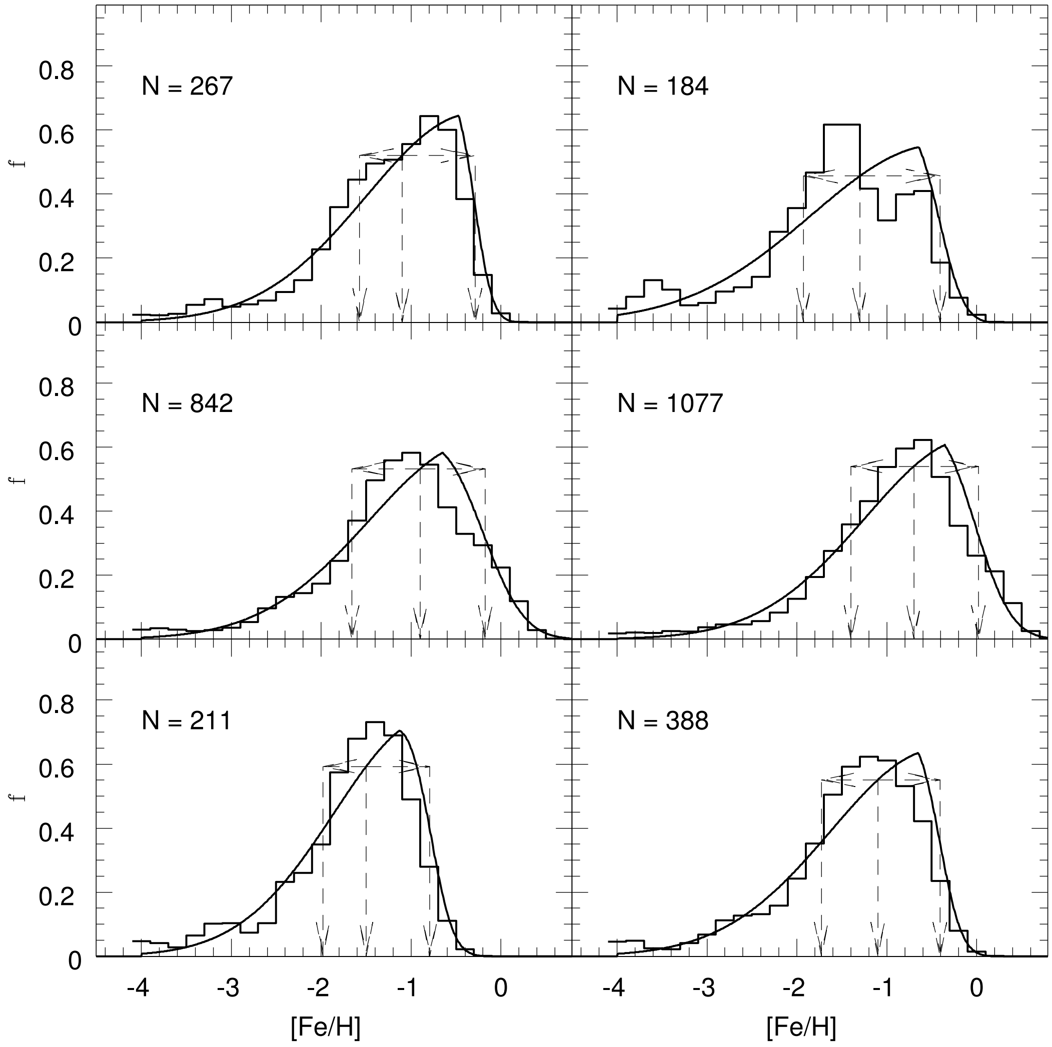

Figure F.8: (continued) Kinematically selected halo MDFs for the $M_{tot} = 5\times10^{12}$ $M_{\odot}$ semi–cosmological simulations in Renda et al. (2005b). The 68% Confidence Level range and the number of stellar particles each MDF relates to are also shown. Each MDF refers to the stellar particles in the simulation which are counter–rotating with $v_{\theta} < 0$ at a projected radius $R > 15$ kpc.

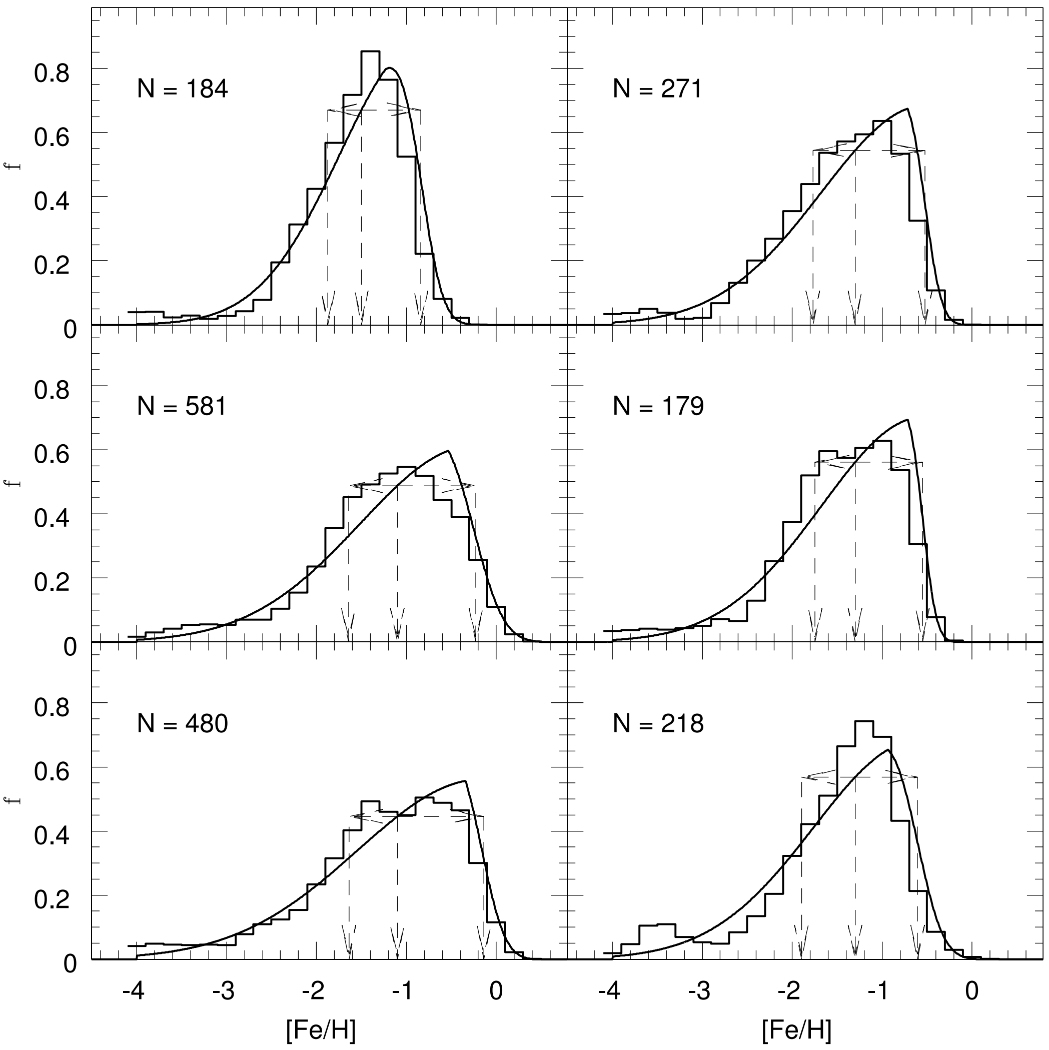

Figure F.9: (continued) Kinematically selected halo MDFs for the $M_{tot} = 5\times10^{12}$ $M_\odot$ semi–cosmological simulations in Renda et al. (2005b). The 68% Confidence Level range and the number of stellar particles each MDF relates to are also shown. Each MDF refers to the stellar particles in the simulation which are counter–rotating with $v_\theta < 0$ at a projected radius $R > 15$ kpc.

Appendix G

Stellar Halo (V - I) Colour Distributions

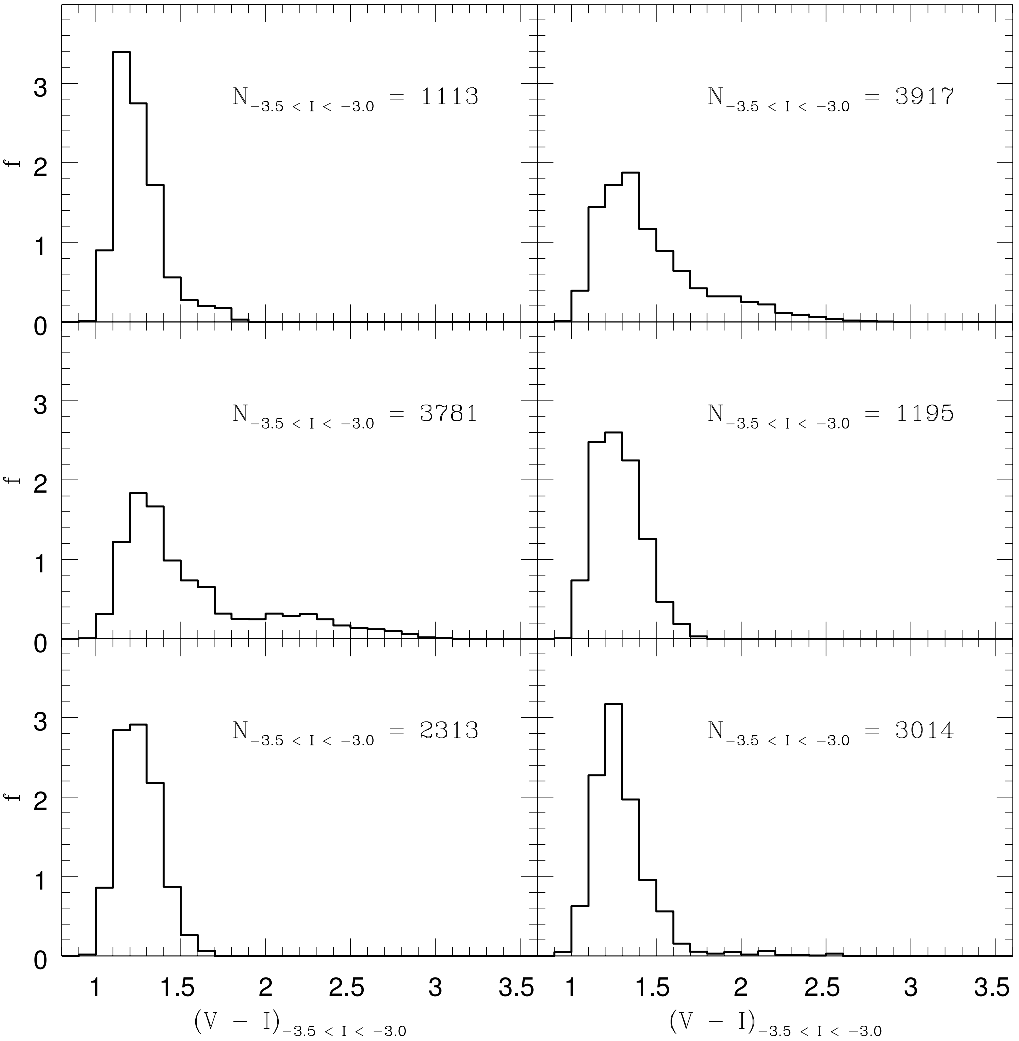

Figure G.1: Halo synthetic CMD (V - I) colour distribution at -3.5 < I < -3.0 for the $M_{tot} = 5{\times}10^{11}\ M_{\odot}$ semi–cosmological simulations in Renda et al. (2005b). Each panel also shows the number of generated stars at -3.5 < I < -3.0 in each synthetic CMD.

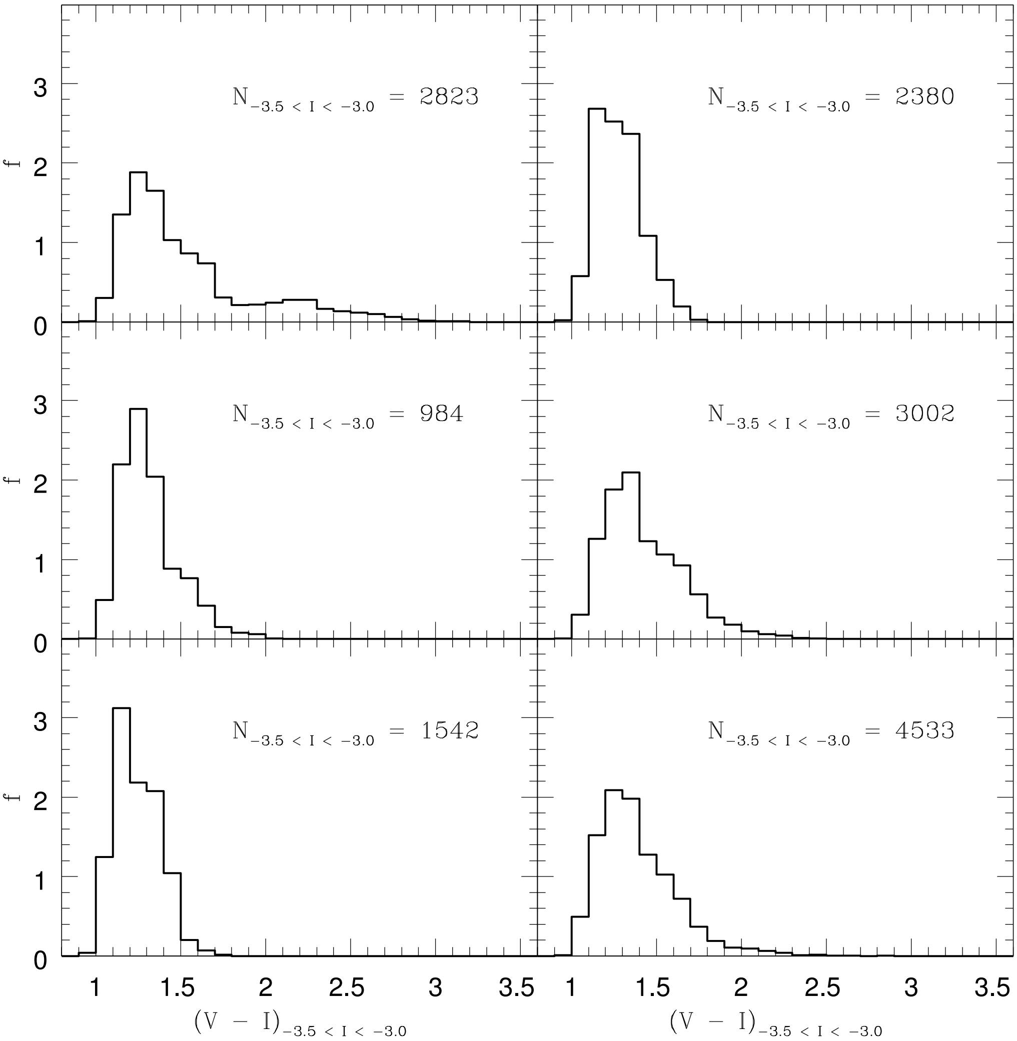

Figure G.2: (continued) Halo synthetic CMD (V - I) colour distribution at -3.5 < I < -3.0 for the $M_{tot} = 5\times10^{11}$ $M_\odot$ semi–cosmological simulations in Renda et al. (2005b). Each panel also shows the number of generated stars at -3.5 < I < -3.0 in each synthetic CMD.

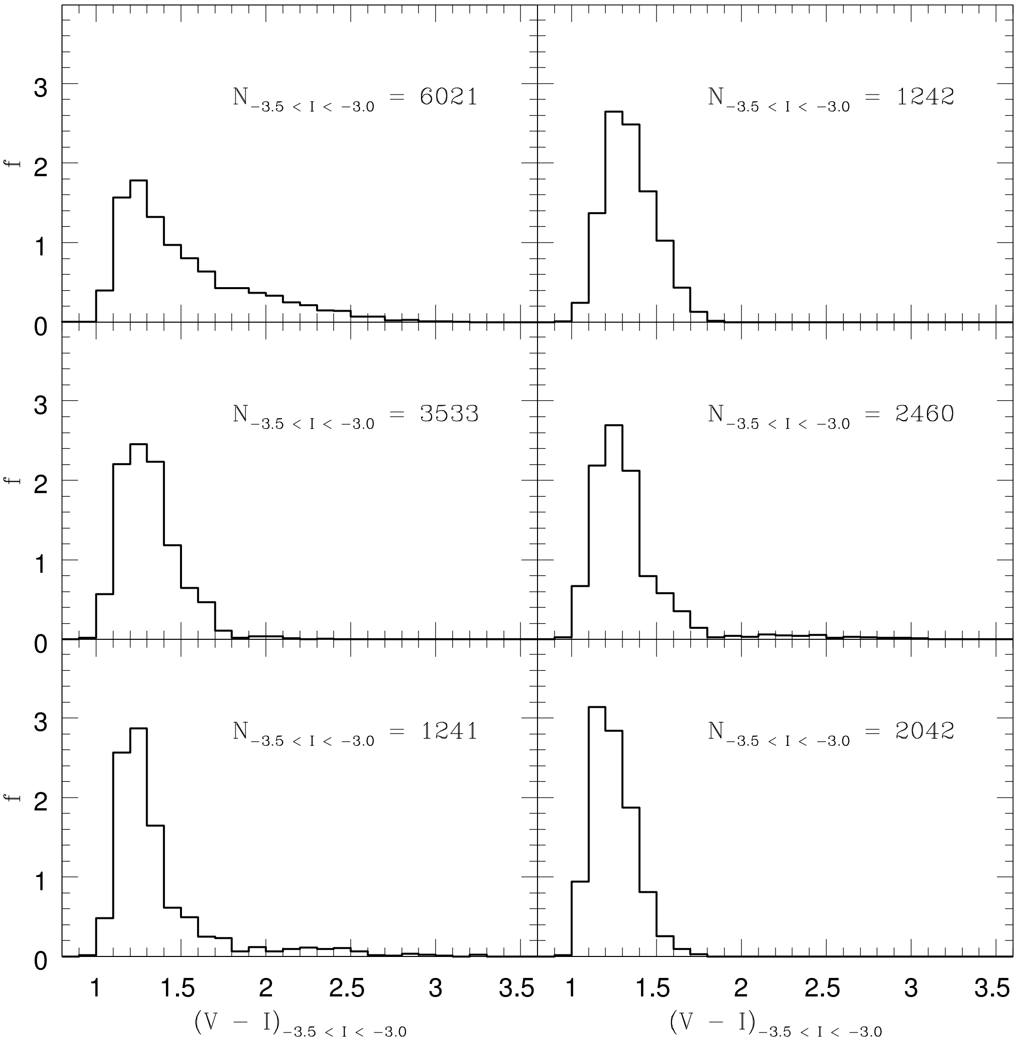

Figure G.3: (continued) Halo synthetic CMD (V - I) colour distribution at -3.5 < I < -3.0 for the $M_{tot} = 5\times10^{11}$ $M_{\odot}$ semi–cosmological simulations in Renda et al. (2005b). Each panel also shows the number of generated stars at -3.5 < I < -3.0 in each synthetic CMD.

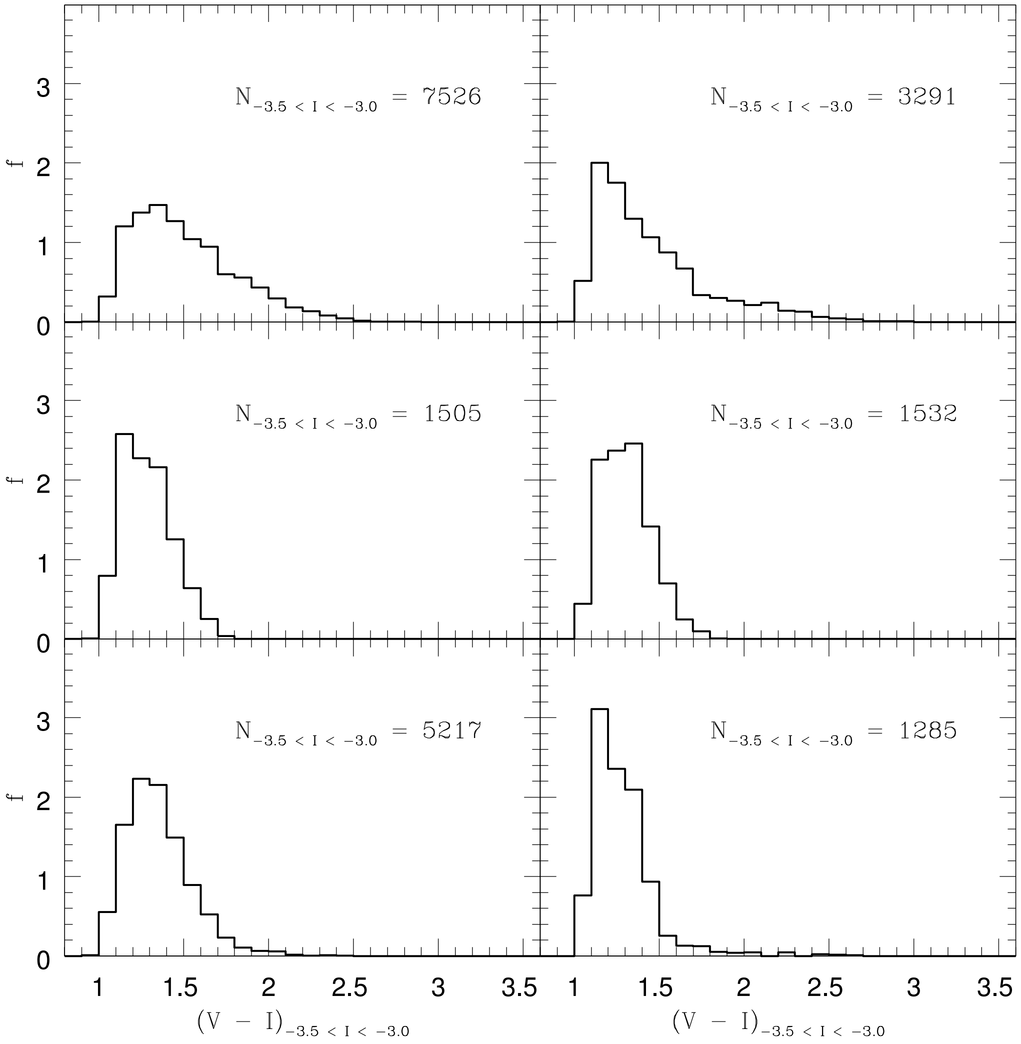

Figure G.4: (continued) Halo synthetic CMD (V - I) colour distribution at -3.5 < I < -3.0 for the $M_{\rm tot} = 5\times10^{11}$ $M_\odot$ semi–cosmological simulations in Renda et al. (2005b). Each panel also shows the number of generated stars at -3.5 < I < -3.0 in each synthetic CMD.

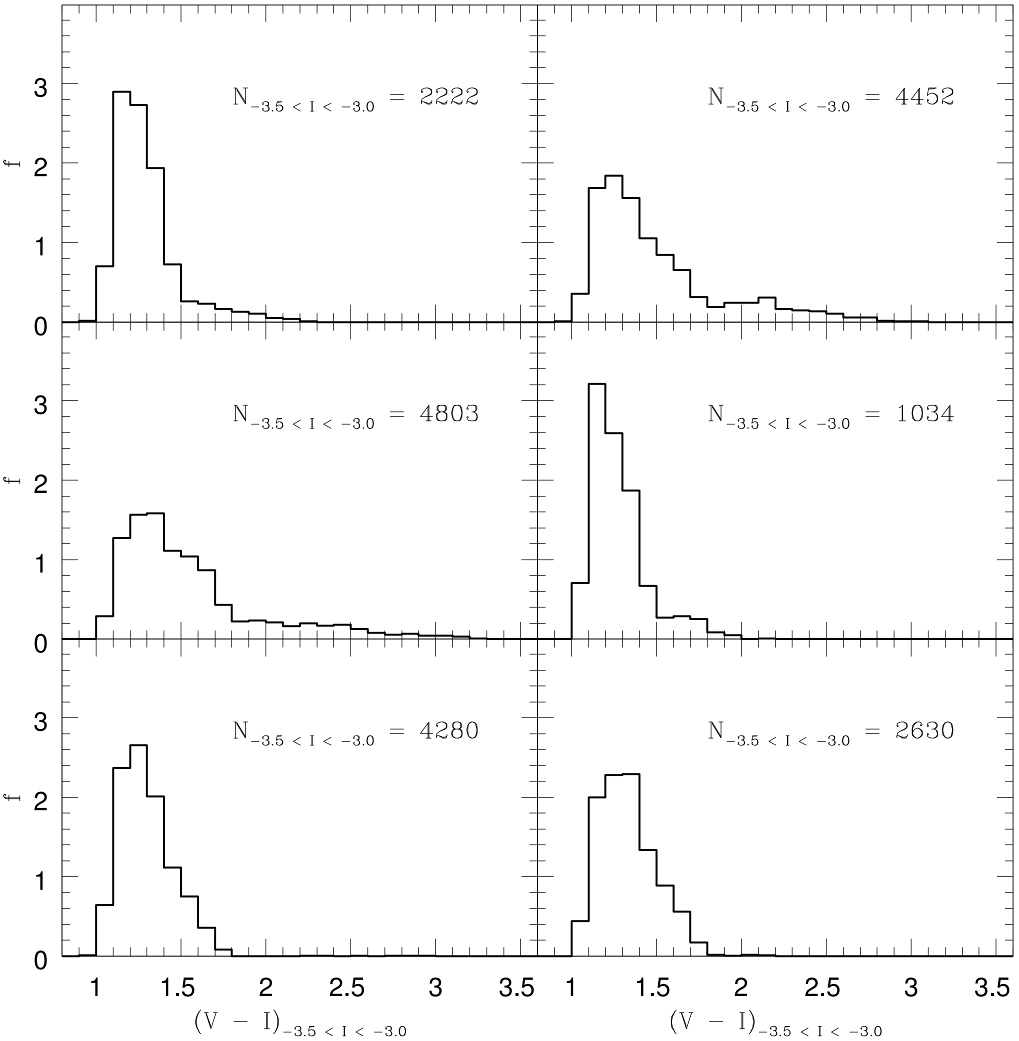

Figure G.5: Halo synthetic CMD (V - I) colour distribution at -3.5 < I < -3.0 for the $M_{tot} = 1{\times}10^{12}\ M_{\odot}$ semi–cosmological simulations in Renda et al. (2005b). Each panel also shows the number of generated stars at -3.5 < I < -3.0 in each synthetic CMD.

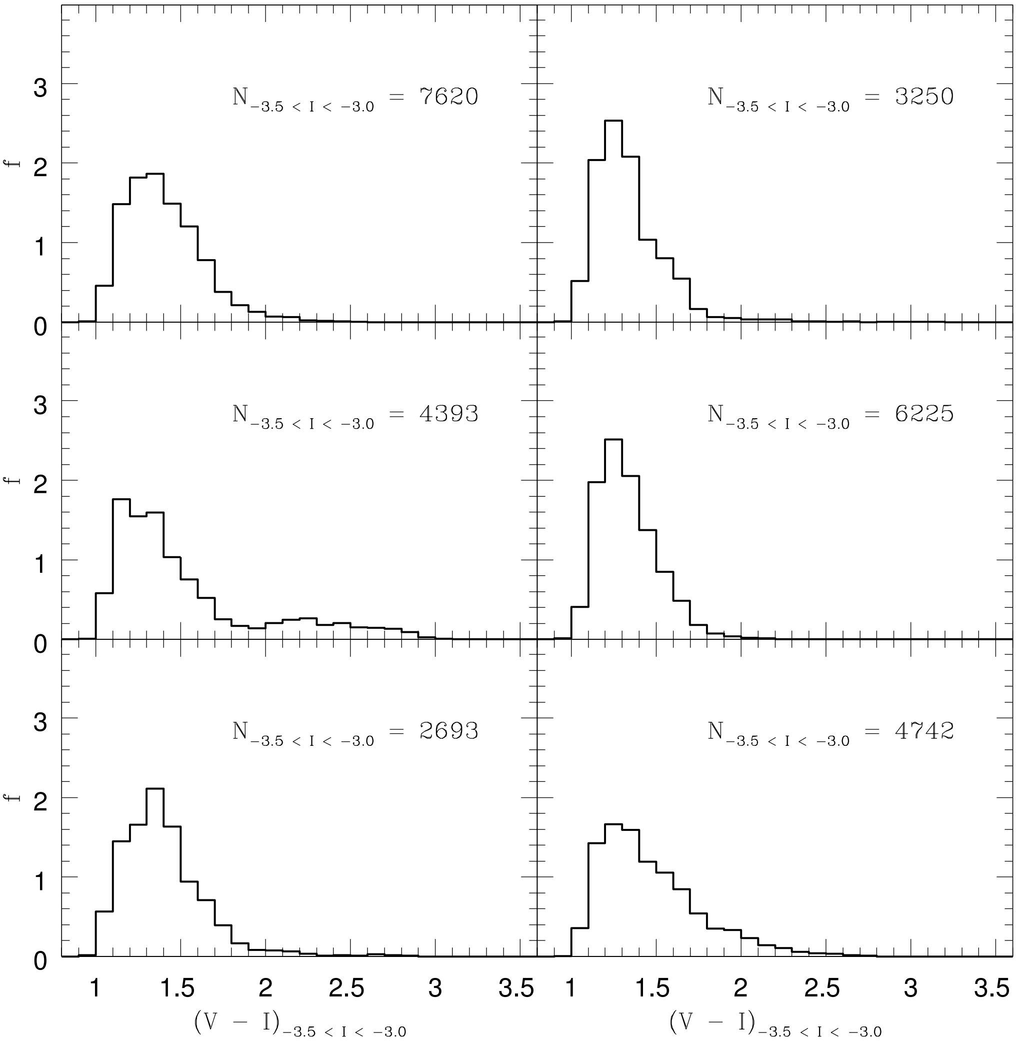

Figure G.6: (continued) Halo synthetic CMD (V - I) colour distribution at -3.5 < I < -3.0 for the $M_{tot} = 10^{12}$ $M_{\odot}$ semi–cosmological simulations in Renda et al. (2005b). Each panel also shows the number of generated stars at -3.5 < I < -3.0 in each synthetic CMD.

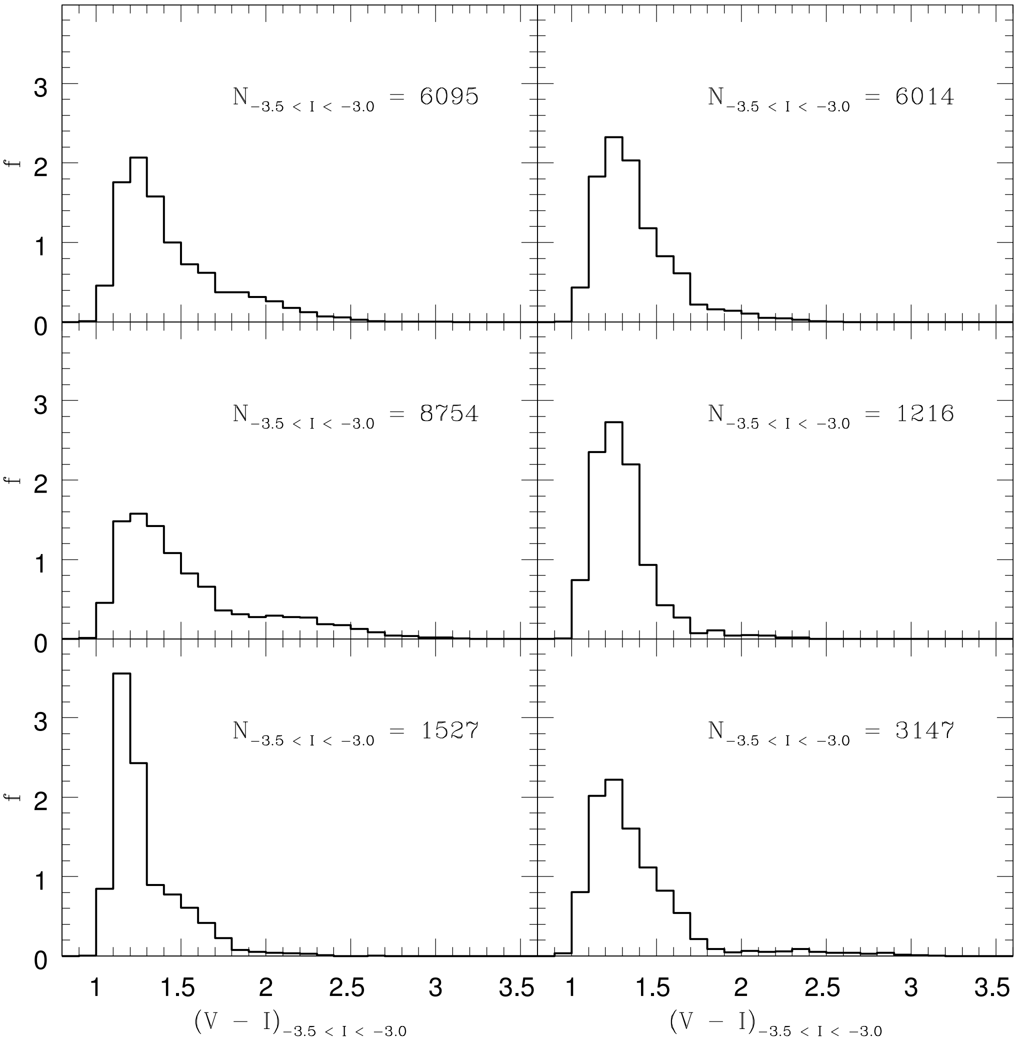

Figure G.7: (continued) Halo synthetic CMD (V - I) colour distribution at -3.5 < I < -3.0 for the $M_{tot} = 10^{12}\ M_{\odot}$ semi–cosmological simulations in Renda et al. (2005b). Each panel also shows the number of generated stars at -3.5 < I < -3.0 in each synthetic CMD.

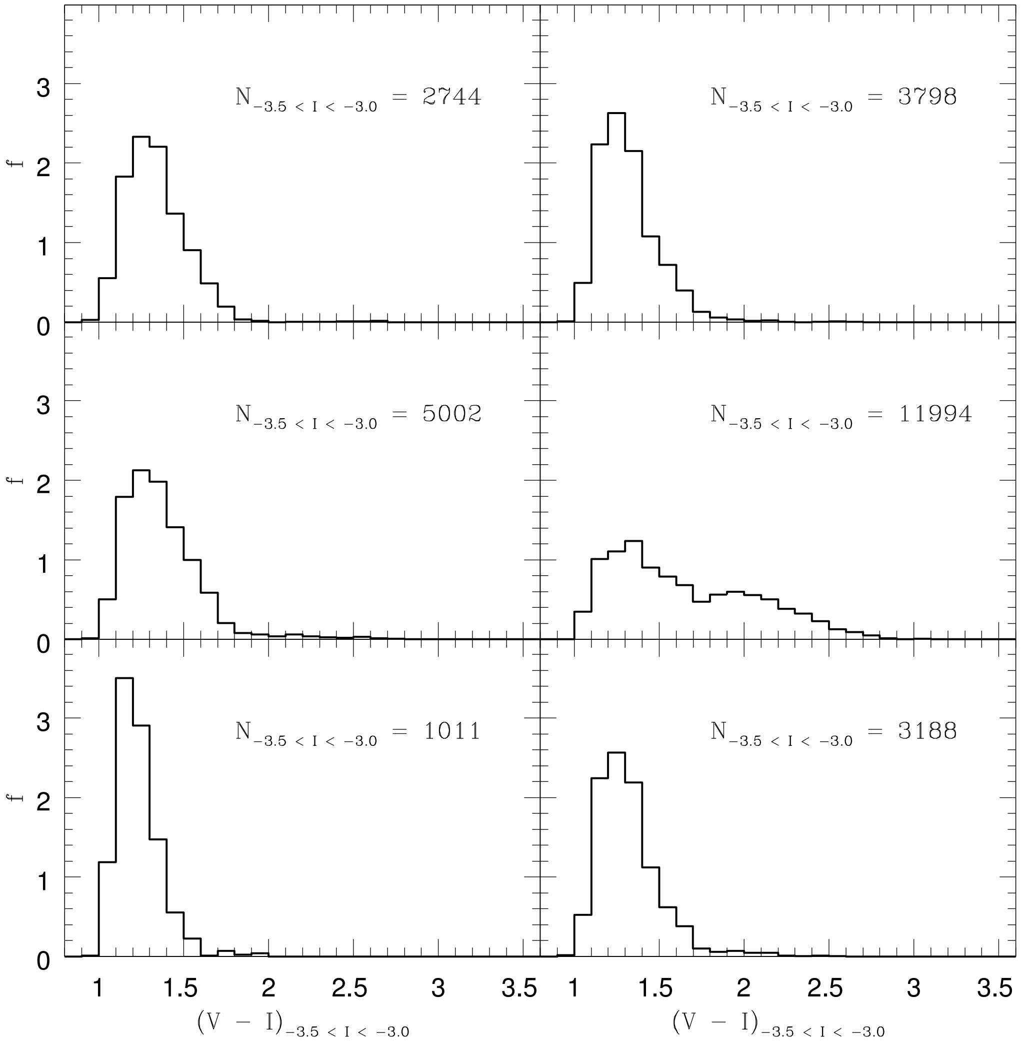

Figure G.8: (continued) Halo synthetic CMD (V - I) colour distribution at -3.5 < I < -3.0 for the M_{tot} = 10^{12} $M_{\odot}$ semi–cosmological simulations in Renda et al. (2005b). Each panel also shows the number of generated stars at -3.5 < I < -3.0 in each synthetic CMD.

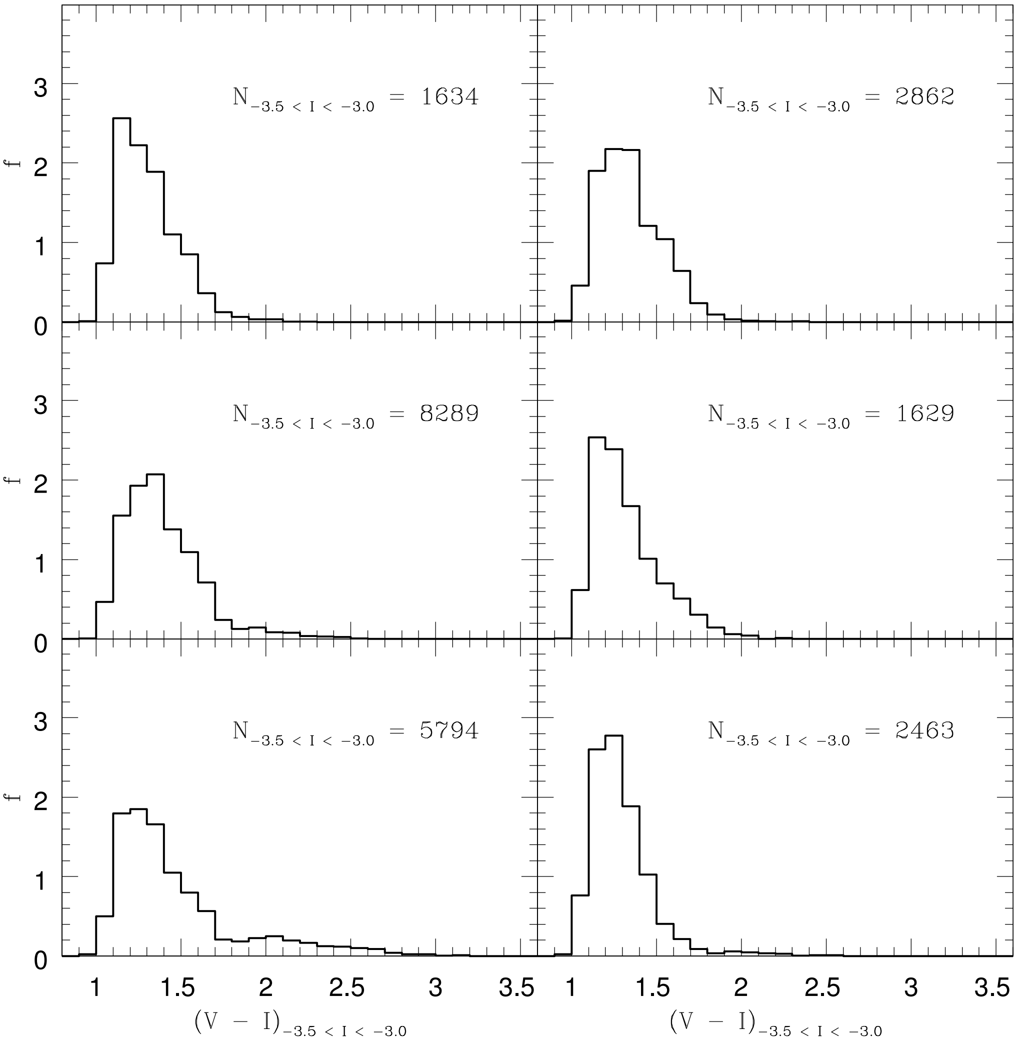

Figure G.9: (continued) Halo synthetic CMD (V - I) colour distribution at -3.5 < I < -3.0 for the $M_{tot} = 10^{12}$ $M_{\odot}$ semi–cosmological simulations in Renda et al. (2005b). Each panel also shows the number of generated stars at -3.5 < I < -3.0 in each synthetic CMD.

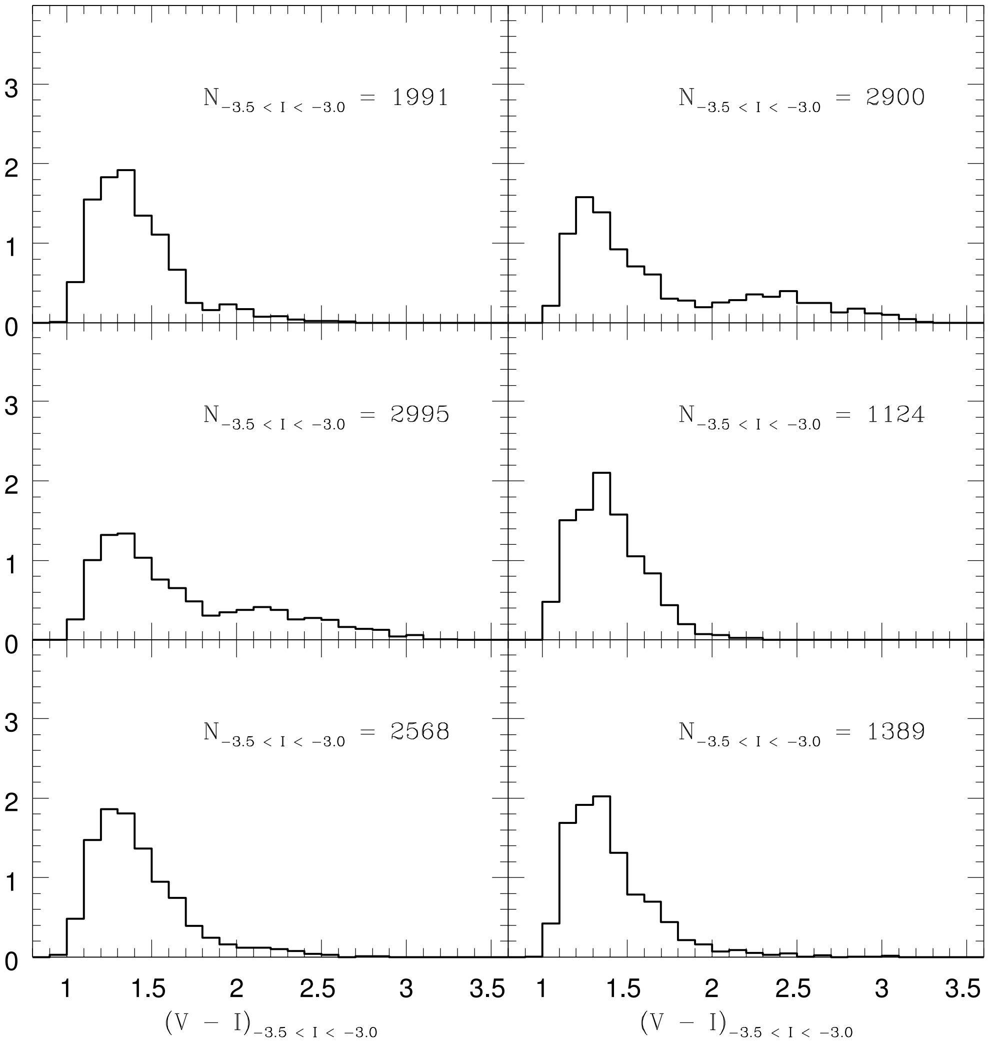

Figure G.10: Halo synthetic CMD (V - I) colour distribution at -3.5 $<$ I $<$ -3.0 for the $M_{tot} = 5\times10^{12}$ $M_\odot$ semi–cosmological simulations in Renda et al. (2005b). Each panel also shows the number of generated stars at -3.5 $<$ I $<$ -3.0 in each synthetic CMD.

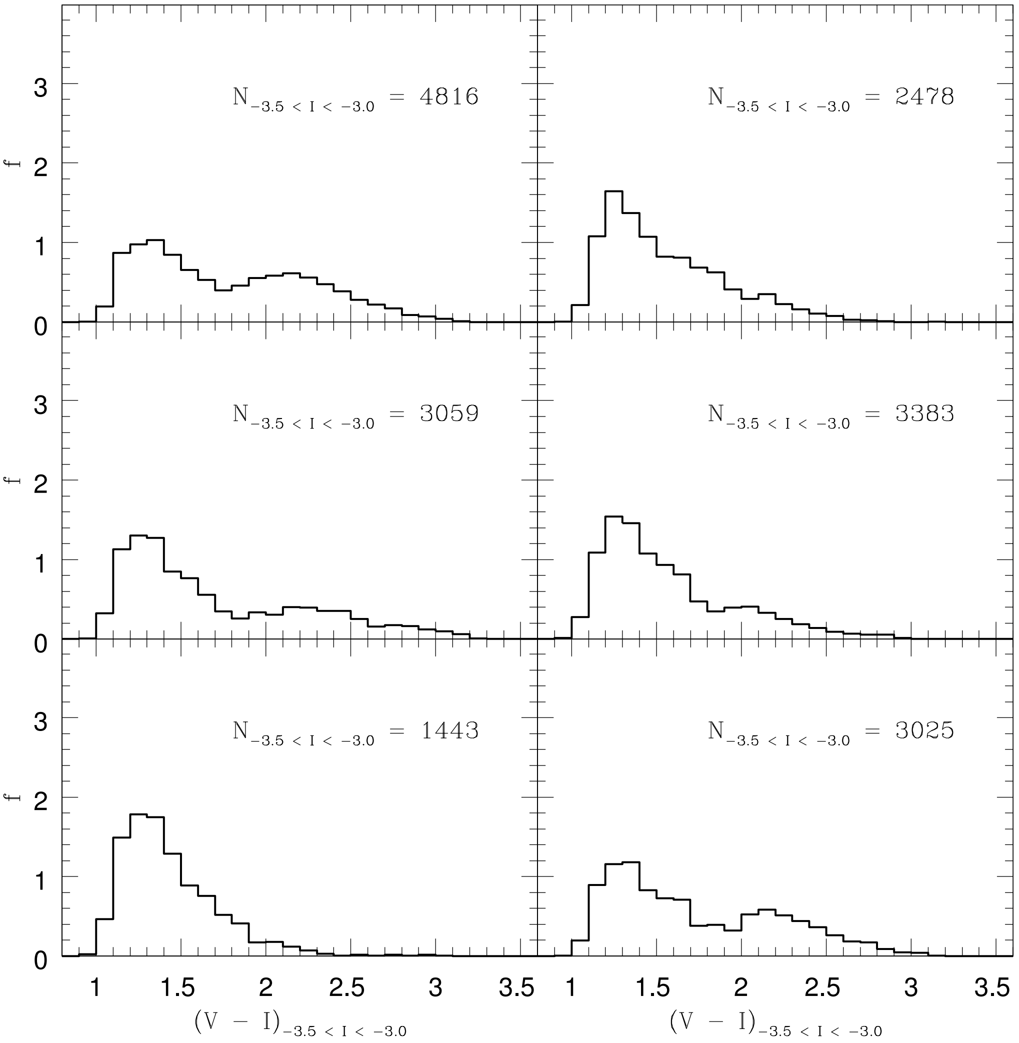

Figure G.11: (continued) Halo synthetic CMD (V - I) colour distribution at -3.5 < I < -3.0 for the $M_{tot} = 5\times10^{12}$ $M_\odot$ semi–cosmological simulations in Renda et al. (2005b). Each panel also shows the number of generated stars at -3.5 < I < -3.0 in each synthetic CMD.

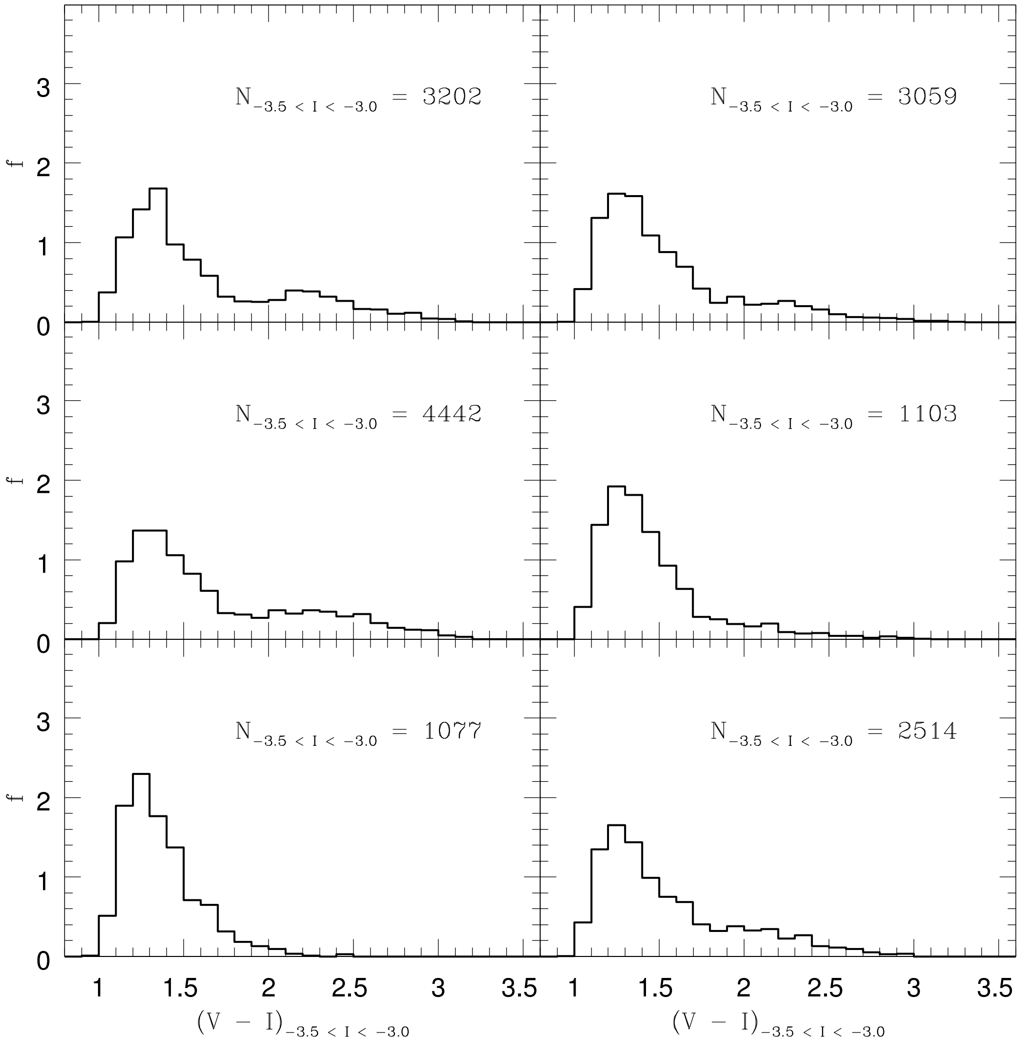

Figure G.12: (continued) Halo synthetic CMD (V - I) colour distribution at -3.5 < I < -3.0 for the $M_{tot} = 5\times10^{12}$ $M_\odot$ semi–cosmological simulations in Renda et al. (2005b). Each panel also shows the number of generated stars at -3.5 < I < -3.0 in each synthetic CMD.

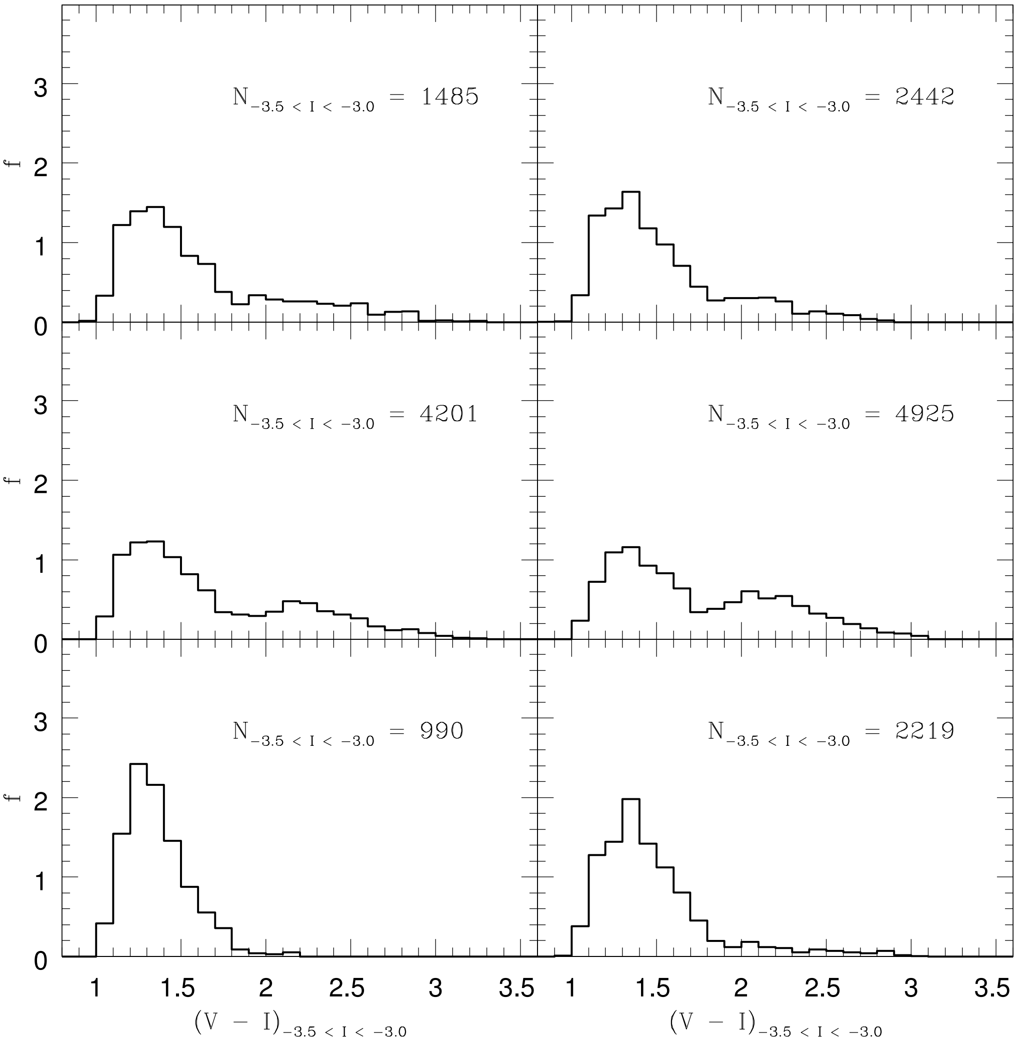

Figure G.13: (continued) Halo synthetic CMD (V - I) colour distribution at -3.5 < I < -3.0 for the $M_{tot} = 5\times10^{12}\ M_\odot$ semi–cosmological simulations in Renda et al. (2005b). Each panel also shows the number of generated stars at -3.5 < I < -3.0 in each synthetic CMD.

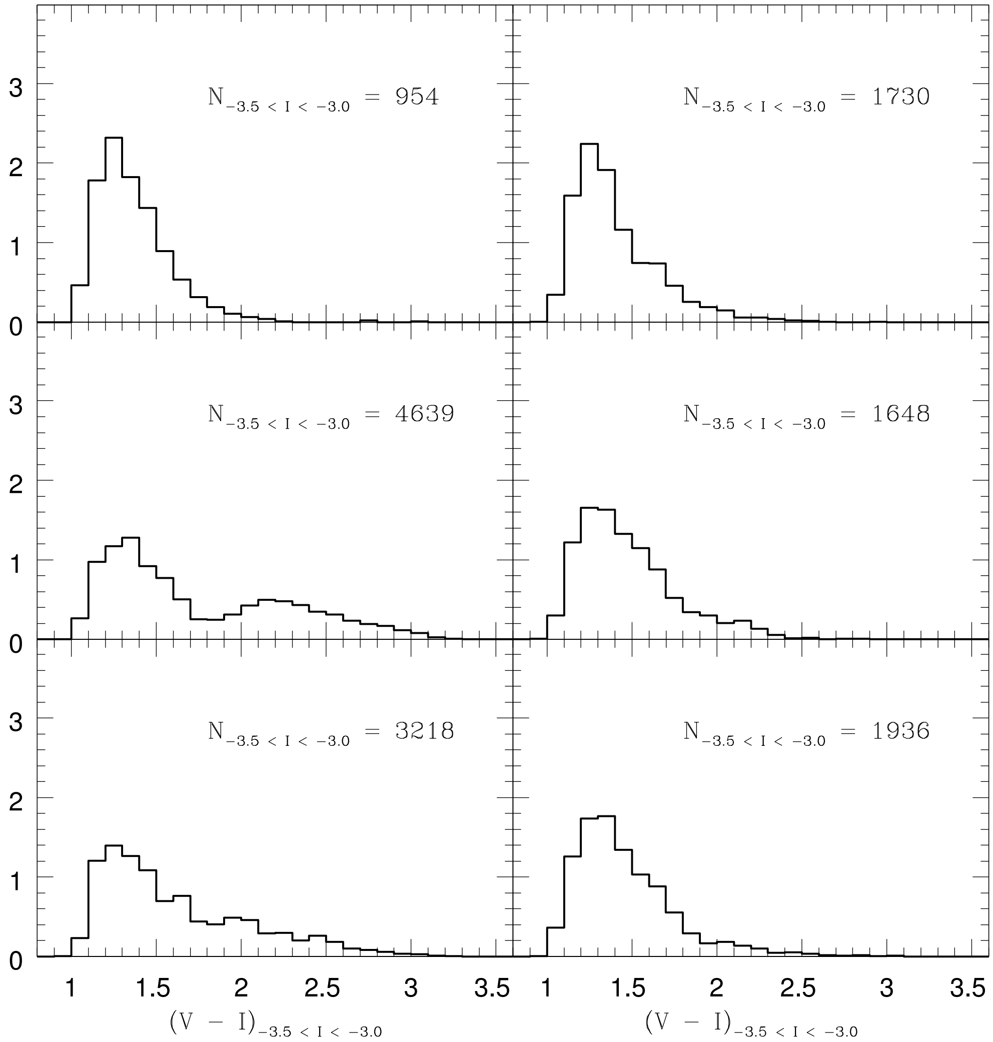

Figure G.14: (continued) Halo synthetic CMD (V - I) colour distribution at -3.5 $<$ I $<$ -3.0 for the M_{tot} = 5×10^{12} $M_{\odot}$ semi–cosmological simulations in Renda et al. (2005b). Each panel also shows the number of generated stars at -3.5 $<$ I $<$ -3.0 in each synthetic CMD.

Appendix H

Stellar Halo MDFs via Metallicity–Colour Relationship

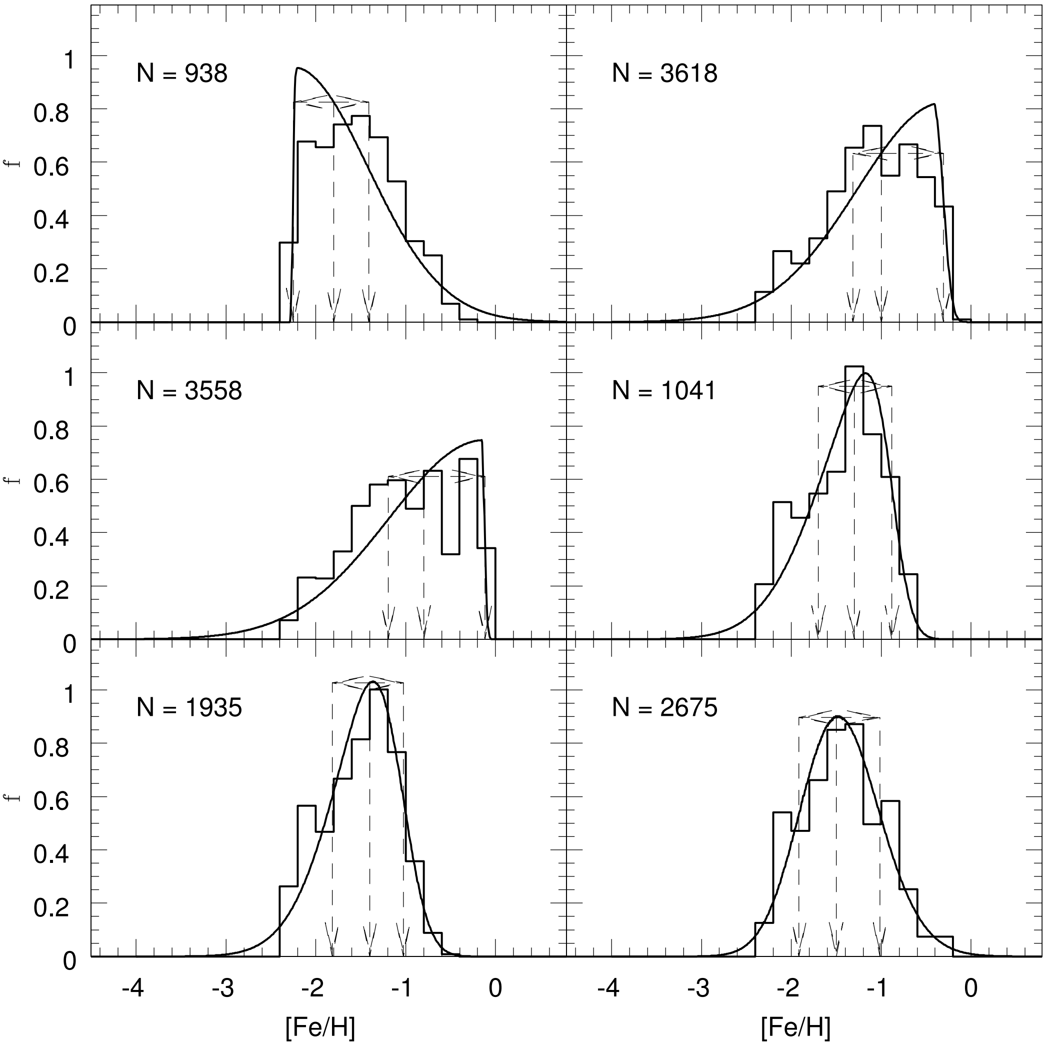

Figure H.1: Halo MDF via Metallicity–Colour relationship by the same pipeline as in Mouhcine et al. (2005) for the $M_{tot} = 5\times10^{11}$ $M_{\odot}$ semi–cosmological simulations in Renda et al. (2005b). The 68% Confidence Level range and the number of stellar particles each MDF refers to are also shown.

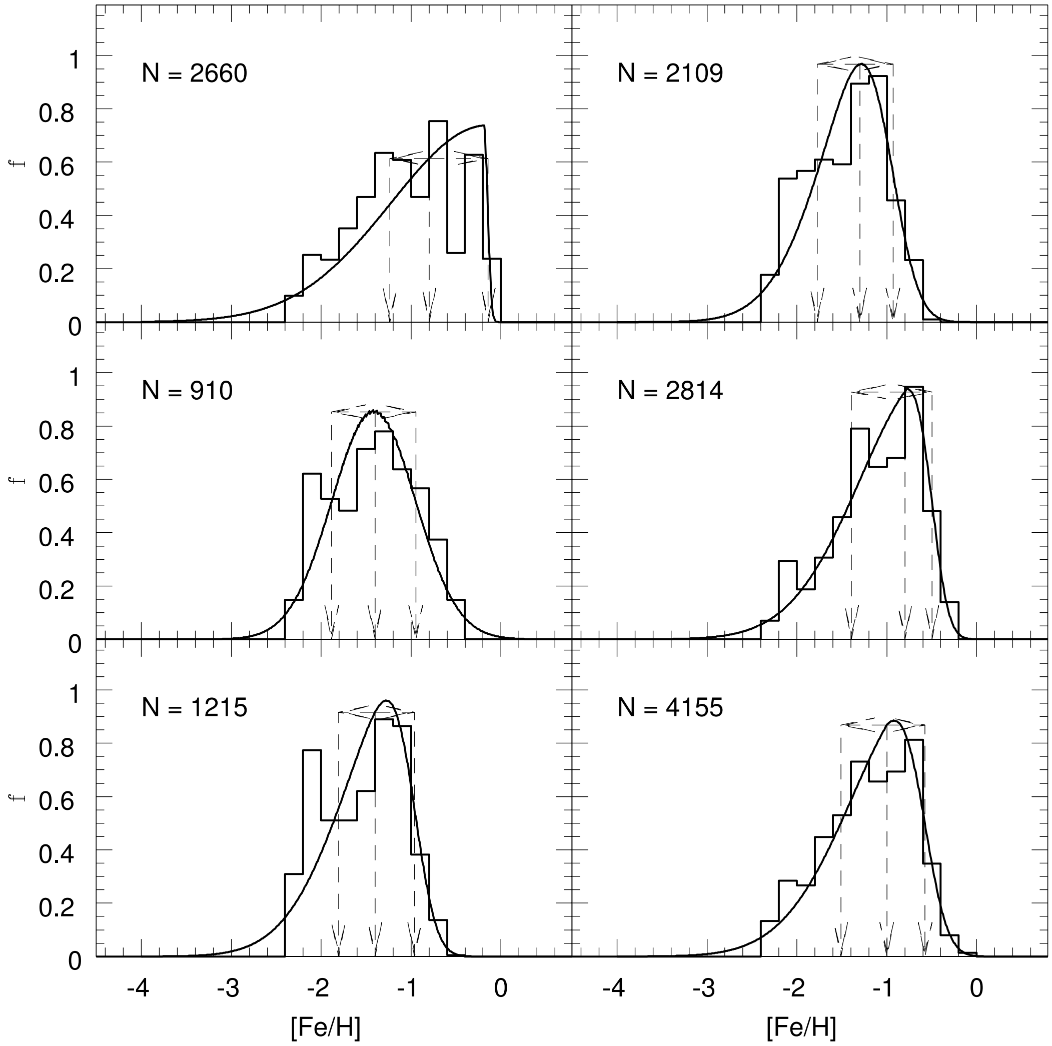

Figure H.2: (continued) Halo MDF via Metallicity–Colour relationship by the same pipeline as in Mouhcine et al. (2005) for the $M_{tot} = 5 \times 10^{11}\ M_{\odot}$ semi–cosmological simulations in Renda et al. (2005b). The 68% Confidence Level range and the number of stellar particles each MDF refers to are also shown.

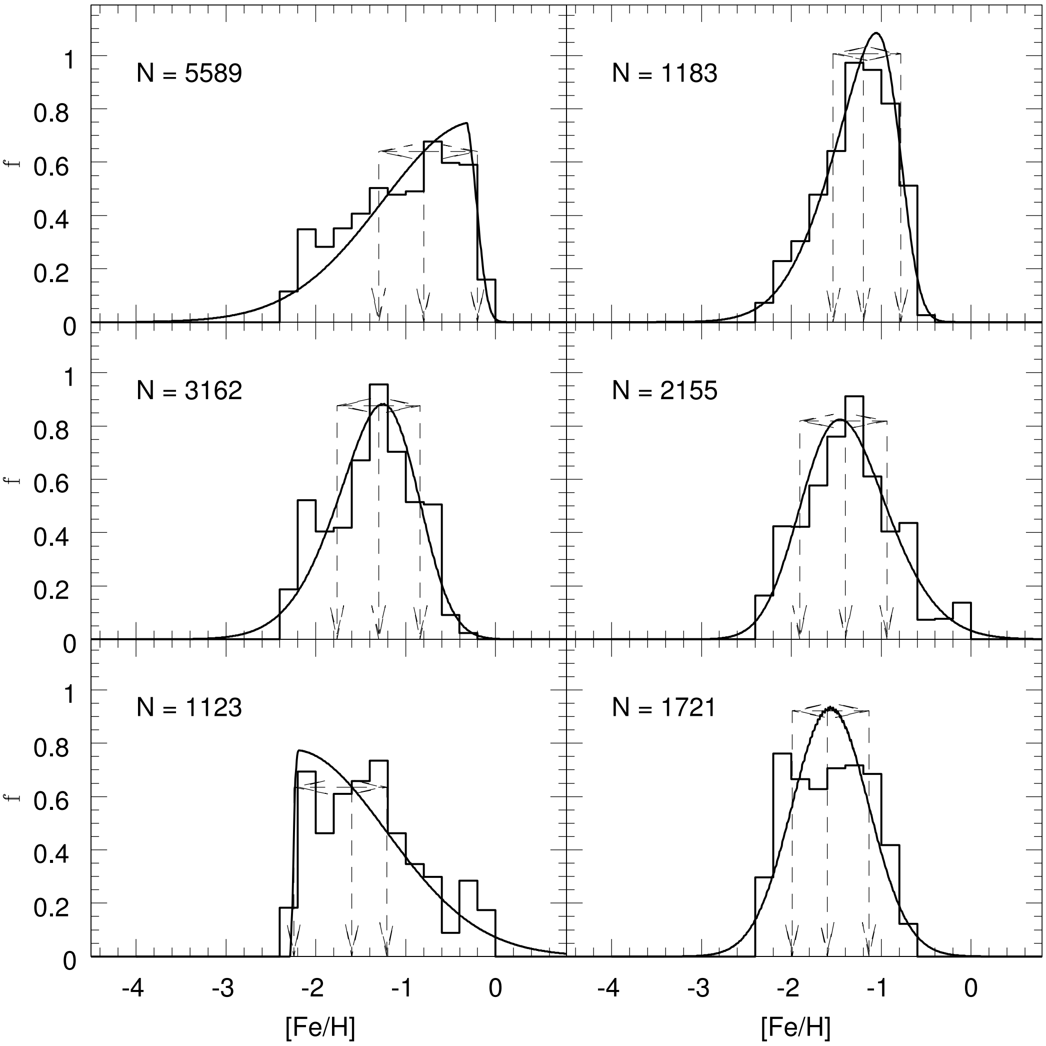

Figure H.3: (continued) Halo MDF via Metallicity–Colour relationship by the same pipeline as in Mouhcine et al. (2005) for the $M_{tot} = 5\times10^{11}$ $M_\odot$ semi–cosmological simulations in Renda et al. (2005b). The 68% Confidence Level range and the number of stellar particles each MDF refers to are also shown.

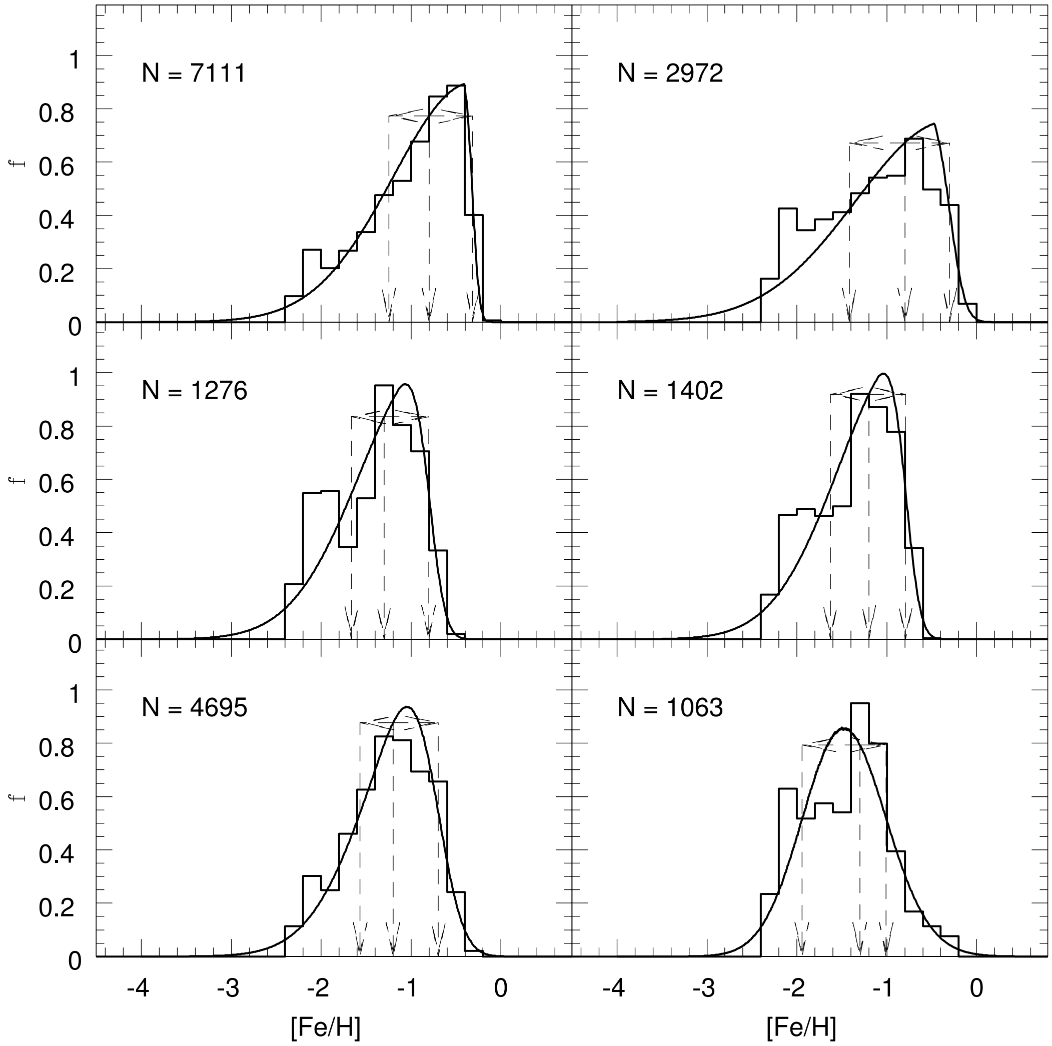

Figure H.4: (continued) Halo MDF via Metallicity–Colour relationship by the same pipeline as in Mouhcine et al. (2005) for the $M_{tot} = 5\times10^{11}$ $M_\odot$ semi–cosmological simulations in Renda et al. (2005b). The 68% Confidence Level range and the number of stellar particles each MDF refers to are also shown.

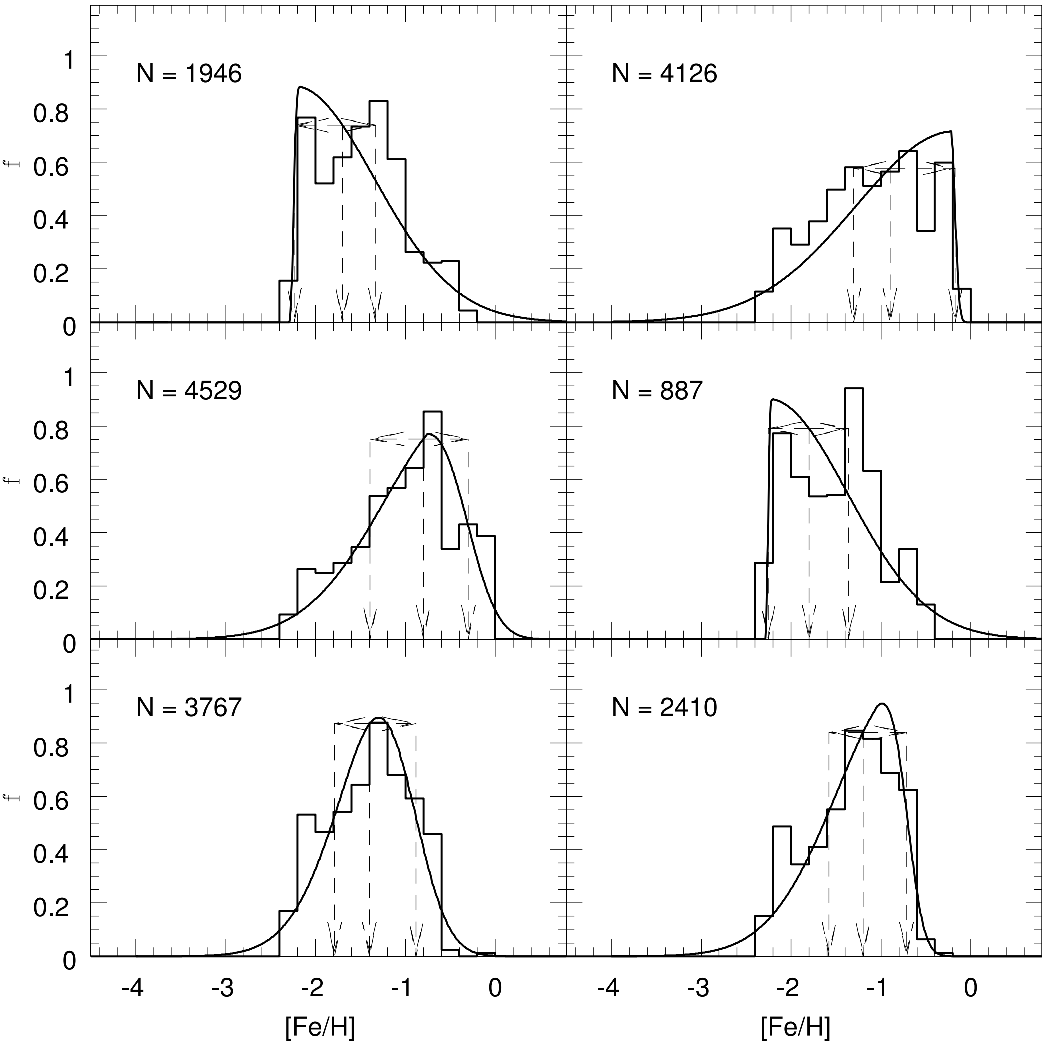

Figure H.5: Halo MDF via Metallicity–Colour relationship by the same pipeline as in Mouhcine et al. (2005) for the $M_{\rm tot} = 10^{12}$ $M_\odot$ semi–cosmological simulations in Renda et al. (2005b). The 68% Confidence Level range and the number of stellar particles each MDF refers to are also shown.

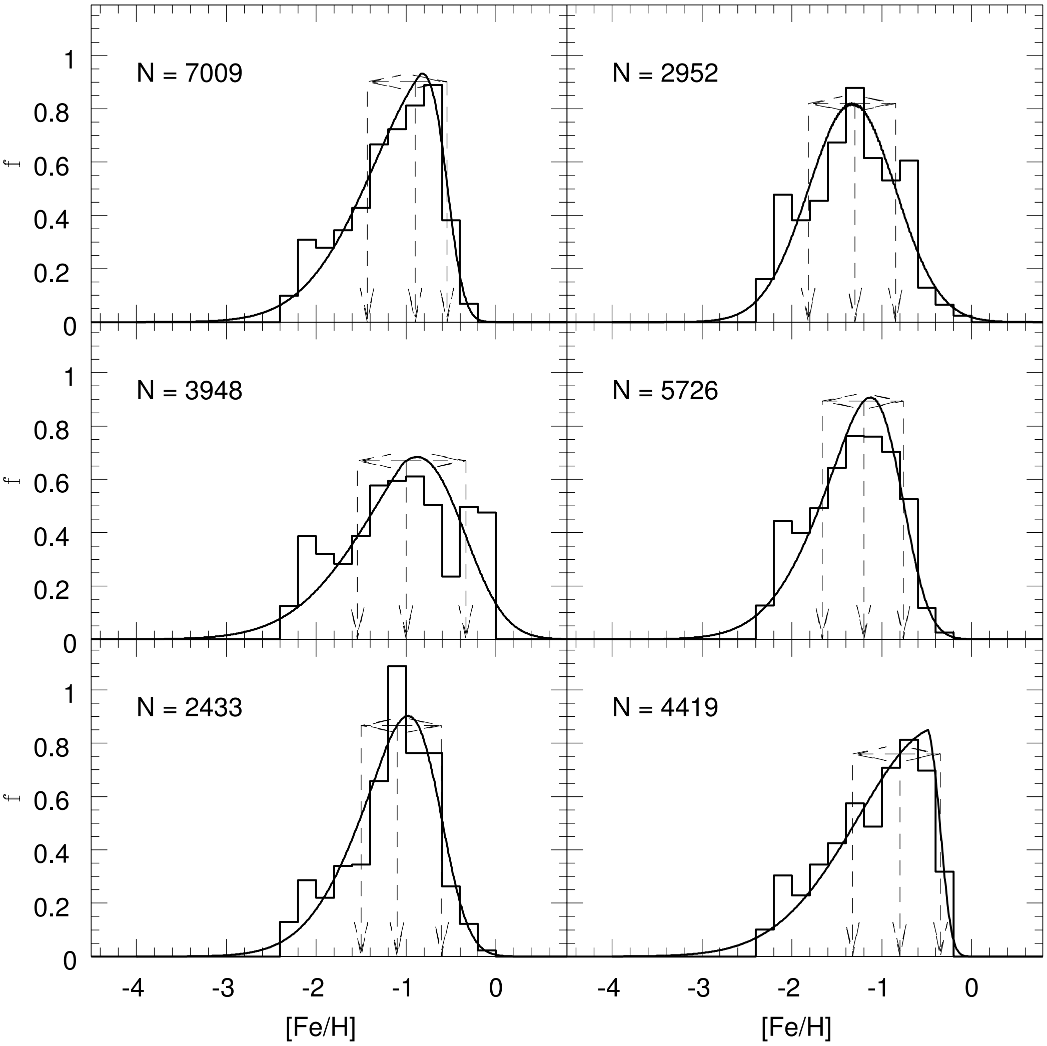

Figure H.6: (continued) Halo MDF via Metallicity–Colour relationship by the same pipeline as in Mouhcine et al. (2005) for the $M_{tot} = 10^{12}\ M_{\odot}$ semi–cosmological simulations in Renda et al. (2005b). The 68% Confidence Level range and the number of stellar particles each MDF refers to are also shown.

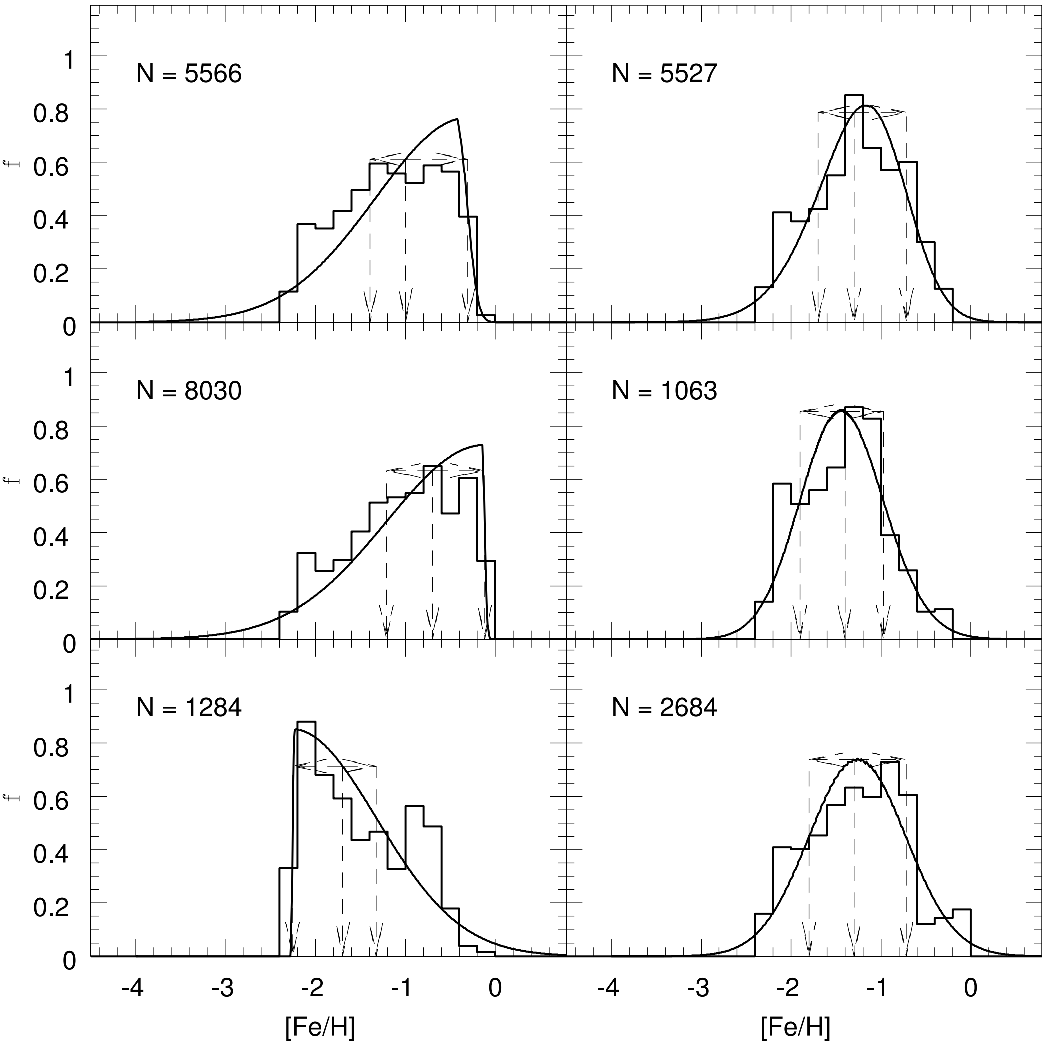

Figure H.7: (continued) Halo MDF via Metallicity–Colour relationship by the same pipeline as in Mouhcine et al. (2005) for the $M_{tot} = 10^{12}$ $M_\odot$ semi–cosmological simulations in Renda et al. (2005b). The 68% Confidence Level range and the number of stellar particles each MDF refers to are also shown.

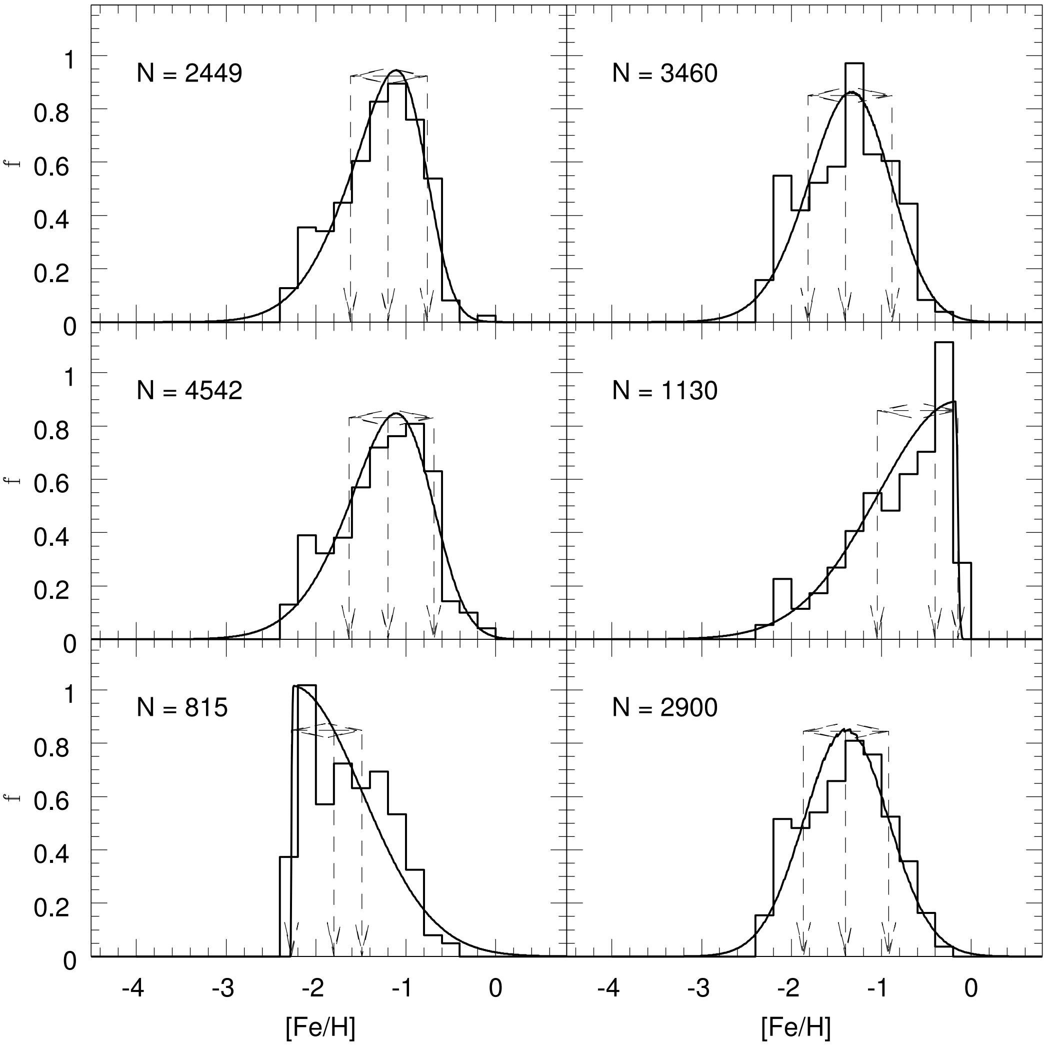

Figure H.8: (continued) Halo MDF via Metallicity–Colour relationship by the same pipeline as in Mouhcine et al. (2005) for the $M_{tot} = 10^{12}$ $M_{\odot}$ semi–cosmological simulations in Renda et al. (2005b). The 68% Confidence Level range and the number of stellar particles each MDF refers to are also shown.

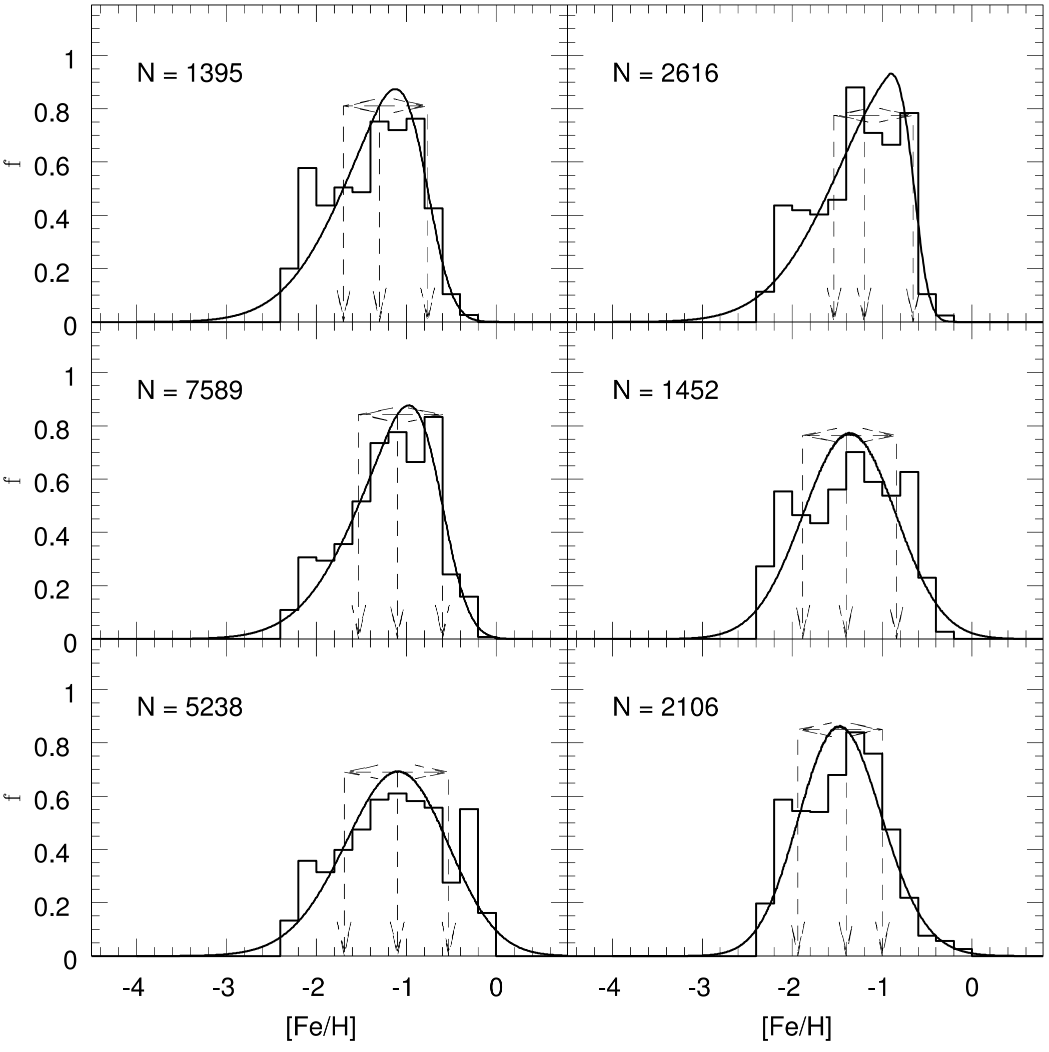

Figure H.9: (continued) Halo MDF via Metallicity–Colour relationship by the same pipeline as in Mouhcine et al. (2005) for the $M_{tot} = 10^{12} M_{\odot}$ semi–cosmological simulations in Renda et al. (2005b). The 68% Confidence Level range and the number of stellar particles each MDF refers to are also shown.

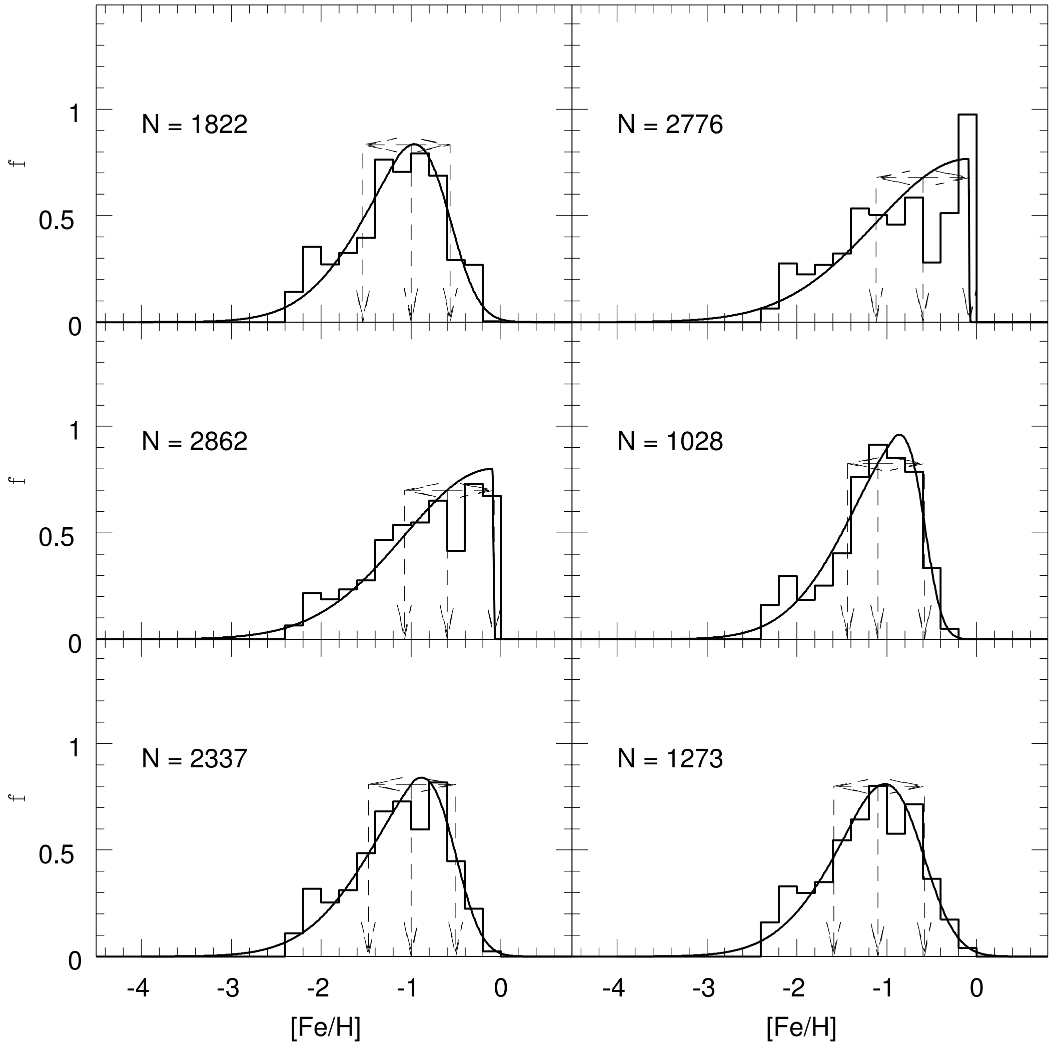

Figure H.10: Halo MDF via Metallicity–Colour relationship by the same pipeline as in Mouhcine et al. (2005) for the $M_{tot} = 5 \times 10^{12}$ $M_\odot$ semi–cosmological simulations in Renda et al. (2005b). The 68% Confidence Level range and the number of stellar particles each MDF refers to are also shown.

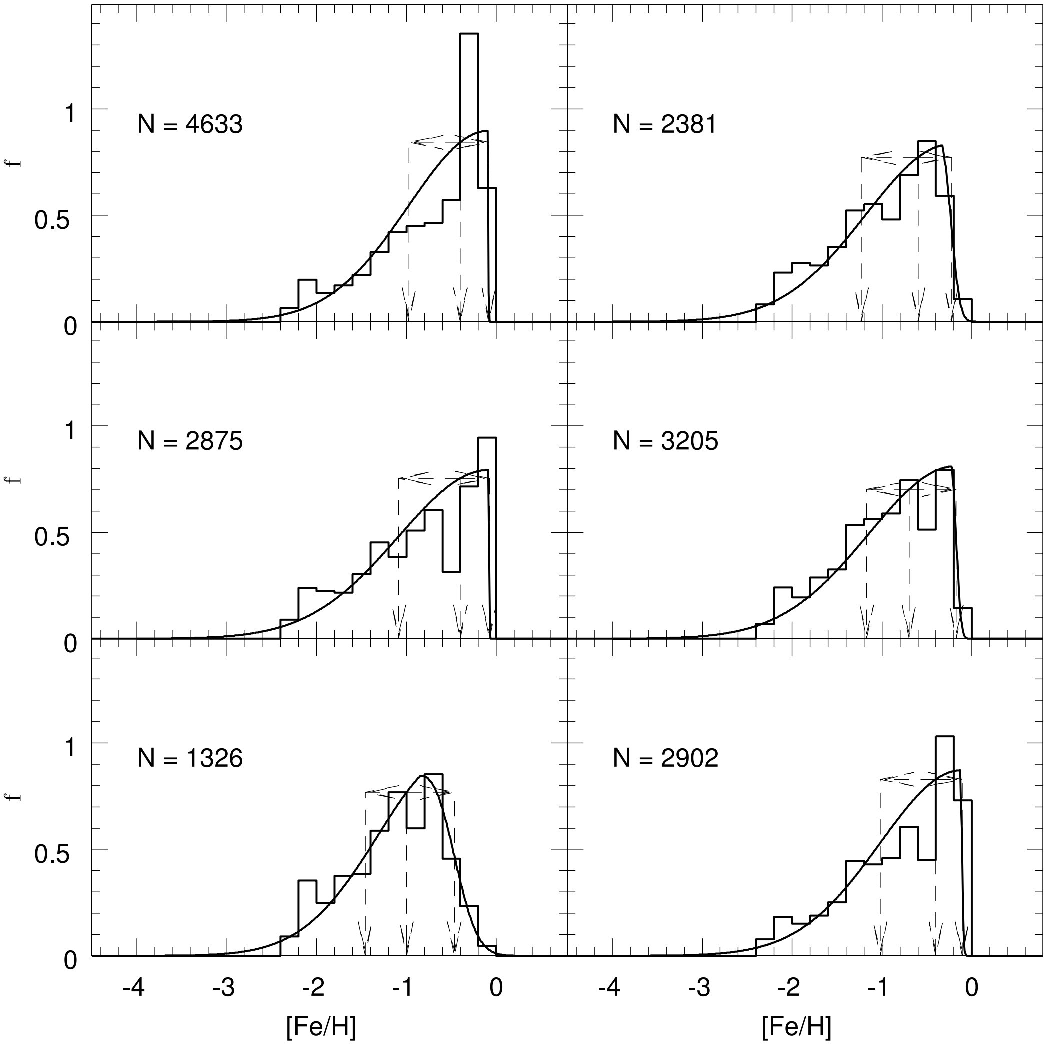

Figure H.11: (continued) Halo MDF via Metallicity–Colour relationship by the same pipeline as in Mouhcine et al. (2005) for the $M_{tot} = 5\times10^{12}$ $M_\odot$ semi–cosmological simulations in Renda et al. (2005b). The 68% Confidence Level range and the number of stellar particles each MDF refers to are also shown.

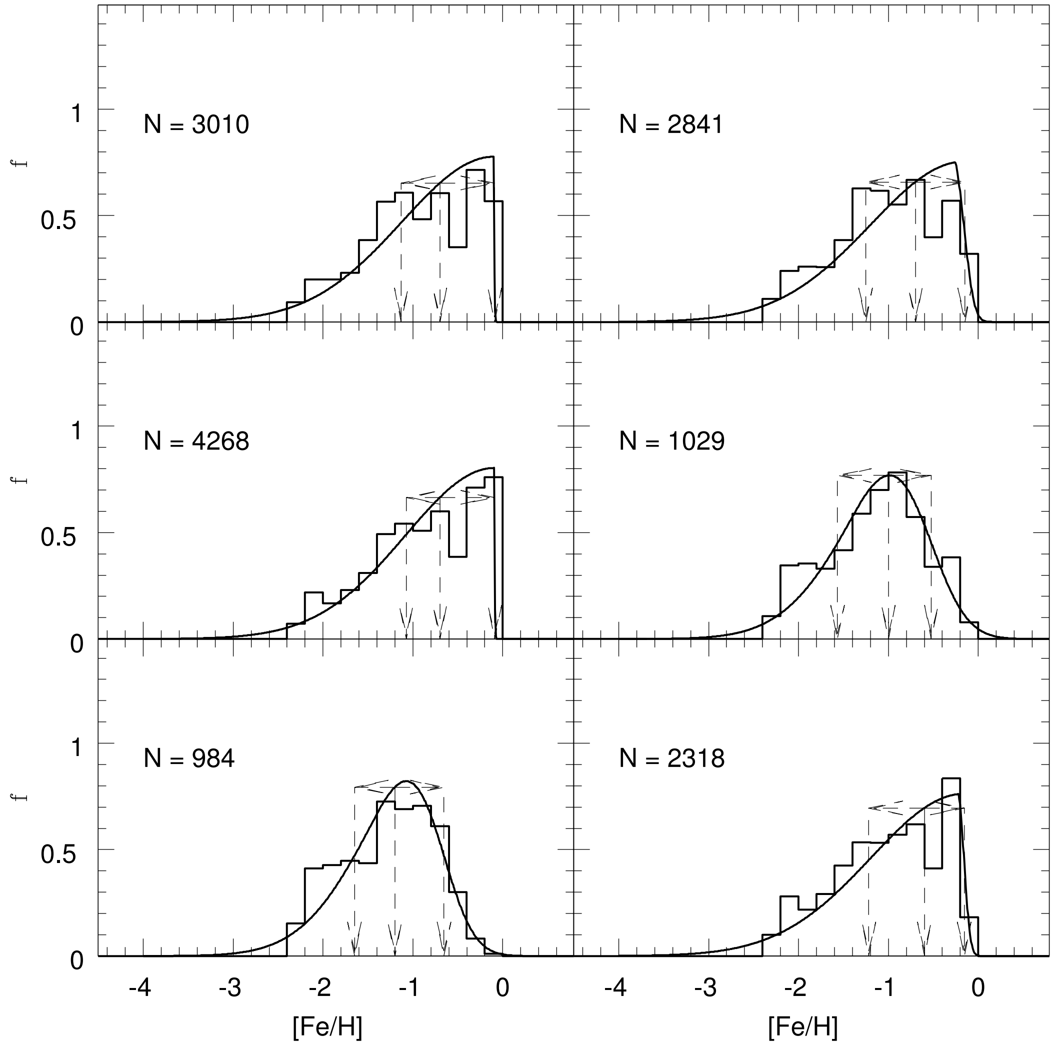

Figure H.12: (continued) Halo MDF via Metallicity–Colour relationship by the same pipeline as in Mouhcine et al. (2005) for the $M_{tot} = 5\times10^{12}$ $M_\odot$ semi–cosmological simulations in Renda et al. (2005b). The 68% Confidence Level range and the number of stellar particles each MDF refers to are also shown.

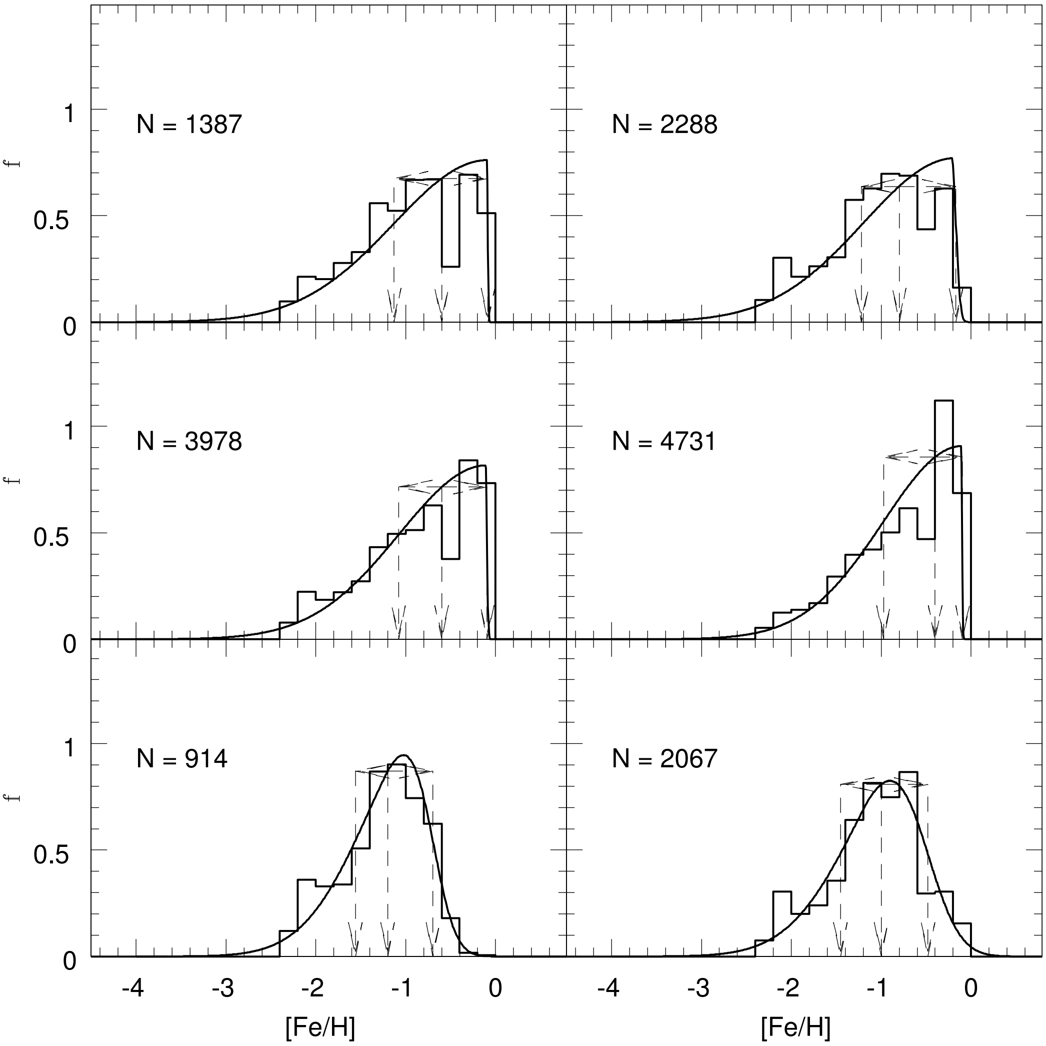

Figure H.13: (continued) Halo MDF via Metallicity–Colour relationship by the same pipeline as in Mouhcine et al. (2005) for the $M_{\mathrm{tot}} = 5\times10^{12}$ $M_{\odot}$ semi–cosmological simulations in Renda et al. (2005b). The 68% Confidence Level range and the number of stellar particles each MDF refers to are also shown.

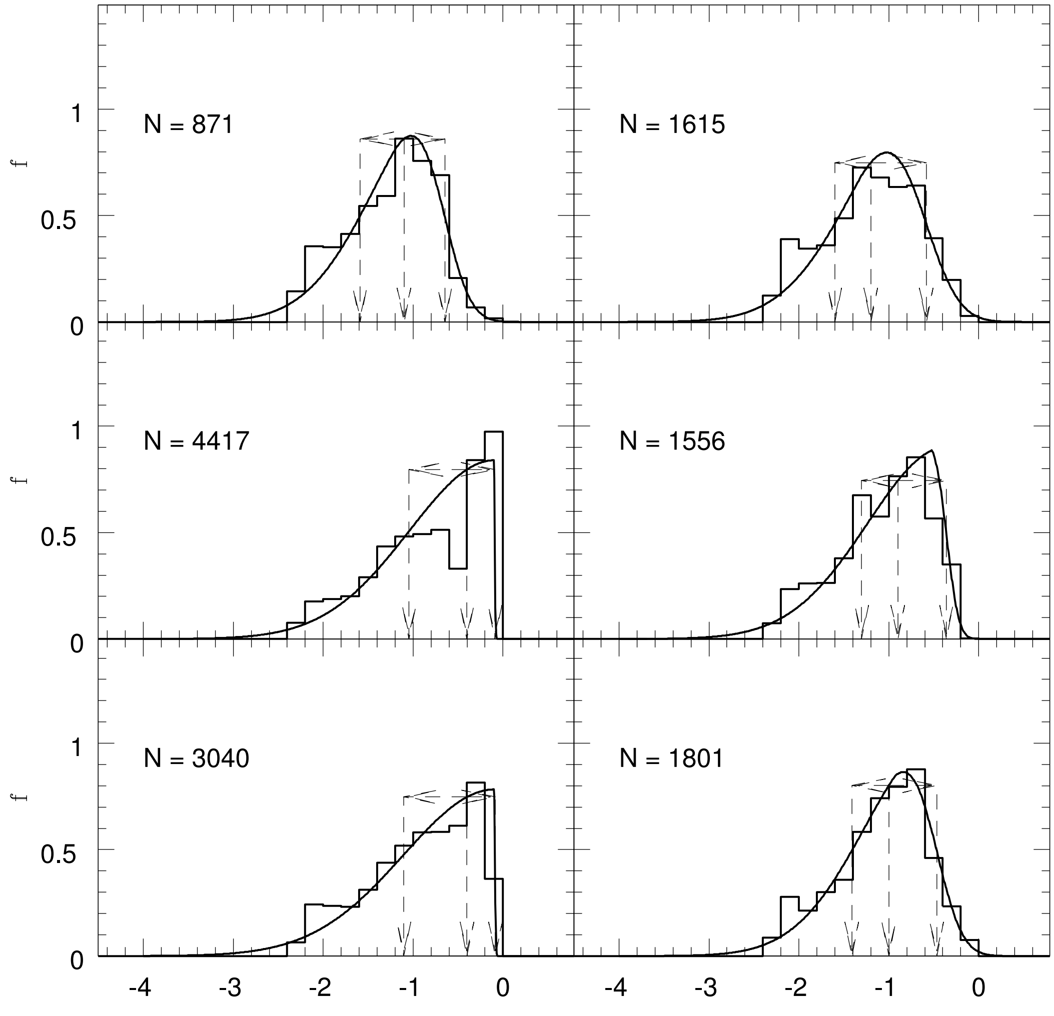

Figure H.14: (continued) Halo MDF via Metallicity–Colour relationship by the same pipeline as in Mouhcine et al. (2005) for the $M_{tot} = 5 \times 10^{12}$ $M_{\odot}$ semi–cosmological simulations in Renda et al. (2005b). The 68% Confidence Level range and the number of stellar particles each MDF refers to are also shown.

Bibliography

Abadi M.G., Navarro J.F., Steinmetz M., Eke V.R., 2003, ApJ, 591, 499

Afflerbach A., Churchwell E., Werner M.W., 1997, ApJ, 478, 190

Alibés A., Labay J., Canal R., 2001, A&A, 370, 1103

Allende Prieto C., Lambert D.L., Asplund M., 2001, ApJ, 556, L63

Asplund A., in "Elemental Abundances in Old Stars and Damped Lyman α Systems", 25th meeting of the IAU, Joint Discussion 15, 2003, Sydney, Australia

Azzalini A., 2005, Scand. J. Stat., 32, 159

Bahcall N.A., Ostriker J.P., Perlmutter S., Steinhardt P.J., 1999, Science, 284, 1481

Bailin J., Kawata D., Gibson B.K., Steinmetz M., Navarro J.F., Brook C.B., Gill S.P.D., Ibata R.A., Knebe A., Lewis G.F., Okamoto T., 2005, ApJ, 627, L17

Bekki K., Chiba M., 2001, ApJ, 558, 666

Bekki K., Harris W.E., Harris G.L.H., 2003, MNRAS, 338, 587

Bekki K., Freeman K.C., 2003, MNRAS, 346, L11

Bell E.F., 2003, ApJ, 586, 794

Bellazzini M., Cacciari C., Federici L., Fusi Pecci F., Rich M., 2003, A&A, 405, 867

Bensby T., Feltzing S., Lundström L., 2004, A&A, 415, 155

Bertelli G., Nasi E., 2001, AJ, 121, 1013

Bertschinger E., 1998, ARA&A, 36, 599

Binney J., Tremaine S., Galactic dynamics, 1987, Princeton University Press, Princeton

Binney J., Merrifield M., 1998, Galactic Astronomy, Princeton University Press, Princeton, New Jersey, USA

Blair W.P., Kirshner R.P., Chevalier R.A., 1982, ApJ, 254, 50

Blanton M.R., Schlegel D.J., Strauss M.A., Brinkmann J., Finkbeiner D., Fukugita M., Gunn J.E., Hogg D.W., Ivezić Ž., Knapp G.R., Lupton R.H., Munn J.A., Schneider D.P., Tegmark M., Zehavi I., 2005, AJ, 129, 2562

Böhm A., Ziegler B.L., 2006, `astro-ph/0601505`

Brodie J.P., Huchra J.P., 1991, ApJ, 379, 157

Brook C.B., Kawata D., Gibson B.K., Flynn C., 2003, ApJ, 585, L125

Brook C.B., Kawata D., Gibson B.K., Flynn C., 2004, MNRAS, 349, 52

Brooks R.S., Wilson C.D., Harris W.E., 2004, AJ, 128, 237

Brown T.M., Ferguson H.C., Smith E., Kimble R.A., Sweigart A.V., Renzini A., Rich R.M., VandenBerg D.A., 2003, ApJ, 592, L17

Cappellaro E., Evans R., Turatto M., 1999, A&A, 351, 459

Carretta E., Gratton R.G., Sneden C., 2000, A&A, 356, 238

Cayrel R., Depagne E., Spite M., Hill V., Spite F., François P., Plez B., Beers T., Primas F., Andersen J., Barbuy B., Bonifacio P., Molaro P., Nordström B., 2004, A&A, 416, 1117

Chang R.X., Hou J.L., Shu C.G., Fu C.Q., 1999, A&A, 350, 38

Chapman S.C., Ibata R.A., Lewis G.F., Ferguson A.M.N., Irwin M., McConnachie A.W., Tanvir N.R., 2006, ApJ, 653, 255

Chiappini C., Matteucci F., Gratton R., 1997, ApJ, 477, 765

Chiba M., Beers T.C., 2000, AJ, 119, 2843

Chiba M., Beers T.C., 2001, ApJ, 549, 325

Conselice C.J., Bundy K., Ellis R.S., Brichmann J., Vogt N.P., Phillips A.C., 2005, ApJ, 628, 160

Cowie L., Songaila A., 1998, Nature, 394, 44

Cunha K., Smith V.V., Lambert D.L., Hinkle K.H., 2003, AJ, 126, 1305

Dame T.M., 1993, in Holt S.S., Verter F. Ed., “Back to the Galaxy”, AIP Conf. 278

Dame T.M., Koper E., Israel F.P., Thaddeus P., 1993, ApJ, 418, 730

Dekel A., Silk J., 1986, ApJ, 303, 39

Dennefeld M., Kunth D., 1981, AJ, 86, 989

Devereux N.A., Price R., Wells L.A., Duric N., 1994, AJ, 108, 1667

Diaz A.I., Tosi M., 1984, MNRAS, 208, 365

Dray L.M., Tout C.A., Karakas A.I., Lattanzio J.C., 2003, MNRAS, 338, 973

Durrell P.R., Harris W.E., Pritchet C.J., 2001, AJ, 121, 2557

Durrell P.R., Harris W.E., Pritchet C.J, 2004, AJ, 128, 260

Edvardsson B., Andersen J., Gustafsson B., Lambert D.L., Nissen P.E., Tomkin J., 1993, A&A, 275, 101

Efstathiou G., 2000, MNRAS, 317, 697

Eggen O.J., Lynden-Bell D., Sandage A.R., 1962, ApJ, 136, 748

Ellison S.L., Kewley L.J., 2005, `astro-ph/0508627`

Elson R.A.W., 1997, MNRAS, 286, 771

Erb D.K., Steidel C.C., Shapley A.C., Pettini M., Reddy N.A., Adelberger K.L., 2006, ApJ, 646, 107

Fenner Y., Gibson B.K., 2003, PASA, 20, 189

Ferguson A.M.N., Johnson R.A., 2001, ApJ, 559, L13

Ferguson A.M.N., Irwin M.J., Ibata R.A., Lewis G.F., Tanvir N.R., 2002, AJ, 124, 1452

Ferguson A.M.N., Johnson R.A., Faria D.C., Irwin M.J., Ibata R.A., Johnston K.V., Lewis G.F., Tanvir N.R., 2005, ApJ, 622, L109

Flores H., Hammer F., Puech M., Amram P., Balkowski C., 2006, A&A, 455, 107

Forestini M., Goriely S., Jorissen A., Arnould M., 1992, A&A, 261, 157

Freeman K.C., 1999, in Gibson B.K., Axelrod T.S., Putman M.E. Ed., "The Third Stromlo Symposium: The Galactic Halo", ASP Conference Series, Vol. 165

Freeman K., Bland-Hawthorn J., 2002, ARA&A, 40, 487

Freudenreich H.T., 1998, ApJ, 492, 495

Frost C.A., Lattanzio J.C., 1996, ApJ, 473, 383

Frost C.A., Cannon R.C., Lattanzio J.C., Wood P.R., Forestini M., 1998, A&A, 332, L17

Fukugita M., Ichikawa T., Gunn J.E., Doi M., Shimasaku K., Schneider D.P., 1996, AJ, 111, 1748

Gallazzi A., Charlot S., Brinchmann J., White S.D.M., Tremonti C.A., 2005, MNRAS, 362, 41

Garnett D.R., Shields G.A., 1987, ApJ, 317, 82

Garnett D.R., Shields G.A., Skillman E.D., Sagan S.P., Dufour R.J., 1997, ApJ, 489, 63

Gibson B.K., Fenner Y., Renda A., Kawata D., Lee H.-C., 2003, PASA, 20, 401

Girardi L., Bertelli G., Bressan A., Chiosi C., Groenewegen M.A.T., Marigo P., Salasnich B., Weiss A., 2002, A&A, 391, 195

Goswami A., Prantzos N., 2000, A&A, 359, 191

Gratton R.G., Carretta E., Claudi R., Lucatello S., Barbieri M., 2003, A&A, 404, 187

Greggio L., Renzini A., 1983, A&A, 118, 217

Hammer F., Gruel N., Thuan T.X., Flores H., Infante L., 2001, ApJ, 550, 570

Hammer F., Puech M., Chemin L., Flores H., Lehnert M., 2007, `astro-ph/0702585`

Harris G.L.H., Harris W.E., Poole G.B., 1999, AJ, 117, 855

Harris W.E., Harris G.L.H., 2001, AJ, 122, 3065

Heger A., Kolbe E., Haxton W.C., Langanke K., Martinez-Pinedo G., Woosley S.E., Physics Letters B, 2005, 606, 258

Helmi A., White S.D.M., de Zeeuw P.T., Zhao, H., 1999, Nature, 402, 53

Hernandez X., Valls-Gabaud D., Gilmore G., 2000, MNRAS, 316, 605

Holland S., Fahlman G.G., Richer H.B., 1996, AJ, 112, 1035

Holweger H., 2001, in Wimmer-Schweingruber R.F. Ed., AIP Conf. Proc. 598, “Solar and Galactic Composition“. Am. Inst. Phys., New York

Ibata R.A., Irwin M.J., Lewis G.F., Ferguson A.M.N., Tanvir N.R., 2001, Nature, 412, 49

Ibata R.A., Lewis G.F., Irwin M.J., Cambrésy L., 2002, MNRAS, 332, 921

Ibata R.A., Chapman S., Ferguson A.M.N., Irwin M.J., Lewis G.F., McConnachie A.W., 2004, MNRAS, 351, 117

Ibata R.A., Martin N.F., Irwin M.J., Chapman S., Ferguson A.M.N., Lewis G.F., McConnachie A.W., 2007, `arXiv:0704.1318 [astro-ph]`

Iglesias C.A., Rogers F.J., 1996, ApJ, 464, 943

Iwamoto K., Brachwitz F., Nomoto K., Kishimoto N., Umeda H., Hix W.R., Thielemann F.-K., 1999, ApJS, 125, 439

Irwin M.J., Ferguson A.M.N., Ibata R.A., Lewis G.F., Tanvir N.R., 2005, ApJ, 628, L105

Jorissen A., Smith V.V., Lambert D.L., 1992, A&A, 261, 164

Kalirai J.S., Gilbert K.M., Guhathakurta P., Majewski S.R., Ostheimer J.C., Rich R.M., Cooper M.C., Reitzel D.B., Patterson R.J., 2006, ApJ, 648, 389

Karakas A.I., Lattanzio J.C., Pols O.R., 2002, PASA, 19, 515

Karakas A.I., Lattanzio J.C., 2003, PASA, 20, 279

Katz N., Gunn J.E., 1991, ApJ, 377, 365

Kauffmann G., Heckman T.M., White S.D.M., Charlot S., Tremonti C., Peng E.W., Seibert M., Brinkmann J., Nichol R.C., SubbaRao M., York D., 2003, MNRAS, 341, 54

Kaufmann T., Mayer L., Wadsley J., Stadel J., Moore B., 2007, MNRAS, 375, 53

Kawata D., Gibson B.K., 2003, MNRAS, 340, 908

Kennicutt R.C., 1998, ARA&A, 36, 189

Kennicutt R.C., Bresolin F., Garnett D.R., 2003, ApJ, 591, 801

Kobulnicky H.A., Koo D.C., 2000, ApJ, 545, 712

Kobulnicky H.A., Willmer C.N.A., Phillips A.C., Koo D.C., Faber S.M., Weiner B.J., Sarajedini V.L., Simard L., Vogt N.P., 2003, ApJ, 599, 1006

Kobulnicky H.A., Kewley L.J., 2004, ApJ, 617, 240

Kotoneva E., Flynn C., Chiappini C., Matteucci F., 2002, MNRAS, 336, 879

Kraft R.P., Sneden C., Langer G.E., Prosser C.F., 1992, AJ, 104, 645

Kroupa P., Tout C.A., Gilmore G., 1993, MNRAS, 262, 545

Kuijken K., Gilmore G., 1991, ApJ, 367, L9

Lamareille F., Mouhcine M., Contini T., Lewis I., Maddox S., 2004, MNRAS, 350, 396

Lamareille F., Contini T., Brinchmann J., Le Borgne J.-F., Charlot S., Richard J., 2006, MNRAS, 448, 907

Larson R.B. in "The Initial Mass Function 50 years later", Corbelli E., Palla F., Zinnecker H. Ed., Kluwer Acad. Publ., Dordrecht

Lemoine-Busserolle M., Contini T., Pelló R., Le Borgne J.-F., Kneib J.-P., Lidman C., 2003, A&A, 397, 839

Lequeux J., Peimbert M., Rayo J.F., Serrano A., Torres-Peimbert S., 1979, A&A, 80, 155

Lewis G.F., Ibata R.A., Chapman S.C., Ferguson A.M.N., McConnachie A.W., Irwin M.J., Tanvir N.R., 2004, PASA, 21, 203

Liang Y. C., Hammer F., Flores H., Elbaz D., Marcillac D., Cesarsky C.J., 2004, A&A, 423, 867

Liang Y.C., Hammer F., Flores H., 2006, A&A, 447, 113

Lilly S.J., Le Fevre O., Hammer F., Crampton D., 1996, ApJ, 460, L1

Lilly S.J., Carollo C.M., Stockton A.N., 2003, ApJ, 597, 730

Limongi M., Chieffi A., 2003, ApJ, 592, 404

Loinard L., Dame T.M., Heyer M.H., Lequeux J., Thaddeus P., 1999, A&A, 351, 1087

Lugaro M., Ugalde C., Karakas A.I., Görres J., Wiescher M., Lattanzio J.C., Cannon R.C., 2004, ApJ, 615, 934

Madau P., Ferguson H.C., Dickinson M.E., Giavalisco M., Steidel C.C., Fruchter A., 1996, MNRAS, 283, 1388

Maier C., Meisenheimer K., Hippelein H., 2004, A&A, 418, 475

Maier C., Lilly S.J., Carollo C.M., Stockton A., Brodwin M., 2005, ApJ, 634, 849

Maier C., Lilly S.J., Carollo C.M., Meisenheimer K., Hippelein H., Stockton A., 2006, ApJ, 639, 858

Majewski S.R., Kunkel W.E., Law D.R., Patterson R.J., Polak A.A., Rocha-Pinto H.J., Crane J.D., Frinchaboy P.M., Hummels C.B., Johnston K.V., Rhee J., Skrutskie M.F., Weinberg M., 2004, AJ, 128, 245

Matteucci F., François P., 1989, MNRAS, 239, 885

McConnachie A.W., Irwin M.J., Ibata R.A., Ferguson A.M.N., Lewis G.F., Tanvir N.R., 2003, MNRAS, 343, 1335

McConnachie A.W., Chapman S.C., Ibata R.A., Ferguson A.M.N., Irwin M.J., Lewis G.F., Tanvir N.R., Martin N., 2006, ApJ, 647, L25

Mehlert D., Noll S., Appenzeller I., Saglia R.P., Bender R., Böhm A., Drory N., Fricke K., Gabasch A., Heidt J., Hopp U., Jäger K., Möllenhoff C., Seitz S., Stahl O., Ziegler B., 2002, A&A, 393, 809

Merrett H.R., Kuijken K., Merrifield M.R., Romanowsky A.J., Douglas N.G., Napolitano N.R., Arnaboldi M., Capaccioli M., Freeman K.C., Gerhard O., Evans N.W., Wilkinson M.I., Halliday C., Bridges T.J., Carter D., 2003, MNRAS, 346, L62

Meynet G., Arnould M., 2000, A&A, 355, 176

Mollá M., Ferrini F., Diaz A.I., 1996, ApJ, 466, 668

Mouhcine M., Lançon A., 2003, A&A, 402, 425

Mouhcine M., Ferguson H.C., Rich R.M., Brown T.M., Smith T.E., 2005, ApJ, 633, 810

Mouhcine M., Ferguson H.C., Rich R.M., Brown T.M., Smith T.E., 2005, ApJ, 633, 821

Mouhcine M., Rich R.M., Ferguson H.C., Rich R.M., Brown T.M., Smith T.E., 2005, ApJ, 633, 828

Mouhcine M., Bamford S.P., Aragón-Salamanca A., Nakamura O., Milvang-Jensen B., 2006, MNRAS, 368, 1871

Mouhcine M., Bamford S.P., Aragón-Salamanca A., Nakamura O., Milvang-Jensen B., 2006, MNRAS, 369, 891

Mould J., Kristian J., 1986, ApJ, 305, 591

Moustakas J., Kennicutt R.C., 2006, ApJ, 651, 155

Mowlavi N., Jorissen A., Arnould M., 1998, A&A, 334, 153

Myra E.S., Burrows A., 1990, ApJ, 364, 222

Nakanishi H., Sofue Y., 2003, PASJ, 55, 191

Navarro J.F., Helmi A., Freeman K.C., 2004, ApJ, 601, 43

Padmanabhan T., 1993, Structure formation in the universe, Cambridge University Press, Cambridge, UK

Pagel B.E.J., Tautvaišiene G., 1995, MNRAS, 276, 505

Pettini M., Kellogg M., Steidel C.C., Dickinson M., Adelberger K.L., Giavalisco M., 1998, ApJ, 508, 539

Pettini M., lectures given at the XIII Canary Islands Winter School of Astrophysics, “Cosmochemistry: The Melting Pot of Elements”, Cambridge University Press

Pizagno J., Prada F., Weinberg D.H., Rix H.-W., Harbeck D., Grebel E.K., Bell E.F., Brinkmann J., Holtzman J., West A., 2005, ApJ, 633, 844

Preston G.W., Shectman S.A., Beers T.C., 1991, ApJ, 375, 121

Pritchet, C.J., van den Bergh, S., 1994, AJ, 107, 1730

Prochaska J.X., Gawiser E., Wolfe A.M., Castro, S., Djorgovski, S.G., 2003, ApJ, 595, L9

Putman M.E., Bland-Hawthorn J., Veilleux S., Gibson B.K., Freeman K.C., Maloney P.R., 2003, ApJ, 597, 948

Rana, N.C., 1991, ARA&A, 29, 129

Reitzel D.B., Guhathakurta P., Gould A., 1998, AJ, 116, 707

Reitzel D.B., Guhathakurta P., 2002, AJ, 124, 234

Reitzel D.B., Guhathakurta P., Rich R.M., 2004, AJ, 127, 2133

Renda A., Fenner Y., Gibson B.K., Karakas A.I., Lattanzio J.C., Campbell S., Chieffi A., Cunha K., Smith V.V., 2004, MNRAS, 354, 575

Renda A., Kawata D., Fenner Y., Gibson B.K., 2005, MNRAS, 356, 1071

Renda A., Gibson B.K., Mouhcine M., Ibata R.A., Kawata D., Flynn C., Brook C.B., 2005b, MNRAS, 363, L16

Renzini A., Voli M., 1981, A&A, 94, 175

Rich R.M., Reitzel D.B., Guhathakurta P., Gebhardt K., Ho L.C., 2004, AJ, 127, 2139

Robertson B., Bullock J.S., Cox T.J., Di Matteo T., Hernquist L., Springel V., Yoshida N., 2006, ApJ, 645, 986

Robin A.C., Creze M., Mohan V., 1992, ApJ, 400, L25

Ruphy S., Robin A.C., Epchtein N., Copet E., Bertin E., Fouque P., Guglielmo F., 1996, A&A, 313, L21

Russell S.C., Dopita M.A., 1992, ApJ, 384, 508

Ryan S.G., Norris J.E., 1991, AJ, 101, 1865

Sakamoto T., Chiba M., Beers T.C., 2003, A&A, 397, 899

Salpeter E.E., 1955, ApJ, 121, 161

Sarajedini A., van Duyne J., 2001, AJ, 122, 2444

Savaglio S., Glazebrook K., Le Borgne D., Juneau S., Abraham R.G., Chen H.-W., Crampton D., McCarthy P.J., Carlberg R.G., Marzke R.O., Roth K., Jørgensen I., Murowinski R., 2005, ApJ, 635, 260

Schaller G., Schaerer D., Meynet G., Maeder A., 1992, A&AS, 96, 269

Schlegel D.J., Finkbeiner D.P., Davis M., 1998, ApJ, 500, 525

Searle L., Zinn R., 1978, ApJ, 225, 357

Secker J., Harris W.E., 1993, AJ, 105, 1358

Sembach K.R., Gibson B.K., Fenner Y., Putman M.E., 2002, ApJ, 572, 178

Skillman E.D., Kennicutt R.C., Hodge P.W., 1989, ApJ, 347, 875

Smith V.V., 2003, in McWilliam A., Rauch M. Ed., Carnegie Observatories Astrophysics Series, Vol. 4: "Origin and Evolution of the Elements", (Pasadena: Carnegie Observatories, `http://www.ociw.edu/ociw/symposia/series/symposium4/proceedings.html`)

Smith V.V., Cunha K., Hinkle K.H., Blum R.D., 2004, submitted

Sneden C., Kraft R.P., Prosser C.F., Langer G.E., 1991, AJ, 102, 2001

Spergel D.N., Verde L., Peiris H.V., Komatsu E., Nolta M.R., Bennett C.L., Halpern M., Hinshaw G., Jarosik N., Kogut A., Limon M., Meyer S.S., Page L., Tucker G.S., Weiland J.L., Wollack E., Wright E.L., 2003, ApJS, 148, 175

Steinmetz M., Navarro J.F., 1999, ApJ, 513, 555

Stinson G., Seth A., Katz N., Wadsley J., Governato F., Quinn T., 2006, MNRAS, 373, 1074

Talbot R.J. Jr., Arnett W.D., 1971, ApJ, 170, 409

Thacker R.J., Couchman H.M.P., 2000, ApJ, 545, 728

Thilker D.A., Braun R., Walterbos R.A.M., Corbelli E., Lockman F.J., Murphy E., Maddalena R., 2004, ApJ, 601, L39

Tiede G.P., Sarajedini A., Barker M.K., 2004, AJ, 128, 224

Tikhonov N.A., Galazutdinova O.A., Drozdovsky I.O., 2005, A&A, 431, 127

Timmes F.X., Woosley S.E., Weaver T.A., 1995, ApJS, 98, 617

Tinsley B.M., 1980, Fund. Cosm. Phys., 5, 287

Tomkin J., Lemke M., Lambert D.L., Sneden C., 1992, AJ, 104, 1568

Tremonti C.A., Heckman T.M., Kauffmann G., Brinchmann J., Charlot S., White S.D.M., Seibert M., Peng E.W., Schlegel D.J., Uomoto A., Fukugita M., Brinkmann J., 2004, ApJ, 613, 898

Tully B.R., Pierce M.J., Huang J.-S., Saunders W., Verheijen M.A.W., Witchalls P.L., 1998, AJ, 115, 2264

VandenBerg D. A., Swenson F.J., Rogers F.J., Iglesias C.A., Alexander D.R., 2000, ApJ, 532, 430

van den Bergh S., in ‘‘The Local Group as an Astrophysical Laboratory’’, 2003, Cambridge University Press

Vassiliadis E., Wood P.R., 1993, ApJ, 413, 641

Vilchez J.M., Esteban C., 1996, MNRAS, 280, 720

Walterbos R.A.M., Kennicutt R.C., 1988, A&A, 198, 61

Williams B.F., 2002, MNRAS, 331, 293

Williams B.F., 2003, AJ, 126, 1312

Woosley S.E., Haxton W.C., 1988, Nature, 334, 45

Woosley S.E., Hartmann D.H., Hoffman R.D., Haxton W.C., 1990, ApJ, 356, 272

Woosley S.E., Weaver T.A., 1995, ApJS, 101, 181

Woosley S.E., Heger A., Weaver T.A., 2002, Reviews of Modern Physics, 74, 1015

Woosley S.E., Heger A., Weaver T.A., 2002, Rev. Mod. Phys., 74, 1015

Worthey G., España A., MacArthur L.A., Courteau S., 2005, ApJ, 631, 820

Wyse R.F.G., Silk J., 1989, ApJ, 339, 700

Zaritsky D., Kennicutt R.C., Huchra J.P., 1994, ApJ, 420, 87

Zibetti S., White S.D.M., Brinkmann J., 2004, MNRAS, 347, 556

Zucker D.B., Kniazev A.Y., Bell E.F., Martinez-Delgado D., Grebel E.K., Rix H.-W., Rockosi C.M., Holtzman J.A., Walterbos R.A.M., Ivezić Ž., Brinkmann J., Brewington H., Harvanek M., Kleinman S.J., Krzesinski J., Lamb D.Q., Long D., Newman P.R., Nitta A., Snedden S.A., 2004, ApJ, 612, L117

Publications

Refereed Journals

[1] **Renda A.**, Gibson B.K., Mouhcine M., Ibata R.A.,
Kawata D., Flynn C., Brook C.B.,
Mon. Not. R. Astron. Soc. Lett. **363**, L16 (2005)

[2] **Renda A.**, Kawata D., Fenner Y., Gibson B.K.,
Mon. Not. R. Astron. Soc. **356**, 1071 (2005)

[3] **Renda A.**, Fenner Y., Gibson B.K., Karakas A.I., Lattanzio J.C.,
Campbell S., Chieffi A., Cunha K., Smith V.V.,
Mon. Not. R. Astron. Soc. **354**, 575 (2004)

Proceedings

[1] **Renda A.**, Fenner Y., Gibson B.K., Karakas A.I., Lattanzio J.C.,
Campbell S., Chieffi A., Cunha K., Smith V.V.,
Nuclear Physics A **758**, 324 (2005),
Buchmann L., Comyn M., Thomson J. Editors,
Proceedings of The 8th Int. Symposium on Nuclei in the Cosmos,
Vancouver, British Columbia, Canada, 2004

Poster Presentations

[1] **Renda A.**, Gibson B.K., Mouhcine M., Ibata R.A.,
Kawata D., Flynn C., Brook C.B.,
The Stellar Halo Metallicity-Luminosity Relationship for Spiral Galaxies,
"The Fabulous Destiny of Galaxies: Bridging Past and Present"
Laboratoire d'Astrophysique de Marseille 5th Int. Cosmology Conf.,
Marseille, France, 2005

[2] **Renda A.**, Fenner Y., Gibson B.K., Karakas A.I., Lattanzio J.C.,
Campbell S., Chieffi A., Cunha K., Smith V.V.,
The Evolution of Fluorine in Galactic Systems,
The 8th Int. Symposium on Nuclei in the Cosmos,
Vancouver, British Columbia, Canada, 2004

Colloquia

[1] *The Stellar Halo Metallicity-Luminosity Relationship for Spiral Galaxies*,
held June 9, 2005, at L'Observatoire Astronomique de Strasbourg,
Strasbourg, France

[2] *The Stellar Halo Metallicity-Luminosity Relationship for Spiral Galaxies*,
held May 31, 2005, at The Obs. of the Carnegie Inst. of Washington,
Pasadena, Cal., U.S.A.